Investigation of Novel Methods for Manufacturing Polyimide Aerogel Stock Shape

A thesis in fulfilment of the requirements for the degree of
Doctor of Philosophy

By

Shima Dayarian

Department of Mechanical and Aerospace Engineering

University of Strathclyde

Glasgow, Scotland

Declaration of Authenticity and Author's Right

This thesis is the result of the author's original research. It has been composed by the author and has not been previously submitted for examination which has led to the award of a degree. The copyright of this thesis belongs to the author under the terms of the United Kingdom Copyright Acts as qualified by the University of Strathclyde Regulation 3.50. The due acknowledgement must always be made of the use of any material contained in, or derived from, this thesis.

Signed:

Date: 28/02/2023

ACKNOWLEDGEMENTS

First, I would like to express my sincere gratitude to my supervisors, Dr Liu Yang and Dr Ashleigh Fletcher, who gave me the guidance, support and attention essential for accomplishing this work. I appreciate their expertise which was so necessary for making it possible for me to complete this investigation.

I am also thankful for all the help provided to me by the various members of the Advanced Composites Group. I am incredibly grateful for all the help that Wichain Chailad provided me during the writing-up stage. The departmental technicians and staff at the Advanced Materials Research Laboratory have greatly assisted this research. Further gratitude is also due to the University of Strathclyde for funding my research.

I would also like to thank Blueshift as a company who provide technical support, raw materials, and equipment for my project.

Finally, throughout the completion of this work, my parents encouraged me to pursue my studies and always demonstrated an interest in what I was doing. Appreciation is also due to my husband for his unconditional love, support and encouragement.

PUBLICATION

Some results presented in the following thesis have been published in the following journal articles and one patent was filed with our industrial partner.

S. Dayarian; H. Majedi Far; L. Yang, Macroporous Polyimide Aerogels: A Comparison between Powder Microparticles Synthesized via Wet Gel Grinding and Emulsion Processes, *Langmuir*, 2023, 39, 5, 1804–1814.

S. Dayarian; L.Yang; H. Majedi Far, Development of Polyimide Aerogel Stock Shapes Through Polyimide Aerogel Particles; Accepted at *Journal of Porous Materials*, May 2023.

D. Irvin; S. Dayarian; L. Kagumba; G. Poe; L.Yang, Aerogel Articles Made from Aerogel Particles and Methods for Making the Same, 63/041,805, filed June 19, 2020.

ABSTRACT

Polyimide aerogels have excellent thermal and mechanical properties that make them suitable for a wide range of applications, especially in insulation. They can be fabricated in powder-based, film-based and monolithic forms. However, conventional methods for producing monolithic aerogel can be time-consuming and expensive, especially given the lengthy process required for solvent exchange and drying. Polyimide aerogel in the form of powder particles has therefore attracted significant attention relating to its wide variety of applicable properties, including its high mass diffusion rate and thermomechanical properties, especially as compared with monolithic shapes.

Although this project's industrial partner, Blueshift International Materials, currently manufactures polyimide aerogel in the form of film and stock shape; but there is a desire to further reduce the costs for their stock shape products.

Therefore, it is necessary to develop and modify this method to increase its viability. This PhD project comprises two main work packages to address needs relating to this process. Firstly, the polyimide aerogel particles are synthesised using three different methods: dry-milling, wet gel grinding, and emulsion in ambient pressure drying; secondly, the stock shape form is fabricated by consolidating synthesised particles. Although polyimide aerogel particles can be used directly as a finished product, it is nevertheless desirable to develop a cost-effective process in order to convert polyimide aerogel particles into stock shape. To the best of our knowledge, such an attempt has not been reported within any existing literature on polyimide aerogel.

This study details the development of an alternative technique (adding epoxy and dimethyl sulfoxide solvent) to obtain polyimide aerogel stock shape by consolidating polyimide aerogel particles. Using this technique, the solvent exchange is performed on the powdered form (in less than 3 h), and this results in a significant reduction in the solvent exchange step compared to the stock shape form (144 h). This approach also reduces the cycle time involved in processing polyimide stock shape aerogel by nearly 60%, which has a clear potential for reducing production costs.

In order to produce particles of a variety of sizes, dimethyl sulfoxide was added in different concentrations to dilute it. Microscopic properties of interest, including skeletal and porous structure, microparticle size and assembly, were then examined using nitrogen sorption, mercury intrusion porosimetry and SEM. Macroscopic properties, such as thermal stabilities (up to 500 °C) and conductivities, were also compared and correlated with other parameters, such as densities and dilution ratios. These methods involved using produced particles with diameter sizes between 4 and 20 µm and porosities as high as 94%. The stock shape samples obtained from particle consolidation were characterised by mercury intrusion porosimetry, nitrogen sorption, thermogravimetric analysis and compression testing. Compared with the stock shape made using the existing method, the powder-to-stock shape samples with epoxy addition are promising in terms of appearance and mechanical properties. Compression tests also showed that the addition of epoxy improves the mechanical properties and compressive strength at 10% strain by 18%. In the same context, the samples made using dimethyl sulfoxide as the solvent exhibited higher thermal stability and porosity than stock shapes made using traditional methods. These results suggest that a range of useful thermal and mechanical properties can be obtained for PI aerogel stock shape prepared using particles.

TABLE OF CONTENT

Declaration of Authenticity and Author's Right **2**

ACKNOWLEDGEMENTS **3**

PUBLICATION **4**

ABSTRACT **5**

NOMENCLATURE **13**

LIST OF FIGURES **18**

LIST OF TABLES **26**

Chapter 1 Introduction **27**

1.1 Background 27

1.2 Aims and objectives 29

1.3 Outline of thesis 30

Chapter 2 Literature review: polyimide aerogel chemistry and manufacturing processes **32**

2.1 Polyimide aerogel chemistry 32

2.2 Synthesis of polyimide aerogel 33

2.2.1 Synthesis of polyimide aerogel with dianhydrides and diamine 34

2.2.2 Synthesizing polyimide aerogel using dianhydrides and isocyanates 42

2.3 Solvent exchange 43

2.4 Sol-gel process 45

2.5 Ageing process 48

2.6 Drying process 49

2.6.1 Ambient pressure drying 50

2.6.2 Freeze drying 53

2.6.3 Supercritical drying 55

2.7 Properties of polyimide aerogel 59

2.7.1 The flexibility of polyimide aerogel 60

2.7.2 Moisture resistance and dielectric properties of PI aerogel 60
2.7.3 Thermal stability of PI aerogel 61
2.7.4 Transparency of PI aerogel 61
2.8 Different applications for aerogel 63
2.8.1 Dielectric, communication devices and moisture-proof materials 66
2.9 Different forms of polyimide aerogel 66
2.9.1 Polyimide aerogel stock shape 66
2.9.2 Polyimide aerogel film 70
2.9.3 Polyimide aerogel powder 71
2.10 Consolidation of powder particles 74
2.11 Epoxy resin introduction 76
2.11.1 Properties of epoxy 78
2.11.2 Epoxy resin application 79
2.11.3 Curing process for epoxy 81
2.12 Polyimide-epoxy composite 83
2.13 Different methods for synthesizing the PI aerogel powder 84
2.13.1 Milling process 85
2.13.2 Wet grinding 86
2.13.3 Emulsion polymerisation 87
2.14 Emulsion process 90
2.14.1 Pickering emulsion 91
2.14.2 Stability of emulsion 92
2.14.3 Emulsifier (surfactant) role in the emulsification system 93
2.14.4 Size distribution in the emulsion process 97
2.14.5 PI aerogel synthesis using the emulsion method 98
Chapter 3 Literature review on material characterization 103

3.1 Physical and structural parameters 103
3.1.1 Microscopy 103
3.1.2 Particle size measurement 105
3.1.3 Helium pycnometer 107
3.1.4 Gas sorption porosimetry 108
3.1.5 Mechanical characterisation 114
3.1.6 Heat transfer 119
3.2 Conclusion 123
Chapter 4 Preparation and characterization of polyimide aerogel powder 124
4.1 Experimental work 125
4.1.1 Material 125
4.1.2 Synthesis of polyamic acid (PAA) 125
4.1.3 Synthesis of polyimide aerogel stock shape 128
4.1.4 Dry milling of PI aerogel stock shape 131
4.1.5 Synthesizing PI aerogel powder using wet gel grinding (PI-WGG) 131
4.1.6 Synthesis of polyimide aerogel powders using emulsion (PI-EM) 134
4.1.7 Results relating to the properties of polyimide aerogel powder 137
4.2 Characterization techniques 137
4.2.1 N_2 sorption 137
4.2.2 Mercury Intrusion Porosimetry (MIP) 138
4.2.3 Pycnometer 139
4.2.4 Particle size measurement 140
4.2.5 Thermogravimetric analysis (TGA) 142
4.2.6 Thermal conductivity 143
4.2.7 Scanning Electron microscopy (SEM) 144
4.3 Results of characterizing milled polyimide aerogel powder 145

4.3.1 N_2 sorption for dry-milled powder 145

4.3.2 Mercury Intrusion Porosimetry (MIP) for dry-milled powder 146

4.3.3 Particle size measurement 147

4.3.4 Thermogravimetric analysis (TGA) of dry-milled powder 150

4.3.5 Thermal conductivity of dry-milled powder 152

4.4 Characterization results of the wet gel ground powder (PI-WGG) 154

4.4.1 N_2 sorption for PI-WGG powders 154

4.4.2 Mercury Intrusion Porosimetry (MIP) for PI-WGG powders 156

4.4.3 Particle size measurement for PI-WGG powders 159

4.4.4 Thermogravimetric analysis (TGA) of PI-WGG powders 163

4.4.5 Thermal conductivity for PI-WGG powders 165

4.5 Characterization results of the PI-EM 168

4.5.1 Investigating the effect of stirring speed on a small scale 168

4.5.2 Investigation of the dilution process on particle size during the emulsion process 171

4.5.3 Investigation into solvent exchange and drying 175

4.5.4 Scaling up the emulsion process 180

4.5.5 Characterization of the PI-EM particles at large scale 181

4.5.6 Assessment of mixing time 186

4.5.7 Summary of emulsion synthesis process 191

4.5.8 Investigation of the dilution process at PI-EM for scaling up process 191

4.6 Conclusion 200

Chapter 5 Consolidation of powder particles to produce polyimide aerogel stock shape 201

5.1 Introduction 201

5.2 Experimental 201

5.2.1 Materials 201

5.2.2 PI aerogel particle 202

5.2.3 Incorporation of DMSO 203

5.2.4 Incorporation of epoxy 204

5.2.5 Particle consolidation 205

Chapter 6 Results of characterization of polyimide aerogel stock shape 208

6.1 Introduction 208

6.2 Characterization of dry-milled polyimide aerogel stock shape with DMSO (PI-DMSO) 208

6.2.1 N_2 sorption 208

6.2.2 Mercury Intrusion Porosimetry (MIP) for PI-DMSO stock shape 210

6.2.3 Thermogravimetric analysis (TGA) for PI-DMSO 214

6.2.4 Mechanical properties of PI-DMSO 215

6.2.5 Thermal conductivity of PI-DMSO stock shape 217

6.3 Characterization of the stock shape with epoxy (PI-epoxy) 220

6.3.1 N_2 sorption 220

6.3.2 Mercury Intrusion Porosimetry (MIP) for PI-epoxy stock shape 221

6.3.3 Thermogravimetric analysis (TGA) of PI-epoxy 223

6.3.4 Thermal conductivity for PI-epoxy 227

6.4 Comparison between different types of stock shape in this work 230

6.5 Characterization results of wet gel ground powder stock shape (PI-WGG-epoxy) 232

6.5.1 N_2 Sorption for PI-WGG-epoxy stock shape 233

6.5.2 MIP for PI-WGG-epoxy stock shape 234

6.5.3 TGA for PI-WGG-epoxy stock shape 236

6.5.4 Mechanical properties of PI-WGG-epoxy 238

6.5.5 Thermal conductivity of PI-WGG-epoxy stock shape 239

6.5.6 Summary 242

6.6 Characterization results for emulsion powder stock shape (PI-EM-stock shape) . 243

6.6.1 N_2 sorption for PI-EM-epoxy 243

6.6.2 MIP for PI-EM-epoxy 244

6.6.3 TGA for PI-EM-epoxy stock shape 247

6.6.4 Mechanical properties of PI-EM-epoxy stock shape 248

6.6.5 Thermal conductivity of PI-EM-epoxy stock shape 250

6.6.6 Summary 252

Chapter 7 Conclusion and future work 254

7.1 Conclusion of thesis 254

7.2 Future work 256

References 259

NOMENCLATURE

2-MI	2-methyl imidazole
2-MI	2-methyl imidazole
6FDA	2, 2-bis(3,4-anhydrodicarboxyphenyl) hexafluoropropane
6FDA	4,4′-hexafluoroisopropylidene di(phthalic anhydride)
ABS	Poly(acrylonitrile-*co*-butadiene-*co*-styrene)
AgNW	Ag nanowire
ANF	Aramid nanofiber
APBO	5-amino-2-(4-aminophenyl)benzoxazole
APBO	5-amino-2-(4-aminopheyl)benzoxazole
APD	Ambient pressure drying
BA	Benzoic anhydride
BABB	1,3-bis [4-(3-aminophenoxy)benzoyl] benzene
BAPF	9, 9′- bis(4-aminophenyl)fluorine
BAPN	3-bis(4-amino phenoxy)-2,2- dimethylpro-pane
BET	Brunauer, Emmet and Teller
Bisphenol-S	4,4,'-dihydroxy diphenyl sulfone
BJH	Barrett, Joyner, and Halenda
BPA	Bisphenol-A
BPDA	3,3',4,4'-biphenyltetracarboxylic dianhydride
BTC	1,3,5-benzenetricarbonyl trichloride
BTDA	3',4,4'-benzophenone tetracarboxylic dianhydride
CA	Carbon aerogel
CMC	Critical micelle concentrations
DADD	1,12- dodecyldiamine
DFT	Density-Functional-Theory

DGEBA	Diglycidyl ether of bisphenol A
DGEBF	Diglycidyl ether of bisphenol-F
DGEBH	Diglycidyl ether of bisphenol-H
DGEBS	Diglycidyl ether of bisphenol-S
DMB	4,4’-diamino-2,2’-dimethylbiphenyl
DMBZ	2,2'- dimethyl benzidine
DMF	Dimethyl formamide
DMSO	Dimethyl sulfoxide
DSC	Differential scanning calorimetry
ECH	Epichlorohydrin
EDL	Facilitate entry, descent, and landing processes
EDL	Entry, descent, and landing
EM	Emulsion
f_{coal}	Coalescence frequency
$f_{collision}$	Collision frequency
FTPS	Flexible, thermal and protection
G	Energy
g	Gravitational acceleration
G_{intef}	Interfacial energy
GO	Graphene Oxide
GPS	Global positioning systems
H_E	Height of the initial emulsion
HIAD	Hypersonic inflatable aerodynamic declaration
HIP	Hot isostatic pressi
H_L	Height of the lower phase after separation
HLB	Hydrophile - Lipophile Balance

MDA	m-phenylene diamine
MDI	4,4′- methylenediphenyl diisocyanate
MIP	Mercury intrusion porosimetry
MWS	Microwave sintering
NASA	National Aeronautics and Space Administration
NMP	N-methyl-2-pyrrolidone
O/W	Oil in water
O/W/O	Emulsion oil-in-water-in-oil
OAPS	Octa (aminophenyl)- silsesquioxane
ODA	4,4’-oxydianiline
ODPA	4,4- oxydiphthalic anhydride
PA	Phthalic anhydride
PAA	Polyamic acid
PATP	P- aminothiophenol
P_{coal}	Coalescence probability
PEI	Poly(ether imides)
PEK	Poly(ether ketone)
PES	Poly(ether sulfones)
PI	Polyimide
PI-EM	Polyimide aerogel powders by EM
PI-WGG	Polyimide aerogel powders by WGG
PMDA	Pyromellitic dianhydride
PMDA	Pyromellitic dianhydride
PMMA	Polymethyl methacrylate
PMR	Polymerization of monomeric reactants
PNFAs	Polyimide nanofiber aerogels

POE	Polyoxyethylene
PSD	Particle size distribution
PSD	Particle size distribution
PSF	Polysulfones
ROMP	Ring-opening metathesis polymerisation
SCFs	Supercritical fluids
SEM	Scanning electron microscopy
TAPB	1,3,5-tris(aminophenyl)benzene
TAPOB	1,3,5-Tris(4-aminophenoxy) benzene
TAPP	2,4,6-tris(4- aminophenyl)pyridine
TBA	t-butanol
TEM	Transmission electron microscopy
TENGs	Triboelectric nanogenerator
TENGs	Triboelectric nanogenerators
Tg	Glass temperature
TGA	Thermal gravimetric analysis
TMFB	2, 2′- bis-(trifluoromethyl)- 4,4′- diaminobiphenyl
TPI	Thermoplastic PI
TPS	Transient plane source
TPU	Thermoplastic polyurethane
TREN	Tris(2-aminoethyl)amine
VD	Vacuum drying
W	Work
W/O	Water in oil
WGG	Wet gel grinding
wt	Weight

XRD	X-ray diffraction
η	Viscosity
ρ_b	Bulk density
ρ_s	Skeletal density
σ	Specific surface area
υ	Creaming (or settling) velocity

LIST OF FIGURES

Figure 2.1 Molecular structure of (a) aromatic PI and (b) aliphatic PI [36] 32

Figure 2.2 Synthesis route for PI aerogel: (a) two-step method, (b) isocyanate method [39] 34

Figure 2.3 Chemical structure of Kapton PI [44] 35

Figure 2.4 PI aerogel manufacturing and drying [47] 36

Figure 2.5 Synthetic route for PI aerogels crosslinked with TAB [48] 37

Figure 2.6 SEM image for produced PI using different diamines and dianhydrides, ODA: 4,4-Oxydianiline, BPDA: 3,3,4,4-Biphenyltetracarboxylic dianhydride, DMBZ: 2,2-Dimethyle benzidine, BTDA: 3,4,4,4-Benzophenone tetracarboxylic dianhydride [21] 42

Figure 2.7 Sol-gel reaction for alkoxysilane [81] 46

Figure 2.8 Preparation of aerogels using sol-gel chemistry [82] 47

Figure 2.9 A meniscus in a pure wet gel [108] 51

Figure 2.10 Phase diagram of the liquid phase removed from the gel [124] 56

Figure 2.11: Silica aerogel obtained by supercritical drying (left) and ambient drying (right) [124] 56

Figure 2.12 Flowsheet of supercritical drying with CO_2 [92] 57

Figure 2.13 Methods for improving the properties of the PI aerogel [39] 59

Figure 2.14 Different applications for aerogels [146] 63

Figure 2.15 Total number of publications examining aerogel over the past 30 years (1988-2019) [2] 64

Figure 2.16 Typical applications of PI nano-aerogels. HIAD: Hypersonic inflatable aerodynamic declaration; EDL: Entry, descent, and landing; FTPS: flexible, thermal and protection Thermal insulation materials [39] 65

Figure 2.17 (a) epoxy group (oxirane), (b) aliphatic, (c)cycloaliphatic [188] 77

Figure 2.18 Chemical structure of diglycidyl ether of bisphenol A (DGEBA) [188] 78

Figure 2.19 Different applications of epoxy; a)flooring; b) adhesive properties; c)chip; d) corrosion resistance [206] 80

Figure 2.20 Soap molecule array in micelles [239] 87

Figure 2.21 Kinetic versus thermodynamic stability [241].....90

Figure 2.22 Measuring creaming stability via visual observation with a long-term storage test [248].....93

Figure 2.23 Schematic of the structure of a surfactant molecule [253] 97

Figure 3.1 The critical structural parameters of a porous material [56].....103

Figure 3.2 Nature of particles, b) relations between particle size and nature [270] 105

Figure 3.3 Schematic setup for helium pycnometer with an initial pressure in the sample [18].....107

Figure 3.4 Chemical and physical adsorption on a solid surface [275] 108

Figure 3.5 Different types of physical adsorption isotherms [278] 112

Figure 3.6 Three isotherms for silica aerogels with a different equilibration time [160] 113

Figure 3.7 The stress-strain curve of a silica aerogel under compression [286].....115

Figure 3.8 Schematic diagram of the stress-strain curve in a tensile test [286].....116

Figure 3.9 The typical stress-strain curve in a compression test [286].....117

Figure 3.10 Schematic diagram for an aerogel structure and heat transfer mechanism. The heat can be transferred by means of a solid backbone (indicated by the red particle chain), by molecular gas inside the porous structure of the aerogel (blue dots) and by thermal radiation (wavy yellow arrows) [18].....119

Figure 4.1 (a) Baffled reactor and temperature controller; (b) PAA.....126

Figure 4.2 CGOLDENWALL Digital Rotary Viscosity Meter used in this work 128

Figure 4.3 Synthesis of PAA and PI aerogel from amines (DMB, ODA, TAPOB) and anhydrides (BPDA, PA), catalysed with 2-MI [315].....130

Figure 4.4 (a) PI stock shape, (b) stinger for milling the PI stock shape, and (c) PI powder aerogel produced through dry milling of PI stock shape 131

Figure 4.5 (a) reactor used for mixing the solution in the closed area, (b) mixing the polyamic acid resin in the reactor overnight, (c) draining the PAA from the reactor, (d) chemical imidization induced by adding 2-MI, (e) leaving for 24 h at 23 °C, (f) wet gel PI after 24h, (g) grinding the wet gel to produce the powder with kitchen blender, (h) solvent exchange and filtration process, (i) dried powder (24h RT, 30min at 200°C) .133

Figure 4.6 a) mixing the cyclohexane with emulsifiers, b) performing the dilution and adding the catalysts into the PAA as a dispersed phase during the emulsion process..135

Figure 4.7 (a) cyclohexane with emulsifiers at 500 RPM, (b) the addition of PI to the cyclohexane, followed by mixing for 1 h at 500RPM, (c) sedimentation, (d) solvent exchange and suction filtration, (e) dried powder (45minRT, 2h 50°C,30min 200°C in air) 136

Figure 4.8 Micromeritics ASAP 2420 Surface Area and Porosity Analyser 138

Figure 4.9. Autopore V model 9605, surface area and porosity analyser 139

Figure 4.10 Helium Pycnometr used in this work 140

Figure 4.11 Different steps for using Image-Pro for particle size measurement, a) opening a optical microscopic image in Image-Pro, b) counting the number of the particles, c) applying manual split to separate any particles that are overlapping, d) counting the number of particles after separation, e) extracting the measurement data from the software 141

Figure 4.12 Different diameters for a non-uniform particle 142

Figure 4.13 TA Instruments Q50 thermogravimetric analyser (TGA) 143

Figure 4.14 Schematic image detailing the technique for measuring thermal conductivity 144

Figure 4.15 Thermal conductivity measurement set-up: a) TC3000E thermal conductivity meter sensor, b) powder measurement, c) stock shape measurement 144

Figure 4.16 N_2 sorption for milling powder, (a) pore size distribution, (b) N_2 sorption isotherms (at -196 °C) 145

Figure 4.17 MIP pore size distribution for Aero-Zero powder 147

Figure 4.18 a) optical and b-e) SEM image from Aero-Zero powder 148

Figure 4.19 Particle size distribution for dry-milled powder 149

Figure 4.20 Frequency of particle size for dry milling powder using sieve measurement data 150

Figure 4.21 correlation of weight change against (a) temperature and (b) time for Aero-Zero powder 151

Figure 4.22, (a) weight changes and (b) rates of weight change as a function of temperature for Aero-Zero powder 151

Figure 4.23. N_2 sorption for wet gel ground powder, (a) pore size distribution, (b) N_2 sorption isotherms (at -196 °C) 155

Figure 4.24. MIP (a) pore size distribution; (b) correlation of cumulative intrusion with pressure for PI-WGG 157

Figure 4.25. Correlation of porosity with density for wet gel ground powders.....158

Figure 4.26. Correlation of skeletal density with the ratio of dilution for wet gel ground powders 159

Figure 4.27. The particle size of the PI-WGG powders for the different ratios of dilution 160

Figure 4.28. Particle size distribution for wet gel ground powder (produced using Image Pro).....161

Figure 4.29. SEM and optical images for PI-WGG powders, a) DMSO:PAA=0,b) DMSO:PAA =0.5, c) DMSO:PAA=1, d) DMSO:PAA=1.5.....162

Figure 4.30. (a) weight, and (b) rates of weight change as a function of temperature for dry wet gel ground powder 164

Figure 4.31. Onset temperature and temperature at 10% decomposition for PI-WGG powders at different ratios of dilution.....164

Figure 4.32. Correlation of the rate of weight change with particle size.....165

Figure 4.33 Correlation for thermal conductivity for PI-WGG powder with a) particle size and b) density.....166

Figure 4.34. N_2 sorption for PI aerogel synthesised using an emulsion-based method at different stirring speeds, a) pore size distribution, b) N_2 sorption isotherm at -196 °C. 169

Figure 4.35 SEM image for PI-EM with different stirring speeds in small scale (a) 300 rpm, (b) 400 rpm, (c) 500 rpm 170

Figure 4.36. a) pore size distribution, (b) N_2 sorption isotherms (at -196 °C) for emulsion at different ratios of dilution.....172

Figure 4.37. Optical microscopic image for the PI-EM with different DMSO ratios on a small scale 173

Figure 4.38. Frequency of particle size for PI-EMs at different ratio of DMSO:PAA at small scale 174

Figure 4.39. a) weight changes and (b) rates of weight change as a function of temperature for PI-EM with different DMSO ratios on a small scale 175

Figure 4.40. Correlation of weight change with time for samples subject to different washings (5washes: 3 washes every 20 min, two extra washed every 45 min; 4 washes: 3 washes every 20 min followed by one more wash for 45 min) 177

Figure 4.41. Correlation of weight change with temperature regarding removing the acetone using different drying processes 178

Figure 4.42. Stirring speed experiments used for scaling up the emulsion process.....181

Figure 4.43 N_2 sorption for the PI-EM at 300 and 500 rpm at a large volume, (a) pore size distribution, (b) N_2 sorption isotherms (at -196 °C) 182

Figure 4.44 Pore size distribution for PI-EMs at a large scale.....183

Figure 4.45 SEM micrographs for PI-emulsion particles at stirring speed; a)300 rpm, b)500 rpm 184

Figure 4.46. Correlation of weight change with temperature during the emulsion process for large scale production.....185

Figure 4.47. SEM micrograph for emulsion particles, (a) 1 h of mixing, (b) 2 h of mixing, and (c) 24 h of mixing.....187

Figure 4.48. FTIR spectra of Aero-Zero and PI-EM with different stirring times 188

Figure 4.49. MIP pore size distribution at different stirring times.....190

Figure 4.50. a) pore size distribution, (b) N_2 sorption isotherms (at -196 °C) for PI-EM at different dilution ratios and large volumes 192

Figure 4.51 MIP characterization for PI-EM; a) pore size distribution; b) correlation of cumulative intrusion with pressure 194

Figure 4.52. Correlation of density for emulsion PI powder aerogel with (a) porosity and (b) ratio of dilution.....196

Figure 4.53. SEM microstructures of the PI-EMs with ratios of (a) 0, (b) 0.5, (c) 1, (d) 1.5, (e) single particle that can be detected by an optical microscope.....197

Figure 4.54. Frequency of different sizes of particles for PI emulsion particles at different dilution ratios.....198

Figure 5.1. Photograph and SEM images of (a) dry milled PI powder, (b) PI-WGG-0.5, and (C) PI-EM-0.5 203

Figure 5.2. A Photograph of (a) the addition of DMSO to the PI aerogel particles, and (b) the mixing of the particles with DMSO after the addition of acetone.....204

Figure 5.3. Photographs of (a) a slurry of water-PI aerogel particles, (b) the mixture after the addition of epoxy, and (c) filtering of the overall mixture 205

Figure 5.4. A photograph of the tooling used to consolidate the particles and produce the stock shape samples after demoulding.....206

Figure 5.5. a and b) Aluminium and c and d) PTFE mould.....207

Figure 6.1. N_2 sorption PI-DMSO stock shape, (a) pore size distribution, (b) N_2 sorption isotherms (at -196 °C).....210

Figure 6.2. (a) MIP pore size distribution, (b) correlation of porosity with concentration of DMSO 212

Figure 6.3. Correlation of bulk density with DMSO content 213

Figure 6.4. SEM images of PI-DMSO samples with (a) 0.0; (b) 5.0, and (c) 30% DMSO 213

Figure 6.5. (a) Weight, (b) rates of weight change as a function of temperature for PI-DMSO samples 214

Figure 6.6 Instron 5969 series universal used for mechanical testing 215

Figure 6.7. Stress-strain curve for PI-DMSO stock shape 216

Figure 6.8. Compressive modulus of PI-DMSO stock-shape as a function of the concentration of DMSO 217

Figure 6.9. Correlation of thermal conductivity with (a) DMSO content, and (b) bulk density for PI-DMSO samples 218

Figure 6.10. N_2 sorption PI-epoxy stock shape, (a) pore size distribution, (b) N_2 sorption isotherms (at -196 °C) 221

Figure 6.11. (a) MIP pore size distribution, (b) correlation of porosity with epoxy content for PI-epoxy samples 222

Figure 6.12. Correlation of porosity with density for PI-epoxy samples 222

Figure 6.13. SEM microscopic images of PI-epoxy samples at (a) 0.0; (b) 5, and (c) 20% epoxy 223

Figure 6.14. (a) Weight, (b) rates of weight change as a function of temperature for PI-epoxy samples 224

Figure 6.15. Relation between onset temperature and epoxy concentrations Mechanical properties of PI-epoxy 225

Figure 6.16. Correlation of stress with strain for PI-epoxy 226

Figure 6.17. (a) Compressive strength and (b) compressive modulus of PI-epoxy stock shape as a function of the concentration of epoxy. 227

Figure 6.18. Correlation of thermal conductivity of PI-epoxy stock shape samples with (a) concentration of epoxy, and (b) density of stock shape 228

Figure 6.19. SEM microscopic images of Blueshift stock shape 230

Figure 6.20. PI-WGG-0% epoxy sample after demoulding 232

Figure 6.21. N_2 sorption of PI-WGG-epoxy stock shape, (a) pore size distribution, (b) N_2 sorption isotherms (at -196 °C) 234

Figure 6.22. MIP pore size distribution for PI-WGG-epoxy 235

Figure 6.23. SEM for PI-WGG stock shape with 5% epoxy with different dilution ratios in powders; (a) 0.0; (b)0.5; (c) 1.0; (d) 1.5 236

Figure 6.24 Correlation of weight change with temperature for PI-WGG-epoxy 237

Figure 6.25. Correlation of weight change with time for PI-WGG-5%EP sample under the isotherm condition 237

Figure 6.26. Stress-strain curve for PI-WGG-epoxy stock shape 238

Figure 6.27. Correlation of (a) compressive modulus and (b) compressive strength with types of powder for PI-WGG-5% epoxy stock shape 239

Figure 6.28. Compressive modulus-density for PI-WGG-5% epoxy samples 239

Figure 6.29. Comparison between properties of the most optimal PI-WGG stock shape and the Aero-Zero stock shape with 5% epoxy and the stock shape produced directly by Blueshift 242

Figure 6.30. a)Pore size distribution, (b) N_2 sorption isotherms (at -196 °C) for PI-EM-5% EP at different dilution ratios 244

Figure 6.31. MIP pore size distribution for PI-EM-5% EP 245

Figure 6.32. Correlation of porosity and density with the type of powder in the stock shape samples 246

Figure 6.33. SEM micrograph of the PI-EM-5%EP stock shape sample with powder of different dilution ratios 247

Figure 6.34. Correlation of weight change with temperature for PI-EM-5%EP 248

Figure 6.35. Correlation of weight change with time for PI-EM-5%EP sample under the isotherm condition 248

Figure 6.36. Stress-strain curve for PI-EM-5%EP samples with powders with different dilution ratios 249

Figure 6.37 Compressive Modulus-density correlation for PI-EM-EP samples 249

Figure 6.38. Change in thermal conductivity as a function of density for PI-EM-EP stock shape 250

Figure 6.39. Comparison between properties of PI-EM-1 stock shape, the Aero-Zero stock shape with 5% epoxy and the stock shape produced directly 252

Figure 6.40. Comparison between properties of the most optimal PI-EM-1 stock shape, the directly-produced Blueshift stock shape and PI-WGG-0.5.....253

LIST OF TABLES

Table 1.1 Properties of some common organic aerogels [18] 28

Table 2.1 Values of capillary tension for different solvents and pore sizes calculated for T = 20 °C and δ = 1 nm using equation (1) [109] 52

Table 2.2 Two-phase colloidal systems [239] 88

Table 2.3 HLB number and corresponding applications [248] 95

Table 4.1 A formulation for the synthesis of PAA 127

Table 4.2 Formulations for the preparation of PI-WGG aerogel powders 134

Table 4.3 Formulations for the preparation of PI-EM aerogel powders 136

Table 4.4 Property of Aero-Zero powder 153

Table 4.5 Properties of PI-WGG powders 167

Table 4.6 properties for PI-EM at different stirring speeds (small scale) 171

Table 4.7 Residual solvents at different stages of drying 179

Table 4.8. Properties of the PI-EMs on a large scale 185

Table 4.9 Properties of emulsion particles at different mixing times 190

Table 4.10 Properties of emulsion PI powder aerogels 199

Table 6.1. Key materials properties of PI stock-shapes produced with PI aerogel particles treated with DMSO 219

Table 6.2. Key materials properties of PI stock-shapes produced using PI aerogel particles treated with epoxy 229

Table 6.3. Key material-related properties of directly produced PI stock shapes with Blueshift 232

Table 6.4. Key properties of PI-WGG-5%EP at a different dilution ratio of powder .. 241

Table 6.5 Key properties of PI-EM-5%EP with different dilution ratios 251

Chapter 1 Introduction

1.1 Background

The term “aerogel” describes a solid three-dimensional material with high porosity up to 99% [1]. This material can be in the form of organic, inorganic or hybrid molecular precursors created using the sol-gel processing method [2]. Aerogels were first developed in 1931 by Steven Kistler [3] at the College of the Pacific in Stockton, California, and have since been reported for silica, polymers [4, 5], transition metals and hybrid materials [6]. These first aerogels were made using silica by replacing the liquid component with gas so that this did not result in the collapse of the solid gel network [7]. With extremely low density (0.003 g/cm^3), excellent physical properties, low thermal conductivity (0.005 W/m.K), a low dielectric constant, a high surface area (>1000 m^2/g) [8] and other wonderful properties due to their fine pore structure [9], aerogels remain a highly useful material in a range of different commercial applications. These applications include the architectural domain and appliance insulation [10, 11], catalysts [12], filters [13] and nanoparticle detectors [14].

The first organic aerogel was prepared by Pekala in 1987 using resorcinol and formaldehyde [15], and the resultant product of the condensation reactions between resorcinol and formaldehyde yielded a porous network structure. After supercritical drying, resorcinol formaldehyde aerogels were obtained. Since then, many organic aerogels have been produced, including polybenzoxazine [16], polyurethane [17] and polyuria.

Table 1.1 includes the properties of some common organic aerogels, including their porosity, surface area and average pore diameter.

Table 1.1 Properties of some common organic aerogels [18]

Organic aerogels	Porosity (%)	Surface area (m^2/g)	Average pore diameter (nm)
Resorcinol formaldehyde	80-94	400-900	<50
Polyimide	90-98	500-1000	15-30
δ-form syndiotactic polystyrene	85-94	200-300	100-300
Polyurethane	71-80	50-170	30-43
Polyuria	79-86	100-300	9-16
Polybenzoxazine	60-90	40-80	30-40

One of the most well-known organic aerogels detailed in this table is polyimide (PI) aerogel, which has unique thermal and mechanical properties. After development of tPI aerogel in 2004 [19], a significant level of attention arose around the process of fabricating this substance and improving its properties. Synthesising the PI in recent years has involved the use of several different diamines and dianhydrides, such as 3,3',4,4'-benzophenone tetracarboxylic dianhydride (BTDA), 2,2'- dimethyl benzidine (DMBZ), 3,3',4,4'-biphenyl tetracarboxylic dianhydride (BPDA) pyromellitic dianhydride (PMDA), 2,2'-dimethylbenzidine (DMBZ) and 4,4'-oxydianiline (ODA). Different cross linkers have also been used to optimise the synthesising reaction and reduce production costs [20-22]. Following work undertaken to synthesise PI aerogel, several studies have characterised the resulting PI under different conditions [23-26]. There has also been a focus on developing different applications for PI aerogel in terms of taking advantage of its several advantageous properties, including their use in the insulation of aircraft to facilitate entry, descent and landing (EDL) processes and as acoustic absorbers [14, 23, 27].

Evidence has emerged in respect of several types of materials that, by reducing their total size from the scale of centimetres or millimetres to micrometres or nanometres, it is possible to take advantage of properties useful for a variety of applications in areas such as energy, medicine, drug delivery and catalysts [28-30]. These unique properties cannot be observed when these materials are in film or monolithic shape. Blueshift, the industrial partner to this research project, is one of the worldwide companies producing polyimide aerogel in film and stock shape forms. However, the high costs incurred during the production of the stock shape, together with the high level of demand for this particular product, make it necessary to investigate other possible methods. The findings of this project suggest that it would be viable for Blueshift to synthesise the PI aerogel microparticle first before converting the powder into the stock shape.

1.2 Aims and objectives

As a result of several unique properties, several applications have been identified for PI aerogel particles. However, as noted above, the manufacturing process currently used by Blueshift to produce the PI in stock shape form is very costly. Therefore, there is a need to investigate how this method might be modified to reduce such production costs. In collaboration with Blueshift, the findings of this project investigate the viability of synthesising PI aerogel powder and developing a manufacturing route to convert the PI particles into the stock shape form.

The methodology utilised in this research has four essential features:

1- Two forms of PI aerogel – powder and stock shape – are in hand for use in different applications.

2- It was considered that there was a need to reduce the total production cost in terms of using the pre-existing method for manufacturing the PI stock shape. At a general level, the two elements of the aerogel fabrication process that result in the greatest costs being incurred are solvent exchange and drying. Using these techniques enables the solvent exchange to be placed in the powder particles to reduce costs in terms of time, chemicals and energy.

3- Ambient pressure drying is used with both powder and stock shape samples. It was considered that using the ambient drying method would reduce the total manufacturing cost even if the duration of the drying process was longer than that of supercritical drying.

4- At the end of each stage, the fabricated powders and stock shape samples were characterised and compared, both with each other and with other types of produced aerogels.

1.3 Outline of thesis

This thesis is the result of three years of work. This work involved PI aerogel microparticles being synthesized using milling, wet gel grinding and emulsion processes. The characterized particles were converted into a stock shape with a specific size and shape using two different methods, incorporating both the epoxy and solvent. The stock shapes produced using different powders were then characterised and compared with each other and with the properties of the stock shape, produced directly by Blueshift. This work is detailed in the following seven chapters:

Chapter 2 reviews the existing literature on polyimide chemistry in terms of properties, different synthesis methods, applications, and background information.

Chapter 3 considers the existing relevant literature on characterisation techniques used with aerogels.

Chapter 4 discusses different methods for synthesising and characterizing PI aerogel in powder form. Three different methods, dry milling, wet gel grinding, and emulsion method applied in order to make the polyimide aerogel particles. The synthesized particles were then characterized using different methods.

Chapter 5 considers different methods for producing the PI aerogel stock shape using the powder form. Two different methods, adding solvent and adding epoxy, were applied to the powders and moulded the particles to make the polyimide aerogel stock shape.

Chapter 6 discusses and analyses the results of characterising the PI aerogel stock shape samples made in this work using the methods introduced in Chapter 3.

Chapter 7 summarises the main findings of this study and highlights potential future directions for research in this area.

Chapter 2 Literature review: polyimide aerogel chemistry and manufacturing processes

2.1 Polyimide aerogel chemistry

Polyimides (PI) are high-performance polymers that have higher levels of thermal stability and lower dielectric constants [31, 32] and more favourable mechanical properties compared with silica and polymer–silica hybrid aerogels [21]. The combination of these properties has resulted in these materials being appropriate in a wide range of applications, including lightweight substrates for high-performance antennas [33], flexible insulation for space suits [34], and inflatable structures for aircraft in terms of entry, descent and landing. Among the different organic aerogels, the porously structured PI aerogel is the most sought-after, especially in the areas of thermal insulation and aerospace materials [33].

PI is a polymer consisting of imide group linkage in its backbone. Depending on the different structural units of the molecular change, it can be divided into two main aromatic and aliphatic groups. The aromatic PI has more desirable thermal and mechanical properties due to the presence of benzene and imide rings in the molecular structure [34]. For this reason, much of the existing research focuses on this type of PI [34, 35]. Figure 2.1 shows a typical structure for the PI backbone in different species.

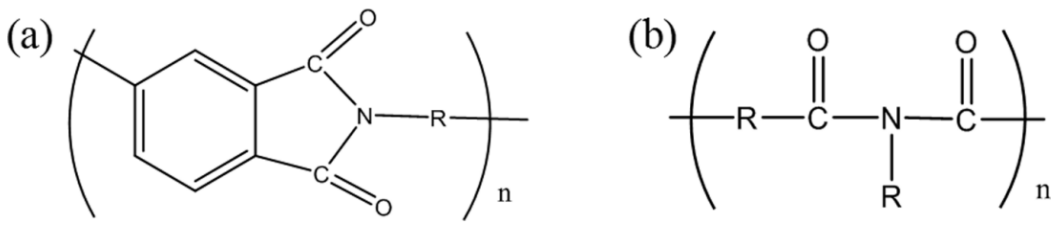

Figure 2.1 Molecular structure of (a) aromatic PI and (b) aliphatic PI [36]

By another method of classification, PI can be divided into two main groups depending on its behaviour after heating, which can be formed in a thermoset or thermoplastic shape. As the thermoset types of PI are insoluble, it is typical for the thermoplastic one to be chosen to optimise the materials. The thermoplastic PI, which is corrosion-resistant, has high thermal and mechanical properties [36]. These properties are demonstrated in the

study of Ke *et al.* [36]. In this study, the researchers used thermoplastic PI (TPI) to toughen thermosetting PI (TMPI) and prepare reinforced PI (TPI/TMPI) blends, which showed a high level of increase in thermal stability and glass transmission temperature for the TPI/TMPI blend sample with a high level of toughness. They used a thermoplastic oligomer soluble at high temperatures. A network structure was formed, causing a crosslinking reaction of the end groups of the imide oligomer. Results of 190 MPa were obtained for the compression test results for carbon fibre-reinforced PI composites prepared using the toughening system.

In accordance with their different chemical structures, PI aerogels can be divided into linear and crosslinked varieties. The linear PI aerogel, first synthesised by Rhine *et al.* [37] has a large volume of shrinkage along with physical crosslinking among the molecules. The cross-linked PI aerogels, meanwhile, can withstand the shrinkage that may occur during the drying process while maintaining a porous structure [38].

Synthesis of the cross-linked PI aerogel was first undertaken by Kawagishi *et al*. [20]. They used Pyromellitic dianhydride (PMDA) and 4,4-oxydiphthalic anhydride (ODPA) as dianhydride with p-phenylenediamine (PDA) and 4,4-oxydianiline (ODA) as diamine. 1,3,5-tris (4-aminophenyl) benzene was applied as a cross-linker. Thermal imidization was followed by supercritical drying. The fabricated pores are reported as being in the range of 50-800 nm.

2.2 Synthesis of polyimide aerogel

The existing literature reports several methods for synthesizing PI aerogel. Among these methods, there are two that are used most extensively [5, 39]. The first, taking place over two steps, is the addition of diamine and dianhydride as raw materials. The second, the isocyanate method, involves dianhydride and isocyanate being used as raw materials. Figure 2.2 shows the synthesis route for these two methods.

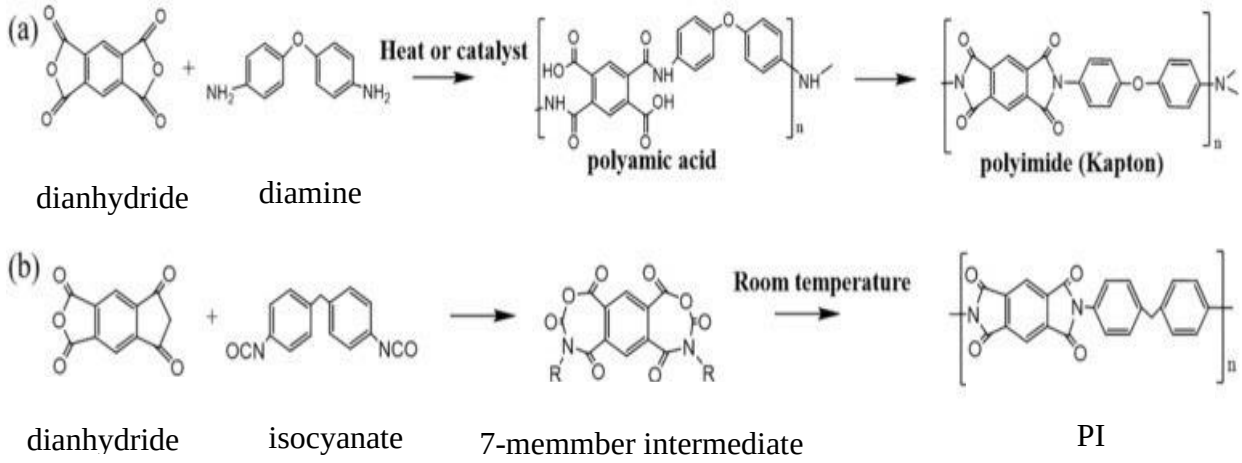

Figure 2.2 Synthesis route for PI aerogel: (a) two-step method, (b) isocyanate method [39]

2.2.1 Synthesis of polyimide aerogel with dianhydrides and diamine

Synthesizing the PI aerogel is based on two different steps. In the first step, the nucleophilic substitution reaction of dianhydride and diamine is done in order to form a polyamic acid (PAA) solution. It is very important that the proper amount of diamines and dianhydride monomers are added to the system to achieve complete imidization and to prevent any unreacted monomer in the system [40]. In the second step, the PAA is subject to the imidization process to be dehydrated and to form an imide ring. There are two methods for conducting this process of imidization: (i) thermal imidization, which requires high-temperature treatment; and (ii) chemical imidization, which should be performed under the action of a catalyst and a dehydrating agent, for example Benzoic anhydride [41, 42]. Occasionally, both types of imidization can be utilised to remove the organic volatiles and increase the speed of imidization [43]. The final PI wet gel and aerogel are obtained from a series of operations, including ageing, solvent exchange and drying. The first PI, which is synthesised with dianhydride and diamines (using pyromellitic dianhydride and 4,4'-oxy aniline), is Kapton [44]. Figure 2.3 shows the chemical structure of Kapton PI.

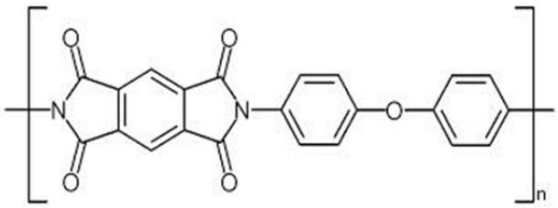

Figure 2.3 Chemical structure of Kapton PI [44]

One of the most crucial considerations in the fabrication of PI aerogels is the choice of diamine and dianhydride monomers. Depending on their functional groups, rigidity and inherent characteristics, the chemistry of the backbone can affect the chain's interaction, gelation time, shrinkage and morphology, and thus also the properties of the final aerogels (physical, mechanical, thermal, electrical and optical) [40]. Synthesizing the PI can be undertaken using several types of dianhydride, including pyromellitic dianhydride (PMDA), benzophenone tetracarboxylic dianhydride and naphthalene tetracarboxylic dianhydride. Examples of diamines include 4, 4'- oxydianiline (ODA), 3,3'-diamino diphenylmethane, and m-phenylene diamine (MDA). The solvent for this process, which may affect the aerogel polymerization and the open-cell content, can be a dipolar aprotic solvent. Most studies have used N-methyl-2-pyrrolidone (NMP) as the solvent material because the essential aprotic nature of NMP can improve the imidization reaction [40]. Dimethylacetamide (DMAc) and dimethylformamide (DMF) are other types of solvents that can be used for synthesising PI [43]. PI aerogels were obtained for the first time via the DuPont process (using chemical dehydration and high temperature for imidization operation)[45]. After that, monomeric reactant (PMR) polymerisation was used as a second method. Leventis *et al.* [46] synthesized the PI aerogel using the PMR route from Bifunctional NAD (bis-NAD). This involved using a second low-temperature process to produce PI aerogels via monomeric reactants (PMR) polymerisation. A proper bisnadimide, bis-NAD, polymerized via ring-opening metathesis polymerization (ROMP), was used as the second-generation Grubbs' catalysts GC-II. Their aerogel is reported as showing a varied range of density from 0.13 to 0.66 g/cm^3 according to changes in the concentration of the bis-NAD. They also report the existence of a high porosity aerogel despite the high level of shrinkage of the wet gel. The robust synthesized PI obtained using this technique is also reported as having thermal conductivity and

mechanical properties comparable to crosslinked aerogels. Figure 2.4 shows the ring-opening polymerization for synthesizing the PI aerogel [47].

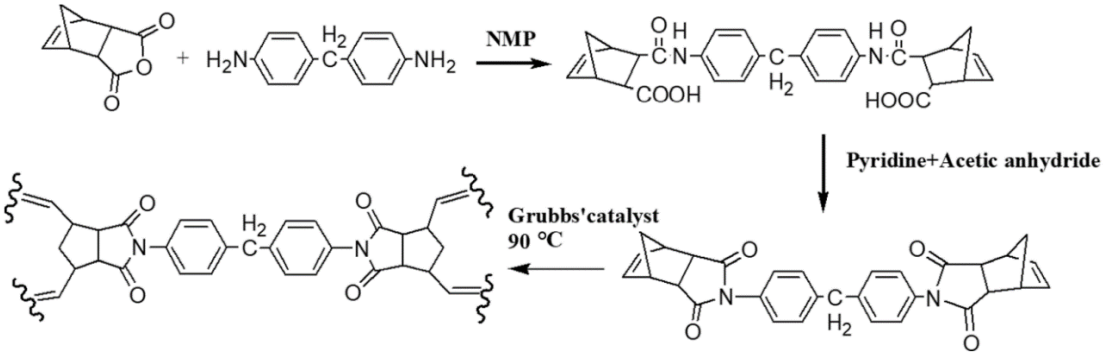

Figure 2.4 PI aerogel manufacturing and drying [47]

The long-chain macromolecule reaction that occurs with these methods results in the PI aerogels tending to exhibit a greater degree of shrinkage during the drying process, which can increase density and affect the material's thermal and mechanical properties [7, 44]. Such a high degree of shrinkage is disadvantageous. Unlike linear PI aerogels, crosslinked ones tend to be more successful and have useful properties. Different types of crosslinkers have been used in the process of synthesizing PI aerogel. The literature also reports that, in the PI synthesis process, the type and concentration of the crosslinking agents may also affect the properties and final structure of the produced gels [40]. For example, in one study, a research group at the National Aeronautics and Space Administration (NASA) introduced 1,3,5- triaminophenoxybenzene (TAB) as a crosslinker for synthesizing the PI (see Figure 2.5) [48]. TAB has been used in several research areas for synthesizing PI aerogels [49-52]. Further crosslinkers used for fabricating PI aerogels include 1,3,5-tris (aminophenyl)benzene (TAPB) [20, 26, 53, 54], 2,4,6-tris(4-aminophenyl) pyridine (TAPP) [32], tris(2-aminoethyl)amine (TREN) [55-57], octa (aminophenyl)-silsesquioxane (OAPS) [54, 58]. As the rate of crosslinking is low for all of these crosslinkers, reducing the oligomer's molecular weight is obligatory to reduce the imidization rate [38].

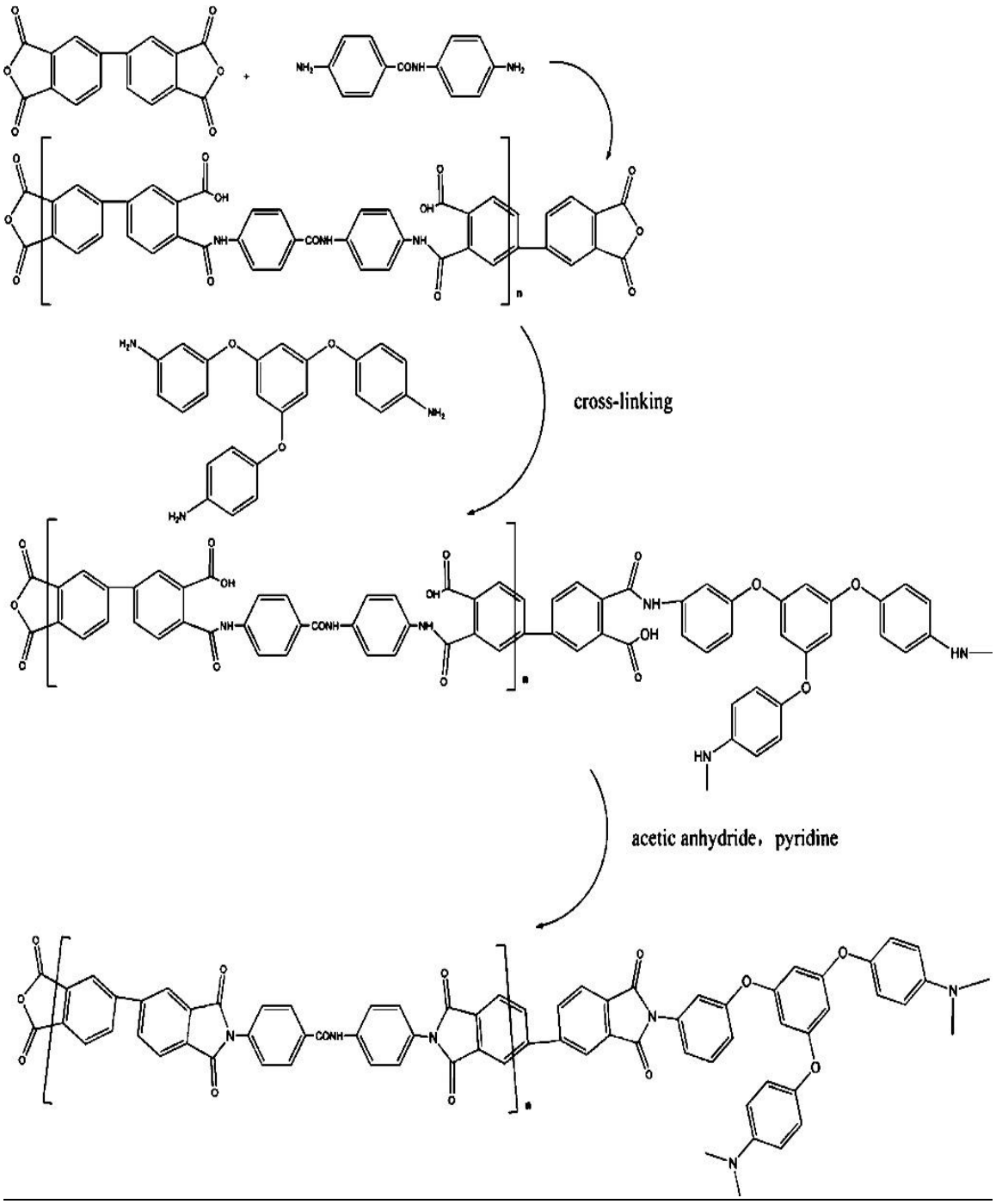

Figure 2.5 Synthetic route for PI aerogels crosslinked with TAB [48]

There is also literature, including a study undertaken by the Nguyen research group, on the potential for conducting the synthesis process for PI aerogel using triisocyanate as a crosslinker [22]. Triisocyanate is cheap and commercially available, as reflected in its extensive use in constructing and insulating buildings and clothing. However, it has low

thermal stability levels and is therefore unsuitable for aerospace applications. The aerogels resulting from triisocyanate have a density of 0.06 to 0.20 g/cm^3, and the BET surface area is 580 m^2/g. Triisocyanate as a crosslinker results in a lower onset of decomposition compared to TAB, octa(aminophenyl) silsesquioxane (OAPS) or 1,3,5-benzenetricarbonyl trichloride (BTC), which have also been used [21, 59, 60]. The mechanical properties of these PI aerogels (with triisocyanate as a crosslinker) are also reported as being similar to or better than those of previous aerogels [22].

Another study [66] compares the effects of the two crosslinking agents 1,3,5 tri amino phenoxy benzene (TAB) and OAPS, on 4,4- biphenyltetracarboxylic dianhydride (BPDA) backbone PI aerogels. In general, the TAB crosslinked aerogels presented higher levels of shrinkage and density and lower porosity than those crosslinked with the OAPS. The TAB crosslinked aerogels demonstrated 26% higher density than the same formulations crosslinked with OAPS. Generally, the aerogels modulus is expected to increase with increasing density. Based on this, the TAB crosslinked aerogels presented a factor of four higher compressive modulus and significantly higher levels of surface area [24, 26].

In recent years, significant research has been conducted to investigate PI aerogel's thermal and mechanical properties. The findings of this research indicate that the chemical structure of the crosslinker and molecular chain both have a remarkable influence on PI aerogels' thermostability and mechanical properties. As part of this literature, Jiang *et al.* [61] used tri(3-aminophenyl) phosphine oxide (TAPO) as a crosslinker for PI to investigate its different thermal and mechanical properties.

Several studies on the PI synthesis process have recently examined various dianhydrides and diamines to gain insight into the physical, chemical and processing characteristics. A noteworthy aspect of this research has been researchers' efforts to investigate the precursors to striking a balance between the PI's thermal stability, molecular weight, and mechanical and dielectric properties [62]. For example, by adding a rigid structure, such as a benzene ring, to the PI, thermal stability can be improved; however, solubility is reduced due to the high rigidity, which reduces the ease of post-processing [62].

Another example of work undertaken in this area relates to introducing ether bonds and aliphatic chains to the PI structure to increase the solubility and processability of the PI films [62]. Most of the time, these properties run contrary, making it necessary to strike a balance between these characteristics for different applications [62]. Molecular structures and the number of different monomers used in the polymerization process can determine the properties and, thus, the areas of application of PIs. By choosing a combination of monomers, such as two or more different dianhydrides with one diamine, or one dianhydride with two or more different diamines, it is possible to optimise PI structures [6, 7]. Important factors affecting PI products' properties include solvent exchange, polymer chain orientation, chemical conversion, gel thickness reduction and changes in chain mobility. However, because all of these factors coincide, it is rarely straightforward to predict the effect of each factor on the final properties [43]. It is for this reason that many studies have considered initial conditions, such as the chemical structure of the molecules and the solvents used in the reaction.

The molar ratio of the diamines and dianhydride is another factor that can affect the morphology and properties of the final product. The required monomers' concentrations can be calculated using the information on the final required molecular weight and polymeric chain length and by understanding the crosslinking mechanism [40]. For example, Gue *et al.* [54] found an increase in gelation time (from 30 min to 1h) by reducing porosity and modulus by increasing the length and number of repeat units, highlighting increased shrinkage and density [21]. Providing further support for these findings, Nguyen *et al.* [22] also report increasing the density and shrinkage of the PI aerogels through increasing polymer concentration by increasing the repeat units. Herrero et al. [62] also synthesized the linear and crosslinked PI aerogel with the thermal imidization process in their study. This involved conducting imidization freeze-drying and characterising samples with different techniques.

Meador *et al.* [49] report on the synthesis of crosslinked PI aerogel with very low density (0.14 g/cm^3), high thermal stability (up to 600 °C) and high surface area (512 m^2/g). As part of their synthesizing method, TAB was added as a crosslinker to react with anhydride, and acetic anhydride and pyridine were used to conduct the chemical imidization at room temperature. Finally, the aerogels were supercritical dried with

CO_2.Formulations made using 4,4′-oxydianiline or 2,2′dimethylbenzidine can be fabricated into continuous thin films using a roll to roll casting process. The films are flexible enough to be rolled or folded back on themselves and recover completely without cracking or flaking, and have tensile strengths of 4–9 MPa. They used chemical imidization at room temperature with pyridine/acetic anhydride to yield fully imidized cross-linked gels [49].

Zhang *et al.* [63], meanwhile, report on a synergistic strategy using ultrahigh-speed homogenising, freeze-drying and high-temperature imidization methods to fabricate an ultralight aramid nanofiber/PI (ANF/PI) composite aerogel.

Feng *et al.* [64] designed 3D printable inks to fabricate PI/CNC composite aerogels. This ink was mainly composed of water-soluble poly(amic acid) ammonium salt gained through the complexation of polyamic acids and TEA. The PI aerogel composite in their work was made with chemical imidization followed by thermal imidization and freeze-drying. The degree of imidization in the produced composites was analyzed by FTIR. The absence of signals at 1540 and 1660 cm^{-1} (amide II and C=O stretching of amide) for pure PI aerogel implies that the imidization was successful. The partially imidized aerogel is reported as having shown high mechanical strength for PI aerogel.

Feng *et al.* [50] investigated the thermal conductivities of different PI aerogels. The PIs were produced using 4,4′- diaminodiphenyl ether and 3,3,4,4′-biphenyl tetracarboxylic dianhydride, crosslinked with 1,3,5-triaminophenoxybenzene. They found the PI aerogels' thermal conductivity [30.80 mW/m.K] to be lower than other organic foams, such as polyurethane foam, phenolic foam, and polystyrene foam with similar apparent densities under ambient pressure at 25 °C. These results indicate that PI aerogel is an ideal insulation material in the context of aerospace (for air craft and air suits application) and other applications. The density of PI aerogel was changed by changing the concentration of the crosslinker. The researchers also found that increasing the temperature led to increases in thermal conductivity [50]. Guo *et al.*[26] meanwhile, the optimised properties of PI aerogels were synthesized using 4,4′-oxydianiline (ODA) in a combination of p-phenylenediamine (PPDA) or 2,2′- Dimethylbenzidine (DMBZ). In terms of optimizing the mechanical properties, thermal stability, resistance to moisture and other properties of the PI aerogels, DMBZ or PPDA were replaced up to 100% with ODA, showing that

using OAPS as a crosslinker can reduce the shrinkage and density compared with the aerogels produced using TAB.

Similar to the aerogel produced using TAB as the crosslinker, aerogel featuring DMBZ exhibits lower density and higher porosity and surface area [65]. Compared to this kind of crosslinker at the same density, aerogels that are made by BTC (1,3,5-benzenetricarbonyl trichloride) have the same or higher modulus and surface area [21]. The thermal stability of the aerogels is affected by the chemistry of the backbone. The thermal stability of the aerogels with 4,4- oxidianiline (ODA) is higher than 2,2-dimethylbenzidine (DMBZ) [21].

Kwon *et al.* [66] synthesized PI aerogel microparticles using pyromellitic dianhydride (PMDA) and ODA, fabricating spherical particles to use PI aerogel as a raw material in different drug release and insulation applications. The porosity and surface area for the produced PI is reported as being 80% and 103 m^2/g, respectively.

Chao *et al.* [67] worked on synthesising semi-crystalline PI aerogels and reported that the presence of crystalline in the material had a noticeable influence on the properties of the materials. Their results indicate that the PIs' glass transition temperature (Tg) was affected by the flexibility of the polymer chain and intermolecular interactions. They also show that thermal stability remains high for different types and amounts of crystallisation, even when the Tg and melting temperature (T_m) are reduced.

Meador *et al.* [49] worked on PI aerogel synthesis to improve the reaction mechanism. This resulted in a product with high performance, produced using common diamines and dianhydrides such as BPDA, ODA, TAB, DMBZ and BTC. Their micromorphology investigation (Figure 2.6) found that selections of dianhydride and diamine were critical to the final performance of the products.

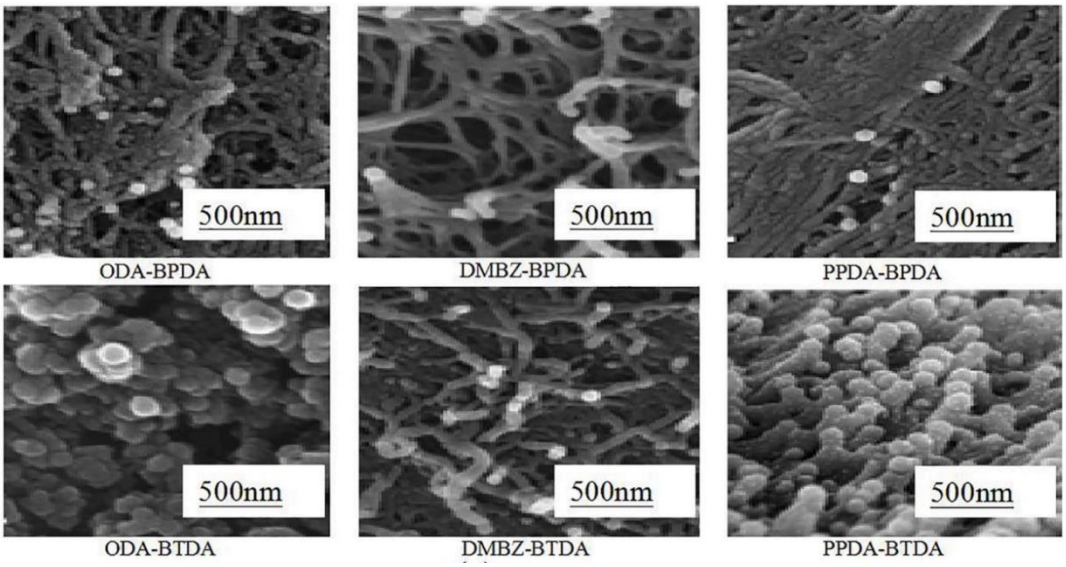

Figure 2.6 SEM image for produced PI using different diamines and dianhydrides, ODA: 4,4-Oxydianiline, BPDA: 3,3,4,4-Biphenyltetracarboxylic dianhydride, DMBZ: 2,2-Dimethyle benzidine, BTDA: 3,4,4,4-Benzophenone tetracarboxylic dianhydride [21]

Other parameters in the PI synthesis process (besides raw material) can also affect the performance and properties of the produced PI aerogel. For example, Tao *et al.* [68] investigated the effect of solid content and concentration of the crosslinker on the performance of the produced PI aerogel. They show that increasing the solid content increases linear shrinkage, density, pore size distribution and compression modulus. They also show that increasing the crosslinker concentration increases linear shrinkage and compression modulus. On this basis, the performance of the produced PI aerogel can be adjusted in terms of both the solid content and crosslinker content [68]. In another investigation, Feng *et al.* [50] investigated the effect of temperature, gas type and air pressure on the thermal conductivity of the PI nano-aerogels. They report lower levels of thermal conductivity for PI aerogel produced using CO_2 gas compared to the N_2 atmosphere.

2.2.2 Synthesizing polyimide aerogel using dianhydrides and isocyanates

The isocyanate method is a one-step method for synthesising PI nano-aerogels. In the first stage, isocyanate is allowed to react with an anhydride to form a seven-member ring; in the next stage, imidization is allowed to occur through the catalysts [33]. The produced

PI aerogel has low molecular weight and poor performance. However, if the reaction is conducted under anhydrous conditions, it is possible to produce a far superior aerogel through the stepwise form of the reactions [69]. The monolithic PI aerogel is synthesised with pyromellitic dianhydride (PMDA) with 4,4′- methylenediphenyl diisocyanate (MDI), followed by drying at room temperature. This reaction goes through a seven-member ring intermediate that collapses to the imide through the expulsion of CO_2[33] . The produced aerogel is compared with the PI-AMNs, obtained via the classic PMDA and 4,4′-methylenedianiline (MDA) reaction. Results reported in relation to this practice show that the seven-member ring has more rigidity; however, it is also shown that the PI-AMNs shrink during processing. Both types of aerogel convert to porous carbon after pyrolysis at 800 °C [33].

Paraskevopoulou *et al.* [70] provide a mini-review focusing on aerogels synthesized using polymers. For this study, the researchers considered PI and phenolic resin aerogels in a broad sense but mainly concentrated on polyurea aerogels. They detail a cheaper process for synthesising the PI using isocyanate to reduce costs, with CO_2 being the only by-product of this reaction. Chidambareswarapattar [71] describe the simulation of an experimental method for synthesizing monolithic micro/meso/macro-porous polymers with potential use in relation to catalysis, gas separations and gas storage. In their approach, PI is synthesized from dianhydrides and triisocyanates and subject to supercritical drying to produce the aerogel.

2.3 Solvent exchange

The solvent exchange or washing step is one of the most important parts of the organic aerogels manufacturing process. This step typically takes place before the drying process. The wet gels are placed in a proper solvent and stirred for a specific time, with the solvent being refreshed until the solvent exchange process is completed. The pores in the wet gel are filled with polar solvents with high surface tension. There are two main reasons for conducting solvent exchange in this way: 1) the need to remove unreacted chemicals; and 2) the need to exchange the synthesizing solvent from the pores with a low surface tension liquid to reduce the solid–solvent interaction and meniscus force [72-74]. There has been a recent increase in the level of attention around aerogels in terms of their industrial

applications. On a large scale, the synthesis method must be engaged for a shorter period and with less energy. While synthesizing a wet gel is straightforward, solvent exchange and drying are more complicated and time-consuming. Depending on the size of the wet gel, the solvent exchange may take several days or perhaps even over a week [75]. It is also likely that shrinkage will result from removing the polar solvent directly from the wet gel due to the exertion of capillary force during drying [76].

Yang *et al.* [75] detail a green approach to fully aromatic PI aerogel manufacturing through ambient pressure drying. In this synthesis, the only solvent used is water. Reinforcing the PI aerogel with graphene oxide can convert the PI to the 2D nanohybrid aerogel. The mechanically robust PI aerogel that results in powder or monolith is subjected to thermal imidization at 200 ℃ for 24 h, and dried directly in an oven at 100 ℃. Lee *et al.* [77] investigated the effect of different types of solvents on the solvent exchange step, focusing on the role of vacuum drying during the PI aerogel manufacturing process. They exchanged solvents six times every 2 h, taking 12 h in total. They also considered how porosity could be controlled with different solvents and showed that increased porosity could be induced using multiple solvents instead of only one. For this purpose, they used toluene, acetone, methylethylketone, ethyl alcohol and cyclohexane with different ratios.

Ghaffari *et al.* [60] reported on the synthesis of the PI aerogel using 3,3’, 4,4’-biphenyl tetracarboxylic dianhydride (BPDA) and pyromellitic dianhydride (PMDA). The method they used for the solvent exchange was conducted over six days, and a transparent PI wet gel was formed from pyromellitic dianhydride (PMDA) and 4,4′-diaminodiphenyl methane (DDM) in a mixture of methanol and tetrahydrofuran with a mass ratio of 4:1. The wet gel was firstly washed with acetone and then with cyclohexane, which has a high freezing temperature (6 °C) and high vapour pressure (13 KPa at 25 °C). High-temperature imidization without any visible collapse followed by freeze drying at vacuum conditions resulted in a green, scalable and cost-effective process for preparing high-performance PI aerogel materials [78]. From the findings of these studies, it can be concluded that solvent exchange and drying are the most expensive aspects of producing PI aerogel in terms of time and energy.

2.4 Sol-gel process

The importance of sol-gel processing has been known for a long time. Indeed, the first silica aerogels were synthesised in 1845 using this method at the "Manufacture de Céramiques de Sèvres" in France [3], and significant progress has been made over the past two decades in relation to this processing technique. For example, in the areas of ceramics and glass fabrication, sol-gel processing has resulted in fresh insight in terms of essential chemistry and the fabrication of materials. In a basic sense, oxide networks can now be created by polymerizing chemical precursors in a liquid solvent [79], with sol-gel processing typically being used to produce a solid material in a liquid at a low temperature (T < 100 °C) [7]. As part of this process, sol is introduced as a suspension of colloidal solid particles surrounded by a liquid. These solid particles must be sufficiently small and denser than the liquid. In this case, the forces responsible for the dispersion are more significant than gravity. In terms of the role of gel, this is a porous three-dimensional solid network that can expand to the size of the container. There are two types of gel in terms of the solid particles used in the gel preparation, named according to whether they are made of colloidal sol particles (colloidal) or macromolecules in a polymeric solution (polymeric). Gelation occurs when the colloidal particles or macromolecules are dispersed in the initial sol, preventing the development of inhomogeneities within the material [79]. Typically, the gelation point is identified in terms of a sudden rise in viscosity and an elastic response to stress [18]. The sol conversion into the three dimensions solid network can be initiated with a change in the ionic strength of the solution or through a solvent exchange process. This process happens through a difference in the pH of the reaction, which reduces the electrostatic barrier to agglomeration and promotes inter-cluster cross-linking, leading to the formation of the three-dimensional gel network [18]. Overall, the structure of the gel forms after consecutive reactions and reverses hydrolysis and condensation. In the hydrolysis process, the nucleophilic attack of water leads to the replacement of alkoxide groups with hydroxyl groups. At the same time, condensation occurs in terms of the formation of M-O-M bonds between two species of M-OH (where M is a metal element) or M-OH and M-OR (where OR is an alkoxide group) [80]. In their study, Maleki *et al.*[81] show that the sol-gel process for metal oxide can be described in terms of three reactions of the formation of the polymeric M-O-M bonds. These are illustrated in Figure 2.7[81].

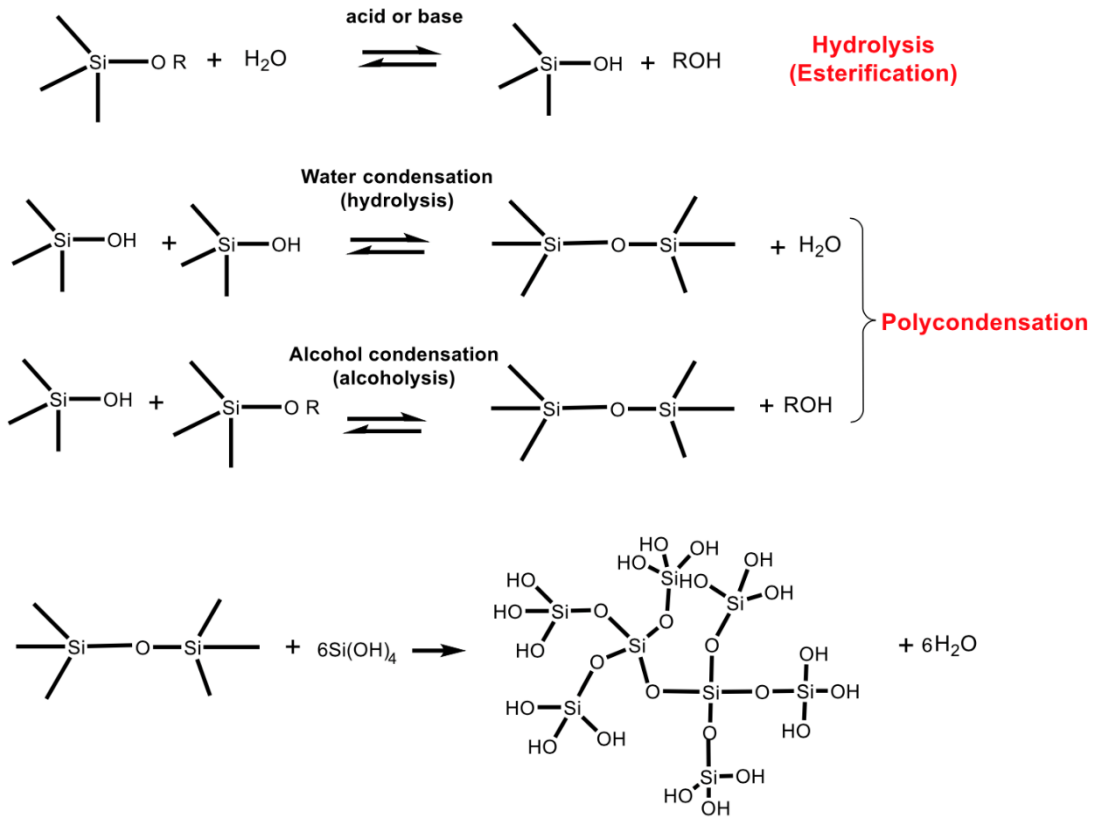

Figure 2.7 Sol-gel reaction for alkoxysilane [81]

In the process of producing the gel, if the liquid is mainly composed of water, the corresponding gel is often called “aqua gel” or “hydrogel,” and this material is soft enough to be cut manually with a knife. If, on the other hand, the liquid phase is composed of alcohol, then the gel is termed “alcogel.”. Depending on the drying method used, “xerogel” or “aerogel” will be produced in the next step. Drying the wet gel by evaporation of its solvent induces a significant contraction of up to 30% of its initial volume. “Xerogel”, first discovered in 1923 by Freundlich [82], is reserved for this gel type. “Aerogel” refers to any type of gel that a gas replaces with its liquid without further shrinkage. Selecting the precursors is the first step of any sol-gel processing, and it is typical for such precursors to be complex chemical molecules that can transfer to dense colloidal particles or polymeric gels with a very open macromolecular network. Figure 2.8 shows the process of producing aerogel through sol-gel processing schematically [82].

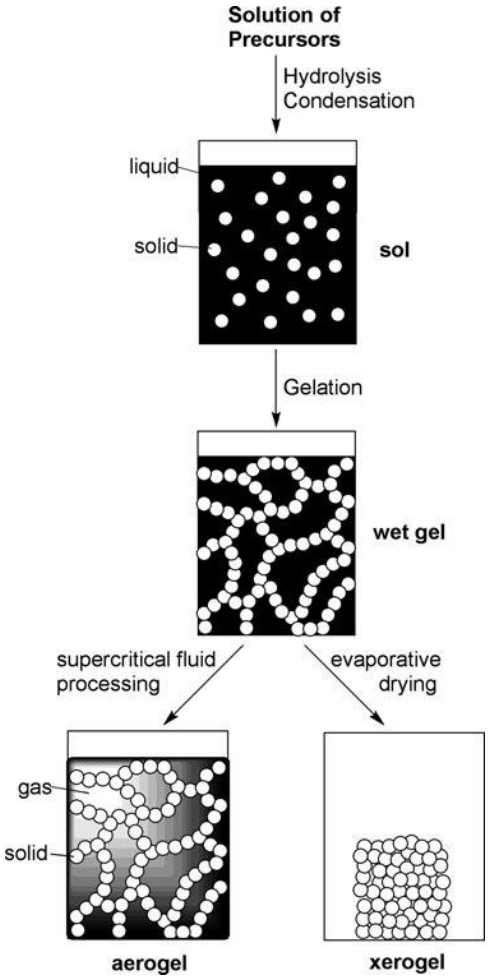

Figure 2.8 Preparation of aerogels using sol-gel chemistry [82]

Sol-gel processing is subjected to influence by a number of different parameters, such as the pH of the solution, temperature, precursor activity and the water/precursor ratio. As Brinker shows, adding specific catalysts can also make it possible to control the rate of the hydrolysis and condensation reactions [83]. Further, Gaurav *et al.* [84] report on how different molar ratios and types of catalysts can be used to control hydrolysis and condensation rates as well as gelation time. And Maleki [81] details how sol-gel processing can emend the aerogel's molecular structure by incorporating different phase or chemical groups such as alkoxide organo-functions or additives and nanoparticles in the porous network.

2.5 Ageing process

The particles are first linked together during gelation to form a necklace structure. However, at this stage, the linkage among such particles is not by itself sufficiently strong [85]. The literature details several ways enhancement might be provided to enhance the gel's strength. For example, Haereid *et al.* [86] detail how heat treatment (hot water) can be used on the wet gel to enhance the mechanical properties of silica aerogel. It is also possible to age the gel by storing it for an extended period in a liquid medium to minimise the potential for shrinkage during the drying process. The type of transformations that may occur during ageing can be chemical or textural [77], and is carried out by immersing the gel in a proper solvent. For example, Einarsrud *et al.* [87, 88] used a mixture of water and ethanol over several hours and days. During the ageing process, any unfinished reaction of reactive species and unreactive monomers is allowed to complete over time. The properties of the gel are subject to influence by the type of solvent used for ageing, as well as parameters such as temperature, pH and length of time allowed [89].

Pei *et al.* [90] investigated the level of shrinkage during the ageing, solvent exchange and drying process as part of the PI manufacturing process. PI containing trimethoxysilane side groups was added to a solution of water and HCl in DMF to obtain the DMF solution. After the mixture was stirred, it was poured into syringes and left to age for two days. The wet gel was then washed with tert-butyl alcohol 4 times every 12 h, and then freeze dried. The researchers report that crosslinking could occur during the ageing process and that the majority of the shrinkage occurred during this step. They also demonstrate that increasing the concentration of trimethoxysilane in the PI structure increased the level of shrinkage in the ageing step.

Viggiano *et al.* [59] investigated a new method for synthesizing the PI aerogel in order to reduce the shrinkage in the ageing step, using 9,9′-bis(4-aminophenyl)-fluorine (BAPF) to disrupt chain packing. To investigate the level of shrinkage during the ageing step, samples with different concentrations of the BAPF were modulated in terms of the length of time allowed for ageing and temperature. They reported that the most significant shrinkage occurs during the first 24 h of ageing. They also show that temperature

increases can decrease surface area during ageing. Using SEM characterisation, the degree of agglomeration is also shown to increase as a result of ageing.

2.6 Drying process

The third and final stage for producing aerogel is drying the wet gel. Conducting this step makes it possible to maintain the gel's initial pore structure, and it significantly affects its final structure and properties. Given the goal of improving the mechanical strength of the gel network and reducing the tensile stress produced by the capillary force, research has been conducted on how stress and shrinkage are induced during the drying process. As a result, several different drying methods are now used to minimise the damage of capillary force exerted on the gel network during the drying process [79]. In general, the process of drying the surface of a wet gel from an organic solvent comprises two steps. The first step is conducted at a low temperature, close to room temperature, over one or two days. The second step is conducted at high temperatures (150-200 °C) and is considerably more energy-intensive [18].

Drying typical aerogels is now commonly done in one of three different ways, these being ambient pressure drying (which implies crossing the liquid-gas equilibrium curve), supercritical drying (which necessitates bypassing the critical point) and freeze-drying (which requires the system to bypass the triple point). Drying is usually conducted as a means of removing solvents from the aerogels, and this has the potential to have a dramatic effect on their final properties [91]. During the removal of the liquid from the pores, there is a need to preserve these pores' volume matrix structure and the desired properties of the aerogel. Therefore, this step is critical in aerogel preparation [92].

Generally, in aerogel synthesis, the preparation of wet gel is a relatively fast and straightforward process; the drying process, on the other hand, gives rise to several more challenges in terms of the cost and quality of the final product. For example, removing the polar solvent directly from the wet gel is likely to cause high shrinkage rates due to capillary force [76]. On this basis, methods such as supercritical drying are recommended as a means, although such methods are costly and necessitate a high level of safety-related procedures [21, 23, 24, 26, 47, 65, 93, 94]. Freeze drying is another extended technique that can be used, although it tends to produce aerogels with high porosity levels and weak

structure [90, 95-97]. While most of the studies on PI aerogels are based on supercritical drying [21-23, 26, 47, 48, 50, 61], the most convenient and cost-effective alternatives are ambient pressure drying (APD) [74, 76, 98-100] and vacuum drying (VD) [26, 55, 73, 101]. However, as the evaporation of the solvent from inside the pores causes capillary force, this method remains challenging to implement. To reduce the meniscus force and the interaction of solid-liquid in the APD and VD methods, surface modification or solvent exchange with a low surface tension liquid is often implemented [77]. However, due to the large capillary force exerted during the evaporation of the solvent from the pores, there is significant potential for shrinkage, causing a loss of porous structure, and this reason that only a few studies have been published on PI aerogel based on APD and VD [102, 103].

2.6.1 Ambient pressure drying

Realising a wider variety of commercial aerogel applications necessitates identifying ways the costs of the preparation process can be reduced. Ambient pressure drying (atmospheric drying) can be conducted at a lower cost and is preferable to other methods. Although xerogels, as the gels produced using this method, demonstrate significant shrinkage and a loss of their porous structure, using this method is typically more efficient in terms of both time and money compared with supercritical drying and freeze drying. Many studies for different aerogels have discussed the ambient drying method [104-106], beginning with Fischer *et al.*'s [48] preparation of resorcinol-formaldehyde (RF) aerogel. Although the RF obtained showed significant shrinkage, this method of drying remains more straightforward, quicker and cheaper to use than others. Pisani [107] shows that, given the goal of reducing the capillary force in the preparation of carbon aerogel with ambient pressure drying, low surface tension can effectively prevent the distraction of aerogel during the drying process. The operation process is more straightforward, and the cost is lower than other methods.

During ambient pressure drying, the solvent evaporates from the pores at ambient pressure, ranging from room temperature to 200 ℃. As this happens, the radius of curvature of the vapour-liquid interface decreases, exerting pressure on the gel surface. Nano-sized pores in aerogels are the most crucial feature as they are the main reason for

shrinkage [108]. The pressure caused by the meniscus in the pore with diameter d is calculated using the following equation:

$$Pcap = -\frac{4\gamma LV}{d-2\delta} \qquad (1)$$

As represented in Figure 2.9, d is the pore's diameter, γ_{LV} is the vapour-liquid interface's surface tension, and δ is the thickness of the liquid layer adsorbed on the solid surface [108].

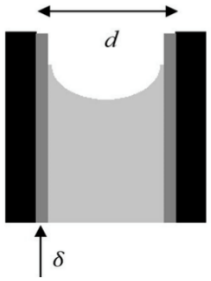

Figure 2.9 A meniscus in a pure wet gel [108]

In wet gel with a fragile porous structure filled with water, the capillary pressure for a pore with almost 5 nm diameter is around 1000 bar. As shown in Table 2.1, the pores cannot withstand such levels of capillary pressure, with the thickness of the adsorbed layer depending on the temperature and vapour pressure of the solvent as well as the strength of hydrogen bonding between the liquid and the solid [109].

Joao *et al.* [110] report the straightforward preparation of ambient pressure-dried aerogel and show that the presence of the vinyl groups prevents network shrinkage during the drying stage, with the maximum linear shrinkage for the obtained aerogel being 11%. The produced aerogel from their work is reported to have been light (bulk density ≤ 183 kg / m^3) with a high level of porosity (> 91%).

Table 2.1 Values of capillary tension for different solvents and pore sizes calculated for T = 20 °C and δ = 1 nm using equation (1) [109]

Solvent	γ_{LV} 10^{-3} (Nm^{-1})	Pc (bar) d= 5nm	Pc (bar) d=50 nm	Pc (bar) d=500 nm
Water	73.1	947	60.9	5.9
Ethanol	22.8	303	19	1.8
Methanol	22.6	301	18.8	1.8
Acetone	23.7	316	19.8	1.9
Hexane	18.4	246	15.4	1.5
Isopropanol	21.7	289	18.1	1.7

γ_{LV} is the vapour-liquid interface's surface tension. Pc is the pressure caused by the meniscus in the pore.

Fidalgo [111] presents details of a novel sol-gel monolithic silica aerogel that is suitable for machining and can be obtained under atmospheric conditions. In her work, the produced xerogel was characterised by scanning electron microscopy (SEM), nitrogen adsorption−desorption and a pycnometer, with the porosity, surface area and average mesopores diameter for the sample with the lowest density, 357 kg/m^3, being reported as 83%, 766 m^2/g and 11.5 nm, respectively. This aerogel is the one with optimal mechanical properties.

Kim *et al.* [112] report on a method for synthesizing the PI aerogel in different shapes, derived from pyromellitic dianhydride (PMDA) and 4,4, oxydianiline (ODA) in one step and without the addition of a catalyst for making connections among spherical PI aerogels. The produced samples were dried in an oven for different lengths of time and at different temperatures. Their results show that PI aerogel could be produced with 45% porosity and good thermal stability and be oil absorbent. They also detail a stepwise drying process for producing the monolithic form and provide a breakdown of how drying can be conducted at temperatures higher than 150 °C.

2.6.2 Freeze drying

Another technique for drying wet gels is freeze drying. In this method, the excess solvent is removed through a sublimation process. First, the solvent inside the pores is frozen by lowering the temperature to a point below freezing, following which the pressure is reduced below the sublimation pressure at this temperature by exerting a vacuum on the system. The solvent thus sublimes and is removed from the pores without forming a liquid-vapour interface. Once the solvent is removed from the pores, the sample is returned to room temperature [113]. Aerogels that are obtained in this way are sometimes termed "cryogels" [18]. Gurave *et al.* [114] and Hering *et al.* [115] describe freeze drying processes that result in an opaque aerogel powder. Hering et al. [116] show how the ice microcrystals that form during the freeze drying process result in more macro-porous aerogels than those dried using supercritical extraction. During freeze drying, the nanostructured gels are vulnerable to damage, potentially due to the process of growing the crystals and the development of stress inside the pores. This highlights certain disadvantages of this freezing method depending on the solvent used. For example, if the solvent is water, then the expansion induced through freezing is particularly likely to result in the pores' structure being destroyed; if the solvent is an alcohol, on the other hand, it is likely to be very difficult to reach the requisite freezing temperature (T_f for ethanol is -113 °C). Typically, freeze drying is used for preparing carbon aerogel [117], but this method is unsuitable for aerogels with small pore sizes. When the pores are so small, the overall shape of the gel is difficult to maintain, so it shrinks during the drying process due to tension exerted by thermal shock.

Nowadays, the freeze drying method is used to prepare graphene aerogel with a large pore size (macro-size)[118]. Carbon aerogels are obtained in this way and are mainly used in applications for which there is no need for a macroporous structure[119].

Hu *et al.* [120] report a novel process for making carbon aerogels using the stepwise freeze drying method, drawing comparisons between the stepwise freeze drying method and the traditional freeze drying method by measuring density, linear shrinkage, specific surface area, pore size distribution, microstructure and compressive strength. Their results show that, compared with traditional freeze drying, stepwise freeze drying results in

reductions in carbon aerogel's density, linear shrinkage and pore size. In this way, stepwise freeze drying is an efficient method for obtaining carbon aerogels with a fine microstructure and desirable mechanical properties.

Herrero *et al.* [121] report on the use of freeze drying for producing carbon nanofiber-reinforced aerogel, highlighting the influence of the different operational conditions and physical properties of the carbon aerogel in terms of its morphology, porosity and conductivity. They demonstrate that density and porosity increased when freezing time was decreased and that the porosity of the carbon nanofiber-reinforced polymer aerogel increased when both the vacuum pressure and the freeze drying temperature increased, respectively. The thermal conductivity of the produced carbon aerogel was in the range of 0.037 to 0.069 W/m.K. They also show that the operation condition did not affect the thermal conductivity of the produced carbon aerogels.

Liu et al. [122] present a facile method for PI synthesis, not featuring chemical imidization but featuring solvent exchange and subsequent freeze drying. The PAA was synthesized by mixing ODA and 2,2-bis(3,4-anhydrodicarboxyphenyl) hexafluoropropane (6FDA) before being poured into cylindrical moulds, frozen at -20 °C and then freeze-dried for 12 h. The PI aerogel was obtained by heating the produced PAA gradually at 80 °C, 150 °C and 250 °C. In order to regulate the microstructure of aerogels, the co-solvent t-butanol (TBA) was added to change the solvent composition and thus change the morphology of the solvent crystal. As the researchers note, TBA that is added in this way can be removed using freeze drying.

Zhang *et al.* [96] report that PI aerogels composites obtained using the freeze drying method have more desirable mechanical properties compared to those prepared with the CO_2 supercritical drying method. They also highlight the benefits of freeze drying to frame it as an inexpensive, green and straightforward method for preparing aerogels and report a novel double-crosslinking strategy to obtain a freeze dried and robust PI/reduced graphene oxide/cobalt (PI/rGO/Co) aerogel.

Xu *et al.* [123] report details of the production of a series of compressible and elastic PI aerogels with three-dimensional architectures using the freeze drying method, including systematic consideration of the effects of processing conditions (the slope angle of freeze

drying and solid concentration) on the micromorphology of resultant aerogels. They compare the mechanical properties of the PI aerogel produced with supercritical and freeze drying. They also use the SEM to highlight an isotropic nanofibrous network for supercritical dried PIs, showing that applying compression to this structure made it weak and unable to revert to its previous state when the stress is stopped; as a result of this, permanent deformation and damage occurred to the supercritical dried aerogel with an isotropic nanofibrous network. However, in the case of freeze dried aerogel with a typical lamellar structure, when compression was applied along the y-direction, the wave-shaped and wrinkled layers flattened, and the displacement energy was stored in the deformed microstructure. After removing the compressive force, the aerogel was observed to recover its original shape through reversible movement [123].

2.6.3 Supercritical drying

Supercritical drying is another technique for drying the wet gel, involving the use of supercritical fluids to extract solvent from the pores. As shown in Figure 2.10, to ensure that it can reach a supercritical condition, the fluid is compressed and heated above its critical pressure and temperature (for CO_2: Tc = 31°C, Pc = 7.4 MPa), giving it liquid-like densities and gas-like viscosities. The high diffusion coefficient of such supercritical fluids allows their functions as solvents and their mass transfer characteristics to be enhanced [124].

The aerogels produced through supercritical drying have higher pore volume and porosity than those produced through freeze drying and ambient drying [125-127]. Figure 2.11 shows the aerogels dried with supercritical and ambient drying methods. It makes clear that the shrinkage in the supercritical dried sample is lower than that of the ambient dried sample, giving rise to greater porosity [124].

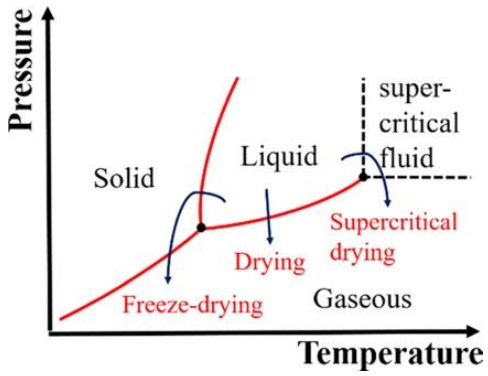

Figure 2.10 Phase diagram of the liquid phase removed from the gel [124]

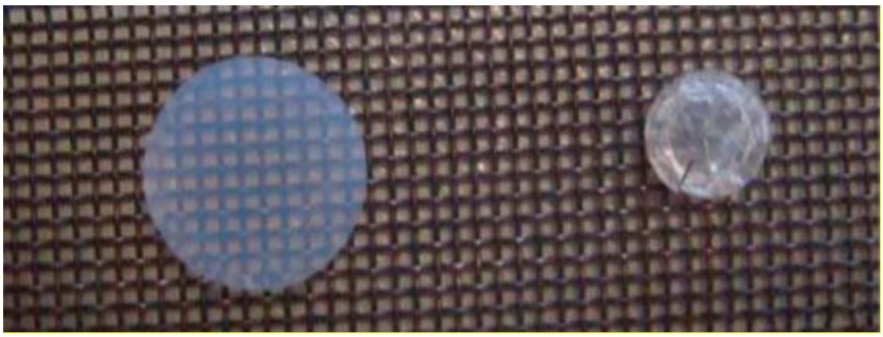

Figure 2.11: Silica aerogel obtained by supercritical drying (left) and ambient drying (right) [124]

Figure 2.12 shows a flow diagram depicting the typical steps in the supercritical drying process. The gel with excess solvent is placed inside the high-pressure sealed vessel. Then the vessel is heated above the critical temperate of CO_2 (~31°C). Sometimes, the vessel is preheated before the gel is placed inside to reduce the time to reach thermal equilibrium and prevent excessive evaporation. In the next step, the vessel is pressurised to a point higher than the critical pressure of the solvent and CO_2 mixture, enabling the CO_2 to extract the liquid inside the pores by passing it through the aerogel. At the vessel's exit, the combination of the CO_2 with the solvent is converted into two phases through the expansion of the mixture such that it is at a lower pressure. This makes it possible to collect and remove the solvent from the gel while the CO_2 is recycled with a pump or compressor. The system is gradually depressurised down to 1 atm, and the aerogel is removed [92].

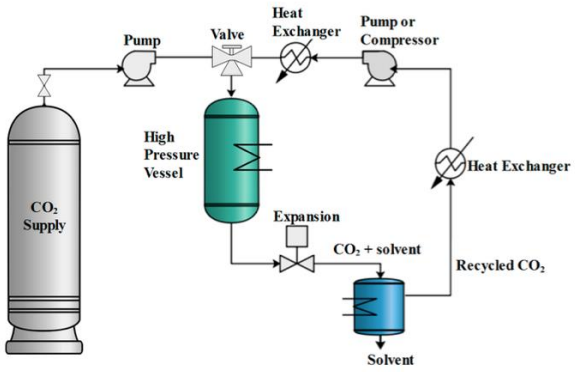

Figure 2.12 Flowsheet of supercritical drying with CO_2 [92]

Supercritical drying is conducted in two ways (1): in the supercritical state of the organic solvents (generally the solvent is alcohol as a pure liquid, above 260 °C if the solvent is ethanol), which is called the hot process; (2) in supercritical CO_2, in which the temperature is slightly above the critical temperature of the CO_2 (~31°C), which is called the cold process. Tewari reports on efforts using the cold process to produce silica aerogel, noting that the liquid penetrating the wet gel must exchange CO_2 either in the typical liquid state or in the supercritical state [128]. Although both cold and hot supercritical drying routes can be used on an industrial scale to prepare monolithic silica aerogels, producing samples in these ways is time-consuming. To speed up CO_2 washing, simple molecular diffusion must be assisted by forced convection, for example, by integrating compression-decompression cycles into the process [129].

After the solvent exchange, aerogels are typically dried using the supercritical drying method. Neither shrinkage nor collapse of the pore's structures occurs during the supercritical drying method because the liquid surface tension at the gas-liquid interface is eliminated. This technique thus involves no interface between gas and liquid; rather, a uniform fluid forms between these two forms (Figure 2.10) [124]. The gas-filled aerogels are obtained when all the fluid is discharged from the gel. In Błaszczyński *et al.*'s [130] work, silica aerogel was prepared using sol-gel and a supercritical drying process. They report that supercritical drying was the most effective process in terms of its ability to yield a product with optimal properties, with the obtained silica aerogel having a high specific surface area, good transparency and comparable density. A supercritical carbon dioxide of alcogels (in ethanol) was used for the drying profile using extraction equipment

[130]. The researchers also investigated the drying process for different precursors (inorganic-silica, organic-starch) with different densities and morphologies (cylindrical monoliths, microspheres). Depending on the nature of the gel precursor, the extent of drying yielded significant differences, in the end, textural properties of the dried gel [131].

In their study, Meador *et al.* [65] investigated the dielectric and other properties of the monolithic PI aerogel, that were synthesized with two different forms of anhydride end cap PI using the following combination: 2,2-bis (3,4- dicarboxyphenyl) hexafluoropropane dianhydride (6FDA) and 4,4′-oxidianiline (ODA); and biphenyl-3,3′,4,4′- tetracarboxylic dianhydride and ODA. The oligomers combined with 1,3,5-triaminophenoxybenzene to form a block copolymer networked structure in which gelation occurred in less than 1 h. The resultant wet gel was then dried using supercritical drying. The PI is reported as having a low dielectric constant and density and is suitable for use in antennas due to its high bandwidth [65]. The same research group also reports on the process of synthesizing the PI aerogel using 1,3,5- benzenetricarbonyl trichloride (BTC) as a cost-effective crosslinker instead of other, more expensive types [21]. In this study, the produced polyamic acid was aged for 24 h and then washed with different ratios of acetone and NMP, following which supercritical CO_2 drying was performed. The resultant PI aerogel with BTC is reported to demonstrate useful mechanical and thermal properties compared to other less commercial and more expensive crosslinkers. As a result of their high modulus and surface area combined with onset decomposition in the manner of other crosslinkers, these types of PI aerogel are a viable option for aerospace applications, insulation for refrigeration, clothing, industrial pipelines and building and construction. However, there are also potential issues with moisture resistance [21].

Zhang *et al.* [94] present details of the creation of a PI aerogel with excellent thermal and dielectric properties synthesized through the polycondensation of 3,3′,4,4′-biphenyltetracarboxylic dianhydride (BPDA), 5-amino-2-(4-aminophenyl) benzoxazole (APBO) and octa (amino-phenyl) silsesquioxane (OAPS) crosslinker, followed by the application of a supercritical carbon dioxide ($SCCO_2$) drying treatment. In this study, the SEM reveals a three-dimensional network microstructure resulting from a highly crosslinked structure. The linear elastic regions under the 10% strain were observed in the stress-strain curve, and the researchers show that, due to the absence of a liquid-

vapour interface, the supercritical drying above the critical point was able to dry the wet gel without inducing capillary stress. On this basis, they present supercritical drying as a clean, environmentally friendly and economical method for drying the wet gel [94].

Zhang *et al.* [132] also report a nanocomposite aerogel produced using PI and Ag nanowire (AgNW). The initial AgNW were surface-modified by p- aminothiophenol (PATP), after which the aerogel was prepared through supercritical drying. A high increase is reported in respect of the mechanical properties of the PI aerogel. The sample with 2 wt% of AgNWs is reported as having a 148% increase in compression strength and a 223% increase in Young's modulus compared to the pure PI aerogel, as well as an increase in density from 0.192 to 0.205 g/cm^3.

2.7 Properties of polyimide aerogel

As previously discussed, PI aerogel has properties such as flexibility, low density, low dielectric constant and low thermal conductivity. However, seeking to optimise these properties, researchers have undertaken work in a number of different areas. Figure 2.13 presents a diagram of the various properties of the PI aerogel and potential ways of enhancing each property [39].

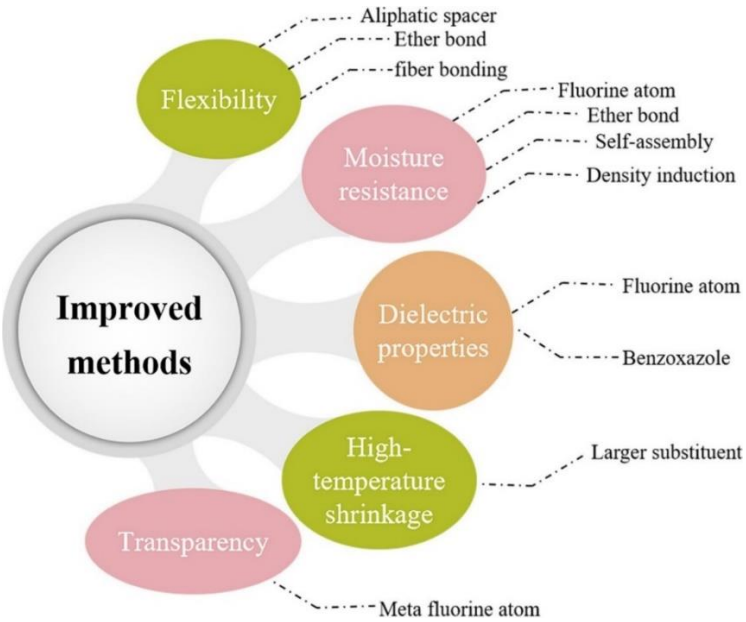

Figure 2.13 Methods for improving the properties of the PI aerogel [39]

2.7.1 The flexibility of polyimide aerogel

Given the goal of improving the flexibility of PI aerogel, research has considered the potential of modifying the main chain by adding an aliphatic monomer. Pantoja *et al.* [133] report an increase in the flexibility of PI aerogel through the addition of methylene units (BAPx) functioning as a flexible spacer. As a result of this modification, they report greater flexibility and lower modulus in the PI aerogel. They also reported low density and increased thermal resistance, flexibility and moisture resistance for the PI aerogel formulated with 25 mol% aliphatic diamines. Cashman *et al.* [134] also report using different concentrations of 3-bis (4-amino phenoxy)-2,2- dimethylpro-pane (BAPN) as a flexible spencer for synthesizing the PI aerogel. The best flexible condition in this study was achieved at 7 wt% polymer concentrations and 50 mol% BAPN. In another study to improve the flexibility of the PI aerogel, Guo *et al.* [135] used a mixture of 1,12-dodecyldiamine (DADD) with 12 methylene groups and DMBZ. They elected to use these resources instead of BAPx, which is not readily available commercially, and BPAN, which is expensive. The produced film is reported as having the ability to be bent 2 mm and as having a higher modulus than BAP10. Furthermore, the shrinkage is less than for BAPx, but with greater moisture resistance. Li *et al.* [38] meanwhile, show that an appropriate degree of flexibility can be achieved when the molar ratio of ODA and aliphatic monomers, used as diamines, is 3:1. They also report the lowest thermal conductivity (0.031 W/m.K) for the produced PI aerogel at this ratio.

Surveying the literature broadly, the PI aerogel produced with the highest degree of flexibility is film with a 0.5-3 mm thickness. Such film can be used in a range of different aerospace and thermal insulation applications. However, it should be highlighted at this point that the flexibility of the PI aerogel stock shape remains understudied [136].

2.7.2 Moisture resistance and dielectric properties of PI aerogel

Several studies have been conducted on the moisture resistance of PI aerogel [53, 137]. For example, Qiao *et al.* [137] added a flexible monomer (2,2-bis(3,4-dicarboxyphenyl)hexafluoropropane dianhydride(6FAPB)) to the PI aerogel structure in order to increase the water contact angle from 87.7º to 112.1º.

Seeking to improve the dielectric properties of PI aerogel, Zhang *et al.* [94] added 5-amino-2-(4-aminopheyl)benzoxazole (APBO) as diamine. This resulted in a very low dielectric content equal to 1.15, making the material suitable for use as an interlayer medium in advanced semiconductor chip interconnections. Wu *et al.* [138] further report that adding the 2, 2′- bis-(trifluoromethyl)- 4,4′- diaminobiphenyl (TMFB) to the PI aerogel main chain can reduce its dielectric content and improve its moisture resistance.

2.7.3 Thermal stability of PI aerogel

PI aerogel is typically thermally stable up to 500 °C [139]. However, the degree of shrinkage below the glass transition and decomposition temperature means that there are limitations constraining the set of potential applications. Consequently, some studies have been conducted with the goal of investigating the different effective parameters that can be manipulated to improve thermal shrinkage [77, 140].

2.7.4 Transparency of PI aerogel

Another parameter that requires consideration is the transparency of PI aerogel. Although this is primarily an opaque material with a yellow colour, Vivod *et al.* [141] report that it is possible to enhance the transparency of this substance without changing its thermal conductivity. They report that this is possible using pyromellitic dianhydride and fluorine-containing monomer 4,4′-hexafluoroisopropylidene di (phthalic anhydride) (6FDA) as dianhydride. They also highlight the possibility of producing a transparent PI aerogel with high surface area and low thermal conductivity due to its small and uniform porous structure using 25 mol% 6FDA[141].

Synthesizing a PI aerogel with high flexibility, low shrinkage and moisture resistance is essential for most practical applications. However, it remains difficult to strike a balance between these properties simultaneously, and this process necessitates optimisation using different diamines, dianhydrides and crosslinkers [39]. For example, in relation to crosslinkers, TAB can promote thermal insulation performance, OAPS can improve moisture resistance and flexibility, and BTC can increase dielectric properties [142].

A selection of diamines and dianhydrides affect PI aerogel products' final performance and applications. For example, Hou *et al.* [143] highlight the potential of creating superplastic PI nanofiber aerogels (PNFAs) with properties relating to high levels of flexibility, hydrophobicity, moisture-resistance, oil absorption and thermal insulation. Furthermore, unlike other types of PI aerogel, which are reusable only to a very limited extent due to fatigue failure, weak mechanical stability, and low-temperature resistance, this type of PI aerogel can also be reused, broadening its field of application.

As previously discussed, high levels of shrinkage during the ageing, solvent exchange and drying processes limit the different applications of PI aerogel. On this basis, Viggiano *et al.* [59] introduce a method that can reduce the level of shrinkage by 50% in the ageing step. For this matter, the polyimide was synthesized using ODA, BPDA and BTC and then BAPF used as a way of distrupting chain packing on the polyimde aerogel with the idea of reducing the shrinkage occurring on te aging at elevated temperature. they reported that the gel time of the polyimide solutions containing 9,9′-bis(4-aminophenyl)fluorene (BAPF) increased due to the increased solubility of the polyimides or lower reactivity of the diamine. The produced aerogel structure at this work showed very little visible physical differences, meaning the addition of BAPF does not impact the development of the fibrillar architecture of the aerogel. In addition, they repoted that, isothermal aging results reveal dramatic reduction in shrinkage for samples made using more amount of BAPF [59].

This kind of PI aerogel can be used in any application with temperatures as high as 200 ℃ for extended periods. As previously noted, although various practical applications demand a combination of flexibility, low shrinkage, moisture resistance, high mechanical properties and thermal stability, striking an appropriate balance informed by the application's precise requirements remains difficult. Producing PI aerogel with most of these properties has given rise to research in manufacturing composites. In addition, PI aerogels have the property of a high rate of adsorption in extreme environments in respect of organic pollutants and grease, having the ability to reach 30–195 times its mass, a rate much higher than those observed for other organic adsorbents [144].

As previously noted, producing PI aerogel with all the simultaneous requisite properties, such as flexibility, low shrinkage levels, thermal conductivity and density, remains

challenging. This highlights the need to consider how such PI aerogel might be synthesized in this way. As part of this research tradition, Zihao *et al.* [145], provide details relating to manufacturing a composite of glass fibre with PI with glass fibre being used in place of an expensive crosslinker to reduce costs. The resulting composite is reported to have high compressive strength, low thermal conductivity and excellent thermal stability.

2.8 Different applications for aerogel

Overall, aerogels demonstrate their suitability in respect of a wide variety of applications, as depicted in Figure 2.14 [146]. As previously discussed, the modern industrial applications for aerogels include thermal insulation for aerospace, construction or any context in which there is a need for high surface area and porosity. These requirements are reflected in the ongoing scientific research into aerogels, and Figure 2.15 illustrates the growth in the number of publications examining such topics in recent years [2, 147].

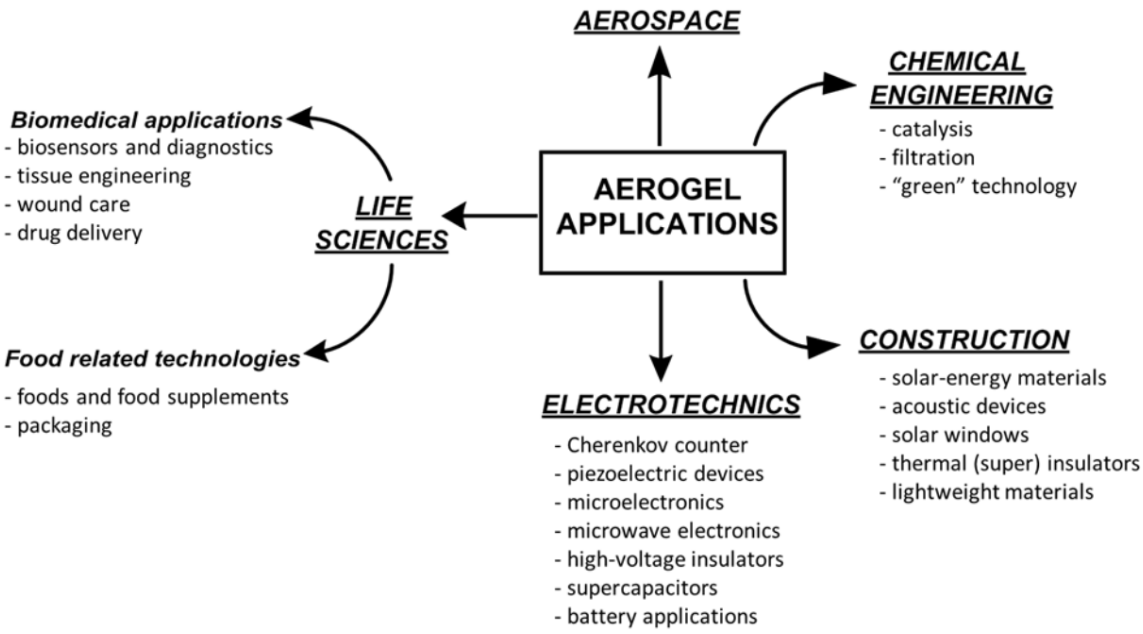

Figure 2.14 Different applications for aerogels [146]

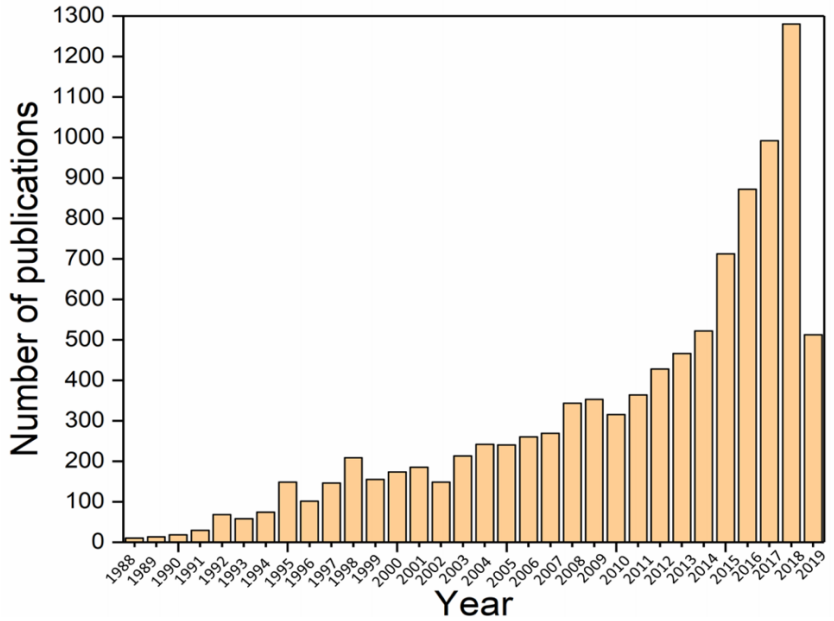

Figure 2.15 Total number of publications examining aerogel over the past 30 years (1988-2019) [2]

The range of aerogel applications has grown recently as industries have become more familiar with this substance's unusual and exceptional physical properties. Hrubesh discusses various specialised applications of aerogels and presents various technical applications in terms of aerogels' differing sizes and shapes [148].

In the case of PI aerogels, their exceptional thermal stability and insulation properties combined with high mechanical properties make this group of aerogels highly useful as thermal insulation materials and dielectric and moisture-resistant materials [39]. Figure 2.16 portrays general applications for PI aerogels across various areas [39].

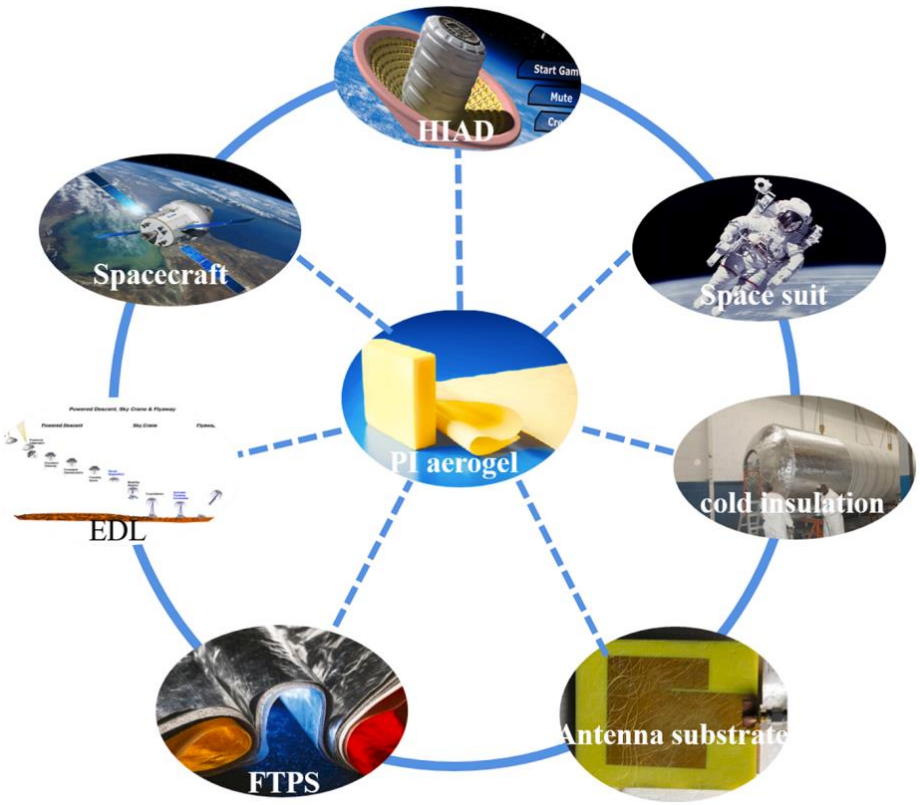

Figure 2.16 Typical applications of PI nano-aerogels. HIAD: Hypersonic inflatable aerodynamic declaration; EDL: Entry, descent, and landing; FTPS: flexible, thermal and protection Thermal insulation materials [39]

Several studies on the nanoporous structure of PI aerogels have provided evidence of their ability to reduce heat transfer at room temperature. For example, 14 mW/m.K rates for PI aerogel thermal conductivity have been estimated [93]. NASA also provide details of the use of PI aerogel in different thermal protection systems, with such an application of PI aerogel demonstrating that it can successfully prevent heat transmission. Based on this property, PI aerogel sees use in several other aerospace systems, including propellant tanks, spacesuits, probe vehicles and aircraft [54]. In addition, it can be used as a polymer in adiabatic applications [142].

2.8.1 Dielectric, communication devices and moisture-proof materials

PI aerogel with a low dielectric constant can be synthesized with different raw materials. There is also a need to consider the aerogel's hydrophobicity to promote its dielectric constant. For example, the PI nano-aerogel can be used in antennas as a substrate material with more desirable properties than traditional substrate materials. The use of PI aerogel in antennae can also expand the communication range by 80% [39]. The low dielectric constant of PI aerogel also means that it can be used in electronic communications and global positioning systems (GPS), although it should also be noted that, in general, PI aerogels can be replaced by all traditional materials in different fields [145].

2.9 Different forms of polyimide aerogel

2.9.1 Polyimide aerogel stock shape

The research that has been conducted has tended to pay attention to PI aerogel on the basis of the fast and facile synthesis method, characterized by its safe and short operation and environmentally friendly process [149]. The polyamic acid can be synthesized in different ways. After the imidization process, it can be moulded in any size and shape and left to age, following which the PI aerogel stock shape will be produced after solvent exchange and drying [150].

2.9.1.1 Moulding process

Moulding is a process for manufacturing shaped liquid, plastic or unformed material using a fixed frame. Different moulding processes are called according to the plastic to be used, and each process involves multi-step handling of molten plastic and leaving this to set. The product can be thermoplastic or thermoset. In terms of the differences between these, thermoplastics can be melted down and reformed if necessary; however, thermoset plastics cannot be reheated in this way. Generally, the mould is made from metal, enabling the plastic material to be poured in and shaped. It can be removed after the material cools and hardens inside the mould. There are different types of moulding processes, and the ensuing sections consider different such processes in turn.

2.9.1.1.1 Casting moulding

Casting is the primary method for moulding plastic material and is typically used for making film and sheets. The solid formed is produced using chemical curing or cooling the liquid inside the mould. Casting moulding is generally simple in terms of this method's technology demands [151].

2.9.1.1.2 Injection moulding

Injection moulding is a technique for reproducing high-quality objects. When this technique is used, the molten plastic is injected into the cold and closed mould, and, following the completion of the shaping of the plastic, it can be released simply by opening the mould. Different types of components are produced using this technique[152].

2.9.1.1.3 Blow moulding

Blow moulding is a process used for making products such as piping and milk bottles. When this technique is used, the plastic is heated until molten and injected into a cold mould. The mould has a tube set within it, which has a particular shape when inflated. When the plastic is molten, the air is blown into the tube, and the plastic is formed around the tubing. It is then left to cool and removed from the mould[153].

2.9.1.1.4 Compression moulding

Compression moulding is a forming process that is generally used for making large-scale products involving the application of pressure and the press technique. To use this technique, pressure is applied, and the molten plastic is pressed between two mould plates of the desired shape. The plastic is left to cool and then removed from the mould. This method is typically used when the target components are flat or only moderately curved. The advantage of this method relates to its low costs and the minimisation of waste, which is an essential consideration when working with expensive materials, especially in large quantities [154].

Pekala *et al.* [155] used compression moulding for making rod, block and monolithic silica aerogel composite. As part of this approach, the micro spherical particles were moulded under pressure and heated to a point between 50 and 70 °C. This approach to

compression moulding produced a monolithic silica aerogel composite with densities ranging from 0.05-0.80 g/cm^3.

Joshi *et al.* [156] investigated the effect of mould design on manufacturing silica composite sheets. This was done by applying different moulding techniques and investigating their influence on aspects of the composite, such as shape, shrinkage and other properties. They show that optimising the mould design and condition can help achieve perfectly uniform, thin, geometrically flat aerogel composites with no curvature or warpage.

Kim *et al.* [112] report the results of an investigation into a one-step method for synthesizing PI monolithic aerogel. Pyromellitic dianhydride (PMDA) and 4,4-oxydianiline (ODA) polymerization was used to produce a homogenous structure with high thermal and mechanical properties using the thermal curing and swelling method (the process of penetration of solvent molecules into a polymer matrix causing a change in the volume). Instead of using supercritical drying, a multi-step process typically incurring significant costs, the researchers used ambient pressure drying. Thus, the synthesized polyamic acid was stirred and slowly added to acetone for 1 h. The space in the baker was filled with acetone making the porous structure swell. The mixture was then put in an autoclave and a vacuum oven for 6 h at 150 °C. The produced PI aerogel is reported as being thermal stable up to 577 °C with a Tg (glass transmission temperature) of 432 °C, bulk density and porosity of 490.7 kg/m^3 and 45%, respectively. Compared with supercritical dried aerogels, a relatively lower compression modulus of 0.122 MPa at a higher density of 0.49 g/cm^3 and significantly lower porosity of 45% are reported for this method. Based on the thermal properties of supercritical dried aerogels, the produced PI aerogel monolithic is reported as having a high onset of decomposition of $Td_{10\%}$(10% decomposition temperature) = 577 °C. Moreover, samples are reported as having an ability of about 100 wt.% oil uptakes and reusability after 24 h of 100 °C atmosphere pressure drying for water filtering applications [112].

Chidambareswarapattar *et al.* [157] detail a method involving monolithic multiscale micro/meso/macro-porous polymers with potential use in catalysis, gas separations and gas storage. The system is based on hyperbranched PIs synthesized via an unconventional route from dianhydrides and triisocyanates. For their synthesizing reaction, pyromellitic

dianhydride (PMDA) or benzophenone tetracarboxylic dianhydride (BTDA) were put to react in a 3:2 mole ratio with a rigid aromatic (TIPM) or aliphatic triisocyanate. The gelation process was conducted at 90 ℃ and left at room temperature before supercritical drying. They also report using different techniques in order to control micro, meso and macroporosity. Macroporosity is reported as being controlled mainly in terms of the reactants' concentration, while mesoporsoity and how the particles fill space were controlled in terms of the monomers' chemical identity[157]. This study also details how a continuous fabrication method was applied to manufacture the PI aerogel's pill shape during the oil emulsion process. The deformable spherical sol is processed through a contraction flow downstream of the microfluidic droplet generator. Using this technique, the sol droplets transformed into sol microparticles. The pill-shaped PI aerogel microparticles are reported as having a diameter of approximately 200 μm and a length of roughly 1000 μm, and so heating of the pill-shaped microparticles at 80 °C was conducted to accelerate the sol−gel transition and fix the pill-shaped geometry. The researchers also detail how microparticle length could be controlled by varying the ratio of the flow rates of PI sol and silicone oil [158].

Meador *et al.* [23, 49] produced a flexible and mechanically robust PI aerogel using a version of the sol-gel process. Three different diamines (ODA, DMBZ, or PPDA) and two dianhydrides (BPDA or BTDA) in different stoichiometric ratios were used to synthesize the polyamic acid. Immediately after mixing various diamines with dianhydrides, the mixture was poured into a mould and aged for 24 h. The PI aerogel was made and ready for characterising after a solvent exchange with N-methyle-2-pyrrolidone (NMP) and acetone in different ratios and steps, followed by supercritical and vacuum drying.

Zhai *et al.* [52] synthesized PI aerogel in monolithic form. The solid mass was calculated according to the final solutions' weight concentrations of PI products. Manipulation of different solid content (2.5%, 5%, 7.5%, and 10%) and changing the types of solvent (NMP and DMF) were undertaken to produce the samples. The caste moulding was applied such that the monolithic sample was 32 mm in diameter and 2.5–5 mm in thickness. Different gelation techniques were also used depending on the solid weight in

the mixture, from 10 min to 3 h. After ageing for 24 h, solvent exchange was applied six times. After supercritical drying, the samples were prepared with liquid CO_2.

2.9.2 Polyimide aerogel film

PI aerogel can be fabricated in film form with different thicknesses and different properties. The main aerogel products currently offered on the market are film and blankets manufactured by sol-gel casting and processing in fibre matrices, followed by drying under supercritical or ambient conditions [159, 160].

Mi *et al.* [26, 161] introduced a new high-performance triboelectric nanogenerator (TENGs) using the PI aerogel film and mat on triboelectric nanogenerators (TENGs). This involved the application of the electrospinning method for preparing the PI mat. Polyamic acid was synthesized using NMP in a molar ratio of dianhydride to total diamines of 26:25. Different types of diamines and dianhydride, such as ODA, OAPS, TAB, DMBZ and PPDA, were used in different ratios. The synthesized polyamic acid was then cast onto a PET carrier using a 12′ wide blade at 80 cm/min speed. The gel film was peeled away from the carrier film, and these films were then washed in 24-h intervals in 75% NMP in acetone, followed by washing in 25% NMP in acetone and then three more times with acetone. The washed film was finally subject to supercritical drying.

Meanwhile, Hou et al., [153] fabricated super flexible PI aerogel by crosslinking the PI membrane with PI nanofiber. For this reason, firstly, PI nanofiber was prepared by mixing pyromellitic dianhydride (PMDA) and 4,4′-oxidianiline (ODA) in dimethylacetamide (DMAc). The produced polyamic acid was then poured into the syringe, following which electrospinning was applied at a voltage of 100 kV/m and speed of 1.5 mL/h to produce the PI nanofibers. The produced nanofibers were added to the separate polyamic acid and mixed to achieve uniform dispersion after 12 h. Propionic anhydride and pyridine were then added into the PI nanofiber/PAA solution as gelation agents and poured them into the mould. The washed wet gel with ethanol was finally subject to supercritical drying.

Qian *et al.* [53] introduce a new method of creating thermally crosslinked aerogels from electrospun PI nanofibers as building blocks to avoid the neck and the crosslink stress concentrations proposed from the gels and the chemical crosslinkers, respectively. In this

method, the prepared PAA from ODA and PMDA monomers was processed by means of electrospinning, followed by thermal imidization. The nanofibers were then homogenized in dioxane, followed by freeze drying to maintain the integrity of the solid network. Finally, thermal treatment at 500 °C for 15 min was used to crosslink the nanofibers by means of intermolecular condensation. The thermal crosslinking resulted in relatively low shrinkage of less than 4% and a weight loss of about 18%, and the main functional groups of PI remained intact after the thermal treatment. Highly flexible aerogels with a very low-density range of 4.6 –13.1 mg/cm^3, a 99.0–99.6% porosity, and various shapes were formed [162].

2.9.3 Polyimide aerogel powder

Gelation and processing of sol on a large scale, as in the production of a blanket or stock shape, are tasks of high complexity that are made even more complex and that take longer to complete by the longer diffusion lengths for solvent exchange and the inserts of hydrophobisation agents and catalysts into the gel body [163]. Such processing is both costly and time-consuming. However, particle-based aerogel is a promising alternative in sol-gel processing that can accelerate manufacturing and reduce costs, especially those associated with solvent exchange and drying processes.

Recently, evidence has emerged that reducing the dimension of such materials from a few millimetres to a micrometre or even a few nanometres induces many unique properties [164]. Typically, aerogel microparticles with 50-200 µm diameter have advantages that make them particularly appropriate for use in ion transport or ion adsorption, the removal of toxic liquids and the delivery of drugs, in which tasks large surface areas and short diffusion paths are likely to be beneficial [165].

Aerogel microparticles from thermally stable polymers such as PI have a variety of applications, many of which can be said to be due to the advantages they have as compared with large-size monoliths. For example, PI aerogel microparticles of a few nanometres or micrometres have a triple mass diffusion rate compared to monolithic ones with similar porosities and surface areas. For this reason, monoliths cannot be used in applications requiring powders or microparticles, such as catalysts, energy storage

devices, drug delivery systems, scaffolds or the absorption of small organic molecules [164].

Powder particles can be produced using a variety of techniques, such as spray drying [166-168], emulsion [169-173], jet-cutting [174-176] and dry milling, in which the powder is obtained using mechanical crushing of previously formed monolithic aerogel structures [177, 178]. However, regardless of how they are made, such dry-milled powder exhibits weak mechanical properties [164]. In their study of PI microparticles, Lee *et al.* used swelling methods in order to control pore size and porosity. Using this simple technique, which did not require a solvent exchange or supercritical drying, the researchers were able to increase pore size and pore volume from 4 nm to 20 nm and 1.29 to 2.06 cm^3/g simultaneously [179]. The polyamic acid was synthesized to prepare the particles by adding the ODA and PMDA into the NMP pore in the glass vial. The free volume was filled with acetone, and the vial was placed into the autoclave at 4 MPa at 250 °C. While the outer solvent evaporated to create a critical atmosphere, the liquid phase NMP is reported as having played an essential role in the system, retaining the gel structure against shrinkage with the vapour pressure of 0.4 MPa at 250 °C.

In their study, Yamaguchi *et al.* [180] used spray drying at 120 °C to produce PI powder and the uniform solution produced using BPDA, DMZ and methanol was mixed and sprayed at 120 °C and then dried over multiple steps.

Cano *et al.* [181] investigated different effective parameters for making PI foam from powder precursors, including the evaluation of parameters such as particle morphology, volatile concentration and sorption-desorption. The PI particles were synthesized from poly(amic acid) of 3,3′,4,4′-benzophenonetetracarboxilic dianhydride, (BTDA) and 4,4′-oxydianiline (ODA) with sizes in the range of 75 to 300 μm being used in the foam processing. The particles were heated to glass transmission temperatures and converted into foam.

Yun *et al.* [182] improved a modelling method for synthesizing PI powder using the 1,3-bis [4-(3-aminophenoxy)benzoyl] benzene (BABB) and pyromellitic dianhydride (PMDA). They considered the morphological structure, melt viscosity, powder's thermal stability, and mechanical properties of the moulded powders and report that, compared to

PI made in the traditional manner, the glass transmission temperature and melt viscosity of the moulded powder were lower. They also report that the reason for this relates to the introduction of the flexible monomer into the polymer chain. At the same time, the moulded PI powder is also reported as showing desirable mechanical properties, low water absorption and high thermal stability.

Instead of using supercritical drying, Kwon *et al.* [66] synthesized PI aerogel microparticles using a newer, simpler method. A soluble PI was replaced with Kapton chemical structure PI polymer (developed by DuPont), with superior mechanical properties and chemical stability. The polyamic acid prepared through the reaction of PMDA-ODA was placed in an autoclave and the space between the autoclave and the glass of polyamic acid was filled with acetone. PI aerogel microparticles were then formed by placing the autoclave in an oven and applying step-wise heating from 150 ℃ to 250 ℃ with a 2 ℃/min ramp. At 250 ℃, the acetone was in the supercritical stage but NMP, as the main solvent, was still in the liquid phase. Therefore, the polyamic acid was able to cure into PI without solvent evaporation. After 400 min of processing in the oven, the autoclave was removed, and the PI aerogel microparticles were extracted from the solvent in the form of colloid and dried at 130 ℃ in a vacuum environment in order to complete the curing reaction and produce the PI aerogel microparticles. Using the dynamic light, it was observed that the size of the spherical particles was in the range of 3.6 and 4.9 µm, with 0.306 g/cm^3 density and 80% porosity. The TGA characterization results also confirm that the PI aerogel microparticles had been subject to the imidization reaction to the required standard [66].

Lee *et al.* [179] used swelling methods to investigate PI aerogel's spherulitic formation. Using this simple technique, which did not require solvent exchange or supercritical drying, it was found that pore size and pore volume increased from 4 nm to 20 nm and 1.29 to 2.06 cm^3/g simultaneously.

Vaganov *et al.* [183] used selective laser sintering to manufacture a thermoplastic semi-crystalline polyamide powder. Narrow particle size distribution was achieved using SEM characterization. The DSC results for the PI particles showed endothermic melting peaks at a temperature of ~318 °C, indicating that they were crystalline. At the same time, the specific thermal transitions corresponding to Tg could be observed only by reheating the

powders. In order to produce the PI powder [183], polyamic acid was synthesized using polycondensation of anhydride with a diamine. After the amines were mixed with anhydride in a specific ratio, phthalic anhydride was added for 4 h to control the molecular weight. In the following step, a mixture of acetic anhydride, triethylamine and benzene was added and vigorously stirred for 1.5 h to induce the chemical imidization and produce the powder particles. The filtered particles were then washed with ether and methyl alcohol and dried at 220 ℃ for 2 h. In order to measure and study the shape and size of the particles, image-J was utilised as a means of gaining SEM images. SEM characterisation was then possible to achive a narrow particle size distribution. The fabricated particles were mostly irregular and in the 2-30 μm range. The data from the distribution plot showed that the primary particle size fraction lay at 6-15 μm. The DSC results for the PI particles also demonstrated endothermic melting peaks at a temperature of ~ 318 °C, indicating that they were crystalline.

2.10 Consolidation of powder particles

Recently, a new PI aerogel has been developed at NASA's Glenn Research Centre [21]. This PI aerogel represents a revolutionary advance over the fragile silica aerogels currently available on the market. The industrial sponsor of this project, Blueshift International Materials, has an exclusive licence for this technology. Although, as previously discussed, PI can be synthesized using various methods, the most versatile may be the crosslinking of amine-terminated or anhydride-terminated oligomers [43], which makes it possible to produce highly porous aerogels in either flexible thin films or rigid thicker substrates. PI aerogel can be prepared in different forms such as monolithic, film and microparticles. The more straightforward fabrication methods that can be used to produce PI monolithic mean that this aerogel is likely to be the focus of increasing levels of attention [172]. As part of the research considering this aerogel, Meador *et al.* [184] reviewed the properties of PI aerogels and formulated oligomer chain lengths using different diamines and dianhydrides. They state that the resultant wet gel must be subject to solvent exchange and drying processes. Such processes are costly in terms of time and money when conducted to produce PI monolithic and stock shape.

In order to use all the unique properties of the metastable material, consolidation and densification of the particles are necessary to produce a specific shape and size of stock shape material. There are several applications for which it is necessary to produce a particular type of material in terms of its geometry, size and properties. Given this, the consolidation process is typically conducted to densify the powder with minimum coarsening. If this goal is to be achieved, some restrictions must apply [185].

The consolidation method can be selected as informed by the initial particle size, the acceptable degree of (in)stability and the available equipment. Rapid consolidation is usually used with powder in the micron range, which necessitates using a high temperature over a lengthy period. Using consolidation for particles with a size below the micron range causes agglomeration due to friction and contamination, and so the recommended method of dealing with these particles is typically pressure [185].

In general, densification and consolidation processes are used to convert initial powders into bulk materials to produce no pores or only a minimum number of pores between the particles. This is also done to consolidate the powder particles by reducing the free surface energy as a driving force, which depends on the type and condition of the initial powder and the level of stability that is required by the end of the process. The main step in consolidating powder is collapsing the pores and filling the void spaces between the particles using a binding agent. Generally, the powder particles are thermodynamically unstable, with their morphological metastability depending on the size and shape of the particle. As the following equation demonstrates, the surface area of the particles will be increased by reducing the size of the particle:

$$6/(\sigma \times \rho_s)=d \qquad (2)$$

Where ρ_s is skeletal density, σ is specific surface area, and d is the diameter of the particle.

When selecting the optimal consolidation method from the specific particles, several parameters can be considered: the initial particle size, its application and the level of metastability required of the usage particles. There are also different methods of densifying the material. Sintering, compression and adding binder material such as epoxy are all methods that can be used to solidify such material.

Joshi *et al.* [156] report on the moulding of silica aerogel granules in a rectangular mould using Porcine gelatine as a binder and sodium dodecyl sulphate as a foaming agent. Freeze drying under a vacuum was employed for 18-24h with the samples. The mechanical properties of the produced samples were also measured using different moulding conditions.

Woignier *et al.* [186] meanwhile, made use of sintering by means of heat treatment in order to densify the silica. In their study, finding that the type of thermal treatment, the final density and other properties of the produced silica aerogel vary accordingly. They detail an increase in the bulk density of the produced silica aerogel induced by increasing the temperature. They also report a significant relationship between the pore volume of the samples and their mechanical properties and the strengthening of the material. They also note that heat treatment would increase the material's connectivity and mechanical properties [186, 187].

Kim *et al.* [112] fabricated PI aerogel monolithic using pyromellitic dianhydride (PMDA) and 4,40 -oxydianiline (ODA) without adding any other component for the purpose of connecting the microspherical particles. For this process, the PAA was poured into a glass bottle and then placed in an autoclave. The space between the glass and the autoclave was then filled with acetone. The PI monolithic was fabricated from the microspherical particles using stepwise drying throughout a gradual heating-up process. The researchers report TGA showing similar thermal properties for both the particle and monolithic samples.

2.11 Epoxy resin introduction

Pre-polymers with low molecular weight contain one or more reactive functional groups called epoxy, which, in IUPAC, is known as the oxirane group[188]. The other parts of the molecule (non-epoxy part) can be aliphatic, aromatic or cycloaliphatic, all of which relate to the epoxy group. Epoxy resin was discovered for the first time in 1909 [188]. The general structure of the epoxy group is detailed in Figure 2.17 [188].

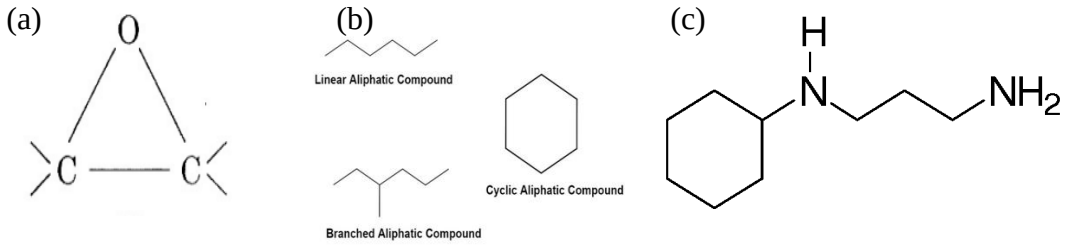

Figure 2.17 (a) epoxy group (oxirane), (b) aliphatic, (c)cycloaliphatic [188]

Different types of curing agents can react with epoxy rings as part of treatment to cause the insoluble and infusible state of thermoset polymers to take a soluble, fusible form. Different types of solvents, plasticizers and accelerators can all be used to improve and modify the properties of cured resin in this way. This process can be analyzed as comprehending two distinct stages: conversion and crosslinking. During conversion, the chemical reaction occurs so that the reactive group (the epoxy group) disappears. In the next step, the three-dimensional network known as crosslinking is shaped. The degree of crosslinking is affected by the chemical reaction, the conversion, and the compounds' functionality within the reaction [236]. Due to the electronegativities of carbon and oxygen atoms in the epoxy group, compared with other ethers[189], epoxy resin is highly reactive.

The first and the most common epoxy resin is the reaction product of bisphenol-A (BPA) and epichlorohydrin (ECH) in the presence of sodium hydroxide, which produces diglycidyl ether of bisphenol A (DGEBA) (see Figure 2.18)[188]. This epoxy group can be cured using various chemicals, such as alcohols, amines, anhydrides, carboxylic acids and phenols. The curing agent is the determining factor in the kinetic of the curing reaction and dramatically affects the performance of an epoxy system. Amines are the most common hardener, having more than three reactive sites that can be used in order to produce a three-dimensional network. Three main reactions (primary amine-epoxy addition, secondary amin-epoxy, Hydroxyle-epoxy addition)[190] define the curing in the epoxy/amine systems, and these reactions may happen simultaneously or sequentially based on temperature and component reactivity [188].

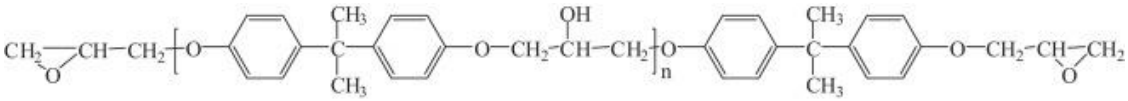

Figure 2.18 Chemical structure of diglycidyl ether of bisphenol A (DGEBA) [188]

In the late 1950s, several new epoxies were developed to have excellent properties, setting them apart from diglycidyl ethers. This epoxy was produced to be able to duplicate the performance of the thermosetting plastics. Due to their wide range of applications and properties, epoxy resins can be used in a wide range of applications relating to coatings, electrical goods, electronics, casting resins, dipping compounds, and moulding powders [189]. It is also possible to use epoxy to bond different materials to each other, including metal, glass, wood and many plastics. On this basis, epoxy is considered so versatile across many industries.

2.11.1 Properties of epoxy

The properties of epoxy can be categorised into the following groups [191]:

Versatility: Epoxy resins are the most common among different types of plastics. Other types of their properties can be improved by selecting the proper curing agent and blending different types of resins.

Easy cure: Epoxy resin can cure quickly, depending on the selected curing agent, at temperatures between 5 and 150 °C.

Low shrinkage: One of epoxy's most advantageous properties is the low degree of shrinkage exhibited during the curing process.

Adhesive properties: The presence of polar hydroxyl and ether in epoxy means that it has excellent adhesive properties. In plastic technology, adhesive strength without extensive costs being incurred in terms of time or pressure is highly sought after.

Useful mechanical properties: The low degree of shrinkage compared to other casting resins means that epoxy has beneficial mechanical properties.

In the epoxy system, the networking process is divided into three stages. The first stage relates to the point before gelation, at which point there are unreacted monomers and low molecular weight oligomers. In the second stage, gelation and the initial appearance of an infinite molecular weight network occur. In the third stage, network growth ceases as the crosslinked structure prevents the diffusion of unreacted species to active reaction sites [192]. In addition, depending on the application and required properties of the epoxy, other types of bisphenols can be used to modify the properties of the resin. For example, bisphenol F is used for synthesizing the diglycidyl ether of bisphenol-F resin (DGEBF), giving rise to a resin of lower viscosity. Bisphenol-H (hydrogenated bisphenol-A), meanwhile, is used to synthesize diglycidyl ether of bisphenol-H (DGEBH), which demonstrates a high degree of weather resistance [191]. Bisphenol-S (4,4,'-dihydroxy diphenyl sulfone) is used to obtain thermally stable epoxy resin known as diglycidyl ether of bisphenol-S (DGEBS) [192]. In this way, it can be seen that the properties of resin depending on the combination of the epoxy resin and curing agent. A significant volume of literature considers the properties of the different types of varieties of epoxy resin and curing agents [193-199].

Determining the presence of epoxy is done using infrared spectroscopy. This technique uses the adsorption band at 10.92 microns to show the epoxy group. When the epoxy is cured, this band will disappear as a result of the opening of the epoxy ring [200]. It is also observed that the chemical and mechanical properties of the cured epoxy depend on the types of curing agent, time and temperature of the curing.

2.11.2 Epoxy resin application

Research on epoxy resin technology began in the United States and Europe just before World War II [201]. As a result of this long research tradition, it has emerged that epoxy resins can match the performance of most other thermosetting plastics and that their performance can be improved to make them suitable for a high number of specialized applications. Due to their excellent mechanical properties, high degree of adhesion in respect of many substrates, and a high degree of resistance to heat and chemicals, epoxy resins are used across many fields. They are used as fibre-reinforced materials, general-purpose adhesives, high-performance coatings and encapsulating materials [202-205].

Recently, epoxy resins with high strength, versatility and the ability to adhere well to a variety of surfaces have gained attention due to their wide range of applications in many fields, such as coatings, electrical, electronics, casting resins, dipping compounds, moulding powders and reinforced plastic industries [30]. As noted previously, the properties of the epoxy depend on the types of epoxy resin, the curing agents and the specifics of the curing process.

2.11.2.1 Paints and coatings

Due to its toughness, chemical resistance, generally safe mode of operation, outstanding adhesive properties and mechanical and corrosion resistance, one particularly important application of epoxy is as heavy-duty anticorrosion coating. For example, metal containers can be coated with epoxy to prevent rust. Epoxy resins can also be used in flooring and chips. Figure 2.19 shows different applications for epoxy [206].

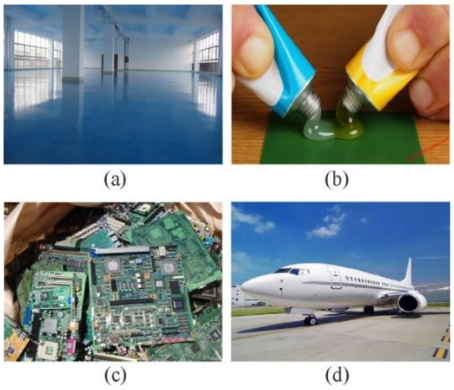

Figure 2.19 Different applications of epoxy; a)flooring; b) adhesive properties; c)chip; d) corrosion resistance [206]

2.11.2.2 Adhesives

Epoxy resins can be used to achieve high-strength bonds, such as those required in the construction of aircraft, automobiles, bicycles, boats and skis. Typically, such epoxy adhesives are cured at a specific temperature in order to increase their strength and activate chemical bonding [207, 208].

2.11.2.3 Aerospace industry

Epoxy resins have seen recent use in the aerospace industry due to their desirable adhesive properties and low cost of production. In this context, it is common for the epoxy to be reinforced with high-strength glass, carbon, Kevlar or boron fibres [209, 210].

2.11.3 Curing process for epoxy

The process of curing epoxy is controlled and modified using a curing agent. The choice of curing agent has consequences for the kinetics of the curing and some of the thermal properties of the produced epoxy, such as Tg [211]. Different types of curing agents can be used for curing epoxies, such as amine-type, alkali, anhydrides and catalytic curing agents. In the curing process, the epoxy group reacts with the curing agent in a way that produces the crosslinked three-dimensional network [212]. The curing process can take place at room temperature or through curing with heat. Curing at room temperature can be performed using curing agents such as aliphatic polyamines, alicyclic polyamines, low molecular weight polyamide and modified aromatic amines. Products that are manufactured using this method tend to have lower Tg and higher thermal and electrical resistance as well as greater flexibility. However, when curing is to be performed using heat, aromatic polyamines, acid anhydrides, resol resins, amino resins, dicyandiamide and hydrazides are typically used as curing agents. Using a high temperature for curing in this way tends to result in cured epoxy with high Tg and greater thermal and chemical resistance [213]. In order to improve the toughness of the epoxy resin, thermoplastic components such as poly(acrylonitrile-*co*-butadiene-*co*-styrene) (ABS), poly(ether sulfones) (PES), poly(ether imides) (PEI), polysulfones (PSF), poly(ether ketone) (PEK), and PI, can also be added to the epoxy resin [214, 215]. If the goal is to produce a modified thermoplastic epoxy, then polymerization-induced phase separation of the thermoplastic modifier is performed in a way that this process is initially miscible in the epoxy resin before separation into phases during polymerization [216, 217].

One of the techniques investigated in this project involved epoxy resin, so a brief review of existing research on aerogel modification with epoxy is given below. As noted above, epoxy resins have several advantages in terms of chemical and corrosion resistance, thermal and dimensional stability, and several other desirable mechanical and electrical

properties; as a result, they have use in a broad range of applications in laminating adhesives, surface coating and semiconductor encapsulation [218, 219]. Many surface treatments have also been developed to increase the adhesion between PI and epoxy. For example, Huntrakool *et al.* [220] investigated the surface reactivity of four different PIs with epoxy, making use of contact angle, flow microcalorimetry, Fourier transform infrared spectroscopy and x-ray photoelectron spectroscopy.

Akhter *et al.*[221] meanwhile, studied the composite of PI with epoxy by producing two types of PI, namely one synthesized using DTM and BTDA and another through a reaction of DHTM and BTDA. The PI was blended with epoxy in different compositions to produce an epoxy-amine network and this was characterized using thermogravimetric analysis (TGA), differential scanning calorimetry (DSC) and x-ray diffraction (XRD).For synthesising the composte of polyimide-epoxy, the synthesised polyimides were ground to fine powder. Average particle size of ground polyimide is 15 μ . Polyimide in different weight ratios was blended with epoxy and diamine as curing agent in DMF solvent. The mixture was stirred at room temperature for 24 hours until a homogeneous solution was obtained. The solution was then transferred into Teflon coated petri dishes which were placed in vacuum oven at 100 ˚C for three hours and at 120 ˚C for next three hours. These films were peeled off from Petri dishes and were subjected to further analysis [221]. But the main difference between these methods and this work, is that epoxy is the matrix part in these composite compare to tis work which polyimide is the matrix part.

In their study, Kim *et al.* [222] used various techniques to prevent the aerogel pores from being affected by resin infiltration. The researchers also report the method for producing the composite of silica aerogel with epoxy in different concentrations of the aerogel. This method involved immersing the silica aerogel powder in ethanol in order to fill the pores with ethanol before mixing it with epoxy, thereby ensuring that the pores could be kept in a state such that they could be filled with epoxy. Therefore, ethanol can be consider as a way to prevent the pores from filling.Then aerogel/ethanol, epoxy and hardener were mixed and put through the press at 80 ℃ and 1 MPa for 5 h. This process removed the ethanol from the pores before making the composite hard. The results reported by the researchers show that ethanol was able to preserve the pores, but also that some infiltration inside the pores caused higher thermal conductivity in the composite material,

and to a greater degree than expected. The results also show that the thermal conductivity decreased as the aerogel volume fraction was increased in the composites [222].

Ge *et al.* [223] present details of a dry mixing method for making silica composite with epoxy powder in order to decrease epoxy immersion inside the silica pores. Following this concept, they mixed silica powder with epoxy powder in dry form and then used a hot press at 180 °C and 1 MPa for 30 min.

Zuo *et al.* [11] manufactured PI nanofibrous membranes using electrospinning and reinforced them with epoxy resin. Using different characterization methods, they showed that strength and elongation at the breaking point were four times stronger at the contact points, where there was a fusion of fibres.

Piljae *et al.* [224] produced PI/acrylic/epoxy bricks using 3D printing techniques, choosing to use this method to manufacture a complex shape sample that would have been difficult to produce using a supercritical process. Ambient drying was therefore applied to these samples. To produce this sample, the monolithic PI aerogel was first produced, following which it was crushed into 1mm particles. The mixture of aerogel particles with epoxy was then injected into the bricks and cured at 80 °C overnight. The samples were characterized using a variety of techniques. However, the mechanical properties of these samples are not detailed.

Microwave sintering (MWS) is a rapid technique used for consolidating nanoparticles, relating to the ability of the material to adsorb microwave energy in a way that results in self-heating. Agrawal investigated the effects of the size of the particles and porosity on heat conductivity during MWS [225]. There is also independent evidence from another study that smaller particles with higher porosity transfer heat faster [226].

2.12 Polyimide-epoxy composite

It is believed that the severe shrinkage problems during imidizatoin can result from the removal of condensation water and residual solvent. This shrinkage limits the processability of most PIs in terms of the shapes they can take, such as thin films, with large surface areas and small volumes. Thus, except for a few new moulding compound formulations, they can generally be considered thermosetting polymers. Additionally, the

high cost of many precursor monomers has restricted the more widespread use of PIs, resulting in the market retaining only those that can sustain higher cost/property ratios, such as the electronics and aerospace industries. Epoxy, on the other hand, is inexpensive and is highly regarded for its ease of fabrication with minimal shrinkage and its ability to use a diversity of additives to obtain the desired properties.

Making a composite from different aerogels can also improve aerogels' thermal and mechanical properties. Seeking to prove this idea, Kim *et al.* [227] investigated the synthesis process for making the silica aerogel/PI composite with a multi-step drying process for preserving the pores of the aerogel in the final product. They also worked on a composite of silica aerogels with epoxy, showing that the pores could be filled by adding the epoxy, thus increasing thermal conductivity. They also used a new multi-step drying process to make the silica aerogel/PI composite to preserve the pores and reduce thermal conductivity. Wu *et al.* [177] also worked on PI composition with silica. They showed in their study that combining silica aerogel with PI aerogel can improve a number of mechanical properties of silica and reduce the degree of shrinkage. The researchers report that, although the most significant shrinkage occurred during gelation, adding the silica to the PI aerogel treated as a cross linker made it possible to reduce this shrinkage by up to 50%. They also confirm that adding more silica to the PI increases the surface area and decreases thermal conductivity.

2.13 Different methods for synthesizing the PI aerogel powder

To the best of our knowledge, there are two main methods for synthesizing aerogel microparticles in the literature. The first method, or the splitting method, is applied to transform aqueous polymer solutions into microparticles. The micrometre particles that are produced are then freeze dried. This method is an option in the production of, for example, cellulose aerogel microparticles [228]. The second method, involving water in oil emulsion, is performed by dispersing the micrometre droplets produced from the aqueous sol in an oil. Through the sol-gel process, the micrometre particles convert to the gel. Typically, aerogel microparticles are produced via emulsion polymerization of precursor sol droplets stabilized by surfactants in an immiscible continuous liquid medium [228]. The size of the produced particles in this method depends on the mixing

speed, surfactant type and concentration and the dispersed phase content [229]. In the final stage, the aerogel microparticles are obtained via supercritical drying [230, 231]. This method can be used to produce silica aerogel microparticles. Unfortunately, however, these methods do not apply to the polymeric families of precursors that are insoluble in water, such as PI aerogels.

The three different methods that can be used for synthesizing PI aerogel particles in this work are as follows:

1) Milling process

2) Wet gel grinding method (WGG)

3) Emulsion process (EM)

2.13.1 Milling process

This technique can be used as a means of grinding the dry stock shape to produce a powder. This is typically done using a machine with a cutter on one or two axes. When this method is used, the sharp teeth on the milling equipment cut the material to produce the desired shape. This process is usually used to make particles with holes and slots of non-uniform shapes and sizes. Milling is particularly recommended for use with three-dimensional shapes or when seeking to refine features on parts that have already been made using different techniques. A wide variety of finished surfaces are produced using this milling technique.

By moving the cutting edge of the milling tool, which is a shear strain action on the surface of the workplace, the surface and edges are scraped, and tiny clumps are repelled. The milling process can be controlled in terms of different parameters, such as by using a multi-tooth cutter, low and high rotating speeds, and changing the milling direction and feeding rate. Nalluri *et al.* [232] show that, in the milling process used for their study, feeder speed did not affect particle size but did result in a statistically significant influence on flow response. Dry milling can be considered a critical pharmaceutical unit in manufacturing solid dosages [233]. Given the importance of particle size on product attributes, this has tended to be the focus of greatest attention in this area of study [234].

Kang *et al.* [235] introduce a new method for producing aerogel powder with a long shelf life from drugs to use in the bloodstream of mammals, reporting dry milling as an appropriate second method for shaping the produced aerogel particle in the desired shape and size. Randolph *et al.* [236] also report using a new type of dry machining called turn-milling to machine aerogel foams.

2.13.2 Wet grinding

Wet grinding describes a grinding process performed with the addition of water or another solvent. There are a number of reasons why this approach might be taken:

- the need to cool or lubricate the processed surface
- the need to protect the tool against corrosion
- the need to increase the processing speed
- the need to improve the surface finish
- the need to protect the product against the abrasive

Compared with milling a dried sample, performing grinding in a wet shape (before drying) can increase the rate of the grinding process. Bauer *et al.* [237] detail a patent regarding the production of aerogel particles by wet milling, showing that wet grinding reduces accumulation and makes it possible to reduce particles with an average size of less than 1 micron. They also show that aerogel particles can be ground in the presence of liquid or slurry as a means of performing wet grinding. In this fashion, different types of milling devices such as attritors or ball mills, can also be used for milling aerogel. Depending on the type of aerogel in terms of hydrophobicity or hydrophilicity, the added fluid can be an organic or aqueous liquid. As a result of the use of this fluid, the environment is made wet in a way that results in more optimal mixing, although this may also reduce or prevent agglomeration of the produced particles [237]. In the case of hydrophobic aerogels, there is a restriction that operates in that water cannot be used as the fluid for the grinding process as, even if vigorous agitation is used, the particles float on the water's surface. In the case of these types of materials, at least one wetting agent or surfactant must be added to the water in order to ensure a uniform dispersion between the particles and the liquid [238].

2.13.3 Emulsion polymerisation

2.13.3.1 What is a micelle?

Micelles are groups of 20 to several hundreds of molecules with two main parts, with nonpolar (hydrophobic) hydrocarbon tails trailing toward the centre and the polar (hydrophilic) head facing toward the centre such that it can come into contact with water. Figure 2.20 shows soap molecules in the formation of a micelle [239].

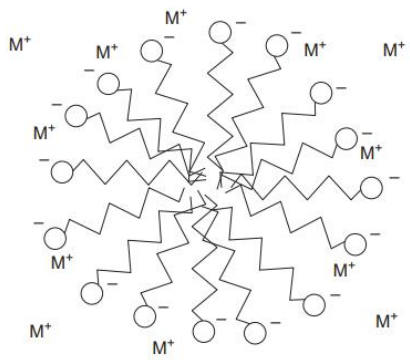

Figure 2.20 Soap molecule array in micelles [239]

2.13.3.2 What is a colloid?

Colloids consist of particles with a size of 1 nm to 1mm that are suspended in a second substance. The small size of colloidal particles means that a high percentage of the molecules will be on the surface, meaning that surface chemistry is a vital aspect of their properties. The dispersion medium forms a continuous phase. Table 2.2 details eight different types of colloids, gases not existing as discrete phases [239].

Table 2.2 Two-phase colloidal systems [239]

Dispersed Phase	Dispersion Medium	Name	Examples
Liquid	Gas	Liquid aerosol	Fog, mist, hair spray
Solid	Gas	Solid aerosol	Smoke, dust, allergens
Gas	Liquid	Foam	Head on beer, foaming
Liquid	Liquid	Emulsion	Italian salad dressing, milk
Solid	Liquid	Sol, paste	Ink, mud, clay slurries
Gas	Solid	Solid foam	Foam rubber, styrofoam
Liquid	Solid	Solid emulsion	Pearl, ice cream
Solid	Solid	Solid dispersion	Acrylonitrile butadiene styrene (ABS), paper, pigmented plastics

Aerosols are solutions in which a gas is used as a dispersion medium, and there is a solid in the form of a dispersed phase. Fog is an example of an aerosol, containing water droplets; smoke is another example of aerosol, containing solid particles. Emulsion, meanwhile, can be defined as a sol in which the suspended particles are liquid droplets, and the continuous phase is also a liquid. In the emulsion system, the two phases are immiscible. The work (W) or surface excess free energy (G) is required to produce a new surface area (A) with surface tension γ [239]:

$$\Delta G = \Delta W = 2\gamma A \qquad (3)$$

Given that surface energy is a bulk property, it is not meaningful to consider this concept in relation to small particles. This value corresponds with the required heat for vaporising water at the boiling point.

A colloid system is considered “lyophilic” (literally “solvent-loving”) if the dispersion phase is dissolved in the continuous phase. On the other hand, if the dispersed phase involves a giant molecule or a cross linked polymer, a gel will be formed. In gel formation, the dispersed phase is also considered a continuous phase. When this happens,

it is sometimes possible for the conditions to result in colloidal particles clumping with each other, forming large particle that is no longer stable in the suspension. This process is called coagulation. The stability of the resulting suspension depends on different parameters such as: relation between the repulsive and attractive forces in the particle, which governs whether the repulsive force is more significant or attractive [232], concentration of particles, dispersant, the viscosity of the base liquid and pH value [240].

Attractive force can be defined as any secondary chemical force against the covalent bond that holds the given material together. The force between the particles is any dipole-dipole interaction, such as a weak van der Waals force. Hydrogen bonding is another attractive force that can hold between particles. When this operates, the repulsive force means that the particles are prevented from being integrated with one other. Although pure materials convert from solid to liquid and gas as a result of increases in temperature and, therefore, reductions in size, in the case of colloid systems, there is a transition from solution to solid as a result of similar increases in temperature, entailing conversion of smaller particles to larger ones. This indicates that increasing the heat in the colloid system increases the repulsive force, whereas increasing the temperature in the vaporization of pure materials overcomes the attractive force [239].

Depending on the distance between particles, the electrostatic repulsive force and van der Waals attraction force may be operated. At a great distance, no interaction occurs between them [241]. However, suppose the particles come closer to each other. In that case, the electrostatic repulsive force acts in such a way that pushes them out, but on the other hand, as a result of increases in the van der Waals forces and the consequent pushing together of the particles, the particles will combine. This shows that the coagulation depends on the ratio between decreases in the electrostatic repulsive force and the force operating on the particles in such a way that they are moved closer together. The electrostatic force, which determines the degree of aggregation, depends on different parameters such as the concentration of polymer in the solution, pH, temperature and the degree of agitation [239].

2.14 Emulsion process

An emulsion is an opaque system of two immiscible liquid phases. The first phase, consisting of colloid particles, is dispersed during the second (continuous) phase. To produce an emulsion, a sufficient level of energy and mechanical agitation must be applied to spread one phase to another. Emulsion systems that are thermodynamically unstable must therefore be kinetically stabilized [242], which typically results in changes towards reduction in the interfacial force between the particles. This can be achieved by reducing the surface area of the produced particles relative to their volume, which is possible if the particles take on a spherical shape. Another route by which the surface tension might be reduced involves adding a surfactant or surface-active particles, which can adsorb strongly at the liquid-liquid interface of immiscible fluid [241]. A surfactant with two different sides, one amphiphilic molecule formed by a hydrophilic behaviour dissolved in a polar solvent and one hydrophobic tail dissolved in a polar solvent, can reduce the interfacial energy between the two immiscible liquids. Figure 2.21 shows the mechanism of the emulsion process that operates in the achieving of thermodynamic stability[241].

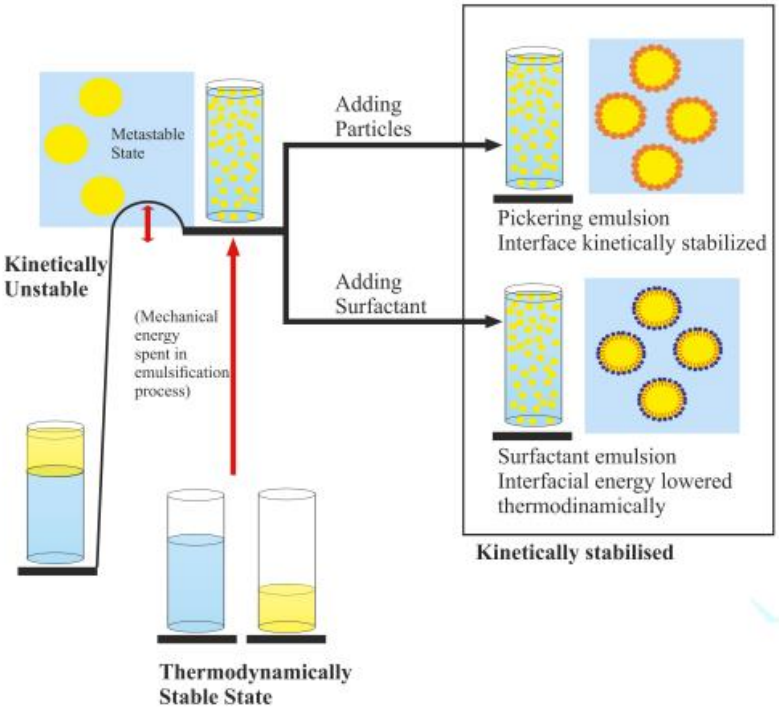

Figure 2.21 Kinetic versus thermodynamic stability [241]

2.14.1 Pickering emulsion

The particles in emulsion systems can kinetically stabilise such systems, in which case the system is considered to be a Pickering system [243], so named after the British chemist who discovered this process in 1907. In this kind of emulsion system, as can be observed in Figure 2.21, the particles, by making a layer around the droplets, can prevent coalescence phenomena without the use of a surfactant. The stability of the particles in these systems is affected by the particles' size, shape and hydrophobicity [30]. Pickering emulsions have several advantages compared to traditional emulsion procedures performed using a surfactant, including greater eco-friendliness and lower toxicity and costs [244].

As an example of a study investigating issues in this area, Binks discusses the preparation process and properties of oil-in-water emulsions stabilised by colloidal silica particles, focusing on the effect of particles' wettability and proportion [245].

Overall, emulsion can be performed in two ways, namely oil in water (O/W) and water in oil (W/O). The Bancroft rule can be considered as a means of predicting the different types of emulsion [246]. According to this rule, the phase in which a surfactant is more soluble is the continuous phase, and a stable emulsion processes necessitates that the surfactant be soluble in the continuous phase [247]. It is also possible to consider this process in terms of the particles instead of the surfactant. This is reflected in the Finkle rule, which states that hydrophilic colloids tend to result in water becoming the dispersing phase while hydrophobic colloids tend to result in water becoming the dispersed phase [238]. These two rules govern whether an emulsion is oil in water (O/W) or water in oil (W/O). These rules do not indicate the ratio of the concentration of the oil in water; however, they do predict which phase is the one in which the surfactant is more soluble or dispersed in the case of the particles. For example, if there is an emulsion system with 40% water and 60% oil, then, if the surfactant is more soluble in the water, it follows that, even if the volume of water is less, it will be an instance of an oil in water system.

2.14.2 Stability of emulsion

There are different types of instability in emulsion systems [248]:

Flocculation: This is due to the aggregation of different droplets and the formation of clusters due to the presence of weak net attraction combined with Brownian motion or sedimentation.

Creaming: This is not an actual breaking of the emulsion but is rather defined as a separation of emulsion into two phases, one of which is richer in the dispersed phase. In this phenomenon, the dispersed phase floats over the continuous phase. This phenomenon can be defined using the stock equation [248]:

$$\upsilon = \frac{2\,r^2\,(\rho 2 - \rho 1)g}{9\eta} \qquad (4)$$

Where υ is the creaming (or settling) velocity, r is the droplet radius, ρ_2 is the density of the droplet, ρ_1 is the density of the continuous phase, η is the viscosity of the continuous phase, and g is the gravitational acceleration. Creaming can be measured using the "creaming index, C_I," which is calculated using the following equation [248]:

$$C_I = \frac{100 \times H_L}{H_E} \qquad (5)$$

Where H_E is the height of the initial emulsion and H_L is the height of the lower phase after separation. Figure 2.22 provides a schematic of a creaming emulsion. All these parameters are measured using visual observation, and the creaming index provides information about the stability of the emulsion. Sometimes the creaming converts to coalescence, causing a complete break in the emulsion such that two separate bulky oil and water phases form [248].

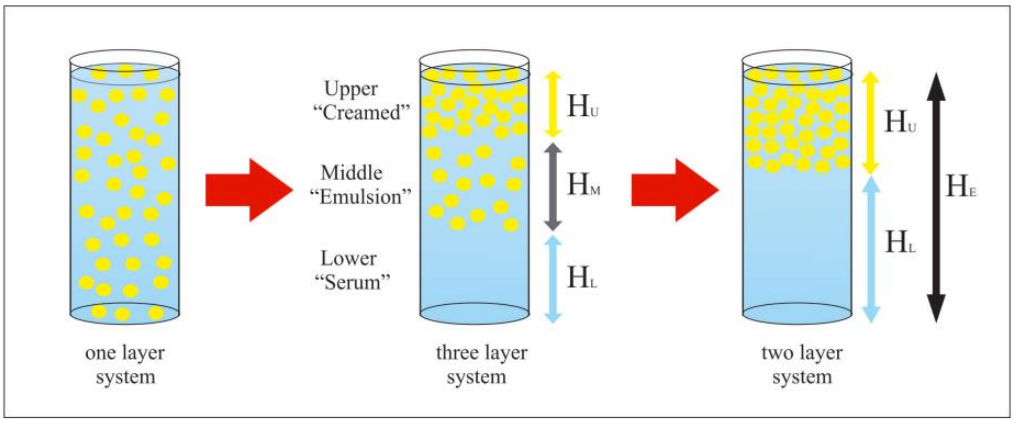

Figure 2.22 Measuring creaming stability via visual observation with a long-term storage test [248]

Coalescence: This is another type of instability of the emulsion systems, defined as an irreversible process in which two or more colloid droplets merge. The following equation sheds light on the kinetics of coalescence [250]:

$$f_{coal} = f_{collisions} P_{coal} \qquad (6)$$

Where f_{coal} is the coalescence frequency, $f_{collision}$ is the collision frequency, and P_{coal} is the coalescence probability [249]. Despite flocculation and creaming, which can be reversed using much less energy compared to what is required to perform the original emulsion, coalescence is an irreversible process that results in a breakdown in the emulsion. Flocculation and creaming can be considered precursors to coalescence and de-emulsification [250].

2.14.3 Emulsifier (surfactant) role in the emulsification system

The properties of the emulsion system can be adjusted by means of a surfactant; a chemical substantiated by adsorption in the boundary of the two immiscible parts. In general, the chemical structure of the surfactant consists of two main parts, namely the hydrophilic and lipophilic parts. In the event of an appropriate surfactant concentration, they can self-assemble in water and produce micelles. A specific concentration of the surfactant can be dissolved in the form of the monomer in the micelle solution, giving rise to kinetic change in the equilibrium between the monomer and the polymer. The

emulsion polymerization begins when one of the critical micelle concentrations (CMC) has been reached. Usually, this condition happens when the concentration of the surfactant is high [251]. In the emulsion system, a micelle occurs when the surfactant is aggregating. The CMC occurs when the particles become spherical. At the CMC point, the repulsive forces between the particles decrease, which causes the emulsion to break.

The concentration of the surfactant can affect the repulsive force. For example, the presence of excess surfactant in the emulsion system causes instability. Another remarkable property of such surfactants relates to reductions in interfacial tension. Surfactants, by absorbing in the interface, can reduce the excess surface energy, which is called "interfacial energy" (G_{intef}) between two phases in the emulsion system [252]. On the other hand, the intermolecular interaction stemming from a gap at the immiscible liquid-liquid interface increases the interfacial energy. Reduction of the polarity of the oil in the emulsion system decreases the G_{intef}. If smaller particles in the emulsion system are to form, a higher concentration of the surfactant must be used. Because smaller particles have larger oil/water interfacial areas, in the case of an insufficient concentration of surfactant to cover the large interfacial area, the system, by leading to phase separation, will optimise the conditions in such a way that the interfacial area is minimised.

As previously explained, the presence of a surfactant results in stability in the emulsion system. Depending on their polar nature, different surfactants are categorised into three main groups: anionic, cationic and non-ionic. Determining the type of emulsion can be done using the Bancroft rule, according to which the continuous phase is the liquid in which the surfactant is more soluble [251, 253]. Different materials, such as amphiphilic polymers, proteins and particles, can stabilize the oil and water interface. One of the critical parameters in selecting the proper surfactant for an emulsion system is the rapid absorption of the surfactant in the newly created interface. If this is to occur, selecting a surfactant with low molecular weight is necessary.

Generally, for the characteristic of a surfactant (alternatively known as emulsifiers in industry), the Hydrophile-Lipophile Balance (HLB) number is defined. This parameter shows the affinity of a surfactant toward a solvent. For example, a higher HLB value indicates a greater degree of compatibility with water. Table 2.3 shows the HLB for a

number of different surfactants; using this parameter, the proper emulsifier can be selected to emulsify oil in water solutions [248].

Table 2.3 HLB number and corresponding applications [248]

HLB Number Range	Corresponding Application
1.5–3	Antifoaming agent
1–4	Emulsifier for W/O emulsions
6–8	Wetting agent
10–13	Emulsifier for O/W emulsions
13–15	Detergent
15–18	Solubilizer

Several methods have been introduced over the past 50 years as means of calculating the HLB. Most recently, this is typically done using the Griffin equation to characterize polyoxyethylene (POE) surfactants. This equation expresses the structural balance between hydrophilic and lipophilic groups in a surfactant molecule as a numeric index from 0 to 20 based on empirical emulsification with POE emulsifiers [248]:

$$\text{HLB}=20\times\frac{MW}{M} \qquad (7)$$

Where Mw is the hydrophilic group's molecular weight, and M is the surfactant's molecular weight. Choosing a suitable surfactant is crucial in order to produce a stable emulsion system. However, having a suitable HLB is not in itself sufficient to produce a stable emulsion system, as sometimes systems with a suitable HLB can be influenced by coexisting components such as electrolytes and their concentrations in water, oil polarity, water-to-oil ratio and temperature [248].

In general, selecting a suitable emulsifier for an emulsion system depends primarily on the type of the oil and sometimes its HLB rating. For example, in the case of the presence of oil with high polarity, a more hydrophilic emulsifier should be used [254].

It has been found that using a combination of a low-HLB emulsifier and a high-HLB emulsifier (i.e., one that is hydrophilic and one that is hydrophobic) results in better stability in the emulsion process as compared with using one surfactant with the intermediate HLB. Two parameters have been highlighted as being relevant for explaining this pattern [255]:

- The combination of two different surfactants with different critical packing parameters results in more complete packing of the interface. (The packing parameter relates the molecular structure of the surfactant to the morphology of the self-organised structure.)

- The combination of emulsifiers causes the rapid supplementation of emulsifiers in the reaction.

In the condition in which the combination of emulsifiers is applied, the average of HLB can be calculated using the following equation [255] (x_i is the molar ratio of each surfactant):

$$\text{Average HLB} = \sum_{i=1}^{n} (HLB_i \cdot x_i) \qquad (8)$$

Generally, given the goal of achieving a stable emulsion system, a fine and complete process of dispersion should be conducted. However, emulsion particles that are not typically thermodynamically in equilibrium do not have uniform size, and emulsions are typically thermodynamically no equilibrium. Such particles' sizes, shapes and size distribution can all be affected by the emulsification process, type and duration of the storage [242]. The role of surfactants is a critical aspect of the emulsion process, with most failed emulsions systems being due to a lack of suitable emulsifiers. Usually, the low molecular weight of surfactant will not carry sufficient polarity to cause stabilization among the organic solvents [256]. Compared to the low molecular weight of surfactants, block copolymers with high molecular weight can produce stable micelles, which can be observed in both phases of the emulsion process [257, 258]. In addition, a lower copolymer concentration is also likely to be more appropriate for use as a surfactant compared to a low molecular one [259]. In their research in this area, Klapper *et al.* [256]

utilised an oil in oil emulsion technique in order to synthesize a nanoparticle polymer, using a wide variety of hydrolysable monomers and sensitive catalysts to yield polyester, polyurethane, polyamide and conducting polymers under ambient conditions. The Hansen parameters were used to calculate the suitable concentration and combination of block copolymer and solvent. Nanoparticles with a size range of between 20 and 100 nm were synthesized using oil in oil emulsion and characterized by dynamic light scattering. Particle size was controlled by changing the concentration of the emulsifier.

The size of the hydrocarbon chain determines the degree of hydrophobicity and lipophilicity of a surfactant, reflecting the degree of solubility of the surfactant on both immiscible liquids. Figure 2.23 shows the schematic of surfactant structure [253].

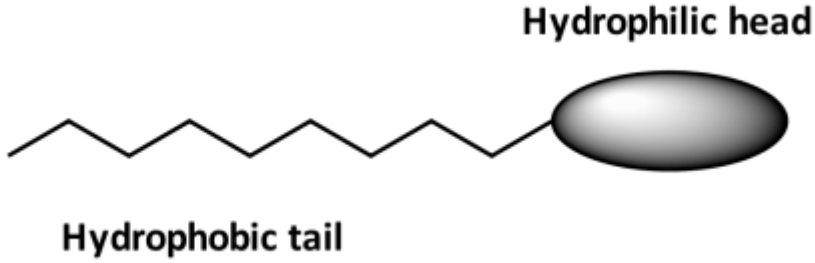

Figure 2.23 Schematic of the structure of a surfactant molecule [253]

2.14.4 Size distribution in the emulsion process

A narrow particle size distribution shows an emulsion with more stability. In order to achieve this condition, a suitable method of mechanical mixing should be used. However, stability begins to return once the emulsion is formed. For the spherical particles, which can be produced using techniques like emulsification [164], more must be done to prevent particles' collapse. It is for this reason that producing microparticles with a uniform particle size distribution is challenging. Numerous studies have been conducted on the topic of how this challenge can be met. For example, Teo *et al.* provide details of a tight particle size distribution that can be achieved for core-shell aerogel microparticles [260]. In another study, Teo and Jana detail the manufacturing of aerogel microparticles with uniform size and shape without using a surfactant [172]. As previously discussed, most

emulsion systems, such as the synthesis method for producing the silica microparticles, are in the form of W/O or O/W and stabilized with suitable emulsifier [261, 262]. Lee *et al.* [263] synthesized silica microparticles using emulsion polymerisation methods, with the span 80 being applied as a surfactant with a low HLB value of around 4.3 and the size of the droplets and particles being controlled through modulation of the size and types of the homogeniser.(Section 4.1.1.1 explain more about span materials and their verity)

2.14.5 PI aerogel synthesis using the emulsion method

The methods discussed above are unsuitable for use with aerogels that are moisture sensitive [169]. It is notable for present purposes that this includes PI. However, it is possible to use O/O emulsion systems with this kind of material, which enables microparticle droplets to be shaped faster and with greater ease. If this method is adopted, then PI microparticles with diameters in the range of 200-1000 µm are produced [169]. In order to accelerate the sol-gel processing and imidization, the droplets can be guided into a heated silicon oil bath [169].

Due to the high coalescence speed in the O/O emulsion system, even with a high surfactant concentration, the amount of produced gel microparticles was found to be impeded. This evidence demonstrates that the sol-gel manufacturing process can be limited by the use of certain O/O emulsion systems, as in the case of PI. To perform O/W emulsion, the produced salt was dissolved in water thoroughly and Op10 and span-80 were added as an emulsifier and mixed for 30 min using a magnetic stirrer. To produce the second emulsion (O/W/O), the first emulsion was mixed for 10 min with a mixture of Op10 and span-80, following which a chemical imidization reagent (consisting of acetic anhydride and pyridine) was added. The produced powder was washed and centrifuged with acetone three times, dried and further imidized at 80 ℃ and 300 ℃, respectively, in a vacuum oven [169].

In their study, Teo and Jana [172] constructed a microfluidic setup to fabricate aerogel microparticles. One advantage to using this method is the absence of surfactants that can affect the washing process, making it possible to remove and clean all the particles from the undesired surfactant molecules.

An emulsion method involving oil in oil is introduced by Teo *et al.* [169] as a means of producing PI aerogel foam with meso and microporosity. F127 was used as a surfactant, and cyclohexane and n-heptane were used as the dispersed phases. The particles with an average size in the range of 30-80 µm were produced using different concentrations of the surfactant. They observed an increase in the bulk density of produced PI aerogel as a result of increasing the concentration of the surfactant.

Wu *et al.* [78] synthesized PI aerogel particles using phase separation. The polyamic acid gel, which was obtained by mixing pyromellitic dianhydride and 4,4'- methylenedianiline in THF/MeOH solvent, was subjected to mechanical agitation with acetone. The clear glass-like viscous PAA solution was then produced upon the addition of acetone. Following this, it was phase-separated and converted into an opaque white wet gel. The acetone was then removed with solvent exchange with cyclohexane. Thermal imidization occurred as a result of successive heating at 100 °C, 200 °C and finally at 300 °C. Addition of acetone into the gel-like PAA and vigorous mechanical stirring resulted in the aerogel taking the form of particles rather than a monolith.

Liu *et al.* [264] used water-in-oil emulsion polymerization for synthesizing titania–silica aerogel microparticles. The microparticles were washed with acetone and subject to ambient pressure drying at 70 °C for two days to prepare the titania–silica aerogel microspheres. This involved using SEM images, and it was observed that the spherical particles had 100 µm average sizes with 0.3 g/cm^3 density. N_2 sorption is reported as showing the pores as having a 17 nm diameter.

In Gu *et al.*'s study [164] , polybenzoxazine and PI aerogel microparticles were synthesized using an oil-in-oil emulsion mechanism in the presence of Hypermer and span-80 as low-cost and commercially available emulsifier. The PI aerogel was then synthesized with pyromellitic dianhydride (PMDA), 2,2-dimethylbenzidine (DMBZ), and 1,3,5-tris(4-aminophenoxy) benzene (TAB). The sol was made in DMF and dispersed in cyclohexane using the introduced stabilizer and magnetically mixed for 3 h. In order to induce chemical imidization, pyridine and acetic anhydride were added into the cyclohexane solvent. The exchanging solvent was performed in a Thinky mixer at 1000 rpm and washed for 5 min with acetone. The produced microparticles were finally dried using the supercritical method. PI monolithic aerogel was also synthesized, and its

properties were compared with the microparticles. The results of this study also confirm that the shape and morphology of the pores of the microparticles were different from those of the monolithic form. Using gas adsorption, the researchers found that the pores were mostly mesopores and macropores in the case of both the particles and the monolithic samples, with a higher surface area emerging for the PI monolithic aerogel as compared with the microparticles. The micro spherical PI particles are reported has having had a broad particle size distribution of 10-90 µm and an average particle size of 25 µm. The researchers also report that, by reducing the solvent exchange time, it would be possible to reduce the degree of shrinkage as compared with that observed for monolithic samples.

Teo *et al.* [172] introduce a novel method for synthesizing PI aerogel microparticles using emulsion. This method is novel in that a microfluidic flow setup was used for the fabrication of aerogel microparticles in order to control the size of these fabricated particles and their size distribution using the oil-in-oil emulsion method. In addition, they also introduce an emulsion method for fabricating PI aerogel microparticles that do not require a surfactant but make it possible for all the undesired molecules of surfactants to be removed.

The researchers detail the use of jetting to disperse the dispersion phase (PI sol in DMF) into the continuous phase (silicone oil). The PI sol produced from PMDA, DMBZ and TREN in DMF was rapidly transferred into the syringe pump to inject it into the droplet generator. Using this setup, the PI sol particles were injected into the silicon oil bath and heated to 80 °C, thereby helping the gelation process to accelerate to the point where it could occur in less than 10 s. The fabricated gel microparticles were aged for 24 h in silicon oil. The solvent exchange was conducted in different steps using different solvents of various concentrations. The researchers also provide a comparison between the properties of PI microparticles and those of monolithic ones in relation to fabrication of the micro-spherical particles, which are reported as having had a less porous structure on their surface as compared with the monolithic ones. Furthermore, due to the longer gelation time associated with the monolithic sample (26 min) compared to the microparticles (10 s), the former developed skin layers with thicker strands. The TGA and FTIR results also showed that, for both types of samples (microparticles and

monolithic), there was a high degree of thermal stability plus complete imidization. The size of 100 particles was measured using optical images and image-J software. The 200-1000 µm micro spherical particles were fabricated using different flow rates for the continuous and dispersed phases. The silicon oil bath temperature on the size of the produced particles also was investigated., and the researchers report that, by increasing the temperature from 60 to 100 °C, the size of the particles was decreased from 546 ± 129 to 376 ± 52 µm. In addition, microscopic images for these samples showed that increasing the temperature resulted in a higher degree of shrinkage, giving rise to samples of higher density [172].

Ji *et al.* [173] report the results of using an oil-in-water-in-oil (O/W/O) multiple emulsion for preparing PI microsphere particles using Op10 and span-80 as emulsifiers. In this emulsion system, polyamic acid salt (PAAS), which is soluble in water, was used for W phase. Lp was used as an emulsifier to construct the multiple emulsion systems' internal and external O phases to produce a hollow microsphere porous structure. The PI microspherical particles were then synthesized with a heat resistance as high as PI films using two different emulsifiers with different HLB numbers. The first emulsion was performed using PSSA and LP. Then, using mechanical agitation, the produced emulsion was added to the Lp (O_2) containing Span-80 to perform the second emulsion. The PI particles were formed after 15 min during the imidization process when acetic anhydride and pyridine were added as imidization reagents. After the exchange of the solvent with acetone, which was used to perform three washes, further imidization and drying was performed at 80 °C and 300 °C, respectively. The SEM results showed that the particles' size reduced after mixing the two emulsions to a lower point than was observed for each individual type of emulsion. To explain this, the researchers draw attention to the shrinkage of the molecular chain during imidization, occurring after the two emulsion systems were integrated [173]. The degree of imidization for the produced microspherical PI particles was measured using infrared curves. The ratio of C-N-C peak intensity and the C=C peak intensity of the sample after chemical imidization and at the end of the 300 °C drying process was considered the imidization ratio. 85.31% imidisation showed that the samples were not fully imidized after chemical imidization, and so heating needed to be applied to the particles to ensure complete imidization. Investigation of the emulsifier content on the morphology of the particles showed that increasing the concentration of

span-80 had not changed the viscosity, meaning that the morphology of the particles had also not changed. However, the number of micelles had increased, and so the particles' size decreased to the same extent as with OP-10. Using the TGA, the researchers showed that the maximum thermal degradation for PI microspherical particles occurred at 600 ℃ [173].

In order to make formulate an emulsion system, two polar/nonpolar aprotic organic solvents can consider forming the immiscible oil phases for the emulsion in reflection of the point that there are carious organic liquid pairs that can be used to construct emulsion systems. However, selecting the proper stabilizer remains challenging when handling such systems.

Following synthesizing different types of aerogels, they need to be characterized and assessed in terms of their properties. In the next chapter different common characterization methods and literature review for aerogel materials are introduced.

Chapter 3 Literature review on material characterization

3.1 Physical and structural parameters

It is generally the case that, in a porous material, the key structural parameters to consider are the fraction of the pores as compared with the solid material, the connectivity of these two phases, the molecular structure of the solid component and the morphology of the interface between the two phases. Figure 3.1 exhibits these parameters in terms of the molecular structure of a porous material [18].

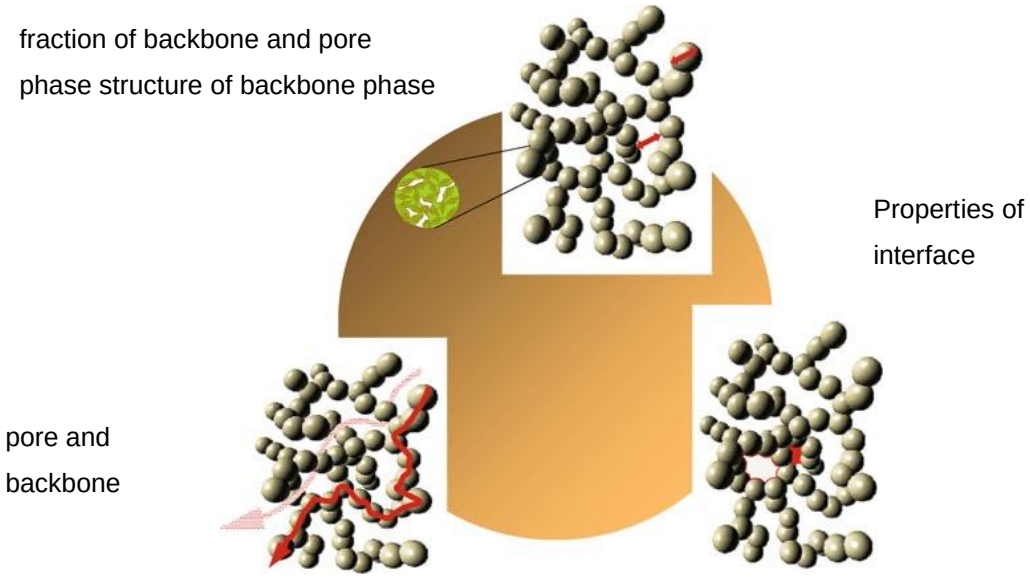

Figure 3.1 The critical structural parameters of a porous material [56]

In the following, the discussion is presented of the most common methods used to characterise and describe this type of material, including their limitations.

3.1.1 Microscopy

Microscopic techniques can be used to gain a visual impression of aerogels by means of investigating their length in terms of the Angstroms scale. The two applicable microscopy methods used to analyse aerogel are scanning electron microscopy (SEM) and transmission electron microscopy (TEM). SEM at high resolutions in the range of around 1 nm is generally applied to observe the backbone of the aerogel. With a higher degree of

resolution, TEM is utilised for analyzing particles forming this backbone. In different studies, SEM and optical microscopes have been used to investigate the microstructure of PI aerogel.

3.1.1.1 Scanning Electron Microscopy (SEM)

In scanning electron microscopy (SEM), an electron beam is focused into a small probe and restored across a specimen's surface. Several interactions will happen that result in the emission of electrons or photons occurring as the electrons penetrate the surface. These emitted particles can be collected with the appropriate detector to yield valuable information about the material [265]. There are some disadvantages such as inability to analyse live specimen, images in black and white and costly technique which may mean that other types of microscopy such as light and super-resolution microscopy can be used. But in this work, due to high and enough magnification, and high quality images with lots of information, this technique and optical microscopy were used to characterise the samples [266].

As an example of work conducted in this area, Kwon *et al.* investigated the surface morphology, structure and shape of fabricated PI microparticles using SEM [21, 47, 50, 66]. Similarly, Kim *et al.* also report on the morphology and size of PI microspherical particles by using SEM [66], noting that the enlarged scanning electron microscopy image of the PI films sheds light on PI's spatial distribution [267]. He *et al.* [268] meanwhile, report a classical three-dimensional PI network consisting of interconnected polymer particles formed via a precipitation–polymerization mechanism. The SEM images considered suggest a decrease in pore size and the number of macropores for the aerogels prepared at 75 °C, corresponding to N_2 adsorption/desorption experiments. Pei *et al.* [90] investigated PI aerogel's morphological characteristics as a density function and report that the three-dimensional network of PI fibres could be observed to tangle together. Their observation is similar to what is said about the morphology of some other PI aerogels considered in the literature [24, 26, 33, 54]. Finally, Wang *et al.* used TEM to investigate the morphology of PI aerogel composite with carbon nanotubes. The TEM-obtained results are reported as demonstrating that amino-functionalised CNTs act as crosslinking

centres to react with the terminal anhydride groups of PAA, eventually forming the crosslinked three-dimensional network structure with enhanced mechanical properties [269].

3.1.2 Particle size measurement

3.1.2.1 What is a particle?

There is no exact definition of what a particle is. Depending on the materials and methods used for synthesizing, drying and storing, they can form in myriad different shapes and sizes. In general, however, after drying, particles can be observed to fall into any of the following three categories of shape (Figure 3.2)[270]:

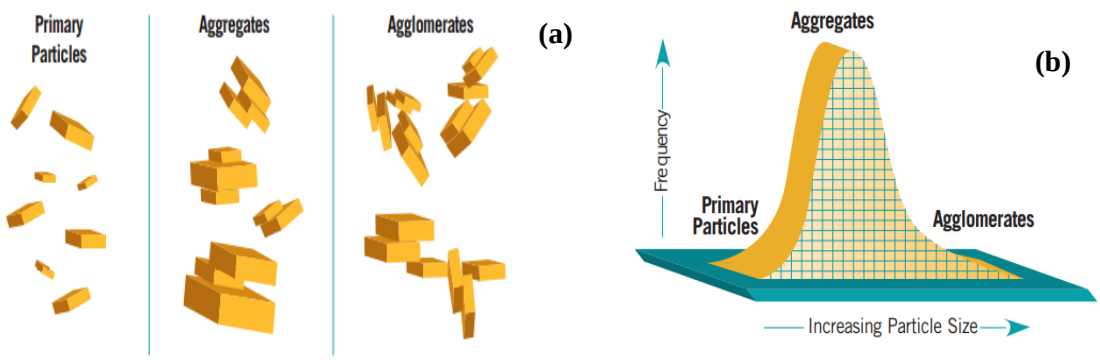

Figure 3.2 Nature of particles, b) relations between particle size and nature [270]

3.1.2.1.1 Primary particles

The primary particles are the smallest organic or inorganic parts of particles more generally, that engage in atomic or molecular bonding. In aerogels, these particles are the smallest components with no porous surface. SEM makes it possible to observe these particles and their structures. By connecting the primary particles using intermolecular bonding, the secondary particles with porous structures (inside and between the particles) are shaped [270].

3.1.2.1.2 Aggregate particles

Bonding two or more primary particles by chemical means results in aggregate particles. They can be shaped by heating and pressure onto surfaces during manufacturing process. Each particle has a large interfacial area that enables it to contact other particles, and so a large force is required if these forms of bonding are to be broken [270].

3.1.2.1.3 Agglomeration

Agglomerate particles are shaped when aggregate particles as a result of electromagnetic force, van der Waals' forces or mechanical friction. Most of the time, agglomeration occurs when the particles are shaped, rolled or stored in the same place without any dispersion; as a result, it is easy for agglomerate particles to separate by means of proper dispersion. Through appropriate dispersion, particle size distribution narrows, and agglomeration tends to aggregate [270].

3.1.2.2 Particle size measurement

There is no method of presenting an exact and accurate value for the size of particles; instead, particle size distribution (PSD) is typically specified in respect of a given time and condition. There are three different parameters that can be measured using a distribution plot to gain the data necessary to calculate PSD [271]:

- Mean is the arithmetic average of the area under the PSD curve.
- The modal value is the value indicating the location of the majority of particles.
- The median is the value such that, at this point, 50% of the particles are larger and 50% are smaller.

Ideally, these three values fit each other to a normal distribution, as would be the case for perfectly spherical particles. However, particles are usually irregular, giving rise to a skewed distribution is achieved. Given this, there is a keen need to establish which of these three values represents the closest value in terms of the planned application.

3.1.3 Helium pycnometer

A helium pycnometer assists with identifying the volume of a given sample that is unreachable to helium atoms. The chamber of known volume containing the sample is filled with helium until this chamber and the second well-defined volume chamber can both expected to contain helium only. The second chamber is filled with helium at a pressure higher than in the sample chamber (Figure 3.3). The gas pressure in the reference chamber is then measured after thermal equilibrium and recorded, following which the valve is opened to allow helium to pass from the reference chamber into the sample chamber until gas pressure equilibration is happened between the chambers [18].

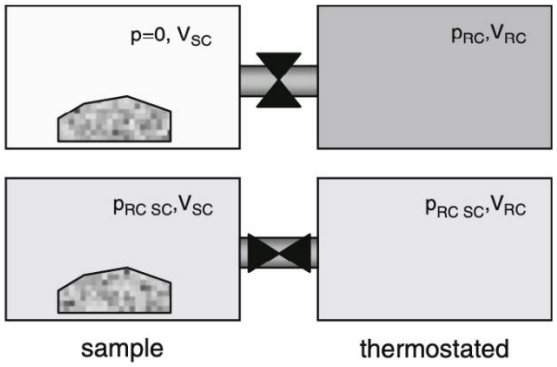

Figure 3.3 Schematic setup for helium pycnometer with an initial pressure in the sample [18]

The specific volume V_{sk} of the sample that the helium cannot reach can be calculated using the ideal gas equation, the volumes of the two chambers, and the equilibrium gas pressures before and after the valve has been opened. V_{SC} and V_{RC} are variables standing in for the sample and reference chamber volumes, respectively[18].

$$V_{\mathrm{Sk}} = \frac{1}{m}\left[\frac{V_{\mathrm{SC}} + V_{\mathrm{RC}}}{1 - p_{\mathrm{SC}}/p_{\mathrm{RC,SC}}} - \frac{V_{\mathrm{RC}} \times p_{\mathrm{RC}} + V_{\mathrm{SC}} \times p_{\mathrm{SC}}}{p_{\mathrm{RC,SC}} - p_{\mathrm{SC}}}\right] \quad (9)$$

The helium pycnometer is typically used to measure the skeletal density of materials [90, 272, 273]. For example, Ghaffari *et al.* used a helium pycnometer (Quantachrome Instrument Ultra-Foam 1000) to measure porosity and skeletal density by the ASTM D6226 standard at 15 psi [274]. In another study, Ghaffari *et al.* used the same

pycnometer equipment and technique to calculate skeletal density and porosity in respect of the open-cell content of PI aerogel foam at around100 kPa [60].

Section 4.2.3 shows the equipment which is used in this work.

3.1.4 Gas sorption porosimetry

Generally, surface energy of the porous materials can be considered relatively high when measured in respect of a clean, solid surface [275]. When this is the case, the solid can release surface energy by adsorbing gases such as oxygen, nitrogen and carbon monoxide. Depending on the interaction between the solid and gas, adsorption can be classified in terms of whether this is a physical or chemical adsorption. Physical adsorption is reversible only when nonspecific van der Waals forces are involved. Generally, physical adsorption is a multilayer process in which the solid surface area does not restrict the number of adsorbed molecules (see Figure 3.4). Despite chemical adsorption, chemical bonding is an irreversible process and is limited to forming a monomolecular adsorbed layer [275].

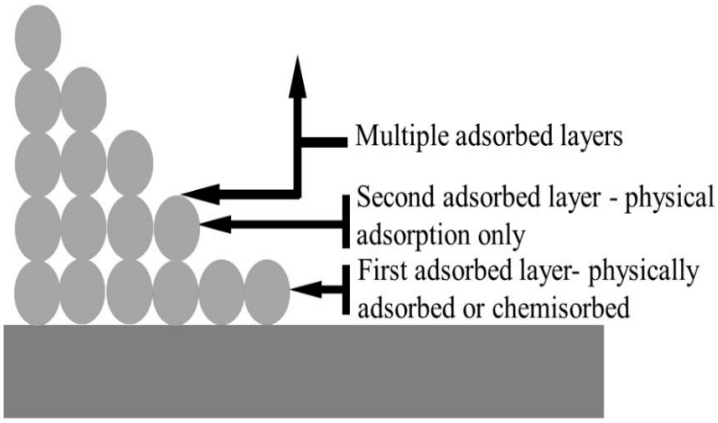

Figure 3.4 Chemical and physical adsorption on a solid surface [275]

It is essential to define the pore sizes that feature in the physisorption process. This is the basis of BET (Brunauer, Emmet and Teller) theory. Depending on the size of the pores, these can be classified into three types [276]:

i) Macropores: the pore width exceeds 50 nm.

ii) Mesopores: the width of the pores is between 2 nm and 50 nm.

iii) Micropores: the width of the pores does not exceed 2 nm.

3.1.4.1 Brunauer, Emmet and Teller (BET) Theory

The BET theory was developed by Stephen Brunauer, Paul Emmett and Edward Teller in 1938. The first letter of each publisher's surname was taken to name this theory. This theory aims to describe the physical adsorption of gas molecules such as N_2, Argon or CO_2 on the surface of a solid to determine the true or specific surface area, including surface irregularities and pore walls, of the solid material [277]. Because most gases and solids interact weakly, the solid material must be cooled, typically using a cryogenic liquid [278].

BET theory applies to systems of multilayer adsorption and usually utilizes probing gases that do not chemically react with material surfaces as adsorbates to quantify specific surface area. Nitrogen is the most commonly employed gaseous adsorbate used for surface probing by BET methods. For this reason, standard BET analysis is most often conducted at the boiling temperature of N_2 [277]. As the relative pressure increases, more molecules absorb on the surface. A thin layer will eventually cover the entire surface. And this is the point that surface area can be determined.

3.1.4.2 Barrett, Joyner, and Halenda (BJH) methods

BJH method is a procedure for calculating pore volumes and pore size distributions from experimental isotherms using the Kelvin equation. It applies only to the mesopore and small macropore size range. The Kelvin equation provides a correlation between pore diameter and pore condensation pressure [279].

To determine the BJH pore volume and pore size distribution, the Nitrogen pressure is increased incrementally, followed by measurement of adsorbed volume in the multilayer adsorption region. At higher relative pressures, capillary condensation occurs, filling the

pores with liquid Nitrogen. The process is then reversed by reducing the relative pressure and measuring desorption equilibrium. Hysteresis can often be observed due to the difference between the nature of the adsorption and desorption process [279].

3.1.4.3 Classification of adsorption isotherms

As a result of an intensive study, Brunauer, Deming and Teller proposed a classification of adsorption isotherm curves, dividing isotherms into five main types and stipulating that all adsorption isotherms must fit into one [280]. Subsequently, De Boer developed the sixth isotherm, which was then supplemented by work by Gregg and Sing [281]. Figure 3.5 presents the IUPAC classification for different isotherms in terms of the requirements of certain unique conditions [278].

Type I isotherm belongs to a few molecular layers and can be characterized as either a chemical or physical isotherm or a microporous solid.

Type I(a) isotherms are typically found in microporous materials having mainly narrow micropores (of width < ~ 1 nm); Type I(b) isotherms are found in materials having pore size distributions over a broader range, including wider micropores and possibly narrow mesopores (< ~ 2.5 nm).

The physisorption of most gases on nonporous or macroporous adsorbents yields type II isotherms. The shape is the result of unrestricted monolayer-multilayer adsorption up to high P/P_0.

In respect of Type III isotherms, it can be seen that there is no Point B and, therefore no identifiable monolayer formation; the adsorbent-adsorbate interactions are relatively weak, and the adsorbed molecules are clustered around the most favourable sites on the surface of the given nonporous or macroporous solid. In contrast to a Type II isotherm, the quantity that is adsorbed remains finite at the saturation pressure (at $P/P_0 = 1$).

Type IV isotherms are yielded by mesoporous adsorbents. The adsorption behaviour in mesopores is determined by the adsorbent-adsorptive interactions and also by the interactions between the molecules in the condensed state. In this case, pore condensation

is followed by the initial monolayer-multilayer adsorption on the mesopore walls, which follows the same path as the corresponding part of a Type II isotherm. This type can be divided into two main groups IV(a) and IV(b) [282].

IV(a): Mesoporous materials such as Silica and Alumina

IV(b) : Mesoporous materials with pore diameters smaller than 4 nm.

The Type V isotherm shape is very similar to that of Type III, and this can be attributed to relatively weak adsorbent–adsorbate interactions. At higher P/P_0, molecular clustering is followed by pore filling. For instance, Type V isotherms can be observed in respect of water adsorption on hydrophobic microporous and mesoporous adsorbents.

Type VI isotherms are representative of layer-by-layer adsorption on a highly uniform nonporous surface. The step-height represents the capacity for each adsorbed layer, while the sharpness of the step is dependent on the system and the temperature. Amongst the best examples of Type VI isotherms are those obtained with argon or krypton at low temperatures on graphitised carbon blacks [280, 283].

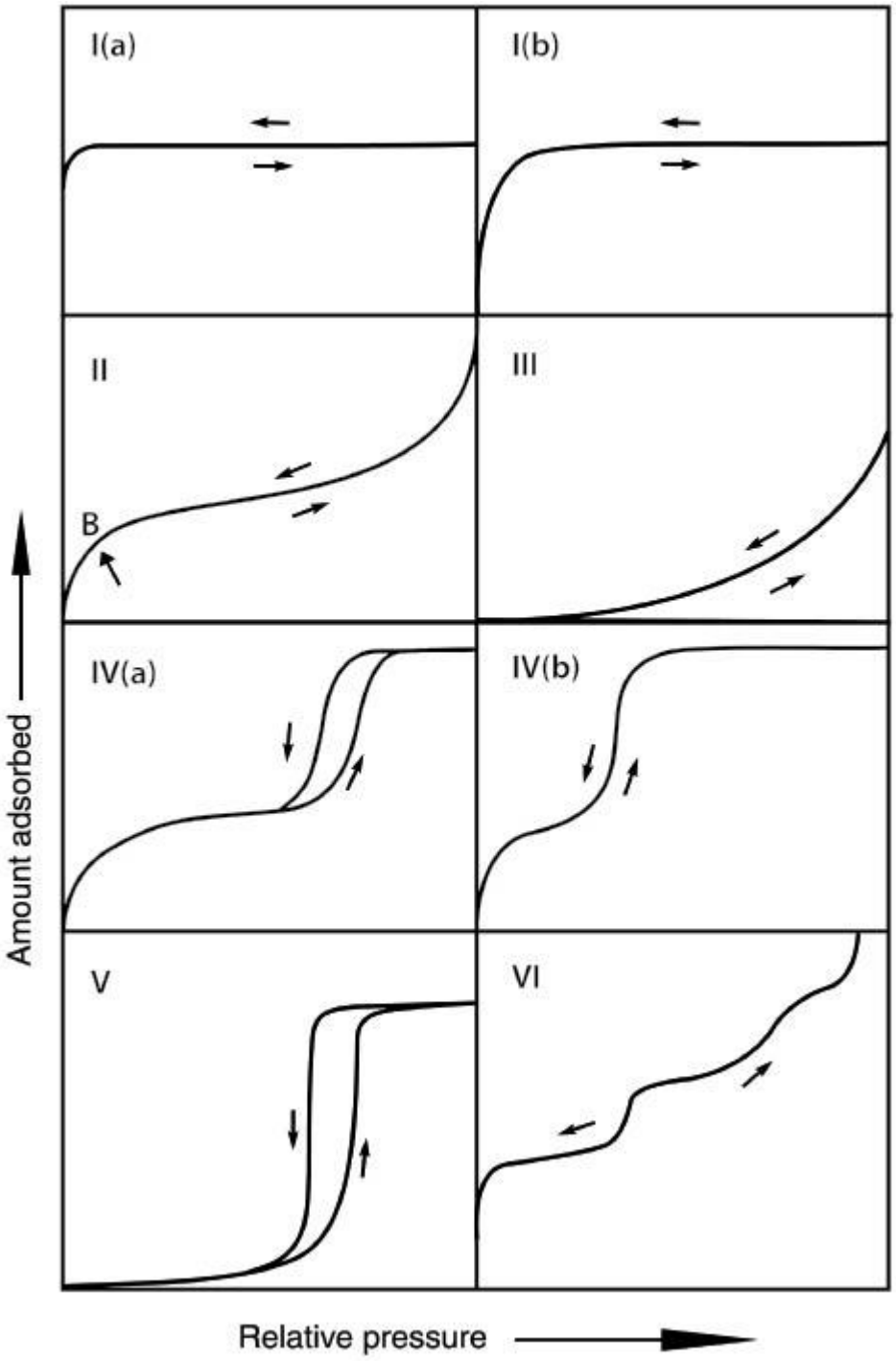

Figure 3.5 Different types of physical adsorption isotherms [278]

In the system consisting of the adsorbent, the isotherm results confirm that the gas phase (adsorptive) and the adsorbed phase (adsorbate) are in equilibrium at each point. Given these results, it can be seen that the equilibrate is insufficient in the case of aerogels with high specific pore volume. Figure 3.6 shows the isotherm for the same sample with

different equilibration times. Given this figure, it is advisable that different equilibration times be tested for each sample [160].

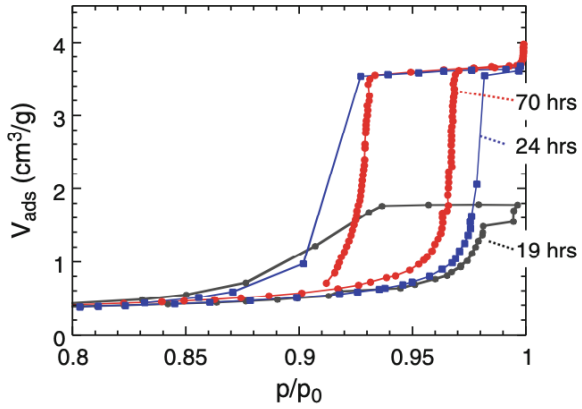

Figure 3.6 Three isotherms for silica aerogels with a different equilibration time [160]

In their study, Guo *et al.* [54] measured the surface area and pore size distribution of monolithic PI by nitrogen adsorption using the Brunauer-Emmet-Teller (BET) method. IUPAC conventions have been developed to classify gas sorption isotherms and their relationship to the porosity of materials, and so, in terms of these, the results of this study yielded type IV curves that identify the porosity in the mesoporous range between 2 and 50 nm. They showed that pore size distribution peaks are in the range of 25-40 nm but trail out to 100 nm. These values show the meso and microporosity for their samples using the IUPAC convention definition.

Pei *et al.* [90] detail type IV curves for PI aerogels containing the trimethoxysilane side group. They are shown to demonstrate an increase in the volume of the adsorbed gas in terms of an accompanying increase in relative pressure due to capillary condensation in mesopores. They also report a lower relative pressure value relating to a rapid increase in the volume of the N_2 sorption by increasing the density of the produced aerogel, with capillary condensation pressure decreasing as pore size decreases. The researchers calculate an average pore size using the $4V_{Total}/\sigma$ method. The $V_{total,}$ which is the total volume per gram of sample, is determined from the maximum amount of the adsorbed N_2 among the adsorption isotherm; alternatively, it can be calculated from $V_{total} = (1/\rho_{bulk}) - (1/\rho_{skeletal})$ [90].

Meanwhile, Li et al. [135] m The presence of mesoporous material is confirmed in terms of the identified IV type isotherm and hysteresis loops. A sharp increase in the volume of the gas adsorption at $P/P_0 = 0.9$, followed by narrow desorption, is also reported, indicating the structure of the mesopores and macropores.

Ghaffari *et al.* [284] report a bimodal micro and nanoporous structure for PI aerogels that can be used for filtering applications. The researchers used Density-Functional-Theory (DFT) and Barrett, Joyner and Halenda (BJH) methods to investigate pore size distribution and show the presence of a H_3 type hysteresis loop and typed III isotherm shape for the neat PI aerogel prepared with ODA and BPDA and samples with 10 and 20% thermoplastic polyurethane (TPU), added into the main chain. The average pore size for the neat PI aerogel is reported as 40 nm, reduced to 36 nm through addition of TPU. They also show that adding TPU has the potential to control the orientation of chains in a way that affects pore size distribution. However, they note that adding TPU in this way increases surface area from 481 to 490 m^2/g.

The detail about the technique and instrument which was used in this work for pore structure analysis is presented in section4.2.1.

3.1.5 Mechanical characterisation

Given different applications of use, different mechanical characterizations are needed to determine aerogels' mechanical behaviour. Several loading conditions must be used to investigate such aerogels' mechanical response. The typical methods used, including methods making use of tension, compression, torsion, bending and multiaxial stress states. ASTM D1621 (Standard Test Method for Compressive Properties of Rigid Cellular Plastics) for mechanical characterization shows that the surface of the sample has to be smooth and free of defects [285]. There is also a requirement that the end surfaces be parallel to each other. As the compression test is used to measure Young's modulus at small deformation, even a tiny misalignment will give rise to a significant error in the result. Aerogels are also usually brittle, so preparing the sample using machining and griping for further testing, including tension, torsion and other multiaxial stresses, is difficult. Flexural and compression tests are the only tests that are feasible for use with for aerogels. Flexural strength makes it possible for the tensile strength of the

aerogel to be estimated [18]. In Figure 3.7, both experimental and simulation methods show the stress-strain curve for silica aerogel with a relative density of 0.098 g/cm3. Three deformation stages are observed that depend on the compression strain. The first stage belongs to the linear elastic region in which the compression strain (ε) is less than 0.1 (lower than yield strength); during this step[286]. The deformation occurs elastically, and the volume exchange corresponds to the applied stress. The sample will recover its initial volume when the pressure is released [287]. A slight increase in the stress above the elastic limit will result in permanent deformation at the yielding point. In the next region ($0.1 < \varepsilon < 0.5$, the applied pressure is higher than yield strength), an irreversible strain is observed, the open structures collapse, and then a prominent plateau feature can be observed. In the final stage ($\varepsilon > 0.5$), the stress is suddenly increased in a manner suggestive of impingement of structural elements against each other, leading to foam densification [286]. During the compression test, as a function of the pressure, ρ increases and porosity decreases**.**

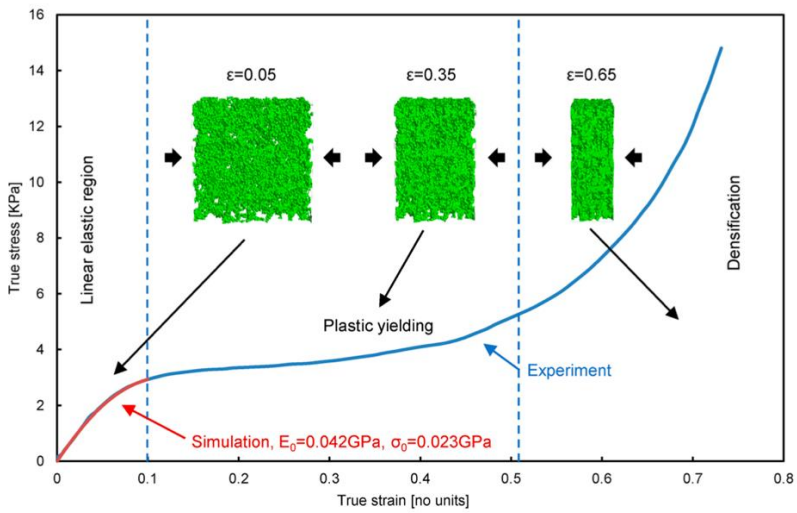

Figure 3.7 The stress-strain curve of a silica aerogel under compression [286]

Figure 3.8 shows a stress-strain diagram for the tensile test. Using this plot, it can be seen that, beyond the yielding point, an additional load can be applied to the specimen, resulting in a cure that rises continuously and becomes flat until it reaches the ultimate strength point. At the fracture point, the specimen will break completely [286].

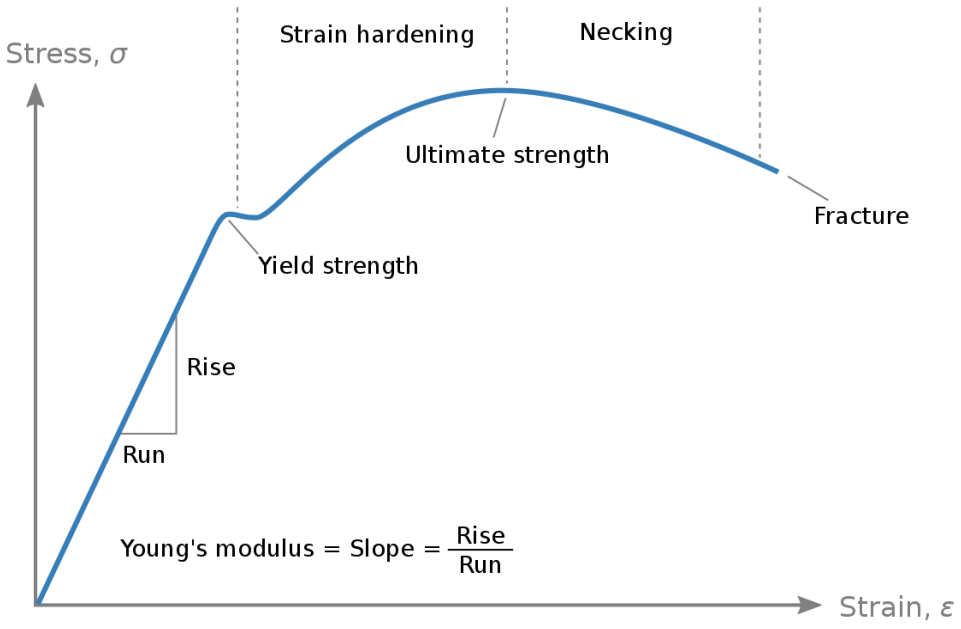

Figure 3.8 Schematic diagram of the stress-strain curve in a tensile test [286]

The compression test is usually used to measure Young's modulus in respect of small deformations. The appearance of the sample has a significant effect on the measurement, and so, once again, even a slight misalignment will yield a significant error in the results. In the tensile test, a failure on one side of the sample will quickly result in the entire specimen fracturing. Using the stress-strain curve makes it possible to obtain the compressive stress at ultimate failure, the strain at failure and Young's modulus. Compressive stress is determined by dividing the force by the initial cross-sectional area. The compressive strain is determined by dividing the displacement by the initial length of the specimen [287]. Figure 3.9 shows the typical compression stress-strain curve. Ductile materials show similar results in the compression and tensile tests. However, brittle materials show higher strength and a more significant strain before a fracture induced by the compression test as compared with the tensile test. Generally, the difference between compression stress-strain curves and tensile curves is the absence of necking phenomena [286].

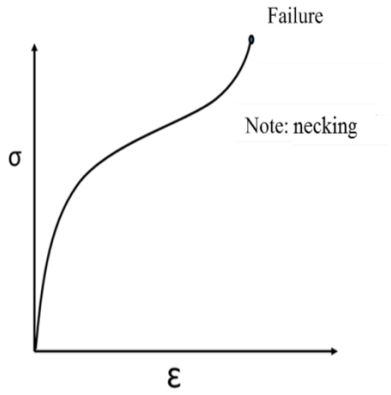

Figure 3.9 The typical stress-strain curve in a compression test [286]

A transparent PI aerogel synthesized by Vivo *et al.* [141] was characterized with compression testing using ASTM D695-10. The researchers used 4,4′-hexafluoroisopropylidene phthalic anhydride (6FDA) to synthesise the PI aerogel, impacting the optical and thermal properties of the PIs that were produced. The measurement was applied to a different molar ratio of the 6FDA. Young's modulus was calculated from the slope of the linear part in the stress-strain curve and an increase in the modulus was shown by an increase in the concentration of the polymers due to the density increase.

In another study, Wang *et al.* [269] introduced a method for preparing the composite of PI aerogel with carbon nanotubes to improve the PI aerogel's macro-structural integrity and mechanical properties. The compressive performance of the PI aerogels was tested at a strain rate of 10 mm/min by an Instron Corporation 5507 universal test machine. The reported results show an improvement in the mechanical properties of the PI aerogel after the addition of the carbon nanotubes. This improvement can be attributed to the amino-functionalized CNTs being fully embedded and well dispersed in the PI matrix .The PI aerogel nanofibers were obtained using an electrospinning device. ODA and PMDA were mixed in DMAc in a 1:1 molar ratio. After 12 h of stirring, nanofiber was prepared by means of electrospinning of the synthesized PAA. Methods involving a teflon mould and freeze drying were then used on the samples. The results of the compression test confirm that adding amino-functionalised CNTs increased the compressive modulus of the PI aerogel.

Zhang *et al.* [288] report the thermal and mechanical properties of aramid nanofiber (ANF)/PI aerogel. In their study, the PAA was synthesized with ODA, PMDA in DMAc. The synthesis process was carried out in an ice-water bath filled with nitrogen. The composite of PI/ANF was prepared in a different mass ratio of these aerogels. A series of compression tests were then applied to investigate their mechanical properties. Compressive stress under 80% strain showed that the aerogel had the ability to almost recover its initial height after the external force was removed, demonstrating a high degree of elasticity. The researchers also report three characteristic stages similar to other ultralight aerogel materials [289, 290], a linear elastic region for $\varepsilon < 18\%$ showing Young's modulus of 4.08 kPa, a plateau region for $18\% < \varepsilon < 60\%$, and a densification region with a sharply increasing slope for $\varepsilon > 60\%$ [63].

Jiang *et al.* [61] used tri(3-aminophenyl) phosphine oxide as a crosslinker to synthesize and characterize the PI aerogel produced for their study. They used different diamines and investigated their effect on the thermal and mechanical properties of the resultant products. For example, for the same solid content level, the compressive modulus of PI aerogels produced by adding PMDA is reported as having shown a significant increase compared with one made by BPDA, with an increase of almost double, from 6.8 to 12.2 MPa. This is because PMDA results in polymer backbones becoming more rigid, which leads to the PMDA-BPDA copolymerisation of the PI aerogels demonstrating a high degree of compressive strength.

To explore the effect of PI aerogel microstructure on compressibility, Yuan *et al.* [291] produced four typical PI aerogels with different solid contents that were compressed cyclically at a 50% strain. They investigated the rules of bridge formation to connect a layered PI aerogel, and layered PI aerogel with bridges was formed through precise control of the PAAC aqueous concentration and imidization condition. Generally, a high degree of aerogel porosity is advantageous for ensuring deformation and recovery . Four PI aerogel with different porosities (96.8%, 95.0%, 93.2%, and 90.9%) were characterized with a compression test, with a relatively thin layer thickness and no bridge structure being observed for the PI aerogel with the greatest degree of porosity. The compressive strength was lowest at 10 KPa, and the plastic deformation after compression was greater, reaching 17.2%. As the layer and bridge thickened, the

aerogel's compressive strength increased, the plastic deformation decreased, and the stress-strain curve became smooth [292].

Section 6.2.4 shows detail and method on how mechanical properties are monitored and determined in this work.

3.1.6 Heat transfer

Following his discovery of aerogel, Kistler sought to develop methods to learn more about its structural properties. This included the discovery of a linear relationship between the mean free path of gas molecules and the thermal conductivity of aerogel in terms of the kinetic theory of gases [293, 294]. Through a study focusing on the heat transfer properties of aerogels, evidence emerged that this ultra-light substance is a highly efficient material for thermal insulation [295], making such aerogels highly attractive in relation to potential uses in the areas of energy-consuming buildings and industrial work. Figure 3.10 shows the mechanism of heat transfer in aerogels. The equation for determining heat transfer in aerogels is as follows [18]:

$$\nabla \vec{q} + \Phi = \rho \cdot c \cdot \frac{\partial T}{\partial t} \tag{10}$$

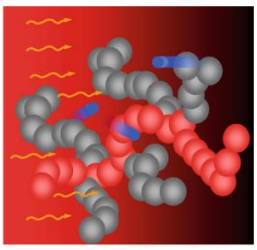

Figure 3.10 Schematic diagram for an aerogel structure and heat transfer mechanism. The heat can be transferred by means of a solid backbone (indicated by the red particle chain), by molecular gas inside the porous structure of the aerogel (blue dots) and by thermal radiation (wavy yellow arrows) [18]

In this equation, q: heat flux density, ρ: density, c: specific heat, Φ: heat source and T: local temperature. This equation reflects the heat fluxes across the boundaries of a finite

volume. Fourier's equation indicates that the heat flux density is reflected by the temperature gradient. On the other hand Fourier's law (q = -k dT/dx) states that heat flux is proportional to thermal gradient, where k is thermal conductivity.

3.1.6.1 Effective thermal conductivity of optically thick aerogels

In most aerogels, heat transfer is based on three mechanisms: conduction through the backbone, convection with a gaseous phase inside the open pores, and radiation. In the case of thick aerogels (in which case optical thickness >> 1), heat transfer occurs by means of diffusion [18].

3.1.6.2 Heat transfer via a solid backbone

Heat transfer in respect of a specific temperature gradient in the case of an aerogel occurs through the diffusion of phonons through the chains of the aerogel's backbone. Thermal conductivity can therefore be analyzed as a property of the aerogel's backbone material in the manner (λ_0) modelled by Debye, who, in his study, draws attention to the specimen's morphology [296]. In the following equation, ρ is the density of the backbone material, C_v is the heat capacity in the constant volume, the frequency-averaged mean free path of phonons l_{ph}, and v_0 is the average velocity of the elastic waves within the backbone material.

$$\lambda_0(T) = \frac{1}{3}\rho_0 \cdot c_v(T) \cdot l_{ph}(T) \cdot v_0(T) \qquad (11)$$

The thermal conductivity of solid material ($\lambda_s(T)$) can be determined using the temperature-independent geometrical factor G above -173 °C [297, 298]:

$$\lambda_s(T) = G(\rho) \cdot \lambda_0(T) \qquad (12)$$

3.1.6.3 Heat transfer via the gaseous phase

Regarding heat transfer via the gaseous phase, the pores under micron range size in aerogels lead to reductions in such heat transfer compared with heat transfer within free gas. For this reason, aerogels' thermal conductivity is below that of free air, which is 0.026 W/m.K at ambient temperature. This is why aerogels have attracted such a level of interest in terms of their potential as a material for insulation applications. The heat transfer in the gaseous phase is obtained by the Knudsen number "Kn." This parameter sheds light on the ratio between the gas molecules' mean free path and the pores' dimension [18]. The heat transfer in the gaseous phase is characterized by the Knudsen number, which is obtained by the ratio of the mean free path l_g of the gas molecules and the effective pore dimension D [18].

$$Kn = l_g/D \qquad (13)$$

Three different behaviours correspond to this ratio:

Kn>> 1: If this is the case, then the mean free path of the gas molecules is larger than the average pore size. The gas molecules collide with the aerogels' solid backbone, so the thermal conductivity is calculated regarding the number of gas molecules and the gas pressure.

Kn << 1: If this is the case, then the average pore size is greater than the mean free path of the gas molecules. Heat transfer is based on diffusion due to the gas molecules colliding [299]. In this condition, the total thermal conductivity is equal to the thermal conductivity of free gas, which is independent of the gas pressure for the ambient condition.

Kn ~ 1: If this is the case, then the gas molecules collide with both the solid backbone wall and each other.

Generally, the most common techniques used to measure the thermal conductivity of bulk materials can be classified into two major categories. The first category includes steady-state methods, including comparative, radial heat flow and parallel conductance methods. Determination of the thermal conductivity in steady-state methods is performed by measuring the difference in temperature through a known distance of a sample under a

steady-state heat flow. The second category includes transient techniques, which involve measurements being performed with a time-dependent heat energy transfer through a sample. The main transient techniques are the pulsed power technique, the hot-wire method, the laser flash method and the transient plane source (TPS) method (also called the hot-disk method) [300]. In this work hot wire which is a transient technique was used (Section 4.2.6).

In their study, Ghaffari *et al.* [301] synthesized double dianhydride backbone (double backbone) PI aerogels for the first time. This type of fabrication and using the same monomers provided a different range of morphology from particles to fibrous and monolithic aerogel. The thermal conductivity of the produced double backbone PI aerogels was measured using the hot-disk method (ThermTest Inc., TPS2500 S) at ambient temperature and room temperature. When the double backbone aerogel method was used, the PI aerogel emerged as having a thermal conductivity of 19.7 mW/m.K, 40% lower than one produced using other methods, followed by low density (0.068 g/cm^3). Among the various aerogels, the PI form is reported as being the one thermally stable up to 400 °C. This property makes the PI a promising candidate for several thermal insulation applications, including clothing worn by firefighters.

In another study, the PI aerogel was synthesised using the crosslinking PI membrane with the PI aerogel nanofibers to achieve high flexibility, strong mechanical properties and highly efficient heat-insulated performance. For measuring thermal conductivity, the flat-plate method (DREIII, Xiangtan Xiangyi Instrument Co, China) was used at room temperature [302]. It is reported that the pure PI nanofiber had small and dense pores at the nanoscale, resulting in ultralow gas thermal conductivity because the mean free path of gas molecules was in the same order of magnitude as the pore size [303]. On the other hand, the pure PI aerogel membrane is also reported as being brittle, resulting in limitations in its potential applications, although producing composites of the PI nanofiber with a membrane might improve the properties of the final product. Hou *et al.*[302] meanwhile, report ultra-low thermal conductivity and high flexibility for these composites, noting that these can be increased by increasing the concentration of the PI nanofiber from 0 to 30% to 0.0251 and 0.0335 W/m.K. This is possible because the addition of PI nanofibers increases the path of heat transfer in the system.

Finally, Guo *et al.* [26] investigated the effect of temperatures in the range of -130 to 50 °C, gas types (nitrogen and carbon dioxide) and gas pressures (5 Pa to 100 kPa) on the thermal conductivity of the aerogels. They also provide a comparison of the results with those of other polymer foams, such as polyurethane foam, phenolic foam and polystyrene foam. Their results show that the thermal conductivity measured in the carbon dioxide atmosphere condition was lower than those measured in the nitrogen atmosphere condition.

3.2 Conclusion

Due to its low density, low thermal conductivity, desirable mechanical properties and porosity, PI aerogel has a variety of applications across different areas. This type of aerogel also has the advantage of functioning to fill gaps left by other properties, including certain mechanical properties associated with the aerogel family. In work conducted for this research project, given the benefits and challenges associated with the different methods discussed in this chapter, the aim was to synthesize PI powder using the wet gel grinding method and the emulsion method, following which the resultant powder would be characterized. The properties such as density, porosity, particle size and thermal conductivity of the Aero-Zero powder, which is the powder made by Blueshift using a dry milling process, were also to be compared with the powders synthesized in this work. In the next step, the particles resulting from the manufacturing process are solidified and converted into stock shape samples using two methods to convert the powders into the stock shape: solvent (DMSO) and epoxy. The subsequent chapters also provide a discussion of how the stock shapes were characterized and compared with the Aero-Zero stock shape made by Blueshift.

Following different explanations about various types of polyimide aerogel, manufacturing process and characterising methods in chapter 2 and 3, in the next chapter three methods will be introduced for synthesizing the polyimide aerogel powders on this work. All powders will be characterized and assessed at this chapter and stored for consolidation.

Chapter 4 Preparation and characterization of polyimide aerogel powder

Compared with larger monolithic, aerogel microparticles from PI and other forms of thermally stable polymers are suitable for use in a larger variety of applications. As an example of the properties that cause this, PI aerogel microparticles of a few nanometres or micrometres have a triple mass diffusion rate compared to monolithic ones with similar porosities and surface areas. Among the applications of such aerogel microparticles are, for example, the manufacturing of double-layer capacitors in energy storage [304] and packed bed reactors in chromatography [305] and use as drug reservoirs in drug delivery [306]. The fabrication of microparticles also presents certain advantages in terms of ease of handling and surface smoothness, which can prevent inflammatory responses from the body [307].

The present study was conducted to detail the production of PI aerogel powders with controlled particle sizes using dry milling, wet gel grinding (WGG) and oil-in-oil emulsion (EM) methods with a short processing time and the performance of solvent exchange. Using WGG and EM techniques, the solvent exchange can be completed in acetone in less than 3 h. For both WGG and EM, polyamic acid (PAA) was first synthesized by mixing 4,4'-oxydianiline (ODA) and 4,4'-diamino-2,2'-dimethylbiphenyl (DMB) as diamine and 3,3',4,4'-biphenyltetracarboxylic dianhydride (BPDA) as an anhydride in two additions. 1,3,5-Tris(4-aminophenoxy) benzene (TAPOB) was also added as a branching agent in this step [33]. As the catalyst, 2-methyl imidazole (2-MI), and benzoic anhydride (BA), as the dehydrating agent, were used to complete the imidization process. Finally, low-density, highly porous aerogel powders were obtained after solvent exchange and drying under ambient pressure. More detail about the drying and solvent exchange process are presented in section 4.5.3.

4.1 Experimental work

4.1.1 Material

This work was undertaken using TAPOB purchased from Wakayama Seika Kogyo and DMB purchased from TCI. Dimethyl sulfoxide (DMSO, ≥ 99% Reagent Plus), ODA, BPDA, phthalic anhydride (PA), benzoic anhydride (BA), 2-methyl imidazole (2-MI, 99%), acetone (technical grade) and cyclohexane (≥ 99% ACS reagent) were purchased from Sigma-Aldrich. Hypermer™ 1599A and Span 85 were purchased from Croda. All reagents and solvents were used without further purification.

4.1.1.1 What is Sorbitan (span)

Sorbitan is a mixture of isomeric organic compounds derived from the dehydration of sorbitol and is an intermediate in converting sorbitol to isosorbide [308].

Sorbitan is primarily used in the production of surfactants such as polysorbates; which are important emulsifying agents, with a total annual demand of more than 10000 tons in 2012 [309]. There is a different grade of span with a variety of properties. For example, Span60 is a non-ionic surfactant which can be used in drugs. Span 80 is more hydrophobic (HLB=4.3) and can be used in the oil in oil emulsion system compared to span 20 with HLB=8.6, which is more hydrophobic [310].

4.1.2 Synthesis of polyamic acid (PAA)

PAA was first synthesized as follows: 225.81 g of DMSO was added to a precleaned baffled reactor, following which 4.98 g DMB, 4.69 g ODA and 0.30 g TAPOB were added simultaneously and stirred with the solvent at room temperature until all components were fully dissolved. There was then sequential addition of BPDA in two equal portions every 20 min of 6.71 g each to the mixture, with this being allowed to dissolve completely after each addition. The resulting homogenous mixture was left to stir overnight. The next day, 0.82 g PA was added to the mixture and stirred for an additional 2 h. The formulation for synthesizing PAA in this way is listed in Table 4.1. The resulting pale orange solution PAA was drained from the reactor (see Figure 4.1),

weighed, and ready for use in the synthesis of PI powder aerogels. The methods adopted for this task are detailed in the subsequent sections [311].

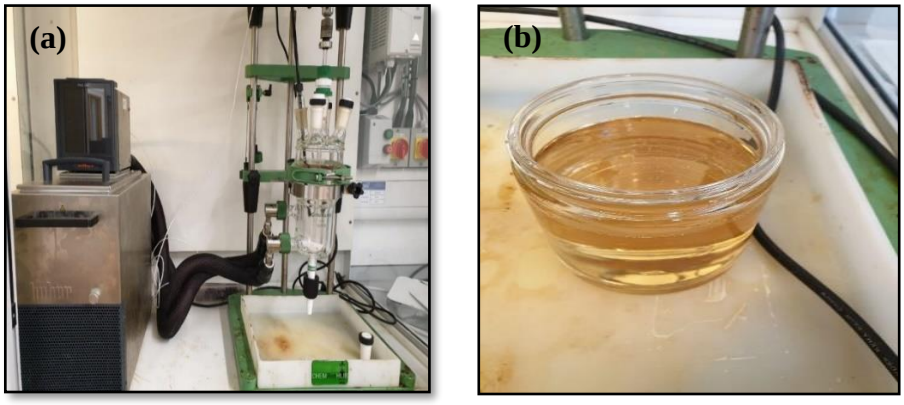

Figure 4.1 (a) Baffled reactor and temperature controller; (b) PAA

Table 4.1 A formulation for the synthesis of PAA

Resin (PAA) chemical content		
Chemical	Weight (g)	Weight (%)
DMSO	225.81	90.32
TAPOB	0.30	0.12
DMB	4.98	1.99
ODA	4.69	1.88
BPDA	13.41	5.37
PA	0.82	0.33
Total	250.01	100.00
Total solid	24.20	
% solid content	9.68	

The molecular weight of the PAA was analyzed in terms of the inherent viscosity, with higher viscosity indicating a greater molecular weight. In the present work, the viscosity of the PAA resin was measured using CGOLDENWALL Digital Rotary Viscosity Meter. This viscometer has different sizes and types of spindles that are selected depending on the range of viscosity; the measured viscosity using this viscometer can be in the range of 0.1- 2000000 cp/mpa.s. The viscosity can be measured at different speeds of rotation for the spindle. The effective parameters on the measured viscosity are temperature and velocity of the rotation. For measuring the viscosity of the synthesized PAA, settings of 30 rpm and spindle S1 were selected. The viscosity for the PAA is 197.8 ± 13.2 mpa.s. Figure 4.2 shows the digital viscometer that was used for this work.

Figure 4.2 CGOLDENWALL Digital Rotary Viscosity Meter used in this work

4.1.3 Synthesis of polyimide aerogel stock shape

Given that PIs are insoluble and infusible, it is typical to use a two-step process for manufacturing PIs [312, 313]. In the first step, soluble polyamic acid (PAA) is prepared to produce thin films or coatings or to be impregnated with carbon fibres. In the second step, PIs are prepared either thermally or chemically from PAA [314].

This study induced chemical imidization by using 2-methyl imidazole (2-MI) as a catalyst after preparing the PAA. During the imidization process, the polyamic acid was converted into PI, with benzoic anhydride (BA) being added as a dehumidify agent in order to remove the water molecules arising as a by-product of the process. Suppose the water had been allowed to remain in the reaction. In that case, the unreacted PI participates would have reacted with this water, giving rise to a reverse reaction through the production of polyamic acid. The ratio between the mass of 2-MI and BA against the mass of the resin was 0.05 and 0.19 in respect of each of these. The chemical reaction used for synthesizing the PI aerogel is presented in Figure 4.3 [315]. After adding 2-MI into the PAA and a 3-min mixing these using a magnetic stirrer, the BA was added and mixed for another 3 min. At the end of this mixing, by which point a clear yellow solution had appeared, the sol was poured into a specific mould and left in the ambient condition (at 20-25 °C) for

18-24 h to produce the wet gel through the process of ageing. After 24 h, the wet gel was demoulded and sent for solvent exchange. The acetone was added 4 times greater than the volume of the stock shape to the container, then placed in the shaker. The acetone was replaced 6 times every 24 hours. After the completion of the solvent exchange, the blocks were placed in an ambient condition so that the acetone could evaporate to the point where the samples would stop losing weight. Then, to achieve curing and to complete the drying process, the blocks were first heated to 200 °C for 90 min under a vacuum and then heated to 300 °C for 12 h under a flow of argon.

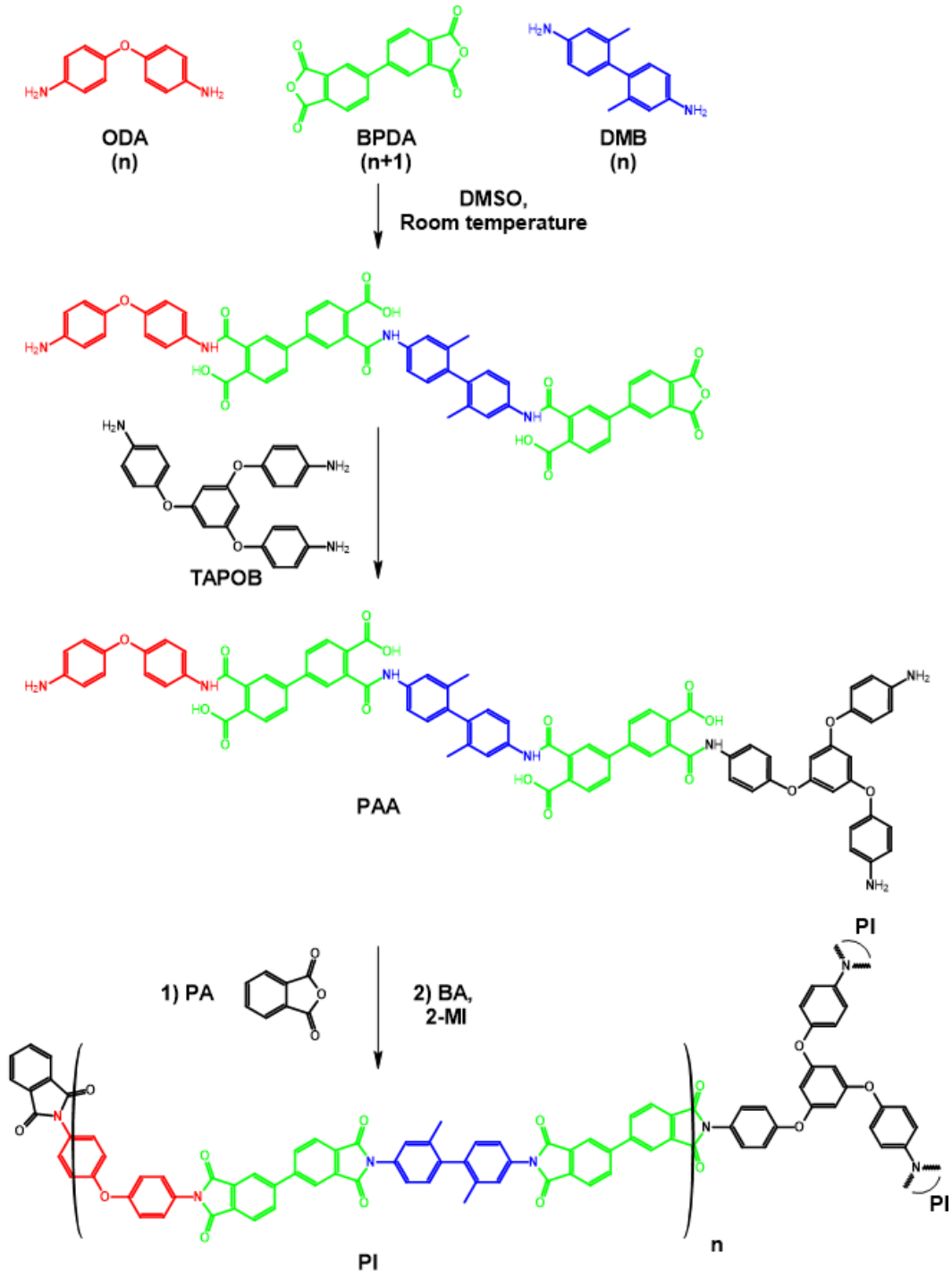

Figure 4.3 Synthesis of PAA and PI aerogel from amines (DMB, ODA, TAPOB) and anhydrides (BPDA, PA), catalysed with 2-MI [315]

4.1.4 Dry milling of PI aerogel stock shape

To produce PI-powder aerogel, Blueshift uses a CAMaster-Stinger I dry miller machine, working with a feed rate of 50 in/min, a plunge rate of 15 in/min and a rotational speed of 12000 rpm. Figure 4.4 shows the PI stock shape being converted into powder in this way. The produced particles are stored in a fully sealed bag for further investigation.

Figure 4.4 (a) PI stock shape, (b) stinger for milling the PI stock shape, and (c) PI powder aerogel produced through dry milling of PI stock shape

4.1.5 Synthesizing PI aerogel powder using wet gel grinding (PI-WGG)

For this research, wet gel grinding was used as the method of synthesizing the PI aerogel powder, necessitating the use a blender and blending the PI wet gel into a small particle. In the first step, the wet gel needs to be synthesized, following which it can be converted into particles. To produce different particles in terms of shape, size and properties, solid content can be changed through dilution. Thus, DMSO, the main solvent used in this process, was added in different volumes to optimise the manufacturing conditions and properties of the resultant particles.

The chemical formulation for synthesizing the PI-WGG is listed in Table 4.2. In a 1-litre glass beaker, 10 g of PAA was diluted by adding DMSO in $\frac{\mathrm{DMSO(g)}}{\mathrm{PAA(g)}}$ ratios of 0, 0.5, 1 and 1.5. The sol was stirred for 3 min using a magnetic stirrer. 0.69 g 2-MI (as the catalyst) was added, and the PAA was stirred for 3 min. 2.09 g BA was then added to the sol, and the mixture was stirred for an additional 3 min. Benzoic anhydride (BA) was then used to remove the H_2O molecules arising as a by-product during the imidization process. The sol was then transferred to a polyethene container for gelation, which took around 30 min. After 24 h of resting under ambient conditions, the resulting PI wet gel was ground using a blender for 3 min. For grinding, water was used in a volume of four times that of the wet gel to prevent explosion during the blending process. The wet powder was exchanged with acetone three times every 30 min. Finally, PI-WGG aerogel powders were obtained by filtering under a vacuum and drying at room temperature for 24 h and 30 min at 200 °C. Figure 4.5 shows the different steps involved in the fabrication of PI-WGG.

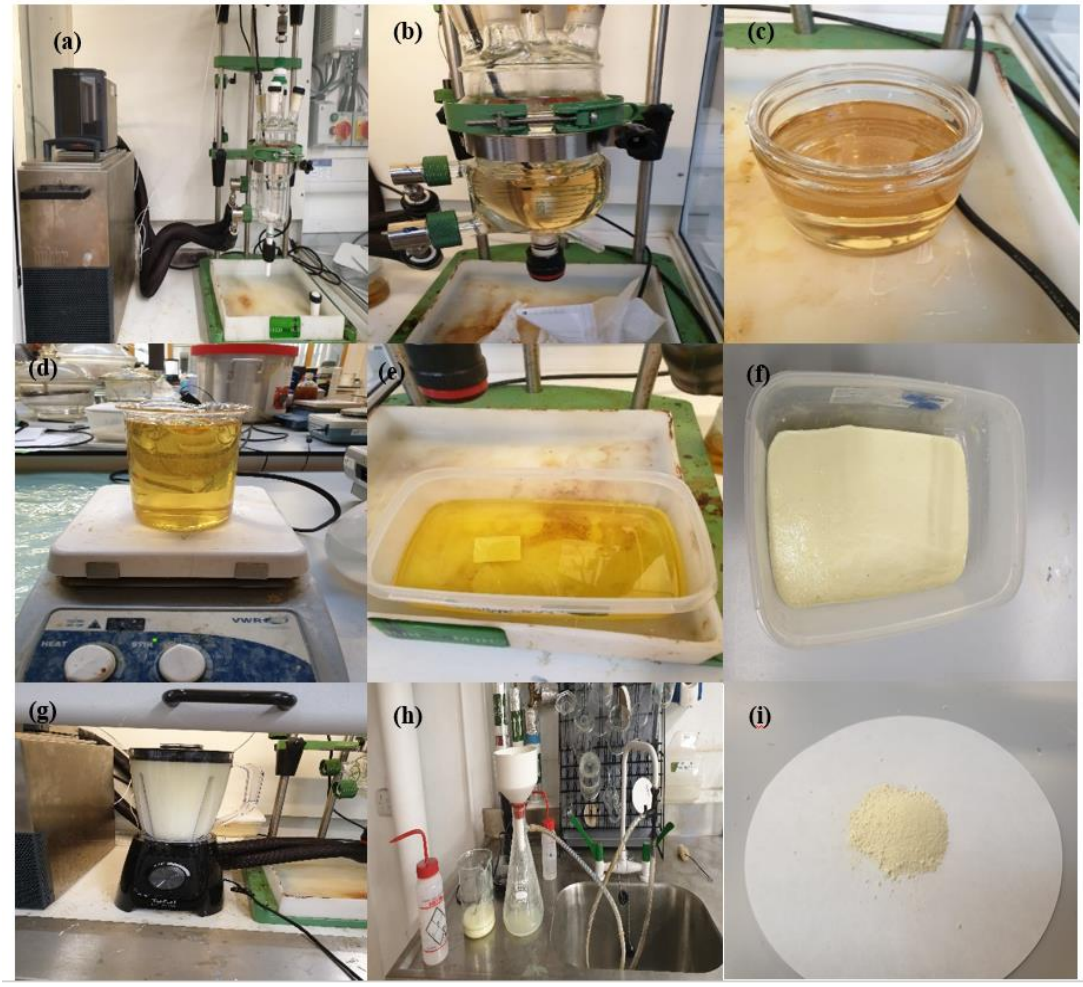

Figure 4.5 (a) reactor used for mixing the solution in the closed area, (b) mixing the polyamic acid resin in the reactor overnight, (c) draining the PAA from the reactor, (d) chemical imidization induced by adding 2-MI, (e) leaving for 24 h at 23 °C, (f) wet gel PI after 24h, (g) grinding the wet gel to produce the powder with kitchen blender, (h) solvent exchange and filtration process, (i) dried powder (24h RT, 30min at 200°C)

Table 4.2 Formulations for the preparation of PI-WGG aerogel powders

DMSO/PAA = 1.5		
monomer	Weight (g)	Weight (%)
DMSO	375.00	54.00
PAA	250.00	36.00
BA	52.25	7.52
2-MI	17.25	2.48
total	694.50	100.00
% solid content	–	13.49
% Yield	-	86

4.1.6 Synthesis of polyimide aerogel powders using emulsion (PI-EM)

The chemical formulation for synthesising the PI-EM is listed in Table 4.3.

In a 1-litre glass beaker, emulsifiers (0.38 g of Span 85 and 0.13 g of Hypemer 1599) were mixed with 20 ml cyclohexane, and the solution was stirred mechanically until the emulsifiers were fully dissolved (~20 min). These emulsifier agents reduced the surface tension operating between the two dissimilar liquids [36]. In a separate sealed round bottom flask, 10 g of PAA was diluted by adding DMSO in $\frac{\mathrm{DMSO(g)}}{\mathrm{PAA(g)}}$ ratios of 0, 0.5, 1.0, and 1.5 and the sol was stirred for 3 min.

Then a catalyst, comprising 0.69 g of 2-MI, and 2.09 g of BA, was added stepwise by mixing for 3 min between each addition. (See Figure 4.6.)

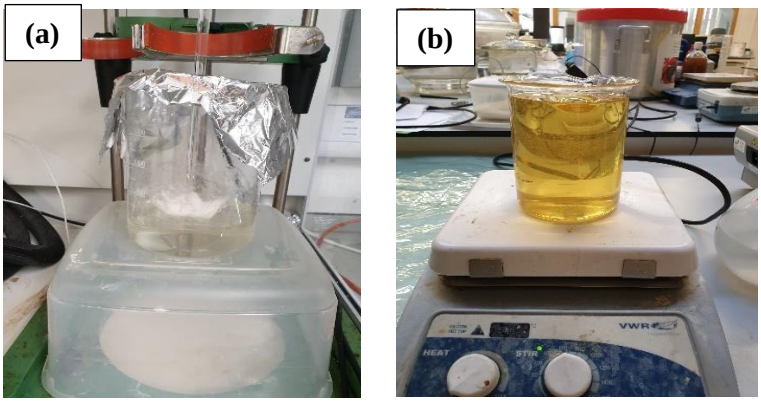

Figure 4.6 a) mixing the cyclohexane with emulsifiers, b) performing the dilution and adding the catalysts into the PAA as a dispersed phase during the emulsion process

Subsequently, the mixture of PAA, DMSO and catalyst was added to the solution of emulsifiers in cyclohexane. This was done slowly using a pipette. The mixture was stirred for 1 h at a rate of 500 rpm (Figure 4.7-a). The cyclohexane was then decanted, and the DMSO layer was poured into a beaker containing 500 ml of acetone (Figure 4.7-b). After 15 min, the PI-EM wet powders were collected in a vacuum filtration funnel. TGA was used to identify the optimal method for exchanging the solvent and drying, and the residual solvent was measured for different washing methods (see section 4.5.3). As discussed below, the most optimal condition in terms of the quantity of residual solvent is reflected in "wash[ing] with acetone three times every 20 min and two times every 45 min" (Figure 4.7-c). Finally, PI-EM aerogel powders were spread on a tray and air-dried for 45 min at room temperature, followed by further drying for 2 h at 50 °C and for 30 min at 200 °C under air (Figure 4.7-d). The drying condition was optimized in terms of timing and the residual solvent in the powder. The results of the optimisation process are presented in section 4.5.3.

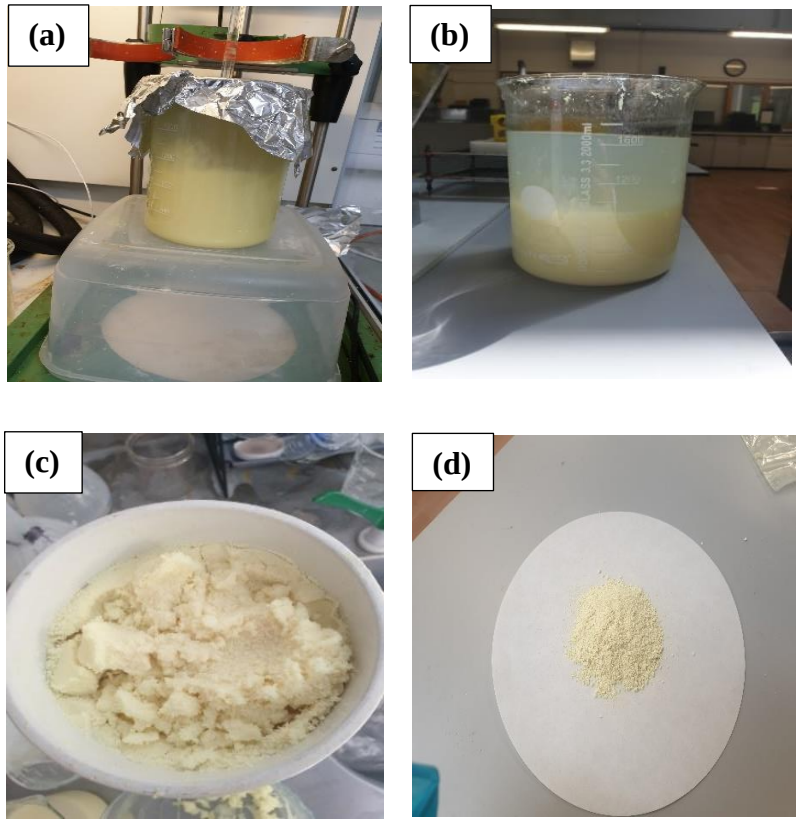

Figure 4.7 (a) cyclohexane with emulsifiers at 500 RPM, (b) the addition of PI to the cyclohexane, followed by mixing for 1 h at 500RPM, (c) sedimentation, (d) solvent exchange and suction filtration, (e) dried powder (45minRT, 2h 50°C,30min 200°C in air)

Table 4.3 Formulations for the preparation of PI-EM aerogel powders

DMSO (g)/PAA (g) = 1.5		
monomer	weight (g)	weight (%)
DMSO	375.00	34.19
Span 85	9.50	0.87
Hypermer 1599-A	3.25	0.30
Cyclohexane	389.50	35.51
PAA	250.00	22.79
BA	52.25	4.76
2-MI	17.25	1.57
total	1096.75	100.00
% solid content	–	9.68
% Yield		77

4.1.7 Results relating to the properties of polyimide aerogel powder

The PI powder aerogel, which, as detailed above, was synthesized using three different techniques (dry milling, wet gel grinding and emulsion), had to be characterized using a range of different techniques. The dried milling powder called "Aero-zero" powder was prepared by Blueshift for this research and was considered the reference for all measurements taken. Different batches of powders were made using the wet gel ground method and emulsion process in different ratios of DMSO: PAA, 0.0, 0.5, 1.0, 1.5. All the batches were mixed and stored in a plastic bag until it came time to characterize them. Properties of interest at the microscopic level, including skeletal and porous structure, microparticle size and assembly, were investigated using nitrogen sorption, mercury intrusion porosimetry and SEM. Macroscopic properties such as thermal stability (up to 500 °C) and conductivity (0.039 W/m.K) were compared and correlated with other properties such as density and dilution ratio. Samples obtained using WGG are referred to as PI-WGG-xx, and samples prepared using EM as PI-EM-xx, with the suffix "-xx" denoting the ratio of DMSO (g) to PAA (g) in the preparation of the powders.

4.2 Characterization techniques

4.2.1 N_2 sorption

Gas adsorption measurements were conducted on a Micromeritics ASAP2420 Surface Area and Porosity Analyser (Figure 4.8). Surface area, pore volume and average pore size were determined by means of analysis of the cryogenic nitrogen adsorption/desorption isotherm.

Figure 4.8 Micromeritics ASAP 2420 Surface Area and Porosity Analyser

Approximately 0.2 g of sample was subject to a degas cycle of 30 min at 50 °C, followed by 120 min at 120 °C, at a pressure of 10 mmHg. This process removed any residual solvent or surface contaminants from the samples. Degassed samples underwent a 40-point adsorption cycle between the relative pressures of 0.01 and 1, followed by a 30-point desorption cycle between the relative pressures of 1 and 0.1. The sample temperature was maintained at a constant value of -196 °C throughout the experiment using a liquid nitrogen bath. Two samples were tested using gas adsorption.

Brunauer–Emmett–Teller (BET) specific surface areas were obtained by means of nitrogen sorption at -196 °C [276, 316]. The desorption branch of the isotherms was used to calculate the Barrett-Joyner-Halenda (BJH) pore size distribution [316]. The total pore volume was calculated from the volume of adsorbed gas at relative pressure equal to 0.99.

4.2.2 Mercury Intrusion Porosimetry (MIP)

Complete pore size distributions and bulk densities were measured with low and high-pressure sweep mercury intrusion porosimetry using an Autopore V model 9605 [317]. Approximately 0.1 g of the sample was subjected to a penetrometer for

low and high-pressure analysis. A sweep of 0-30 psi, followed by a sweep of 30-33000 psi, was used for low and high pressures, respectively. MIP was used to measure the bulk volume of the sample using a subtraction operation between the volume of the penetrometer, defined for the software, and the volume of the adsorbed mercury.

The % porosities were calculated using the bulk density from MIP and skeletal density. Figure 4.9 shows the MIP equipment used for this purpose.

Figure 4.9. Autopore V model 9605, surface area and porosity analyser

The following equation was used for measuring the porosity in terms of bulk density and skeletal density [318]:

$$\% \text{ Porosity} = 1 - \frac{\rho b}{\rho s}$$

ρ_b = bulk density (g/cm^3), ρ_s = skeletal density (g/cm^3)

4.2.3 Pycnometer

Skeletal densities were measured on a Micromeritics Accupyc II 1340 helium pycnometer. Figure 4.10 shows the pycnometer equipment used in this work.

Figure 4.10 Helium Pycnometr used in this work

4.2.4 Particle size measurement

Only for exactly spherical particles can a number be determined as a diameter for the given particle's size. In the case of other regular shapes, as in cubic particles, more than one dimension from the length, width and thickness must be measured. In the case of the samples in powder form, it is typical for the particles to be mostly irregular, and the size of the particles that is yielded depends on the method used to measure this [319]. The typical method for measuring particles' size in this way references equivalent spherical diameter, referring to the diameter of the spherical shape that has a volume equal to that of the current particle. The critical factor that must be considered during particle size measurement is the value of certain size-dependent properties of such particles. It is worth mentioning that determining the particle size distribution and analysing this figure to detect any change is generally more important than measuring the absolute value for particle size.

In powder samples, the particles' size and shape are the most critical parameters for gaining insight into their properties. In the present research, the size of the particles was measured using Image-Pro software, which was used to view microscopic images of these particles. Using the manual split, any overlapping particles could be split and viewed as individual cases. Obtaining the required microscopic images involves powder being poured onto a small glass plate, and the particles can be

dispersed evenly and separately by shaking the plate smoothly. Figure 4.11 shows the different steps involved in using the Image-Pro software when measuring the diameter of such particles.

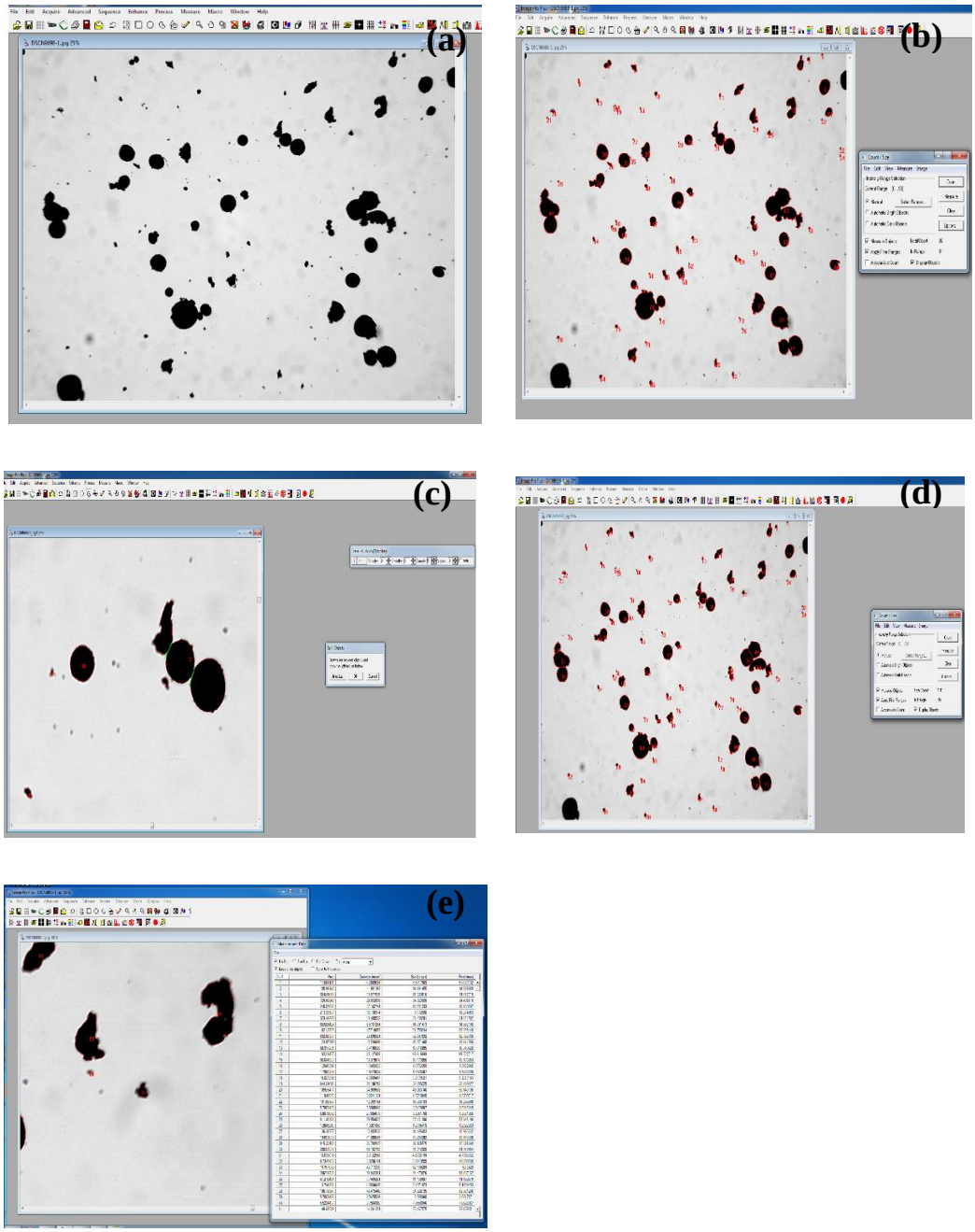

Figure 4.11 Different steps for using Image-Pro for particle size measurement, a) opening a optical microscopic image in Image-Pro, b) counting the number of the particles, c) applying manual split to separate any particles that are overlapping, d) counting the number of particles after separation, e) extracting the measurement data from the software

For the purposes of this study, particles of the sort illustrated in the microscopic images are taken to be the smallest objects remaining on the glass plate after the plate has been shaken. Figure 4.12 shows different diameters for a nonuniform particle. This study proceeded on the basis that the size of each particle could be defined as the average of different diameters in different directions. For each condition, at least 500 particles were measured using different optical images, with the average of all of these being presented as the average diameter for the sample.

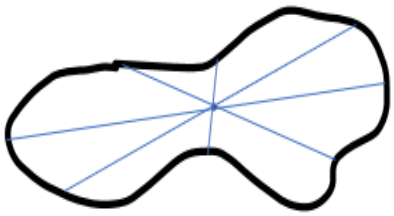

Figure 4.12 Different diameters for a non-uniform particle

There are accounts in the literature providing evidence that particles' geometry changes in terms of mechanical and transport properties such as adsorption-desorption. For example, Decuzzi *et al.* [320] report that increasing the adhesion of a spherical particle on a biological substrate can expand its surface area. Jin *et al.* [158] meanwhile, fabricated a pill-shaped PI aerogel particles using microfluidic flows. The spherical PI sol droplets produced in their experiment using a microfluidic droplet generator were guided into a contraction flow channel to deform them into pill-shaped droplets, synthesizing a pill of roughly 200 µm in diameter and 1000 µm in length. The researchers also found that microparticle length could be controlled by varying the ratio of the flow rates of PI sol and silicone oil.

4.2.5 Thermogravimetric analysis (TGA)

The thermal stability of the powders and the quantity of residual solvent in the produced particles were measured by thermogravimetric analysis using a TA Instruments Q50 thermogravimetric analyser (TGA) (Figure 4.13). The surface of

the pan was covered with a 13-20 mg sample. The temperature was increased from 20 to 700 °C under air at a heating rate of 10 °C/min. At the end of the test, the temperatures corresponding to 10% weight loss and onset were recorded.

Figure 4.13 TA Instruments Q50 thermogravimetric analyser (TGA)

4.2.6 Thermal conductivity

In this work, a XIATECH TC3000E thermal conductivity meter was used to measure the thermal conductivity of the samples. This equipment generally works on the basis that the heat is transferred across a hot wire sensor that is placed between two samples. Before analysing the samples, a polymethyl methacrylate (PMMA) standard sample was tested to calibrate the equipment. For all measurements, a 500g deadweight was placed on the sample to apply pressure and ensure contact between the sample and the sensor's surface. Figure 4.14 provides a schematic image detailing the placement of the sample on this instrument.

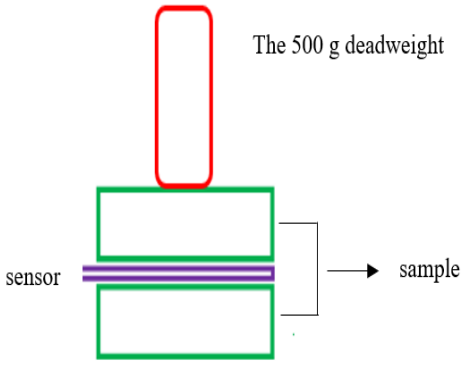

Figure 4.14 Schematic image detailing the technique for measuring thermal conductivity

The minimum edge length for the sample and minimum thickness had to be at least 3 cm and 0.3 mm, respectively. There is no limitation in terms of the sample shape when using this instrument, meaning that the solid sample can be round, square or irregular and in the form of powder. Figure 4.15 shows the sample set-up for powder and stock shape in terms of using the hot-wire technique for measuring thermal conductivity.

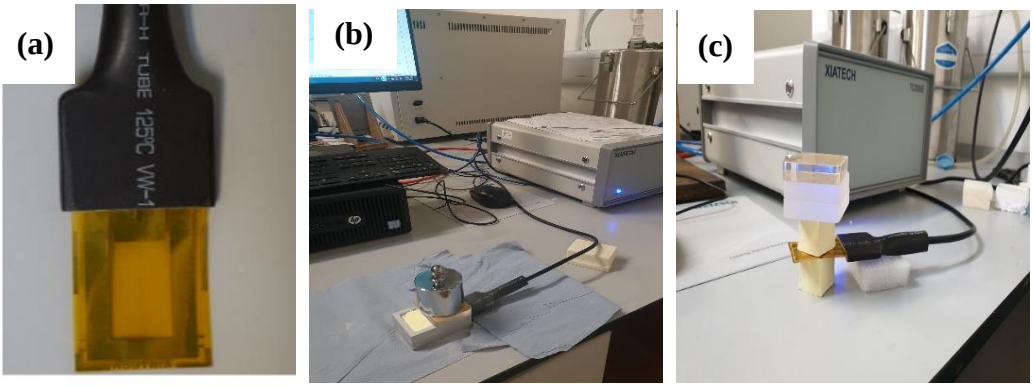

Figure 4.15 Thermal conductivity measurement set-up: a) TC3000E thermal conductivity meter sensor, b) powder measurement, c) stock shape measurement

4.2.7 Scanning Electron microscopy (SEM)

In this work, two different SEM were used for powder and stock shape samples. For the powder samples Phenom Prox/Pro/ Pure instrument was used. And for the stock shape samples, Leica EM ACE 200 sputter coater and a Hitachi TM4000plus scanning electron microscope were used. The samples were attached to aluminium

stubs using double-sided adhesive carbon tabs and then coated in 20 nm of gold using the sputter coater. The SEM was operated with an accelerating voltage of 10 kV in observation mode 2 and standard vacuum.

4.3 Results of characterizing milled polyimide aerogel powder

4.3.1 N_2 sorption for dry-milled powder

When investigating adsorption for various gaseous separations, the sorbent's surface area, pore volume and diameter are three of the most important properties to consider. This is because these parameters determine the quantity of gas that can be stored and the material's ability to selectively capture one species. The Aero-Zero powder was analyzed for basic textural and the results are shown in Figure 4.16.

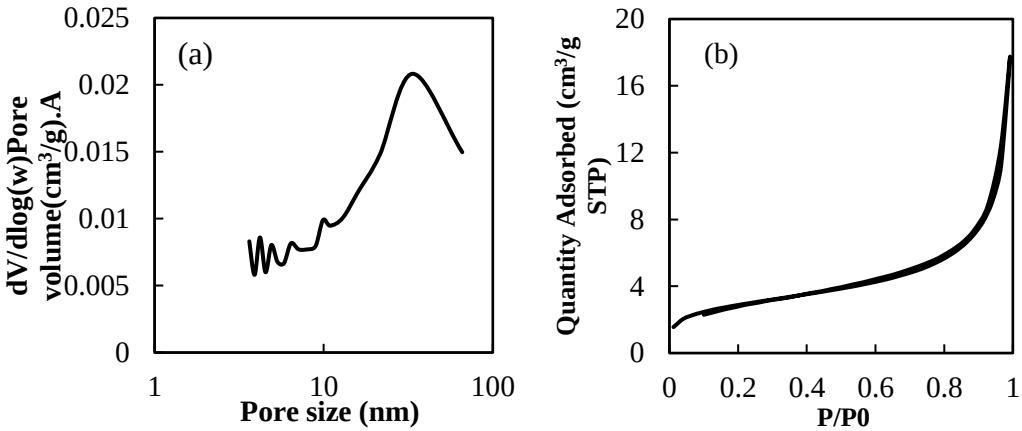

Figure 4.16 N_2 sorption for milling powder, (a) pore size distribution, (b) N_2 sorption isotherms (at -196 °C)

The plots show meso- and microporosity for the Aero-zero particles, with 5 to 70 nm pores. The average pore size with the adsorbed gas at its maximum volume is 34 nm. In addition, the hysteresis loop was found to be apparent in the BET

isotherm curve, demonstrating that mesopores existed in the Aero-Zero powder. This loop also suggested that low pressure ranges would lead to condensing the gas inside the pores and that higher pressure would form mono- and multilayers. The nitrogen adsorption isotherms for this powder rose above $P/P_0 = 0.9$ but without reaching the saturation plateau, indicating their status as type II isotherms. Overall, only a very low quantity of gas adsorbed during the early stages of the adsorption, indicating that the pores were mostly meso- and macroporous. On the other hand, there was significant adsorbing of N_2 at relatively low pressures, implying a microporous status. N_2 sorption indicated the pore volume to be 19.3 cm^3/g, associated with pores up to 100 nm in size.

4.3.2 Mercury Intrusion Porosimetry (MIP) for dry-milled powder

MIP was used to measure the particles' total porosity, bulk density and pore size distribution. The milled particles were found to have a bulk density equal to 0.17 g/cm^3. Furthermore, their low density and high porosity of 89% made the Aero-Zero a useful choice for several different applications. The MIP profile in Figure 4.17 provides important information regarding the characterisation of Aero-Zero. The distribution indicates that most of the pores of this substance are macropores, between 5 nm and 340 µm. MIP was also used to measure the degree of porosity inside the particles (intra pores) and between them (inter pores), which was found to equal 89%. The bimodal distribution showed meso- and macroporosity for the particles, with a median pore diameter indicated by the MIP of 7881.20 nm, confirming a macroporous structure. The intensity of both peaks, start at 0.1 and 10 µm, is almost the same, confirming the status of most of the pores as macropores.

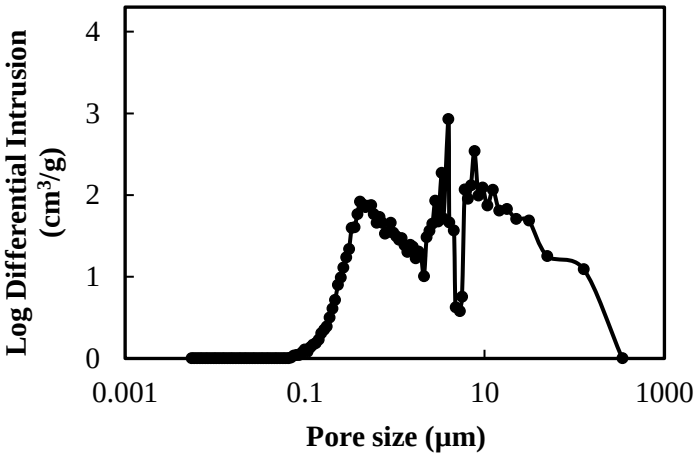

Figure 4.17 MIP pore size distribution for Aero-Zero powder

4.3.3 Particle size measurement

Image Pro was used to measure the size of the particles. This was done on the basis that this would be a property of relevance to most of the powder's properties and applications. The analysis conducted using Image Pro involved considering different optical images to obtain information on at least 500 particles and measuring their diameter. Figure 4.18 shows the microscopic and SEM image for the Aero-Zero powder, indicating a porous structure in each case.

The pores can be seen to exist between the particles and on their surface. A level of aggregation between the particles can also be observed as a result of the milling and storing processes.

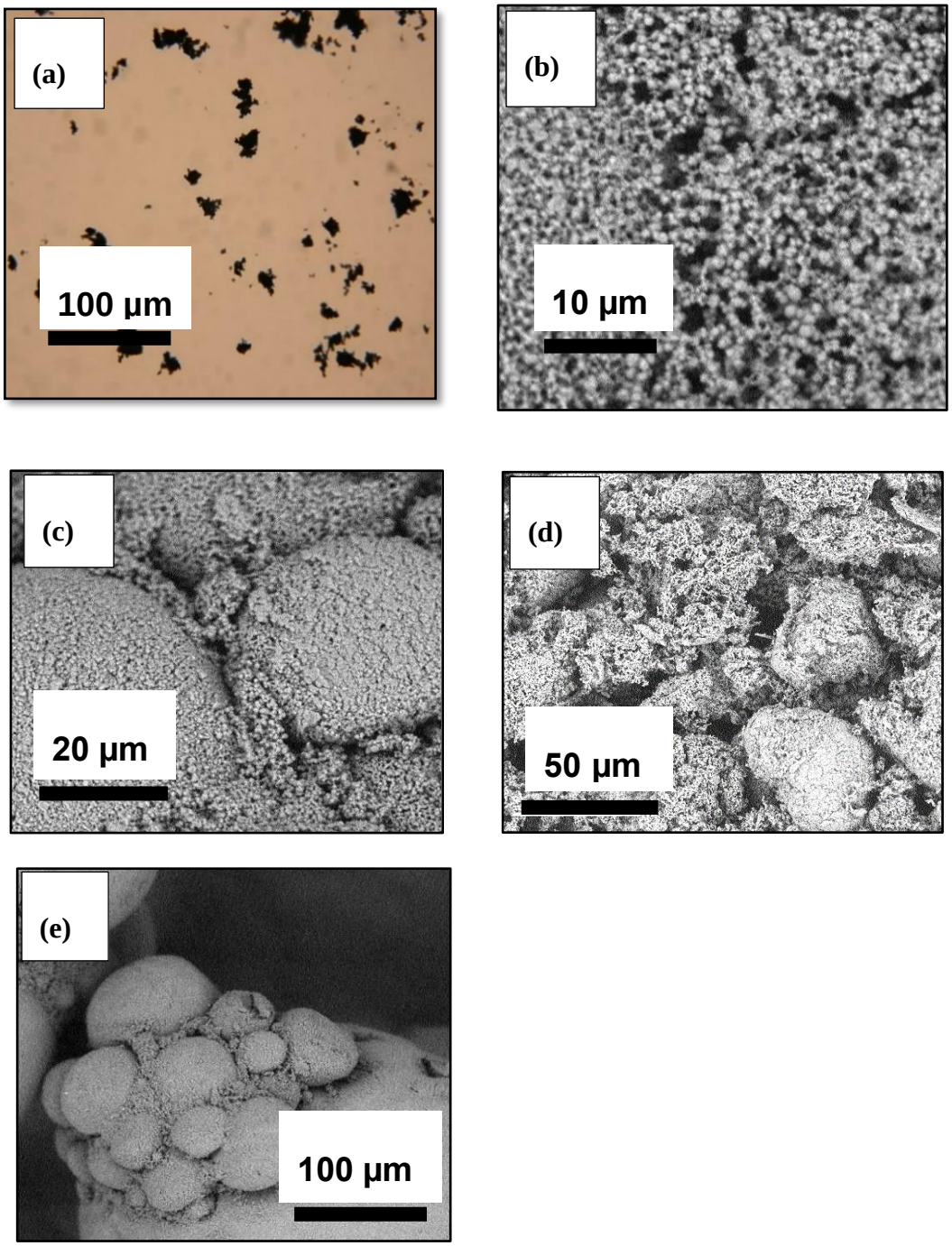

Figure 4.18 a) optical and b-e) SEM image from Aero-Zero powder

A right-skewed particle size distribution for Aero-zero powder is shown in Figure 4.19. These data show that the particles are dispersed in the range of 5-90 µm, mainly in the range of 5 to 10 µm, with an average size of around 17.93 µm.

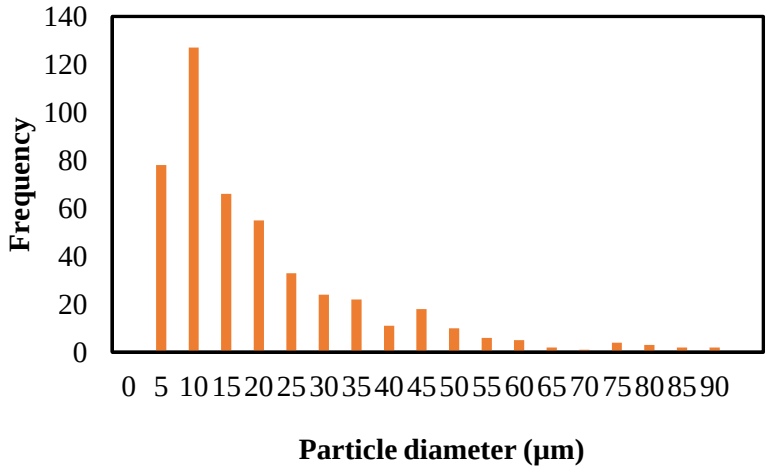

Figure 4.19 Particle size distribution for dry-milled powder

Another commercially viable method for measuring particles' size involves using a sieve. This method was also used in respect of the Aero-Zero particles prepared for this research project, specifically a multi-step micro-size sieve. The sieves contain different sizes of mesh and can detect and measure particles in the range of 53-5000 µm. The relevant sieve and particle size frequency for this method are presented in Figure 4.20, indicating a narrow distribution with a peak in the range of 420-590 µm. However, these results must be interpreted with caution in that shaking the particles to pass them through the sieve may result in these particles attaching to each other, resulting in objects that the sieve shows to be larger than the individual particles would be. This is why this method is considered to be potentially inaccurate and useful only on an industrial scale.

To plot the frequency data, the powder weight in each mesh plate was measured and divided by the total mass of the powder, yielding a value showing the frequency for the particles with a size in the range of a specific mesh. The narrow distribution depicted below shows the presence of uniform particles.

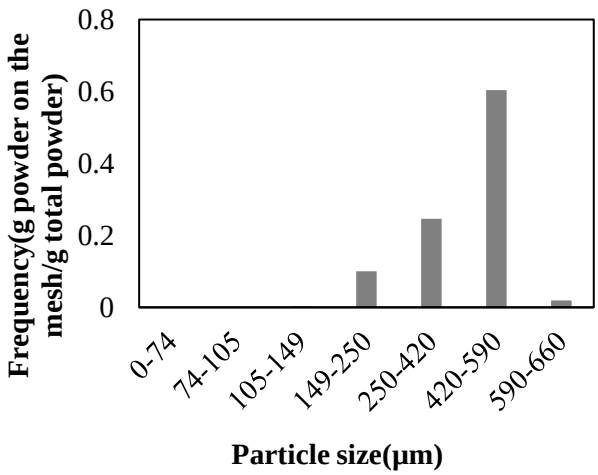

Figure 4.20 Frequency of particle size for dry milling powder using sieve measurement data

4.3.4 Thermogravimetric analysis (TGA) of dry-milled powder

To investigate the thermal stability of the particles and the degree of residual solvent in the Aero-Zero powder, the particles were analysed using TGA. For measuring the degree of residual solvent in the final powder after the drying process, the temperature was increased under air from 20 °C up to 200 °C at a heating rate of 10 °C/min, following which there was heating as an isotherm step for 15 min. Figure 4.21 shows weight change against temperature for Aero-Zero powder to gauge the residual solvent level. To perform this calculation, the following equation was used:

$$\text{Weight at 100\% - \% wt loss = \% residual solvent}$$

Using this equation, the residual solvent for the Aero-Zero particles using Figure 4.21-b, after 15 min, is calculated to be 0.45%. The low residual solvent emerged as having a high degree of porosity combined with large pore size in the particles, a characteristic that would facilitate the evaporation of the solvent from the inside and surface of the pores.

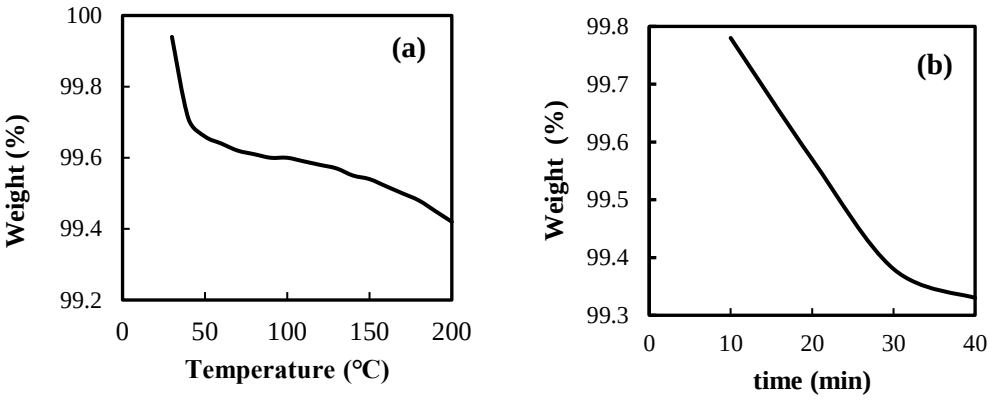

Figure 4.21 correlation of weight change against (a) temperature and (b) time for Aero-Zero powder

Figure 4.22 presents data on weight change and rate of weight change against temperature for Aero-Zero powder. It can be observed that, up to 420 °C, Aero-Zero is almost thermally stable and demonstrates no significant weight change. Thermal degradation can be observed to occur between 420 and 540 °C. Above this point (540-590 °C), the weight change increases at 2 %/°C. The degradation was ultimately complete at 670 °C.

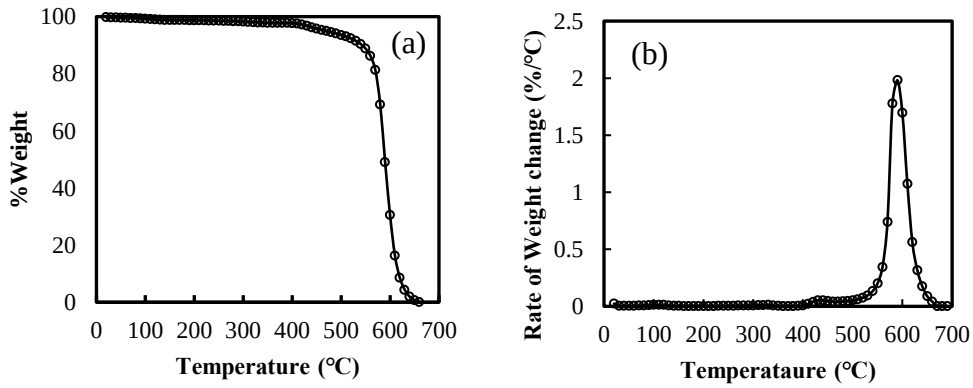

Figure 4.22, (a) weight changes and (b) rates of weight change as a function of temperature for Aero-Zero powder

4.3.5 Thermal conductivity of dry-milled powder

In order to perform measurement procedures for each type of powder, powder from several batches was mixed, following which the relevant measurement procedures were taken and then repeated twice more. The average value of the three measurements was taken to indicate the degree of thermal conductivity for each powder. The thermal conductivity of the Aero-Zero powder was measured using a hot-wire technique (see section 4.2.6). As was expected, the resultant figure was 36.5 mw/m.K, close to the value for the Aero-Zero stock shape from Blueshift (40 mw/m.K). Aero-Zero, with low-density small particle size, low thermal conductivity and high porosity, functioned as a reference point for the comparison of other types of powder with Aero-Zero.

Table 4.4 Property of Aero-Zero powder

Sample	Aero-zero powder
Surface area (m^2/g)[a]	10.7 ± 0.9
N_2 sorption, average pore width (nm) [a, e]	33.1 ± 0.6
Pore volume (cm^3/g) [a] STP	19.3 ± 2.2
Median pore diameter, (nm) [b]	7881.2
Average pore diameter, (nm) [b]	1404.4
Bulk density (g/cm^3)[b]	0.17
Skeletal density, (g/cm^3)[a]	1.5 ± 0.02
Porosity [b,d], (%)	89.00
MIP Porosity[b] , (%)	83.5
TGA (10%) (°C)	540
Onset point (°C)	564.5
Residual solvent (%) [f]	0.45 ± 0.01
Thermal conductivity (mW/m.K)	36.5 ± 0.9
Average particle size (μm) [c]	17.9 ± 8.4

a) average of three samples; b) single sample, measured with MIP; c) average of more than 500 particles. d) via $\Pi = 100 \times (\rho_s - \rho_b)/\rho_s$; e) single point at Vmax; f) at TGA test: 100% - % wt loss = % residual solvent.

4.4 Characterization results of the wet gel ground powder (PI-WGG)

4.4.1 N_2 sorption for PI-WGG powders

Like dry milled powder (Aero-Zero), gas adsorption was used to characterise the pore structure of the produced powders. Surface area, pore volume and pore size distribution were all measured using this technique. The average size of the pores was selected as the point marking the maximum level of adsorbed gas. Figure 4.23 shows the pore size distribution and N_2 sorption isotherm plots for PI-WGG powders at different ratios of DMSO: PAA. The desorption branch of the isotherms was used to calculate the Barrett-Joyner-Halenda (BJH) pore size distribution [316]. The size of the pores for these samples is in the range of 1.7−100 nm, indicating both mesoporosity and microporosity. The pore diameter distribution for PI-WGG powders in different ratios obtained from the Barrett – Joyner −Halenda (BJH) model is presented in Figure 4.23(a). A reduction in the adsorption of the gas by decreasing the dilution can be observed in the pore size distribution plots. The average pore size for all wet gel ground powders is reduced from 37.15 to 23.32 nm by increasing the dilution ratio. This could be due to the particle size reduction induced as a result of the dilution. The volume of N_2 adsorbed in the pores was found to increase with pore diameter starting at 3 nm, reaching a maximum of around 25 nm. Figure 4.23(b) shows that the adsorbed gas volume will increase by increasing the relative pressure. In addition, at low relative pressure, the amount of adsorbed gas is insignificant. These results confirm that macropores constitute a significant proportion of the observed porosity.

Furthermore, the hysteresis loops are apparent in all BET isotherm curves, demonstrating that mesopores exist in all cases. This loop also suggests gas condensation inside the pores at low-pressure ranges and that mono- and multi-layers are formed at higher pressure. The nitrogen adsorption isotherms for all ratios rise above $P/P_0 = 0.9$ but do not reach the saturation plateau, indicating that they are type II isotherms.

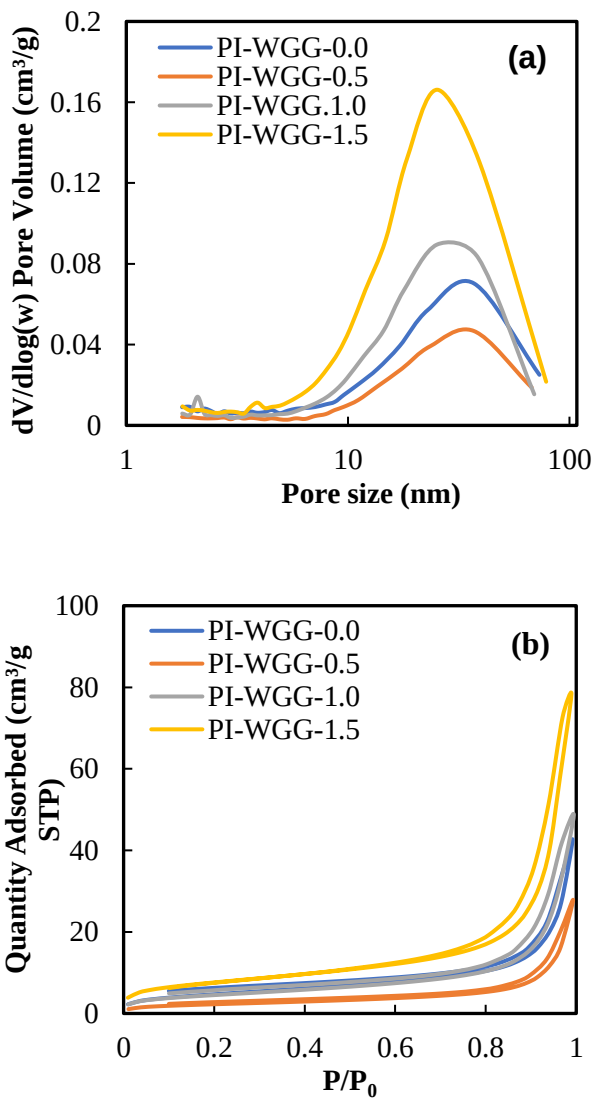

Figure 4.23. N_2 sorption for wet gel ground powder, (a) pore size distribution, (b) N_2 sorption isotherms (at -196 °C)

The BET surface area is in the range of 8.9 to 22.7 m^2/g for a different ratio of PI-WGG powders, indicating that the surface area of PI aerogels in this study is rather low, especially compared to that of PI aerogels discussed in the literature. The surface area for the PI aerogel microparticles made from the polyamic acid in 1-methyl-2-pyrrolidinone (NMP) solution and thermal imidization has been recorded as being as high as 103 m^2/g [66]. Gu *et al.* [164] synthesized PI aerogel microparticles by making the micrometre polyamic acid droplets in DMF, which were chemically imidized by pyridine and acetic anhydride using supercritical

drying. The surface area for these particles was 512 m^2/g. During ambient pressure drying, the surface tension between the solvent and pore walls results in shrinkage and reduces the surface area. Much of the existing research has used supercritical CO_2 instead of ambient pressure drying to minimise the collapse of pores [50].

4.4.2 Mercury Intrusion Porosimetry (MIP) for PI-WGG powders

The particles' total porosity, bulk density and pore size information for PI-WGG powders with different ratios of DMSO: PAA were characterized using MIP.

4.4.2.1 Pore structure

Similar to the dry milling method, the porosity of the particles was calculated using bulk and skeletal density. For each condition, MIP was used to test one sample.

Figure 4.24 presents the pore size distribution for the samples, showing pores in the range of 5 nm to 130 µm. A bimodal distribution can be observed for all the ratios, which belong to inter- and intra-porosity of the samples measured with MIP. In addition, this type of distribution shows that the PI-WGG powders are mostly mesopores and macropores. Unlike N_2 sorption, which demonstrates a reduction in gas adsorption by decreases in dilution, the MIP pore size distribution data show that the sample with a ratio of 1.5 has the lowest degree of adsorption. In the pore size bimodal distribution, the second peak, related to inter porosity, decreases with dilution increases. Smaller particles are made by increasing dilution, placing these closer to each other, and reducing the resultant porosity between the particles. In general, by increasing the ratio of dilution, the size of pores reduces, resulting in greater density and thermal conductivity. Similar to what was observed in gas adsorption results, the same behaviour is observed in the average pore sizes obtained from MIP. As for PI-WGG, by increasing the dilution from 0.0 to 1.5, the MIP average pore size changes from 1743 to 147 nm.

Furthermore, in terms of the results for PI-WGG-1.5, increasing the pressure to 300 Psia results in the volume of the pores filled with mercury becoming less than 1

cm^3/g (see Figure 4.24-b). The MIP pore size distribution for PI-WGG samples shows that, by increasing the dilution and, therefore, the presence of smaller particles, a shorter distribution peak appears, indicating a reduction in the volume of the pores.

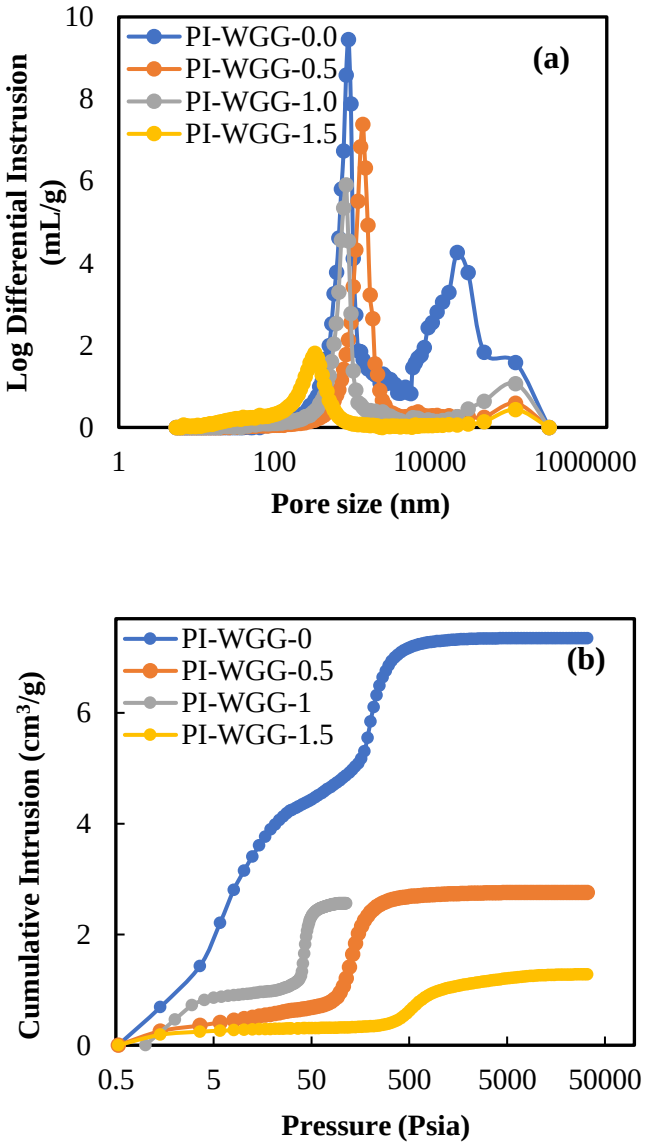

Figure 4.24. MIP (a) pore size distribution; (b) correlation of cumulative intrusion with pressure for PI-WGG

4.4.2.2 Density measurement with MIP for PI-WGG powders

The measured bulk density using MIP for each ratio is presented in Table 4.5. This value moves from 0.12 to 0.48 g/cm^3. By engaging in dilution in the process of synthesizing the powder using the PI-WGG method, the size of the particles reduces. When packed closer to each other, these smaller particles cause a reduction in porosity and an increase in density. Figure 4.25 shows the linear correlation of porosity with bulk density for all the PI-WGG powders. These data show a 30% reduction in the powders' porosity by increasing the DMSO ratio and the particles' density. The skeletal density, which was measured with a pycnometer in this research context, is the density of the solid part in each sample. Therefore, skeletal density will be reduced by increasing the dilution and reducing the solid concentration in the whole mixture. Figure 4.26 presents the correlation of the skeletal density in a different ratio.

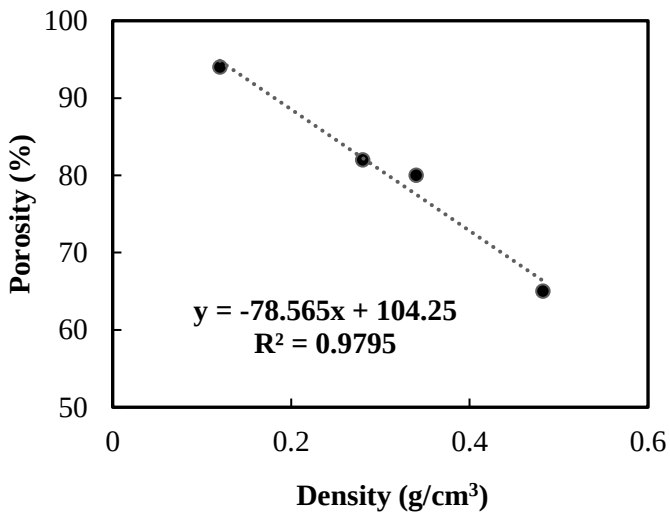

Figure 4.25. Correlation of porosity with density for wet gel ground powders

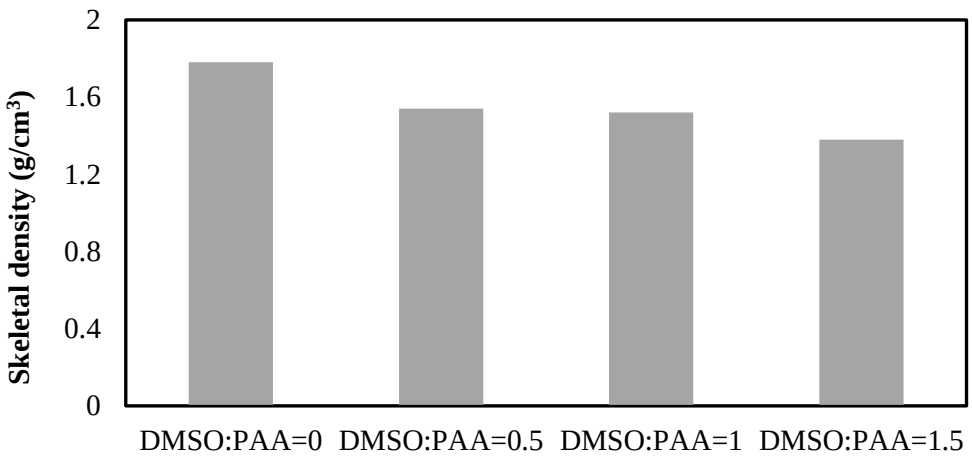

Figure 4.26. Correlation of skeletal density with the ratio of dilution for wet gel ground powders

4.4.3 Particle size measurement for PI-WGG powders

Image Pro used and analysed optical images to measure the particles' size. For each ratio, at least 500 particles were measured. The average particle size for all the ratios is presented in Table 4.5. As can also be observed in Figure 4.27, particle size was reduced by increasing the dilution of PI-WGG powders up to a ratio of 1.5. When DMSO was added to the PAA and left to age, there was less wet gel in the mixture, with a higher volume of DMSO. Therefore, during the process of blending at the same speed, the sample with the lower quantity of wet gel produced smaller particles.

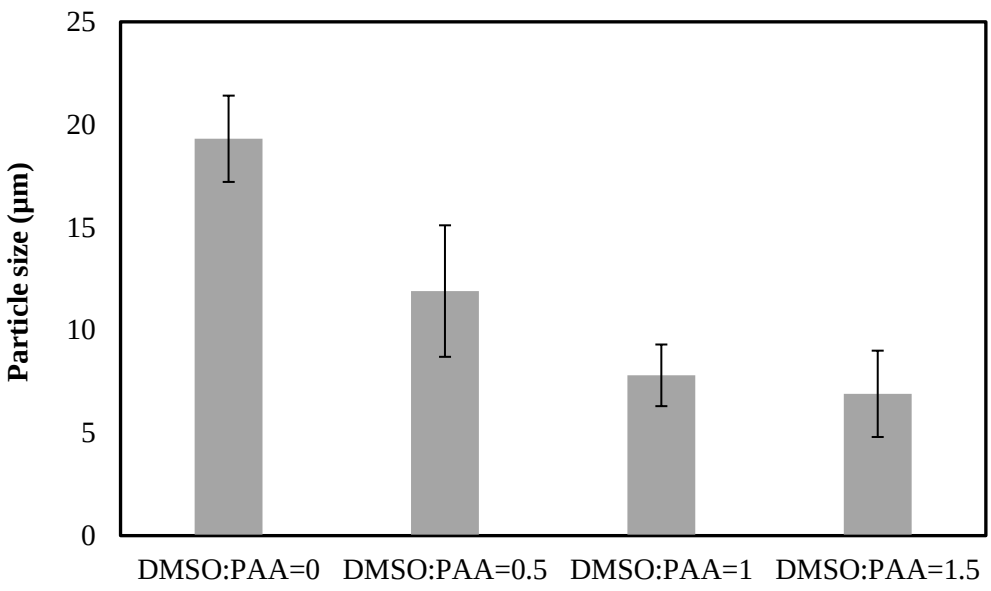

Figure 4.27. The particle size of the PI-WGG powders for the different ratios of dilution

Figure 4.28 shows the frequency of the particle size in each ratio. It can be observed that, for all ratios, a narrow distribution holds in the range of 3-20 µm. The SEM and optical images for each ratio in Figure 4.29 also show that the particles measured using the optical images in this work consist of different primary particles, which in turn connect to form larger agglomerates. Such agglomerations can form during blending, solvent exchange and drying [321].

The SEM image demonstrates that the particles' size increase as dilution increases. These images also demonstrate that dilution can change the morphology of the particles. On the other hand, the fibrillar network can be seen for the PI-WGG particles in a different ratio. This may be due to the gelation occurring in the 2-D layer before growing in the 3-D network within the particles.

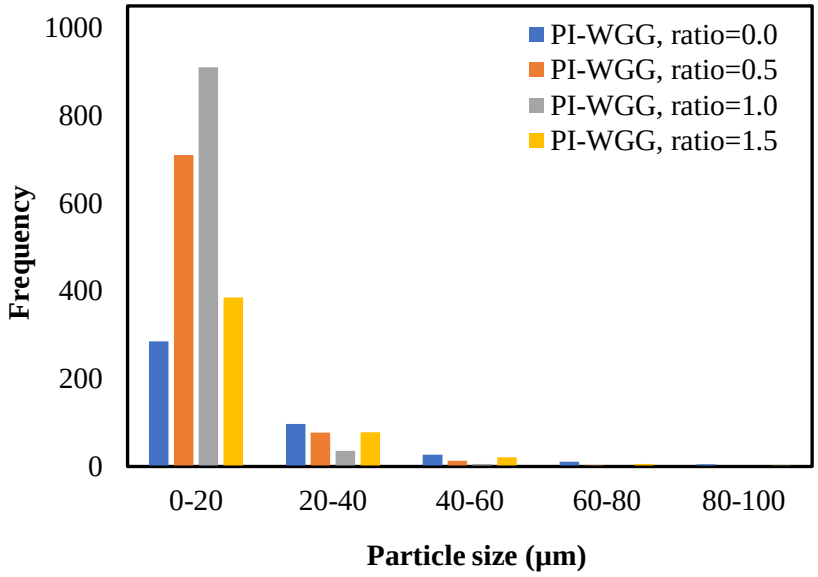

Figure 4.28. Particle size distribution for wet gel ground powder (produced using Image Pro)

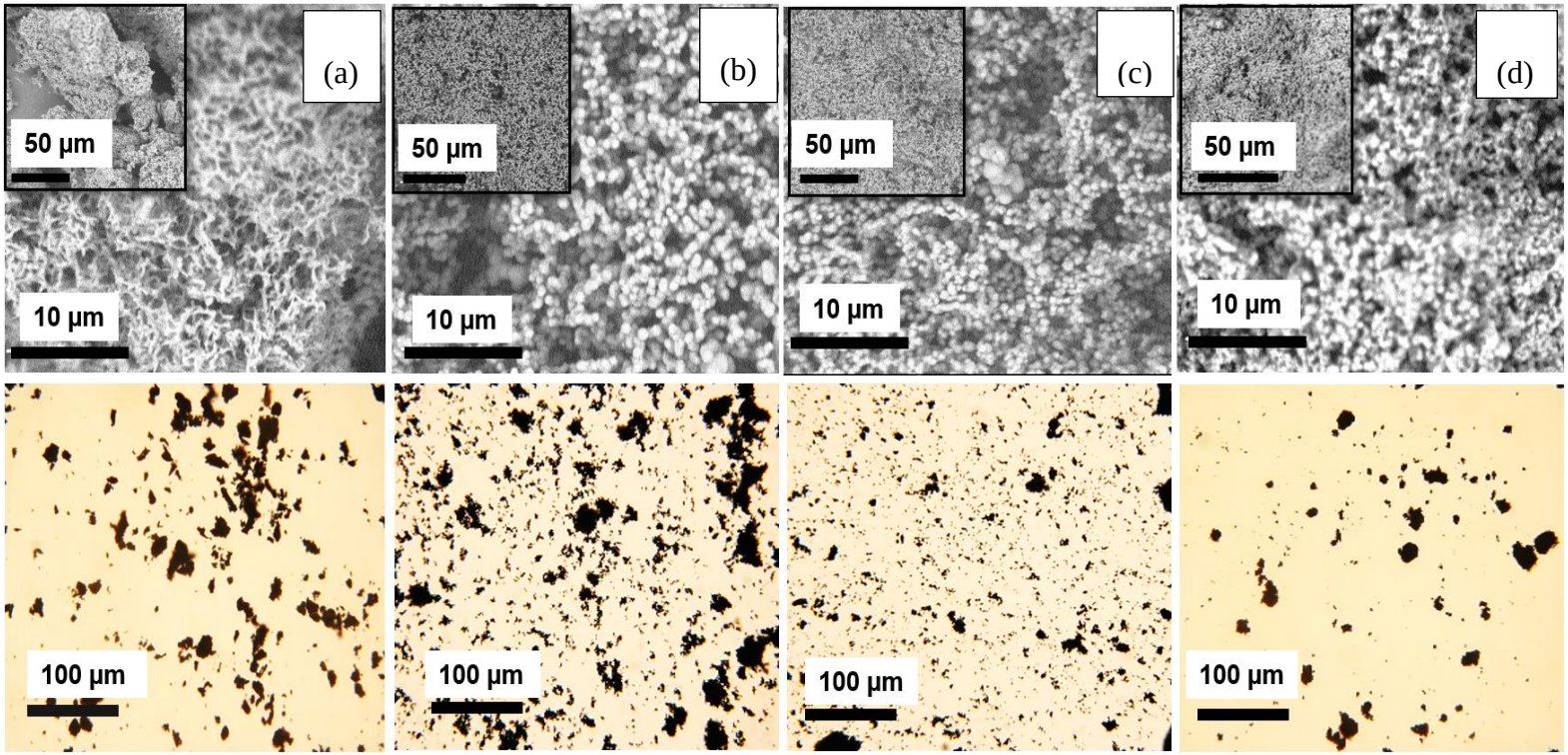

Figure 4.29. SEM and optical images for PI-WGG powders, a) DMSO:PAA=0,b) DMSO:PAA =0.5, c) DMSO:PAA=1, d) DMSO:PAA=1.5

4.4.4 Thermogravimetric analysis (TGA) of PI-WGG powders

TGA was used to measure the change in the weight of the produced powders at different ratios of dilation against temperature to gauge the thermal stability of the particles. For this purpose, each sample was placed in a clean aluminium pan and tested at a heating rate of 10 ℃/min from 20 to 700 ℃ under air. Figure 4.30 shows the produced results from this measurement. Figure 4.30-a shows that, for all the ratios (DMSO: PAA), the wet gel ground particles are thermally stable up to 430 ℃ before decomposing at 540 ℃, and at the end, are all degraded up to 700 ℃. Figure 4.30-b shows a reduction trend for the rate of weight change as the dilution ratio increases. As previously discussed, increasing the dilution ratio causes a reduction in the size of the pores and the total porosity of the wet gel ground particles, which in turn leads to greater thermal stability and, thus, a greater period necessary to ensure complete degradation. A higher ratio of DMSO also means that there is a higher volume of materials to decompose, taking more time and requiring a higher temperature. 10% decomposition temperature and onset temperature are plotted in Figure 4.31. Decreasing particle size increases surface area, leading to increased contact area with air and causing the drying process and oxidation reaction to occur more rapidly [322]. Therefore, the onset temperature is reduced by increasing the dilution ratio.

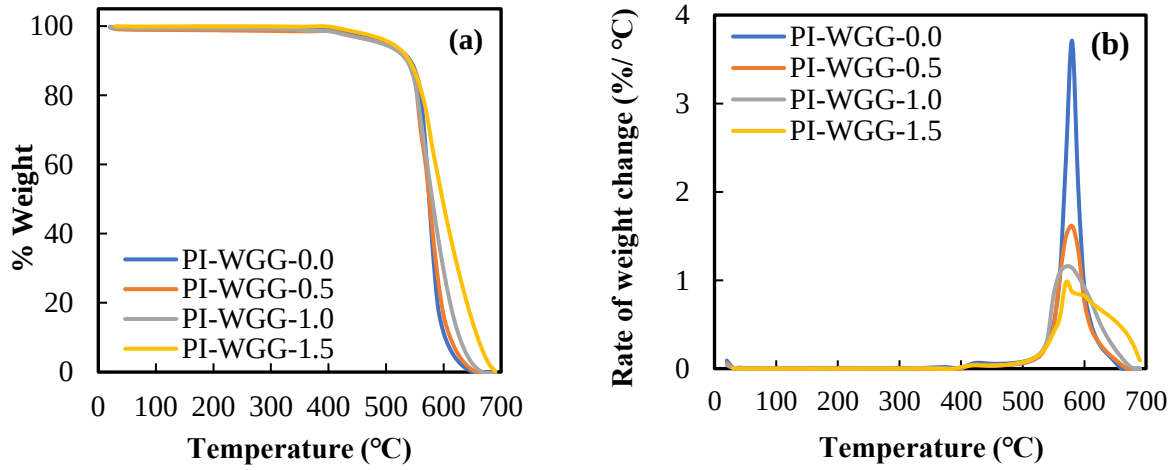

Figure 4.30. (a) weight, and (b) rates of weight change as a function of temperature for dry wet gel ground powder

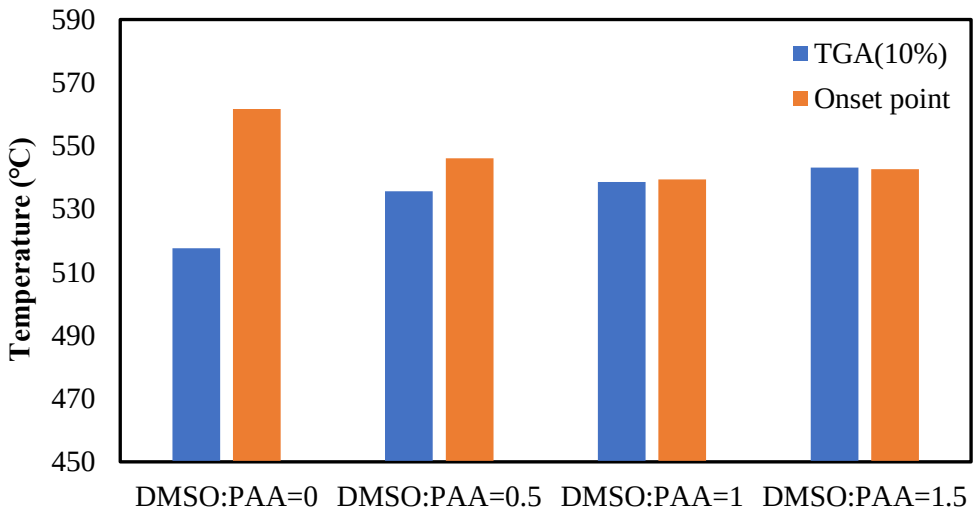

Figure 4.31. Onset temperature and temperature at 10% decomposition for PI-WGG powders at different ratios of dilution

Theoretically, reducing the particles' size will increase surface area, leading to greater surface contact with the air and increasing the rate of decomposition. As Figure 4.32 shows for these samples, increasing the DMSO ratio and reducing

porosity promotes denser solids, increasing the time required for complete decomposition.

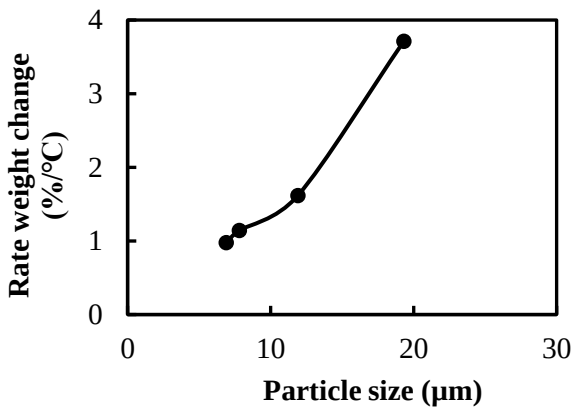

Figure 4.32. Correlation of the rate of weight change with particle size

4.4.5 Thermal conductivity for PI-WGG powders

The thermal conductivity of the wet gel ground powders at different ratios of DMSO: PAA was measured using the hot-wire technique. As discussed in Section 4.2.5, the powder was poured into the sample holder, and the sensor was positioned such that there was powder on either side. In order to fix the sample holder and prevent the movement of the sensor between the particles, a 500g weight was placed on top of the sample holder. A voltage of 0.8V and a measurement time of 10 seconds were set for use with the measurement. Thermal conductivity was measured by analysing an increase in the sample temperature as a result of heating using a thin hot wire, as mentioned above. Table 4.5 shows the thermal conductivity for different samples, which increases as particle density increases due to greater levels of DMSO: PAA in the PI-WGG powders. Figure 4.33 presents information on the correlation of thermal conductivity with density for these particles. As previously explained, smaller particles pack into each other more to increase density. In addition, in the high-density samples, a reduction in the degree of voids and accessible space results in heat transferring faster and thermal conductivity increasing. Figure 4.33-b shows the relationship between the particles' density, the PI-WGG particle size, and the PI-WGG powders' thermal conductivity.

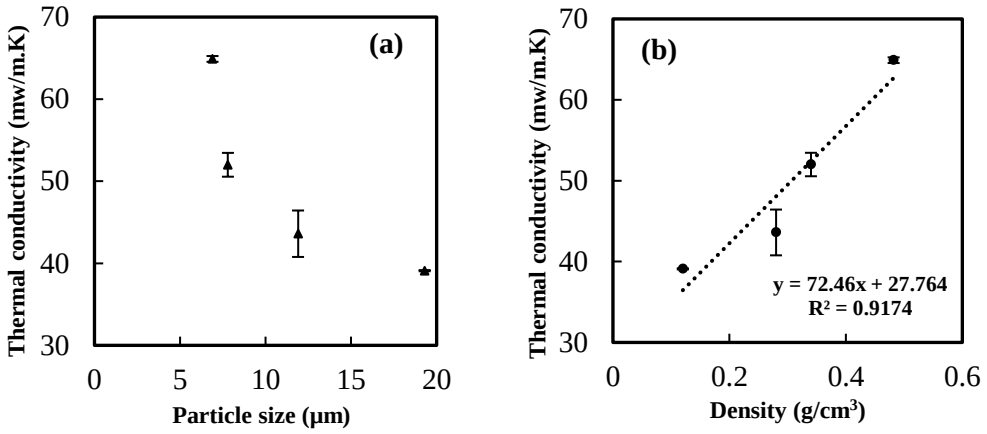

Figure 4.33 Correlation for thermal conductivity for PI-WGG powder with a) particle size and b) density

Table 4.5 Properties of PI-WGG powders

Sample: DMS`O (g)/ PAA (g)	BET surface area (m^2/g) [a]	MIP surface area (m^2/g) [b]	N_2 sorption, average pore size (nm) [a,e]	MIP median pore diameter (nm) [b]	MIP average pore diameter (nm) [b]	Bulk density (g/cm^3) [b]	Skeletal density (g/cm^3) [a]	Porosity (%)[b,d]	TGA (10%) (°C)	Onset point (°C)	Residual solvent (%) [f]	Thermal conductivity (W/m.K)[a]	Average particle size (µm) [c]
0.0	8.90 ± 0.98	9.02	37.15 ± 0.06	11693.30	1742.87	0.12	1.78 ± 0.003	94	517.60	561.7	0.59	0.039 ± 0.001	19.31
0.5	14.91 ±3.33	16.85	36.83 ± 0.33	1499.40	1222.28	0.28	1.54 ± 0.001	82	535.61	546.12	0.16	0.044 ± 0.003	11.90
1.0	16.42 ±0.12	17.54	24.75 ± 0.76	1001.78	755.58	0.29	1.52 ± 0.001	80	538.60	539.35	0.44	0.052 ± 0.002	7.80
1.5	22.70 ±1.34	34.65	23.32 ± 0.04	349.52	147.35	0.48	1.38 ± 0.003	65	543.10	542.64	0.57	0.064 ± 0.004	6.90

a) average of three samples; b) single sample; c) an average of more than 500 particles. d) via $\Pi = 100 \times (\rho_s - \rho_b)/\rho_s$; e) single point at Vmax; f) at TGA test: 100% - % wt loss = % residual solvent.

4.5 Characterization results of the PI-EM

Given the goal of establishing the optimum conditions for synthesizing the PI microparticles by emulsion, this section discusses the effects of parameters such as stirring speed, the concentration of the emulsifier, the volume of the mixture, solvent exchange, and the drying process. At the final approved condition, the particles were synthesised at different ratios of DMSO: PAA (0.0, 0.5, 1.0, 1.5). At all stages of the investigation, the produced PI aerogel microparticles were characterized in terms of N_2 sorption, MIP, SEM, particle size measurement, TGA and thermal conductivity. In the first step, the mixing speed was investigated for a small mixture volume.

4.5.1 Investigating the effect of stirring speed on a small scale

In order to examine the impact of stirring speed, a sample was produced in a small volume (40g PAA, 2.76 g 2-MI, 8.36 g BA, 80cm^3 cyclohexane, 1.52 g SPAN, 0.52 g Hypermer).

As explained in Section 4.1.6, to produce the sample by means of an emulsion process, PAA was mixed with 2-MI and BA in a baker in two separate additions continuously. This mixture was added to the cyclohexane, which was mixed using the overhead stirrer with an emulsifier at 300, 400 and 500 rpm for 1 h. The resultant particles were washed with acetone three times every 30 min and dried at room temperature for 24 h. They were then stored in a plastic bag for characterisation.

4.5.1.1 N_2 sorption for emulsion particles at different stirring speeds

Gas adsorption was used to investigate the particles' surface area and pore size distribution. Figure 4.34-a shows the pore size distribution and N_2 sorption isotherms at -196 °C. The pores are shown to be 2-80 nm, indicating the meso- and macroporous structure for all the samples. The N_2 isotherm in Figure 4.34-b shows the type II isotherms for all the ratios, meanwhile, it shows that the surface area for 500 rpm is higher, possibly due to the presence of smaller particles as compared

with other stirring speeds. For all speeds, the pores are meso- and macropores. The sharp increment in the adsorbed gas volume at P/P_0=0.9 confirms that macropososity constitutes the bulk of the pores in these samples.

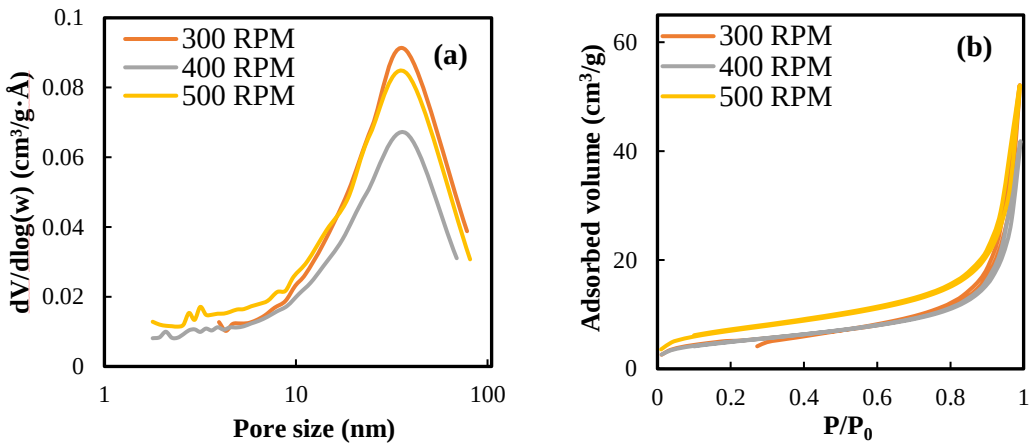

Figure 4.34. N_2 sorption for PI aerogel synthesised using an emulsion-based method at different stirring speeds, a) pore size distribution, b) N_2 sorption isotherm at -196 °C.

4.5.1.2 SEM with emulsion particles with different stirring speeds

The microstructure of the particles synthesised using the emulsion method at the three different stirring speeds of 300, 400 and 500 rpm are shown in the SEM image in Figure 4.35. Micro-spherical particles with solid surfaces can be observed. From these images, it can be seen that smaller particles can be fabricated by increasing the speed of stirring during the emulsion process, although this also results in an increase in agglomeration.

The type of mixing and stirring speed can affect particle size distribution, growth and degree of agglomeration, and nucleation. More specifically, a moderate stirring speed for each process can improve the mixing process and create a more uniform environment. For example, Hussain *et al.* [323] report that, in their study, the size of chitosan nanoparticles reduced gradually from 543 ± 32 nm to 167 ± 18 nm when the stirring speed was increased from 200 rpm to 700 rpm. But in the next increment, stirred using speeds of between 800 and 1000 rpm, the average particle

size increased from 432 ± 34 nm to 712 ± 42 nm. These results concord with those in other published studies [324].

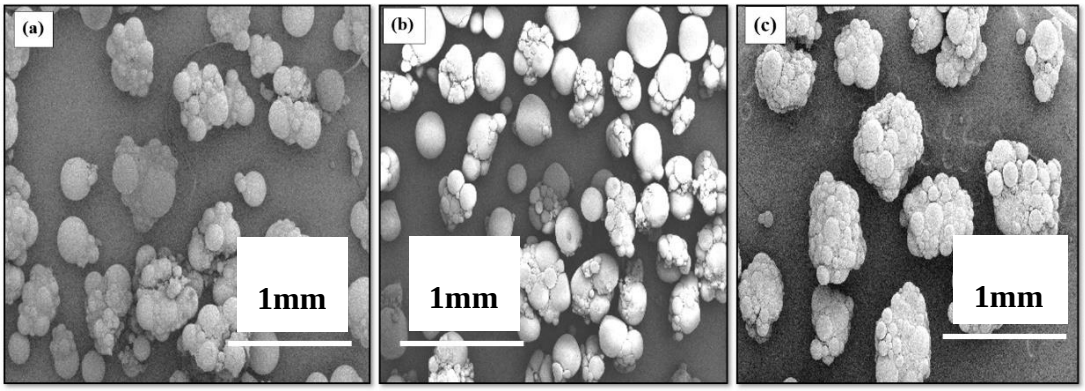

Figure 4.35 SEM images for PI-EM with different stirring speeds in small scale (a) 300 rpm, (b) 400 rpm, (c) 500 rpm

The bulk density of the powders was measured at different stirring speeds using mercury intrusion porosimetry. Unfortunately, the MIP equipment that was to be used for this research could not be run at high pressure, meaning that the porosity and pore size distribution of the samples could not be measured in this way. The size of the particles was measured using microscopic images viewed within Image Pro. As expected from the SEM images, increasing the stirring speed resulted in an increase in the size of the particles detected using the optical microscope due to a greater degree of agglomeration. The different properties of the particles produced using different stirring speeds are presented in Table 4.6.

The ultimate result of this investigation was that 300 rpm was selected as the optimal speed for stirring during the emulsion process, giving rise to lowest degree of agglomeration, the smallest particles and the lowest density.

Table 4.6 properties for PI-EM at different stirring speeds (small scale)

Emulsion powder	MIP bulk density (g/cm^3)	Average particle size (µm)	Specific surface area (m^2/g)	Average pore size for N_2 sorption (nm)
300 rpm	0.20	86.0	17.6	11.7
400 rpm	0.30	134.0	17.1	9.7
500 rpm	0.27	150.0	23.6	10.2

4.5.2 Investigation of the dilution process on particle size during the emulsion process

The size of a powder's particles is an important parameter with the potential to significantly affects its properties and applications, including density, porosity and thermal conductivity. As discussed above, dilution with DMSO can change particles' size by modulating the repulsive and attractive force between these. For the small quantity of resin prepared for this study (40 g), an emulsion process with the following conditions was used to produce the particles in different dilution ratios:

- PAA (40 g), 2-MI (2.76 g), BA (8.36 g), 80cm^3 cyclohexane, SPAN (1.52 g) and Hypermer (0.52 g)
- Dilution of the mixture by adding DMSO to the PAA before adding BA and 2-MI, with DMSO (g)/PAA (g) ratio: 0.0, 0.5, 1.0 and 1.5
- Mixing of all the chemicals using an overhead stirrer at 300 rpm for 1 h
- Exchanging the solvent with acetone before drying at room temperature for 24 h

The following sections discuss the characterisation results for the produced particles in terms of N_2 sorption, particle size measurement and TGA.

4.5.2.1 N_2 sorption for PI-EM at small volumes with different ratios of dilution

The N_2 sorption results are presented in Figure 4.36, in which the pore size distribution plot shows the meso- and macropores structure for all the ratios. The average pore size is in the range of 32-37 nm. The N_2 sorption isotherm (Figure 4.36-b) shows that the volume of the adsorbed gas is reduced as the dilution ratio is increased. It can also be observed that ratios 1 and 1.5 react in the manner of non-porous material as a result of their pores being too large to be detected using the N_2 sorption technique. Or as another explanation, it can be assumed that all the solvents cannot be removed by adding more DMSO and using only room temperature drying for the sample; therefore, it can be assumed that the pores have been filled with DMSO. Unfortunately, the malfunction of the MIP equipment meant that it was impossible to pinpoint the exact reason for this observation. Other methods were therefore used for characterization.

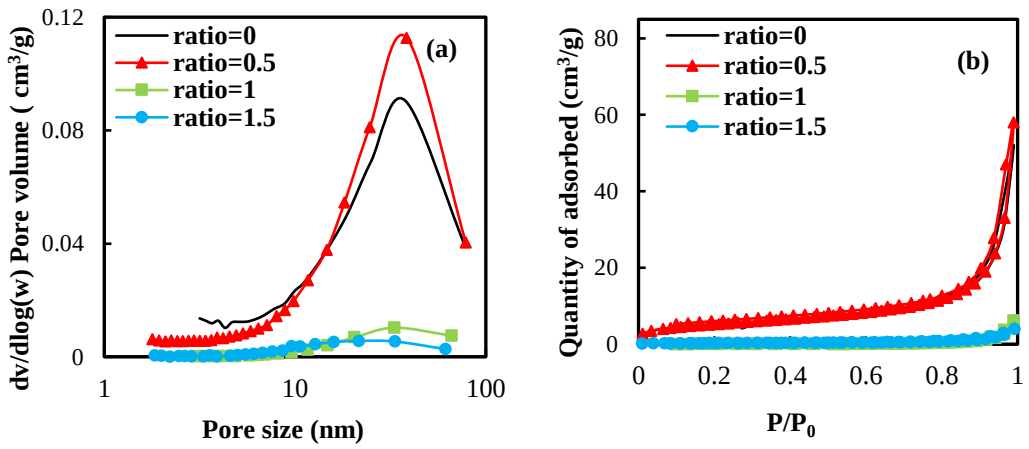

Figure 4.36. a) pore size distribution, (b) N_2 sorption isotherms (at -196 °C) for emulsion at different ratios of DMSO:PAA

4.5.2.2 Particle size measurement

Figure 4.37 shows the optical microscopic images of the particles in different ratios of DMSO. The images demonstrate the particles' size reduction as the dilution ratio increases. These images were used to analyse the size of the particles using Image Pro, and the particle size frequency for the different ratios is plotted in Figure 4.38. Apart from DMSO: PAA=0, for all the ratios, a narrow, right-skewed distribution is observed in which most of the particles are in the range of 40-80 µm. For ratio 0, the sample without dilution, a broad particle size distribution with a maximum range of 180-200 µm is observed. For the powder with a ratio of 1.5, the particles exist in the range of 100-120 µm, which confirms that the smallest particles are shaped for this ratio. Reducing the ratio of DMSO makes it possible to observe a greater distribution with larger particles.

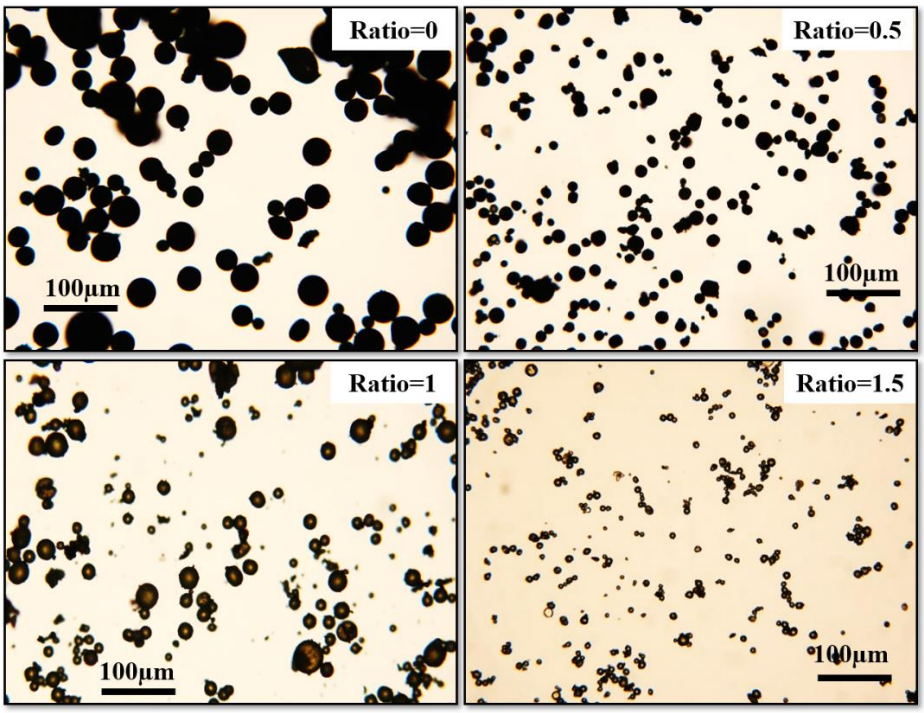

Figure 4.37. Optical microscopic image for the PI-EM with different DMSO ratios on a small scale

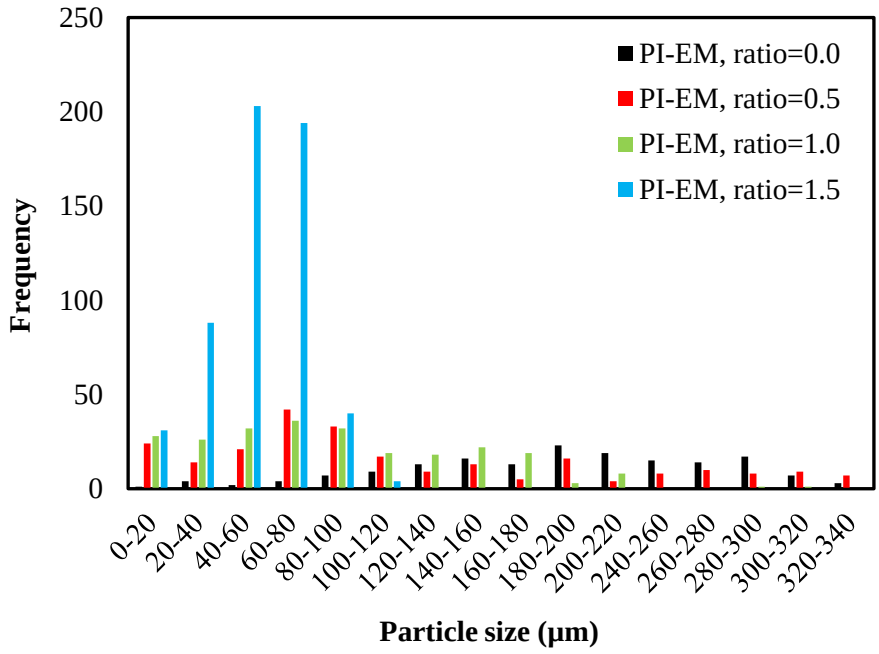

Figure 4.38. Frequency of particle size for PI-EMs at different ratio of DMSO:PAA at small scale

4.5.2.3 Thermogravimetric analysis (TGA) for PI-EM at different dilution ratios and small scale

TGA was used to investigate the thermal stability of the produced particles by means of the emulsion method, with different dilution ratios being used on a small scale. Figure 4.39-a plots the change in weight against temperature. A significant weight loss can be observed before 200 ℃ due to the presence of DMSO inside the particles. Increasing the DMSO ratio increases weight loss in the first part of the plot (0-200 ℃). The reason for this is that a greater volume of DMSO in the sample makes it difficult for this to be removed using the traditional solvent exchange and drying process. In the second part of the plot (200-420 ℃), the particles are thermally stable up to 420 ℃. In the final part, the particles are decomposed up to 700 ℃. Figure 4.39-b shows that the decomposition rate is reduced by increasing the ratio of DMSO, potentially due to the presence of smaller particles packed closer to each other and therefore increasing the density.

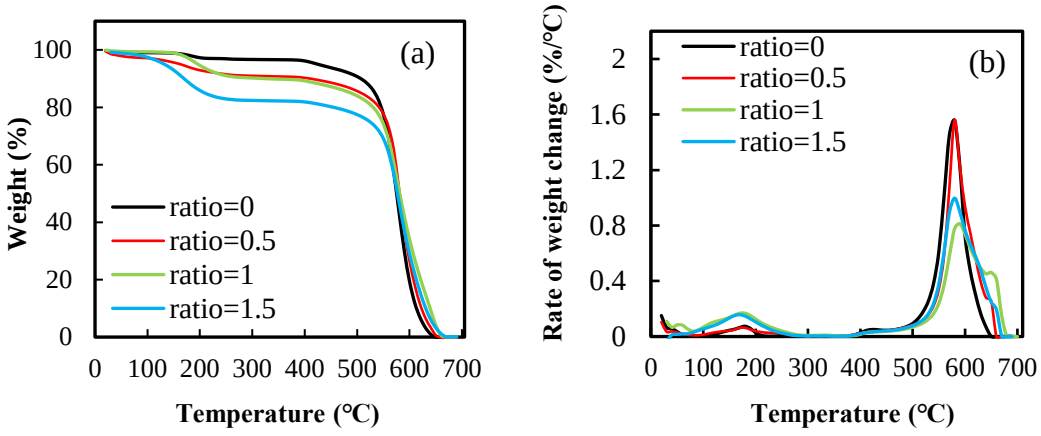

Figure 4.39. a) weight changes and (b) rates of weight change as a function of temperature for PI-EM with different DMSO ratios on a small scale

Given that the target of making it possible for Blueshift to synthesize PI aerogel particles with an average particle size of around 10 µm, ratio 1.5, which was observed to give rise to the smallest particles, was selected as the reference for investigating and optimising other factors such as the solvent exchange and drying processes.

4.5.3 Investigation into solvent exchange and drying

Adding an acetone solvent to PAA is an important part of causing such PAA solutions to swell. If this is done, then the acetone will start swelling into the PAA solution, enlarging the PAA chain volume in a way that results in the final porous structure of the PI aerogel [112].

As previously explained, the process of exchanging the solvent and drying the particles during emulsion is the same as that used with wet gel ground particles (3 washes every 30 min with 24 h of drying at room temperature). Given the N_2 sorption and TGA results, it was clear that dilution would mean that DMSO could not be removed by means of solvent exchange and drying in the traditional manner. Alternative solvent exchange methods were therefore used, as detailed in the

ensuing sections. The produced particles were also characterised using TGA to measure the residual solvent.

As a means of engaging in an alternative solvent exchange and drying process, two washes were added to the method that had been previously used. This involved the addition of two new samples, produced using the emulsion method, with a 1.5 and 300 rpm stirring speed ratio. The solvent exchange process for these samples was conducted as follows:

1- The first sample was washed with acetone three times every 20 min and then one more was for 45 min.

2- The second sample was washed three times with acetone every 20 mins, followed by two more washes every 45 mins

At the end of the solvent exchange, the degree of residual solvent was determined by testing with TGA with a ramp of 10 ℃/min. The TGA was run under the following condition: Temperature was changed from 20 to 200 ℃, and then isotherm for 15 min at 200 ℃. Figure 4.40 shows that significant weight loss occurred for the sample subject to four washes, indicating the continued presence of a large volume of DMSO inside the sample. In terms of the sample subject to five washes, a considerable reduction can be observed regarding the level of residual solvent. Using the equation given in Section 4.3.4, the figures indicating % of residual solvent for the four- and five-wash samples are 27.75 and 12.13, respectively.

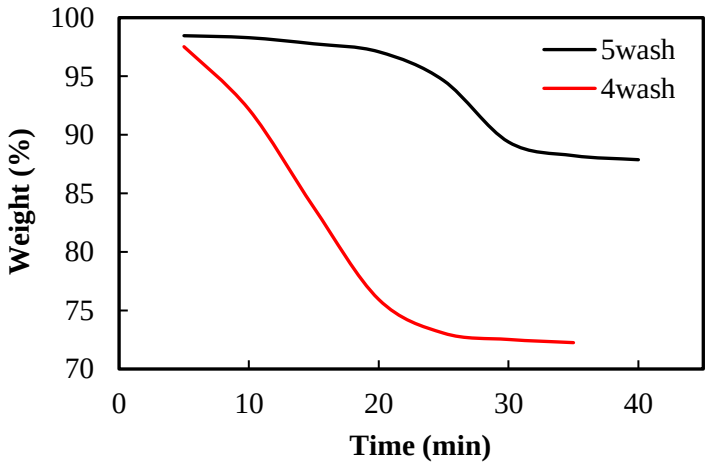

Figure 4.40. Correlation of weight change with time for samples subject to different washings (5washes: 3 washes every 20 min, two extra washed every 45 min; 4 washes: 3 washes every 20 min followed by one more wash for 45 min)

In the next step, two different drying methods were added to the sample subject to five washes. Stepwise drying was used to remove the solvent from the particles. This was also done considering that a rapid increase in temperature would lead to fast evaporation in a way that would affect the formation of a linking structure. This method was therefore chosen as a means of controlling the drying process by increasing the temperature slowly. By slowly evaporating the solvent, the structure of the pores could be preserved [112]. In order to remove the acetone from the pores, two different cycles were used with the particles: i) 1 h at room temperature and then 8 h at 50 ℃ (condition 1); and ii) 1 h at room temperature and then overnight (18-24h) at 50 ℃ (condition 2). The TGA was used in order to measure the % of residual solvent. Figure 4.41 shows the weight loss change at different temperatures for these two drying processes. The plot indicates that increasing the time in order to be removed the acetone did not have any effect. This is likely to be because acetone can remove from pores very quickly, meaning that any additional time gives rise to no further change.

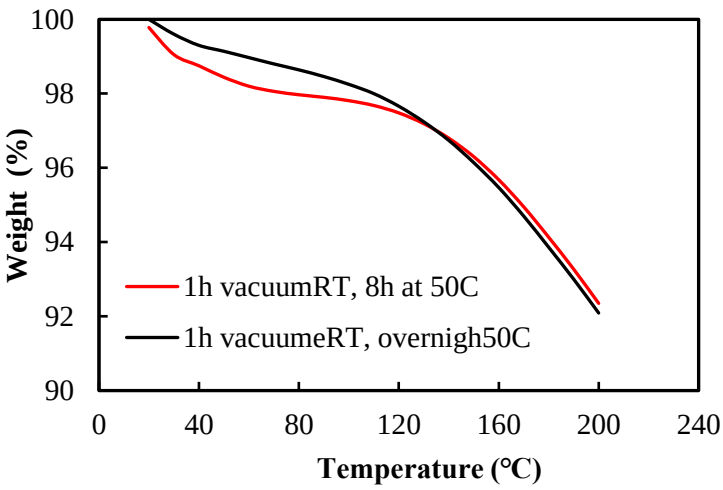

Figure 4.41. Correlation of weight change with temperature regarding removing the acetone using different drying processes

Regarding the next drying step, removing the residual DMSO in the particles necessitated heating to 200 °C to reach the boiling point for DMSO (189 °C). This was done for 15 and 30 min. The figures reflecting the degree of residual solvents in respect of the samples is presented in Table 4.7.

Table 4.7 Different stages of drying conditions

Sample	Condition 1	Condition 2	Condition 3	Condition 4	Condition 5	Condition 6	Condition 7
Total residual solvent (%)[a]	7.33	7.81	1.30	0.92 ± 0.11	0.83 ± 0.15	0.80 ± 0.04	0.8 ± 0.02

Condition 1: 3 washes every 20 min with acetone, followed by 2 more washes every 45 min; dried under vacuum at 23 °C/45min, 50 °C/ 8h.

Condition 2: 3 washes every 20 min with acetone, followed by 2 more washes every 45 min; dried under vacuum at 23 °C/45min, 50 °C/ 18hs.

Condition 3: 3 washes every 20 min with acetone, followed by 2 more washes every 45 min ; dried under vacuum at 23 °C/45min, 50 °C/ 2h, 200°C/15min.

Condition 4: 3 washes every 20 min with acetone, followed by 2 more washes every 45 min ; dried under vacuum at 23 °C/45min, 50 °C/ 18hs, 200°C/15min.

Condition 5: 3 washes every 20 min with acetone, followed by 2 more washes every 45 min; dried under vacuum at 23 °C/45min, 50 °C/ 2h, 200°C/ 30min.

Condition 6: 3 washes every 20 min with acetone, followed by 2 more washes every 45 min; dried under vacuum at 23 °C/45min, 50 °C/ 18hs, 200°C/ 30min.

Condition 7: 3 washes every 20 min with acetone, followed by 2 more washes every 45 min; dried under: vacuum at 23 °C/45min, 50 °C/ 2h , 200°C/ 30min.

TGA test: 100% - % wt loss = % residual solvent

The results indicate that 30 min of drying at 200 °C removed the residual solvent. Following this, the final drying method chosen for the emulsion process was: 45 min at room temperature, 2 h at 50 °C and 30 min at 200 °C. For this selected solvent exchange and drying condition, the value of the residual solvent was % 0.86 ± 0.04. The addition of more washes and time during the final stage of drying did not have any effect on the final residual solvent. Considering the Blueshift target for residual solvent of 0.5%, this was the shortest method yielding an acceptable amount of residual solvent. The next section details the process of scaling up the method to produce a higher volume of powders for characterising thermal conductivity and producing the stock shape.

4.5.4 Scaling up the emulsion process

The next step involved scaling up the emulsion synthesis process to produce 250 g of PAA resin (from 40 g). When the volume of solution is increased, the stirring speed should also be increased to ensure that this process is conducted uniformly. Two different stirring speeds, 300 and 500 rpm, were used to mix the new solution and the resultant powders were characterized to identify the optimum speed. For the emulsion process, 250 g PAA was mixed with DMSO to produce the dilution in a specific ratio. 2-MI and BA were added as a catalyst and a dehydrating agent to one beaker and mixed for 6 min. This mixture was added to the 500 cm^3 of cyclohexane, which was mixed with SPAN and Hypermer at 300 and 500 rpm in another beaker. The whole mixture was mixed for 1 h. The formulation for synthesizing the PAA and the emulsion particle for a large volume are presented in Table 4.1and Table 4.3, respectively.

After the mixture was stirred at two different speeds, the solvent exchange was subject to five washes (3 times every 20 min and twice every 45 min). Finally, the powder was spread on a tray and dried for 45 min at room temperature, followed by 2 h at 50 °C and 30 min at 200 °C. The resultant particles were stored in a plastic bag until characterisation time. Figure 4.42 details the experiment used to identify the appropriate stirring speed in a large volume.

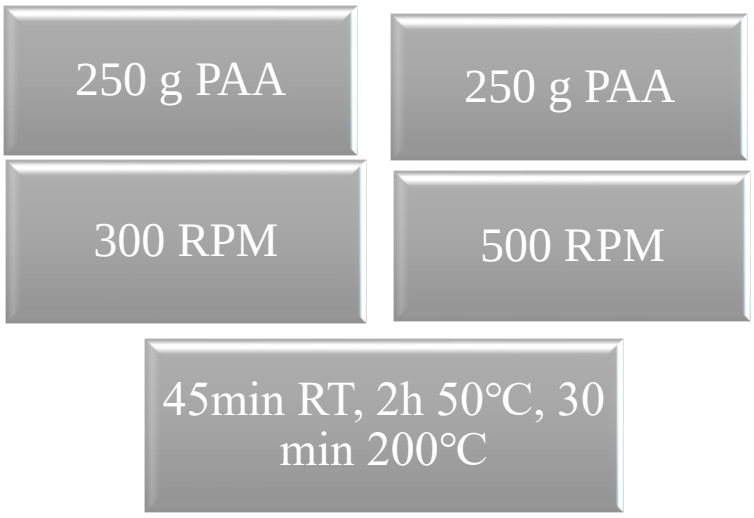

Figure 4.42. Stirring speed experiments used for scaling up the emulsion process

4.5.5 Characterization of the PI-EM particles at large scale

4.5.5.1 N_2 sorption

The particles with 300 and 500 rpm stirring speeds were characterized by N_2 sorption to measure their surface area and pore structure. Figure 4.43-a shows the pore size distribution for the sample stirred at 500 rpm. The pores are shown to have been in the range of 2 to 80 nm, with an average pore size for this sample at the maximum volume of the adsorbed gas being 25 nm. No distribution can be observed for the sample that was mixed at 300 rpm, potentially because of the presence of large pores that cannot be detected using the gas adsorption technique. Figure 4.43-b shows the N_2 isotherm for these samples. Meso- and macroporosity can be observed for the 500 rpm sample. This loop also suggests that gas condensed inside the pores at low-pressure ranges, forming mono and multilayers at higher pressure. The nitrogen adsorption isotherms for the 500 rpm sample are shown to have risen above $P/P_0 = 0.9$ but without reaching the saturation plateau, indicating their status as type II isotherms. As for the sample mixed at 300 rpm, no adsorbed gas can be seen for this case. Possible reasons for this observation were judged to include a non-porous structure or, alternatively, the presence of huge pores, neither of which the employed technique could detect. In order to find the exact cause, MIP was

therefore used. The results of the MIP characterisation are presented in the next section.

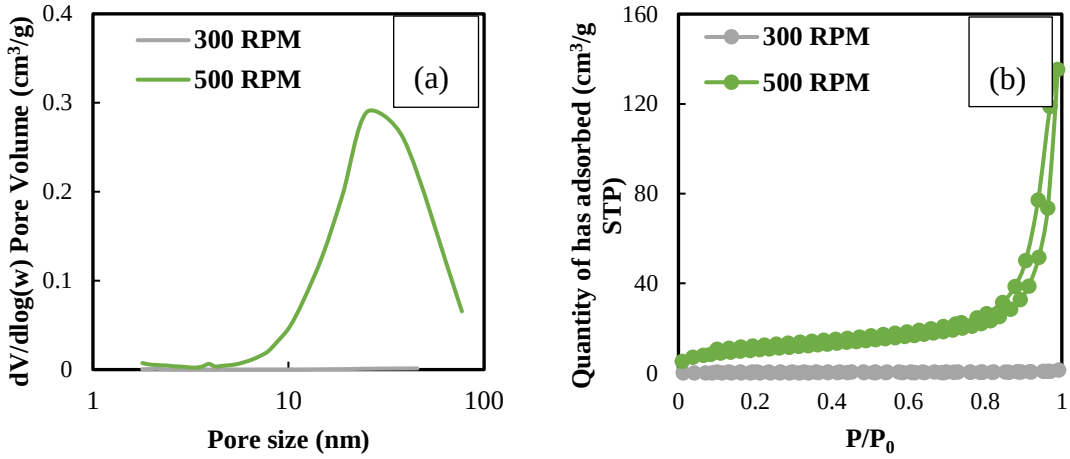

Figure 4.43 N_2 sorption for the PI-EM at 300 and 500 rpm at a large volume, (a) pore size distribution, (b) N_2 sorption isotherms (at -196 °C)

4.5.5.2 Mercury intrusion porosimetry (MIP)

To measure bulk density, porosity and pore size distribution, the samples produced at mixing speeds of 300 and 500 rpm were characterized using MIP, as detailed above. The pore size distribution is presented in Figure 4.44, confirming that, for the 300 rpm sample, the pores start at 1 µm. Only large pores were observed as being present in this sample, mostly inter porosity. For the sample produced at 500 rpm, a bimodal distribution was recorded, with pores in the range of 1 nm up to 345 µm. Both inter and intra porosity were observed for this sample, and the total porosity was 84%. The measured density for the 300 rpm sample was 0.62 g/cm^3, which is 61% higher than that of the 500 rpm sample. The particles of higher density and lower porosity were shaped at a lower speed on this larger scale.

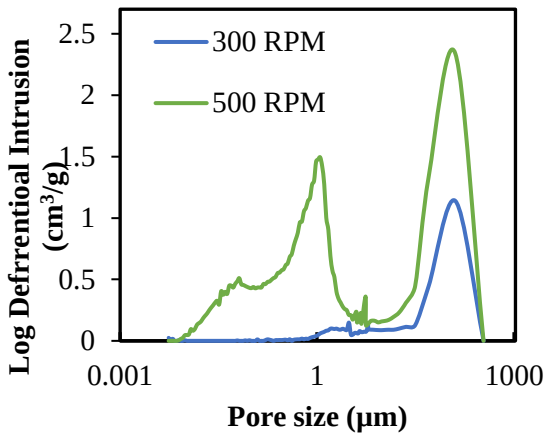

Figure 4.44 Pore size distribution for PI-EMs at a large scale

4.5.5.3 Particle size measurement

Given the shape and size of the particles observed using the SEM and optical microscope, it can be seen the shape and size of the particles are different in the samples produced at stirring rates of 300 and 500 rpm. The SEM images presented in Figure 4.45 show that the particles within the former sample 300RPM had a spherical shape with small pores in the surfaces. These particles also appear larger. In respect of the 500 rpm particles, a porous structure can be observed. These particles are also much smaller and are mostly agglomerate with each other. The microscopic images were examined using Image Pro to calculate the size of the particles, which are presented in Table 4.8. As predicted from the SEM image, the size of the particles produced at 300 rpm is 92% larger than those produced at 500 rpm.

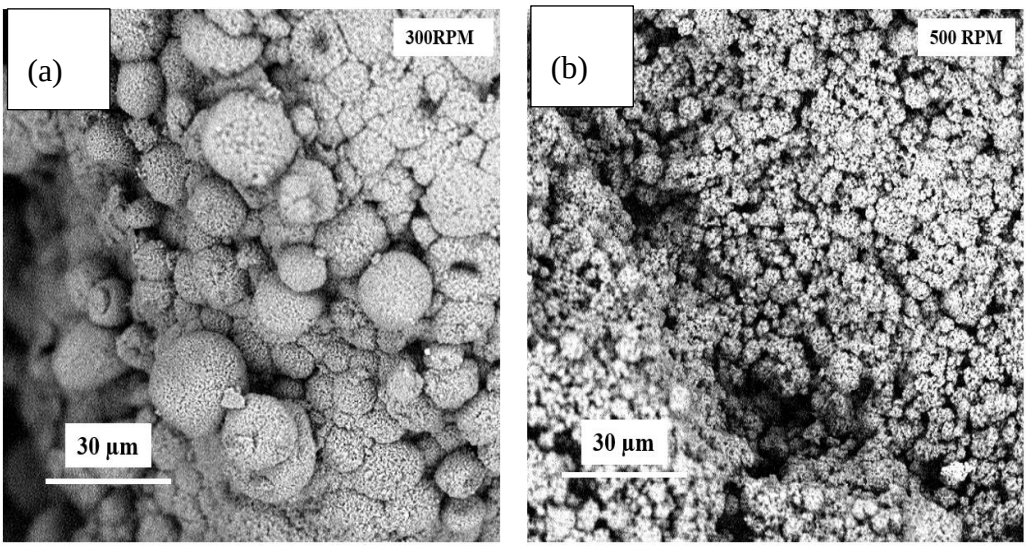

Figure 4.45 SEM micrographs for PI-emulsion particles at stirring speed; a)300 rpm, b)500 rpm

4.5.5.4 Thermogravimetric analysis

Measuring the thermal stability of the samples produced at 300 and 500 rpm was done in terms of analysis with TGA. The powders were heated at a rate of 10 °C/min from 20 to 700 °C under air. The weight change is presented in Figure 4.46. Both samples are recorded as being thermally stable up to 400 °C, after which there was degradation, with the 500 rpm sample being observed to degrade at a higher rate than the 300 rpm sample. As discussed previously, the smaller particles were observed as having a greater surface area, leading to more opportunities for particles to come into contact with air and thus increasing the combustion rate. Furthermore, while the 500 rpm sample degraded before 700 °C, the correlation of weight change with temperature for the 300 rpm sample shows that this temperature was insufficient to ensure complete degradation. This necessitated that a longer time or higher temperature procedure be used with this sample.

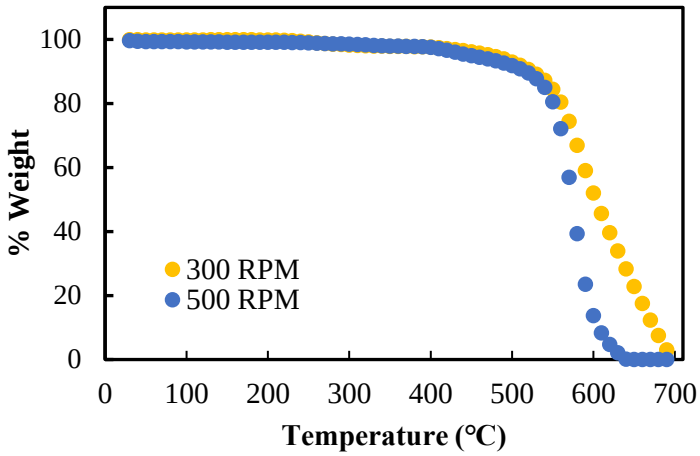

Figure 4.46. Correlation of weight change with temperature during the emulsion process for large scale production

Given the characterization results achieved for the emulsion particles at 300 and 500 rpm stirring speeds, 500 rpm was selected for producing the particles by means of the emulsion process at high volume. Such particles were predicted to have low density, high porosity and thermal stability and to be of small size.

Table 4.8. Properties of the PI-EMs on a large scale

Sample	**Skeletal density (ρ_s) (g/cm^3)[a]**	**Bulk density (ρ_b) (g/cm^3)[b]**	**Porosity (%)[c]**	**TGA (10%) (°C)[d]**	**Particle size (µm)[e]**	**Specific surface area (m^2/g)[f]**	**N_2 sorption average pore size (nm)[f]**
300 rpm	1.43 ± 0.007	0.62	56.9	520	226.8	0.5	9.6
500 rpm	1.53 ± 0.016	0.24	84.0	515	16.3	36.9	10.2

a)an average of three samples produced using a pycnometer; b) a single sample measured using MIP; c) via 100 × [1 - (ρb / ρs)]; d) single measurement taken using TGA in the air; e) an average of more than 500 particles analysed from optical images in Image Pro; f) calculating an average from different pore sizes.

4.5.6 Assessment of mixing time

After finalising matters relating to the concentration and ratio of the chemicals, the stirring speed, the solvent exchange and the drying process, mixing time was then considered for optimization in terms of the degree of imidization and the properties of the final product. Imidization can be completed by means of a chemical reaction or a thermal reaction. Chemical imidization was selected as the method to use. Following the addition of 2-MI and BA as catalysts and a dehydrating agent to the PAA, imidization began. It was important that enough time was allowed so that the maximum degree of imidization could occur. The mixing process also had to be conducted to last enough time for this purpose, involving mixing PAA and catalysts with cyclohexane and emulsifiers. 1, 2 and 24 h were the time periods selected for mixing. Different characterization methods were used for each mixing time to determine the optimum conditions. The properties of the resultant particles in terms of these three mixing times are presented in Table 4.9.

These results show that, for the sample produced using 24 h of mixing, the density involved a 62% increase compared to 1 h of mixing. The particle size of 11.8 μm was yielded as the average particle size for the sample produced using 24 h of mixing, being 27% lower than that obtained for the same produced using 1 h of mixing. However, the SEM image in Figure 4.47 confirms that the 1 h mixing sample had smaller particles, the black circle in Figure 4.47-a highlighting the specific particle that was measured. This pattern can be explained in terms of the agglomeration of the tiny particles in the 1-h mixing process, which prevents the detection of the actual primary particles using the macroscopic image.

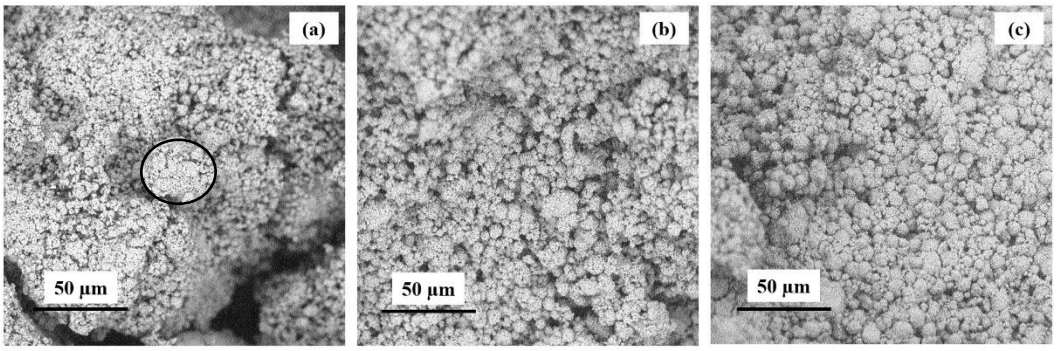

Figure 4.47. SEM micrograph for emulsion particles, (a) 1 h of mixing, (b) 2 h of mixing, and (c) 24 h of mixing

4.5.6.1 Degree of imidization

According to the Beer-Lambert law, the degree of imidization can be determined by monitoring the Fourier-transform infrared spectroscopy (FTIR) intensity of a characteristic peak of imide [173, 325, 326]. The ratio between the intensity of the imide peak at each condition and the fully imidized condition is thus calculated as follows:

$$\text{ID} = \text{imidization degree} = \frac{\text{Number of imidized groups}}{\text{Total number of imidizable groups}} = \frac{(\text{A1370}/\text{A1500})}{(\text{A'1370}/\text{A'1500})}$$

Where A1370 picks out the absorption peak in FTIR at 1370 cm^{-1}, which belongs to the C-N stretching of imide at the measured sample, which in this context is a powder produced through 1, 2 and 24 h of mixing. A1500 cm^{-1} is the absorption peak corresponding to the C-C stretching of benzene. A' is the specific absorption band of the completely imidized PI sample. In the present work, the Aero-Zero powder is considered as the fully imidized condition. For this measurement, the area under each peak should be measured and considered as the intensity of that peak.

The area under the specific peak can be measured using spectrograph software to measure the amount of absorption. Figure 4.48 shows the FTIR graph for the different mixing times.

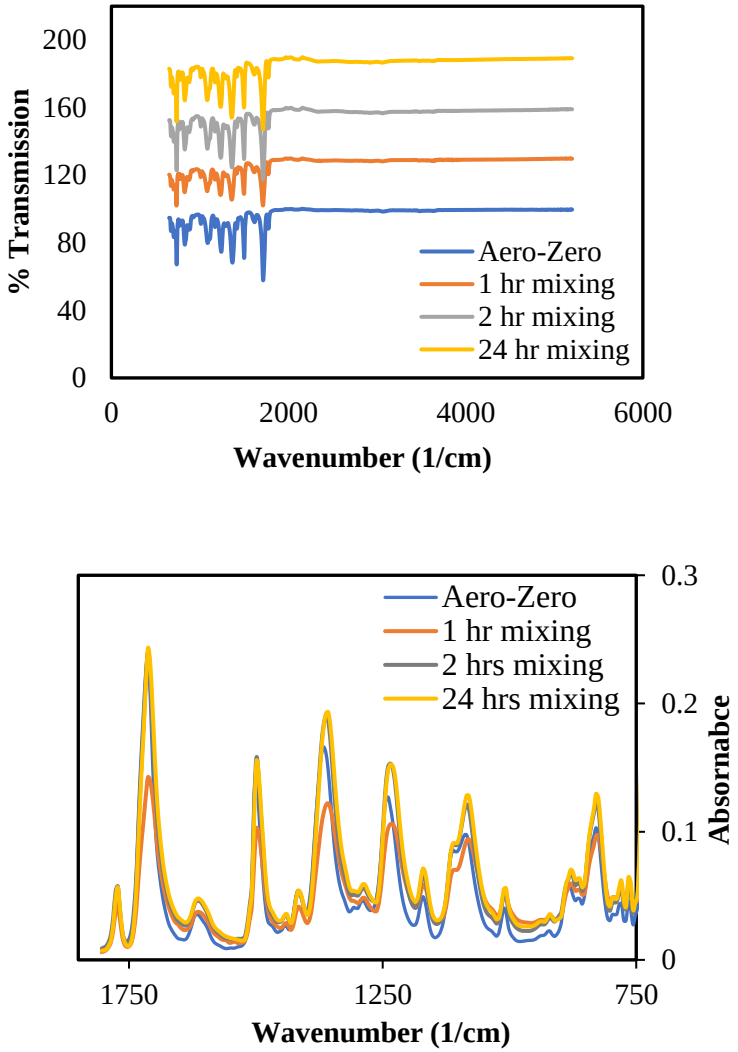

Figure 4.48. FTIR spectra of Aero-Zero and PI-EM with different stirring times

Using the following equation, the ID for all the powder can be calculated as follows:

ID for 1-h mixing= (24.69/14.14)/(3.875/2.197) =0.98

ID for 2-h mixing= (24.72/13.3)/(3.875/2.197) =1.05

ID for 24 h mixing= (24.85/12.4)/(3.875/2.197)=1.14

The calculated imidization degrees show that increases in the time allowed for mixing the emulsion parts result in the fully imidized condition passing. Based on

the calculation results, the optimal length of time for mixing in terms of imidization is 1 h.

It was also found that the length of time allowed for ageing of the microparticles during the mixing process had to be increased. By setting aside a longer time for mixing different parts of the emulsion, the ageing process increased in length in a way that gave rise to greater interaction between the molecules, increasing the surface area of the particles [164]. The data in Table 4.9 also show that extending the mixing time results in the fabrication of smaller particles (~ 11.8 µm), giving rise to greater density. Figure 4.47 shows the SEM for the particles with different stirring times. Microspherical particles with porous structures can be observed in each of these, as can a high amount of agglomeration due to the high stirring speed. To investigate the imidization process, TGA, DSC and a process for the degree of imidization were all used. Regarding thermal stability, the TGA at 10% decomposition for all three mixing times is revealed to be above 500 °C, demonstrating a sufficiently high degree of thermal stability compared to Aero-Zero (542 °C). In addition, the measured glass temperature (T_g) ranges from 230.31 ± 4.95 to 235.51 ± 3.33 °C.

Regarding the degree of imidization calculated in the above section, it can be observed that increasing the mixing time does not affect the degree of imidization. The MIP pore size distribution for different mixing times is presented in Figure 4.49. For all the samples, a bimodal distribution can be observed between 10-100 µm. Furthermore, increasing the mixing time is seen to increase median pore diameter, potentially because of the collapsing of some pores due to an extended mixing period at high speed. One way of taking advantage of this trend is to use a shorter time for the mixing process to prevent breakage of the gel particle, which may happen during the string throughout an extended mixing period [164]. On this basis, it was decided that the shortest time should be selected to reduce the total processing time combined with similar thermal properties and the desirable effect on the degree of imidization.

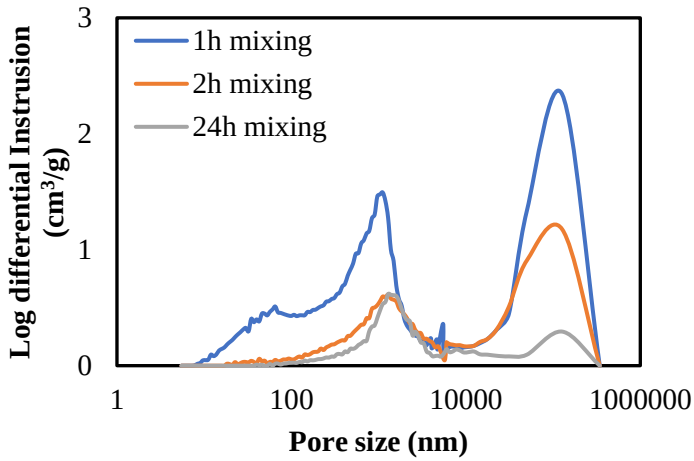

Figure 4.49. MIP pore size distribution at different stirring times

Table 4.9 Properties of emulsion particles at different mixing times

Sample	1 h mixing	2 h mixing	24 h mixing
Specific surface area (m^2/g)	1.9	2.4	4.3
Bulk density (g/cm^3)	0.24	0.42	0.63
Particle size (µm)	16.3	23.4	11.8
MIP Porosity (%)	84	73	40
Median pore diameter (µm)	6.7	8.4	2.4
TGA (10%) (°C)	515	525	535
T_g (°C)	235.51 ± 3.33	232.20 ± 5.10	230.31 ± 4.95
A1370/A1500	1.73 ± 0.04	1.93 ± 0.02	1.97 ± 0.05

4.5.7 Summary of emulsion synthesis process

This section detailed the investigation of the emulsion process. This investigation was carried out to establish the best way of producing PI microparticles with desirable particle size and thermal and mechanical properties. Stirring speed, time, and details of the solvent exchange and drying process were investigated for this purpose. The result of this investigation was the decision to synthesise the PI aerogel using an oil-in-oil emulsion system involving stirring the mixture for 1 h at 500 rpm while exchanging the solvent with acetone. This process also included performing three washes every 20 min followed by two washes every 45 min. Finally, the particles would be dried for 45 min at room temperature, followed by 2 h at 50 °C and 30 min at 200 °C.

4.5.8 Investigation of the dilution process at PI-EM for scaling up process

After optimising all the parameters for synthesising the PI particle using the emulsion process, the powders were produced at 0.0, 0.5, 1.0 and 1.5 dilution ratios (ratio of g DMSO/g PAA) in different batches in a larger volume. The fabricated particles for each condition were then mixed and stored in a plastic bag until characterisation.

4.5.8.1 N_2 sorption

Figure 4.50 provides data on N_2 sorption for the PI emulsion particles at different dilution ratios. These results indicate that increasing the ratio of dilution up to 1.0 results in increases in the quantity of adsorbed gas. Figure 4.50-a shows that the pores were in the range of 2 to 80 nm, with the average pore size at the maximum adsorbed gas point being 25 nm. Low adsorption at low relative pressure indicates that the pores were mostly mesopores and macropores. A low level of adsorbed gas is attributable to the presence of large pores in the sample with a ratio of 1.5. The hysteresis loop in Figure 4.50-b shows type II isotherms for these samples. The presence of a low rate in the quantity of adsorbed gas at low relative pressure up to

0.6 plus a sharp increase in this correlation at a high relative pressure (P/P_0 = 0.9) confirms that the status of most of the pores as mesopores and macropores with relatively lower mesopore content. The calculated total pore volume for PI-EM using the quantity of the adsorbed gas at P/P_0 = 0.9 shows a pore volume in the range of 0.022 to 0.142 cm^3/g. Given the area under the pore size distribution plots, which is approximately equal to the cumulative pore volume, PI-EM-1.0 emerges as having the highest amount of pore volume. This conclusion is consistent with the observation made in respect of the N_2 isotherm plot, as a wider hysteresis loop can be observed for this sample compared to other samples in its group.

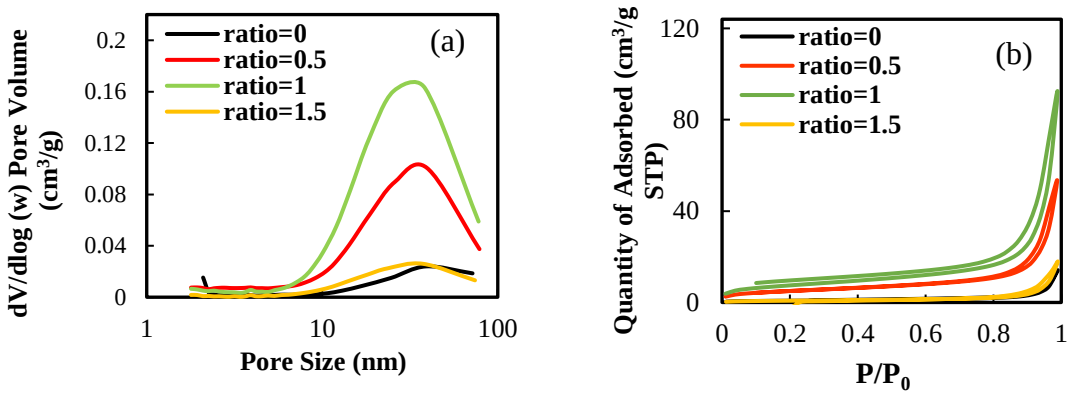

Figure 4.50. a) pore size distribution, (b) N_2 sorption isotherms (at -196 °C) for PI-EM at different dilution ratios and large volumes

4.5.8.2 Mercury Intrusion Porosimetry

MIP was used in this research study to measure the bulk density, porosity and total pore size distribution for the PI aerogel microparticles at different dilution ratios. The resultant data are presented in Table 4.10. The results for PI-EMs show that the total porosity for the smaller particles was found to be less than that of the larger ones. The MIP measured the porosity within the particles (intrapores) and between them (interpores). Figure 4.51 shows the MIP pore size distribution and correlation

of intrusion with pressure for the PI-EM particles in these samples. The pores are in the range of 9 nm to 340 µm. For smaller particles, the level of intra-porosity is less due to the lower space on which the pores can appear. However, it must be borne in mind that smaller particles can group together with relative ease and that this can reduce interporosity. The large pick showing the sample with a ratio of 1.5 at 127 µm shows that most of the pores in this sample are macropores, confirming the very low distribution and low volume of the adsorbed gas for this sample at N_2 sorption.

For PI-EM-0.0, shown in Figure 4.51-b, a large quantity of the pores was filled with mercury due to the presence of larger pores (1046 µm) and the application of a degree of very low pressure at the beginning of the process. However, increasing the dilution resulted in the average size of the pores becoming smaller in such a way that higher pressure is required if the pores are to be filled.

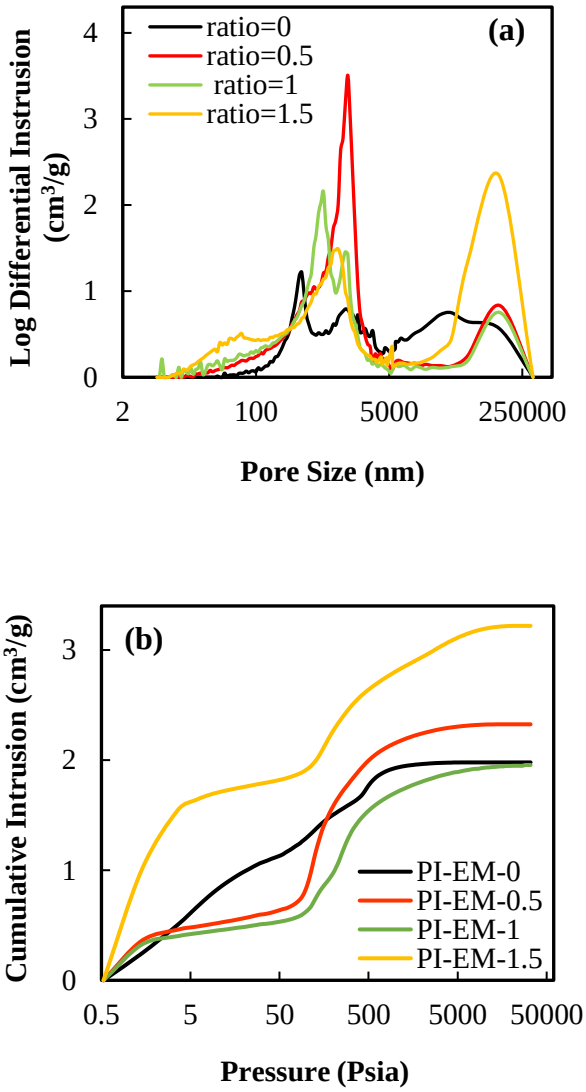

Figure 4.51 MIP characterization for PI-EM; a) pore size distribution; b) correlation of cumulative intrusion with pressure

From these measurements, it can be seen that investigating the pore structure and size of the samples necessitated the use of both N_2 sorption and mercury intrusion on the basis that nitrogen rapidly infiltrates small pores in the interior of microparticles and indicates them in order to measure their size; however, mercury cannot infiltrate the interior of the pore network, which is smaller than the surface pores. Therefore, it was decided to measure the small pores in the interior of the

microparticles using gas adsorption and to measure the pores on the surface of the particles using MIP [66].

The correlation between porosity and density can be observed in Figure 4.52-a. As expected, porosity is seen to decrease as the density of the particles increases. Figure 4.52-b also shows the particles' density reduction as a consequence of increasing the dilution ratio: adding more DMSO, or, in other words, a reduction in the presence of polymers in the powder synthesis process causes an increase in repulsive force. As explained in the next section, particle size increases as a result of an increase in the dilution ratio despite what might be expected, indicating that it is harder for larger particles to fit around each other, which results in lower density and greater porosity. This result agrees with the Feng *et al.* observations. They reported a reduction in the density of the produced PI aerogel when the concentration of PI sol is decreased [50].

The porosities linearly show a 10% increase after bulk densities drop by 30% due to dilution. The largest density belongs to PI-EM-0.0, with 0.34 g/cm^3, with 75% porosity, whereas PI-EM-1.5 has the lowest density of 0.24 g/cm^3, with 84% porosity. The type of mixing and stirring speed can affect particle size distribution, growth and degree of agglomeration, and nucleation. A moderate stirring speed for each process was chosen to improve the mixing process and create a more uniform environment.

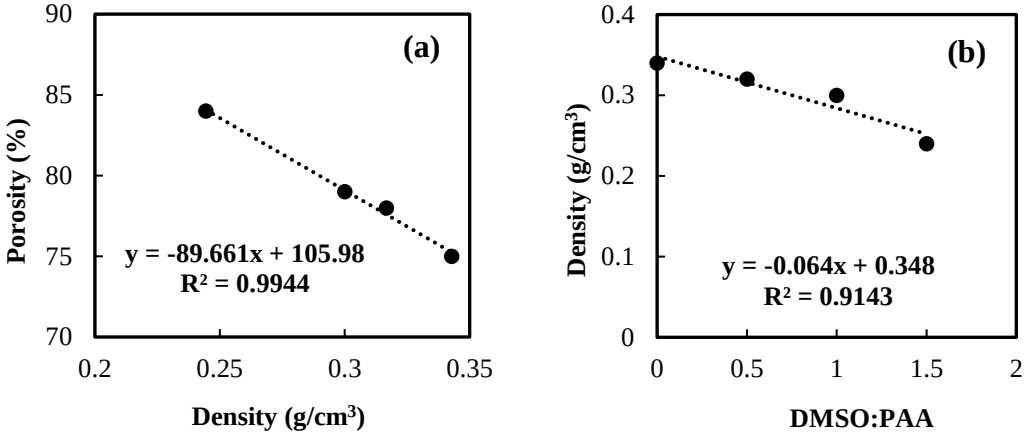

Figure 4.52. Correlation of density for emulsion PI powder aerogel with (a) porosity and (b) ratio of dilution

4.5.8.3 Particle size measurement

Particle size is a property of relevance to a number of other such properties, including rheology, texture, appearance, stability against sedimentation/creaming, droplet coalescence and microbiological growth [327, 328], indicating the importance of gauging particle size in the synthesis of materials. For this purpose, a macroscopic image of each of the different samples was taken to consider within Image Pro. For each sample, at least 700 particles were measured, and the averages of those measurements are presented in Table 4.10. The results show that reducing the polymer concentration in the synthesis method results in the particles becoming larger. It should be noted that the particles measured using this technique were not primary particles; due to the increasing repulsive force, the particles become smaller as the dilution ratio increases.

On the other hand, small particles mixed at high speed (500 rpm) give rise to a high degree of agglomeration. Figure 4.53 shows the SEM images for different PI-EM samples, illustrating the porous structure between and on the surface of the spherical particles in the PI-EM powders. Figure 4.53-e shows the particle detected by the

optical microscope. However, it should be noted that this article also contains different small primary particles that an optical microscope cannot detect.

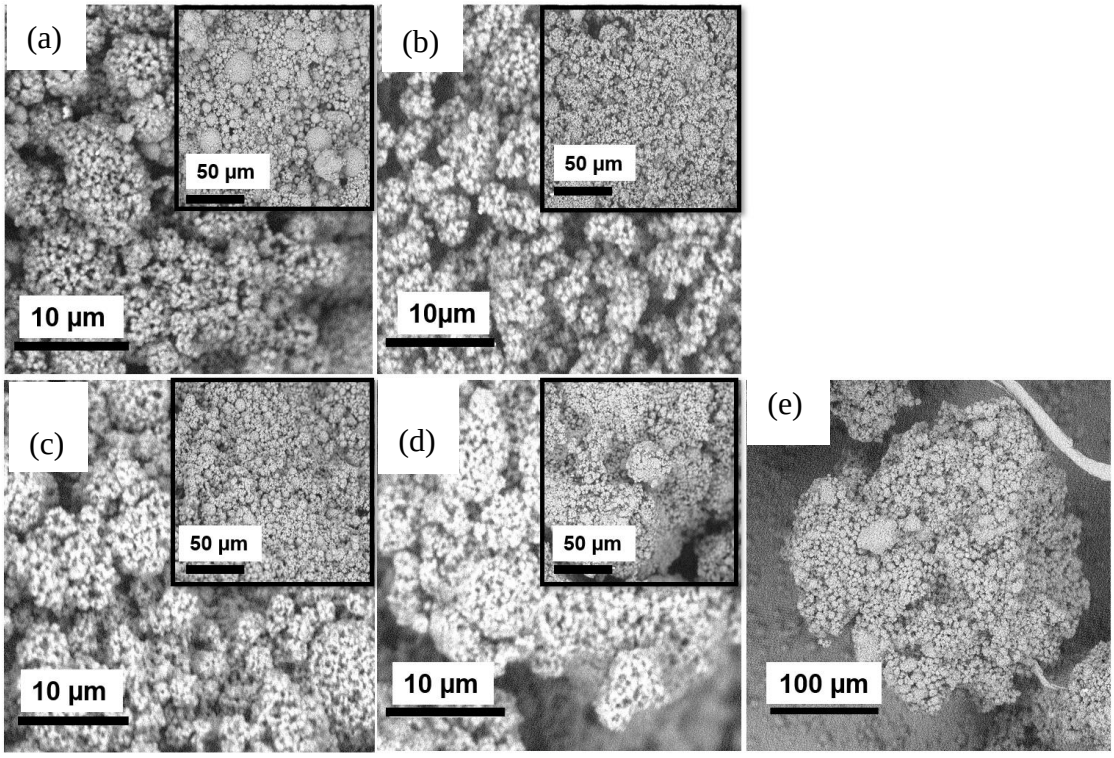

Figure 4.53. SEM microstructures of the PI-EMs with ratios of (a) 0, (b) 0.5, (c) 1, (d) 1.5, (e) single particle that can be detected by an optical microscope

The particle size frequency for the PI-EM powder aerogel is presented in Figure 4.54, demonstrating a right-skewed distribution for all the ratios. The particles are mostly in the range of 3 to 20 µm. The average particle size is presented in Table 4.10, and these data show wider distributions forming for PI-EM samples as compared with those for the PI-WGG samples, indicating the presence of less uniform particles in those samples. A broad particle size distribution is typically observed for particles produced using an emulsion-based method. This is due to a wide shear rate during mechanical mixing and agglomeration of the particles caused by coalescence [172]. This is a relevant consideration in terms of the study by Gu *et al.*, who also detail PI aerogel microparticles with particle sizes in the range of 10-90 µm [164]. The particle size distributions are in line with the density correlation. For powder with a ratio of 1.5, there is a wider distribution compared

with other ratios marked by the presence of more particles of a greater size. These results show that the presence of small particles in the ratio of 0 to 1 facilitates particles existing more closely with each other in a way that gives rise to greater density. However, for the ratio of 1.5, the presence of larger particles results in a higher degree of porosity and lower density as a result of the larger gaps between these particles.

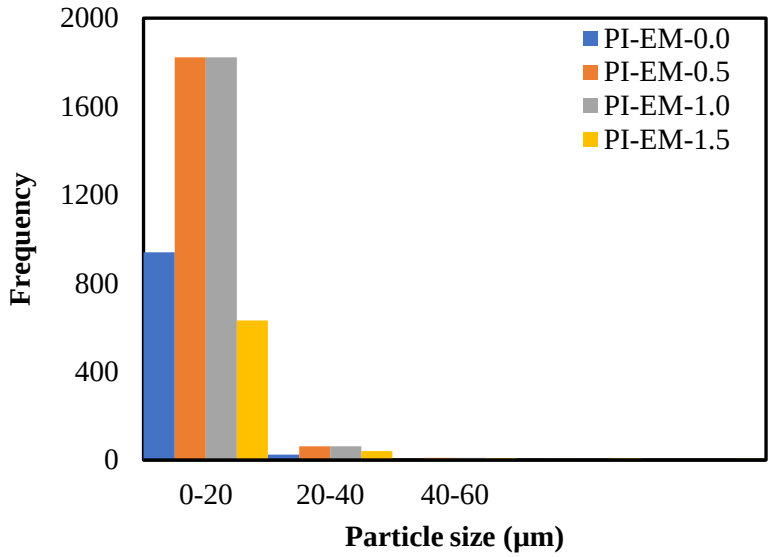

Figure 4.54. Frequency of different sizes of particles for PI emulsion particles at different dilution ratios

Table 4.10 Properties of emulsion PI powder aerogels

Sample DMSO (g)/ PAA (g)	MIP surface area (m^2/g)	N_2 sorption, average pore size (nm) [a]	MIP average pore diameter (nm)	MIP Bulk density ρ_b (g/cm^3)	Skeletal density ρ_s (g/cm^3) [b]	Porosity (%) [c]	Average particle size (μm) [e]	Residual solvent (%) [f]	10 % weight loss (°C) [g]	Thermal conductivity (W/m.K) [h]
0.0	7.60	38.50 ± 0.11	1046	0.34	1.37 ± 0.005	75	6.80	0.95	537	0.061 ± 0.006
0.5	18.40	37.70 ± 0.10	505	0.32	1.41 ± 0.007	78	7.93	0.68	521	0.052 ± 0.002
1.0	32.60	33.21 ± 0.03	240	0.30	1.39 ± 0.007	80	8.12	0.78	526	0.050 ± 0.003
1.5	43.50	25.60 ± 0.04	296	0.24	1.40 ± 0.006	84	16.33	0.89	525	0.068 ± 0.005

[a] average of three samples; single point at V_{max}; [b] single sample, 50 measurements; [c] via $100 \times [1 - (\rho_b / \rho_s)]$; [e] average of more than 500 particles (Image Pro) from optical images; [f] using TGA under nitrogen: 100% - % wt loss (200 °C) = % residual solvent; [g] using TGA in air; [h] average of three measurements.

4.6 Conclusion

This chapter provided evidence that reducing the size of one object from millimeter to micro or nanometer positively affects most of the relevant thermomechanical properties. Furthermore, doing this can also reduce the manufacturing costs incurred during the production of aerogel materials as a result of, for example, less time having to be spent on solvent exchange. In this work, two new procedures, WGG and EM, were developed for manufacturing the PI aerogel microparticles. These methods make it possible to produce PI aerogel powders in a way that involves only a short period of solvent exchange (less than 3 h) and ambient pressure drying. The effect of dilution was investigated on different properties of the particles, such as thermal stability, pore texture and particle size. In terms of particle size, the EM process was found to produce smaller microspherical particles compared to WGG powders. For WGG particles, the density was raised by 75% by diluting the mixture in a ratio between 0.0 and 1.5. In the case of EM particles, the density was reduced by 30% through the addition of diluting agent (DMSO). Both produced powders were found to be thermally stable above 520 °C and to have a highly porous structure, containing up to 94% and 84% air within their microparticles. These techniques provide a basis for manufacturing PI aerogel powders on a larger scale in contexts in which time and cost are at a premium.

In the next chapter, all three types of synthesized particles are consolidated using two methods: addition of epoxy and solvent. The following chapter presents all the experimental details about the consolidation process.

Chapter 5 Consolidation of powder particles to produce polyimide aerogel stock shape

5.1 Introduction

As previously discussed, solvent exchange is the most expensive element in producing PI aerogel in terms of time and energy. In this work, synthesizing the powder particle is a viable means of reducing the cost of manufacturing PI aerogel stock shape. Exchanging the solvent in the powder requires the use of less solvent and less time in a way that helps reduce the total production cost. In addition, the resultant powder can be converted into any size or stock shape for specific applications.

This chapter presents two consolidation methods for manufacturing the PI aerogel stock shape from powder instead of producing this directly. Before consolidation, the PI aerogel particles are treated by mixing in either dimethyl sulfoxide (DMSO) solvent or epoxy resin. The method introduced here uses solvent exchange with the powder particles. By using these techniques for manufacturing the stock shape makes it possible to manufacture Blueshift aerogel composite at a reduced cost in processes involving low-cost solvent exchange and drying. The implications of this are significant in terms of the potential for such composite to be produced to be more competitive than most existing aerogel insulation materials and for their applications to be extended into other sectors.

5.2 Experimental

5.2.1 Materials

DMSO and Chloroform were purchased from Sigma Aldrich. IN2 epoxy infusion resin was purchased from Easy Composites. All reagents and solvents were used as received. The resin was a mixture of bisphenol-A-epoxy resin and epichlorohydrin-formaldehyde phenol polymer.

5.2.2 PI aerogel particle

Figure 5.1 shows a SEM image of the particle at a magnification of 10 µm. All the powders were yellow with fine, small particles with an average size of less than 30 µm. All types of powder in this study (dry milling powder, wet gel grinding powder and emulsion powder) were converted into the stock shape using the methods detailed in the ensuing paragraphs and sections (5.2.3 and 5.2.4).

Two different methods were used to treat the PI aerogel particles produced for this work, involving (i) varying the amount of DMSO, and (ii) epoxy resin. The samples made using these methods are referred to as x% DMSO or x% epoxy, with the prefix "x%" indicating the weight percentage of either DMSO or epoxy content mixed in the samples (g DMSO or epoxy /g PI aerogel particle ×100).

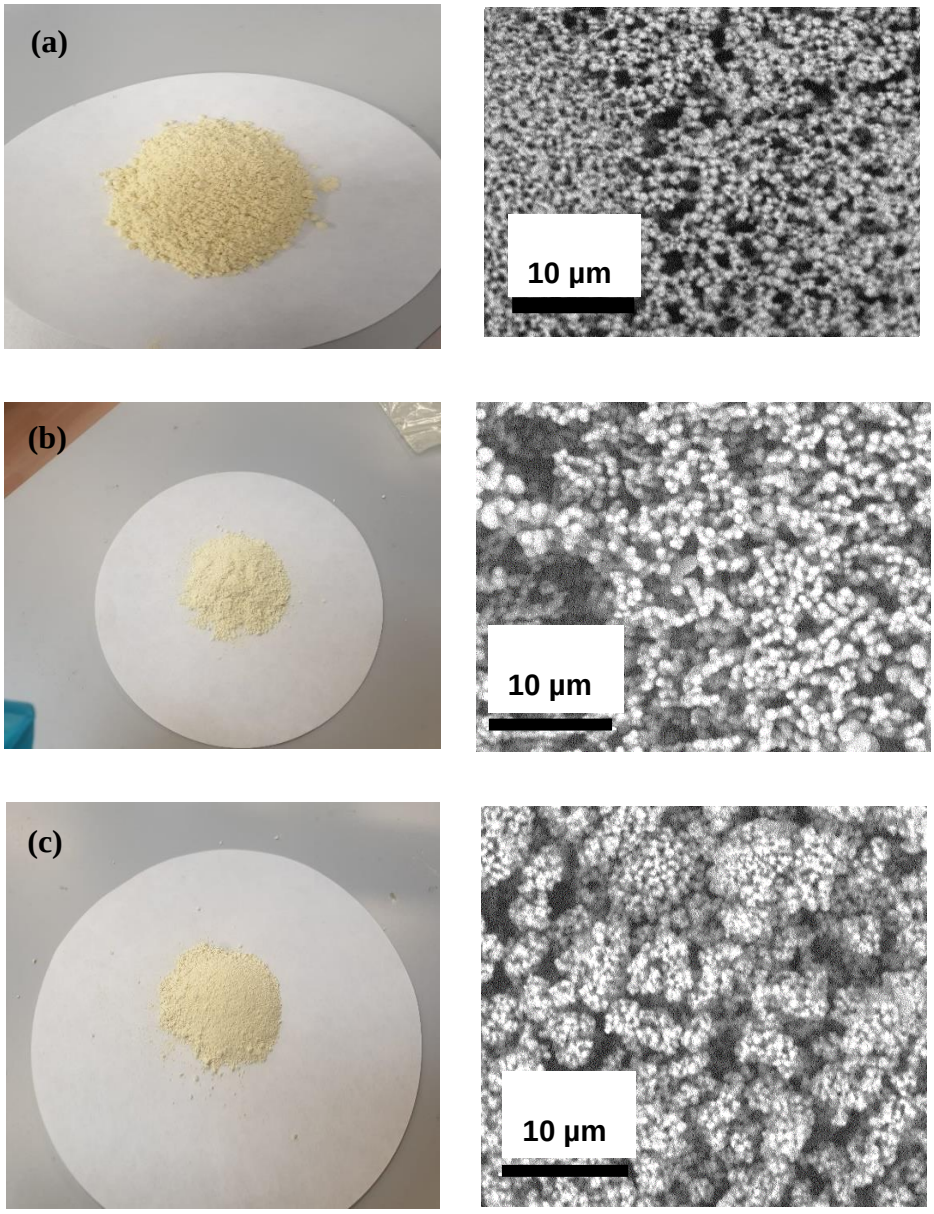

Figure 5.1. Photograph and SEM images of (a) dry milled PI powder, (b) PI-WGG-0.5, and (C) PI-EM-0.5

5.2.3 Incorporation of DMSO

Turning PI aerogel particles into a porous stock shape requires that the PI particles be consolidated without any significant loss of porosity. It was considered that adding DMSO would wet the PI aerogel particles, making them more likely to cling together during the moulding process. DMSO was chosen for compatibility-related reasons, being the original solvent used in the PI aerogel synthesis. DMSO was added to the particle in different contents: 0.0, 3.0, 5.0, 10 and 30 wt%, as shown in Figure 5.2(a). This was done to reduce the tendency of particles to be crushed during the

consolidation process. Acetone was added and manually (as much as a good slurry was formed) stirred for 5 min to yield a uniform dispersion mixture, as shown in Figure 5.2(b). The mixture was left overnight to ensure that the extra acetone would evaporate. The remaining mixture was finally moulded and dried at 250 °C for 24 h.

The idea behind this technique involves using DMSO to soften the space between the particles to facilitate moulding. This technique is also motivated by the point that using a temperature higher than the boiling point of DMSO (189 °C) will result in the evaporation of any extra DMSO in a way that will dry the sample. More details of the rest of the process are presented in section 5.2.6.

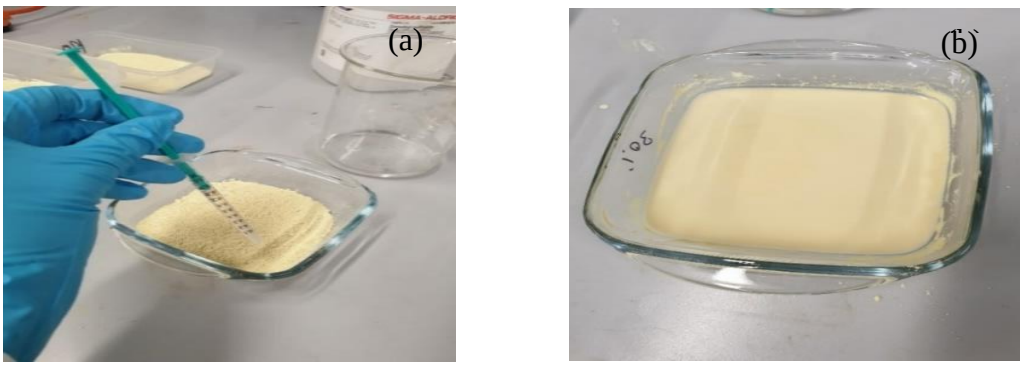

Figure 5.2. A Photograph of (a) the addition of DMSO to the PI aerogel particles, and (b) the mixing of the particles with DMSO after the addition of acetone

5.2.4 Incorporation of epoxy

A water-particle slurry was created by adding 20 ml of water to 1 g of PI aerogel particles. The slurry was shaken vigorously to ensure complete mixing, as shown in Figure 5.3-a. Due to its viscous nature, epoxy cannot mix well with PI aerogel particles directly. Thus, given the goal of achieving uniform dispersion of epoxy around the individual particles, it was dispersed in an organic solvent. Epoxy and hardener were mixed with chloroform at a stoichiometric ratio, 100:30 by weight. For each 5 g of the particles, 20 ml chloroform was added to the epoxy, which was varied at 3, 5, 9, and 20 wt% of the particles. The dispersed epoxy mixture was then introduced into the water-particle slurry and left at ambient conditions for 24 h to let the solvent (water) evaporate, as shown in Figure 5.3-b. Finally, the overall mixture was filtered using the filter paper (VWR, grade 413, medium, 5-13 µm particle retention, 150 mm diameter) to obtain the particle-epoxy mix, as shown in Figure 5.3-c.

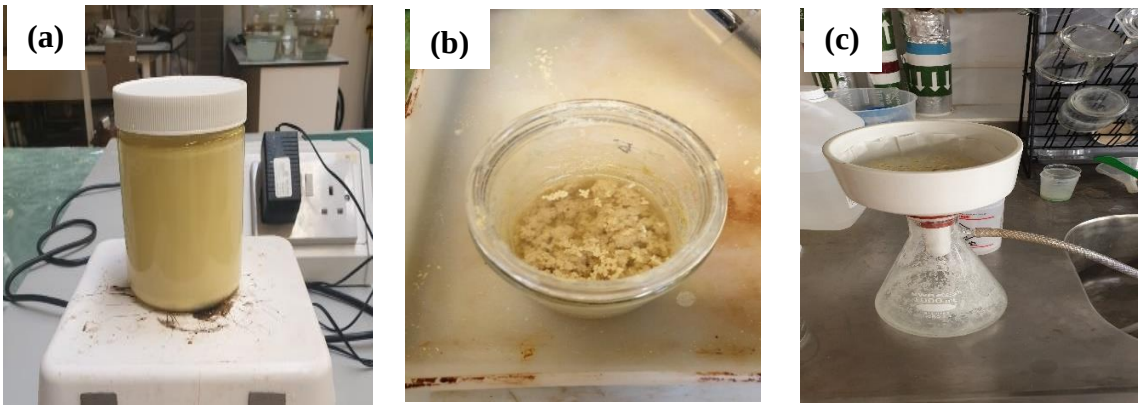

Figure 5.3. Photographs of (a) a slurry of water-PI aerogel particles, (b) the mixture after the addition of epoxy, and (c) filtering of the overall mixture

5.2.5 Particle consolidation

Conversion from PI aerogel particles to their stock shape was carried out using consolidation moulding. An aluminium square tube with an internal area of 1 × 1 inch was machined for this purpose, as shown in Figure 5.4 and Figure 5.5. Two aluminium blocks were also machined, in such a way that they could slide into the tube and be secured by pins through open holes on the tube's side. The distance between the two blocks was 1 inch, and so a cavity of 1 × 1 × 1 inch was created inside the tube. The PI aerogel particles treated with DMSO or epoxy in the manner described in Sections 5.2.3 and 5.2.4 were then transferred into the cavity. 4.5 g of the particles were used in order to ensure that the particle bulk volume was greater than 1 cubic inch, applying pressure to the particles when the blocks were put in place. The particle-filled mould was then transferred to an oven, where the DMSO-treated particles were heated at 250°C for 24 h. The epoxy-treated particles were heated at room temperature for 24 h and 80°C for 6 h. Several approaches were taken to find the right temperature and drying method for the epoxy samples. From the experimental results, it was found that subjecting the sample to a temperature above 80 ℃ resulted in the breaking down of the PI structure into aerogel in the proper stock shape. To achieve the goals of controlling the viscosity increment, keeping the pore structure safe, and ensuring that the block shape was uniformly formed, a stepwise drying process was applied to the samples. It means heating process will be applied in a step after 24 h room temperature

drying for 6h at 80 °C. The final step involved demoulding the sample carefully and obtaining stock-shape samples in the manner shown in Figure 5.4.

Figure 5.4. A photograph of the tooling used to consolidate the particles and produce the stock shape samples after demoulding

Producing aerogels in large and specific sizes is generally more challenging. Thus, several techniques were trialled for moulding the microparticles in a way that allowed these goals to be met. For the first attempt, as mentioned above, an aluminium tube with an internal area of 1 × 1 inch was machined to fit two aluminium blocks that could be secured in place using pins to form a cavity of 1 cubic inch (Figure 5.5). To demould the sample, the pins were removed from the holes in the side of the tube and force was applied on one side of the block to push the sample out. However, it was found that this procedure affected the thermomechanical properties of the produced sample. It was also found that the pressure applied on the blocks could not be measured using this type of mould. A second attempt was therefore made, this time involving a cylinder PTFE mould, which was used on the basis of its high degree of flexibility, chemical and thermal resistance, and non-stick and low friction properties (see Figure 5.5). The applied pressure was set and defined using this type of mould in a specific value to produce a cylindrical sample with dimensions of 50 × 25 mm. However, the glass transition temperature for the PTFE was 114.85 °C; therefore, given the goal of producing the stock shape using the DMSO method, in which the samples would need to be dried at 250 °C for 24 h, the PTFE mould would not be viable even if the melting temperature was 326.85 °C. For this reason and given the need to use a consistent moulding process with all the consolidation methods, the PTFE was ruled out as an option.

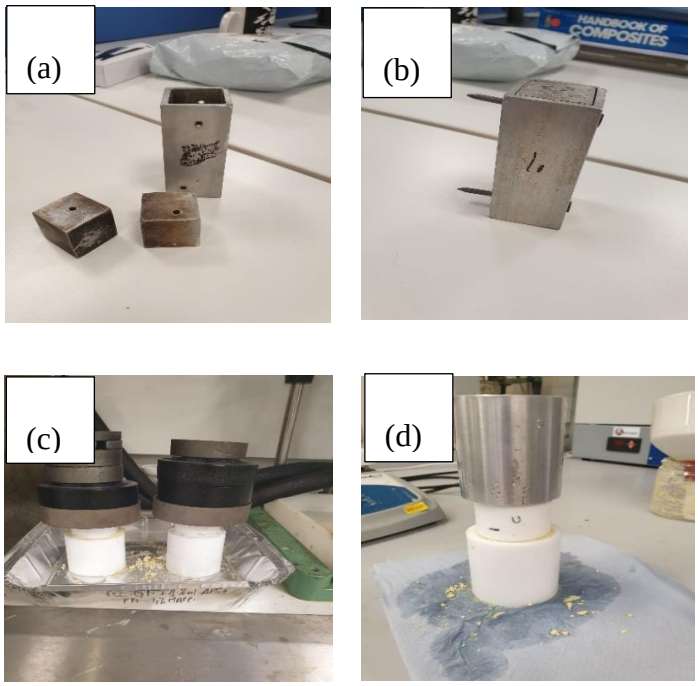

Figure 5.5. a and b) Aluminium and c and d) PTFE mould

Ultimately, an aluminium mould was selected for use due to the associated ease of producing the mould and sample, the ability to produce a sample with a desirable shape and appearance, the possibility of performing the demoulding process in a straightforward manner using the silicon release agent, and its resistance to high temperature.

In the next chapter the characterisation results for PI aerogel stock shape samples which are made using the consolidation of the particles with epoxy and DMSO are presented. At the end of this chapter a comparison will be carry out between different type of stock shape properties.

Chapter 6 Results of characterization of polyimide aerogel stock shape

6.1 Introduction

This research project investigates the appropriate consolidation method for manufacturing PI aerogel stock shape from aerogel particles instead of via direct synthesis. First, the dry milled powder (Aero-Zero) received from our industrial partner, Blueshift, was used to produce the stock shape. The 1×1 inch cubic samples, consolidated with DMSO and epoxy, were then characterized using N_2 sorption, MIP, thermogravimetric analysis, compression testing and a procedure for determining thermal conductivity. At the end of this process, given the possibility of achieving a more optimal result using epoxy treatment, this method involving epoxy was selected to consolidate the wet gel grind and emulsion particles synthesized during this project. As previously noted, the samples produced using these methods are referred to as x% DMSO or x% epoxy, where the prefix "x%" indicates the weight percentage of either DMSO or epoxy content mixed in the samples (g DMSO or epoxy /g PI aerogel particle ×100). The stock shape samples made using the DMSO and epoxy methods are called PI-DMSO and PI-Epoxy, respectively.

6.2 Characterization of dry-milled polyimide aerogel stock shape with DMSO (PI-DMSO)

Given that the properties of aerogel materials, including PIs, have very sensitive relations with their nanostructure assembly, it was acknowledged that it would be essential to control the aerogel's nanostructure configuration to improve performance. However, the engagement of multiple complex parameters, such as intermolecular interactions during gelation, complicates the procedure for controlling aerogel's morphology.

6.2.1 N_2 sorption

N_2 sorption was used to investigate the stock shape samples' pore structure and surface area. Two samples were tested, and the associated data in the form of measurement averages are presented in the following section. Figure 6.1-a shows the pore size distribution for PI stock shape samples with different ratios of DMSO. The pores are in the range of 2 to 60 nm. The average sizes of the pores at the maximum volume of

the adsorbed gas were observed to be in the range of 20 to 37 nm. Nitrogen adsorption-desorption isotherms at -196 °C are shown in Figure 6.1-b. The hysteresis loops are apparent in every BET isotherm curve, demonstrating that mesopores and macropores exist in all cases. This loop also suggests that gas condensed inside the pores at low-pressure ranges and formed mono- and multilayers at higher pressures. The nitrogen adsorption isotherms can also be seen to have risen above P/P_0 = 0.9 but without reaching the saturation plateau, indicating their status as type II isotherms. The BET surface areas of the samples are from 8 to 14 m^2/g. It is not surprising that the surface area of PI aerogels in this study is relatively low compared to those of the PI aerogels considered in the literature. For instance, Kwon *et al.* demonstrate that the surface area of the PI aerogel considered in their work was 103 m^2/g, almost 87% higher than that of the PI samples produced in this study [66]. Feng *et al.* also show that the BET-specific surface area is 320−340 m^2/g [50]. During ambient pressure drying, the surface tension between the solvent and pore walls reduces shrinkage and surface area. For this reason, most such studies have used supercritical CO_2 instead of ambient pressure drying [50].

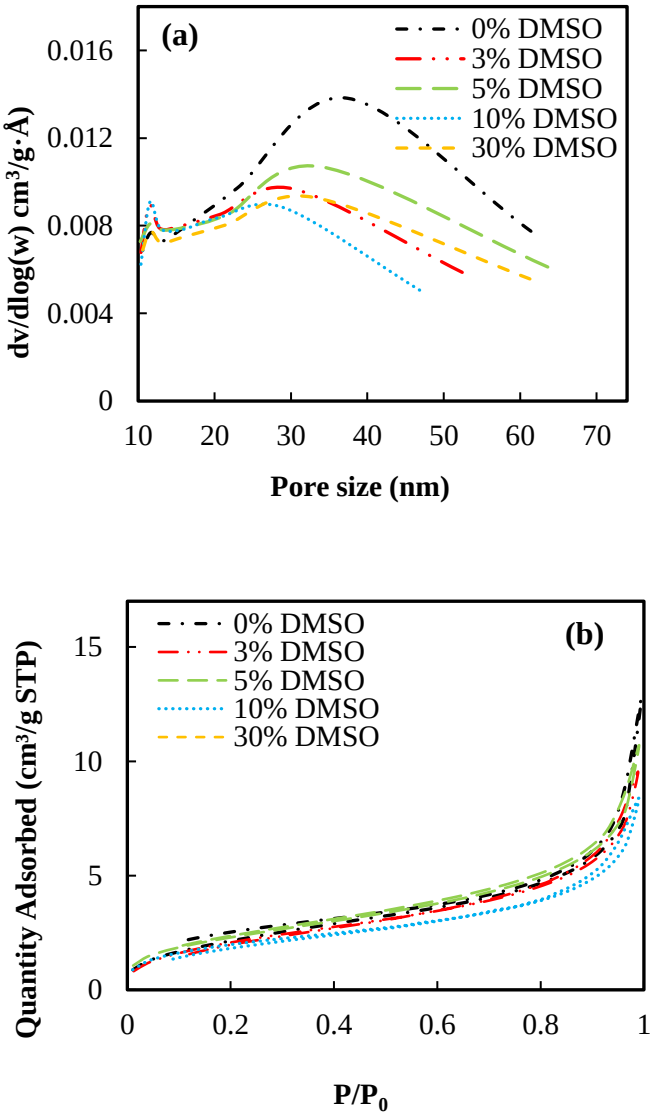

Figure 6.1. N_2 sorption PI-DMSO stock shape, (a) pore size distribution, (b) N_2 sorption isotherms (at -196 °C)

6.2.2 Mercury Intrusion Porosimetry (MIP) for PI-DMSO stock shape

Given that N_2 sorption is constrained in terms of the pore size that can be measured (100 nm), it was judged that MIP had to be used to investigate the size of the pores inside and between the particles and to calculate total porosity. The results of this process are presented in Table 6.1.

6.2.2.1 Pore structure

Pore size distribution for the PI-DMSO samples is shown in Figure 6.2 -a. MIP shows bimodal pore size distributions between 900 and 6000 nm for DMSO samples, indicating that the status of the pores is primarily mesopores and macropores. As the concentration of DMSO is increased for the solidification of the PI, a wider pore distribution can be observed. The first peak is almost the same for all the samples, which differ only in intensity. However, in the case of the second peak, it can be seen that larger pores emerge as a result of an increase in the degree of DMSO, giving rise to a wider distribution. The pore size distribution of the Blueshift stock shape shows a single peak. The pores are 400-780 nm, with an average size of 597.40 nm. These pores are smaller with a more uniform structure than those in the PI-DMSO samples, although these samples are observed to have a larger pore size than those discussed in the literature [112].

As previously explained, the idea behind the addition of DMSO is to plasticise the particles in a way that results in more flexible particles that require less stress to consolidate; as a result, fewer pores are destroyed, and higher porosity will be achieved. In addition, softened particles, due to the addition of DMSO, require less stress to be squeezed during the consolidation process; therefore, the particles do not break into smaller particles in the manner caused by higher levels of stress, as smaller particles can be more densely packed compared to larger ones.

Figure 6.2 (a) shows the correlation of the porosity with the concentration of DMSO in the samples. The value indicating the degree of porosity was measured using the MIP instrument.

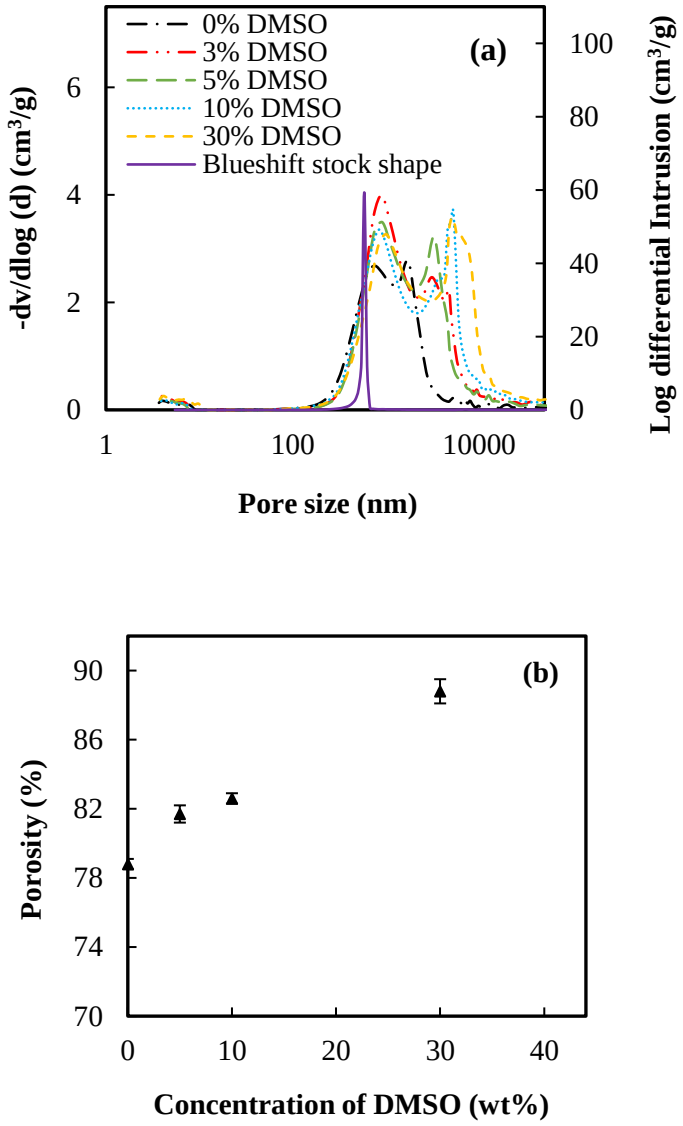

Figure 6.2. (a) MIP pore size distribution, (b) correlation of porosity with concentration of DMSO

6.2.2.2 Density measurement with MIP for PI-DMSO samples

Table 6.1 shows different properties for PI-DMSO stock shapes with a density below 0.30 g/cm^3 and high porosity, ranging from 78.8% to 88.8%. Density was measured using the mass and volume of the cubic samples. For each concentration, an average of three measurements is presented. As explained in Section 6.2.2.1, adding more DMSO and making the particles soften will reduce the density of the stock shape samples (see Figure 6.3).

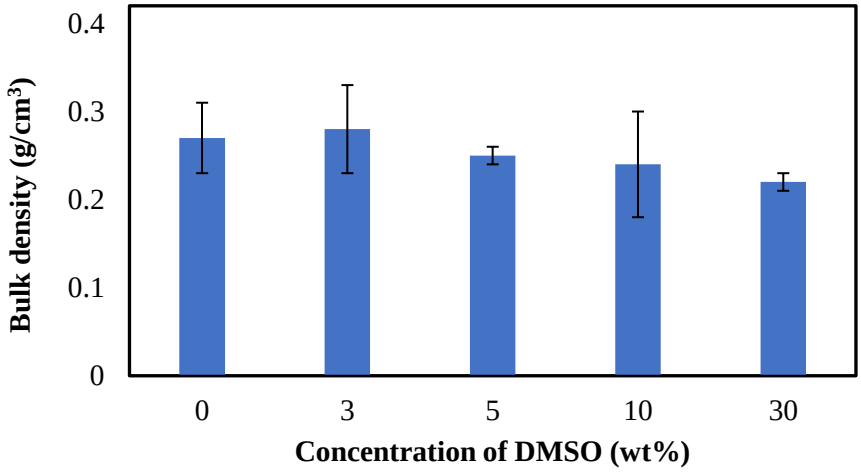

Figure 6.3. Correlation of bulk density with DMSO content

The SEM images for PI-DMSO samples are shown in Figure 6.4, highlighting a porous structure in each of the concentrations. These images confirm that adding more DMSO causes higher porosity in the samples, with the highest value of 88.8% being reported for 30% DMSO.

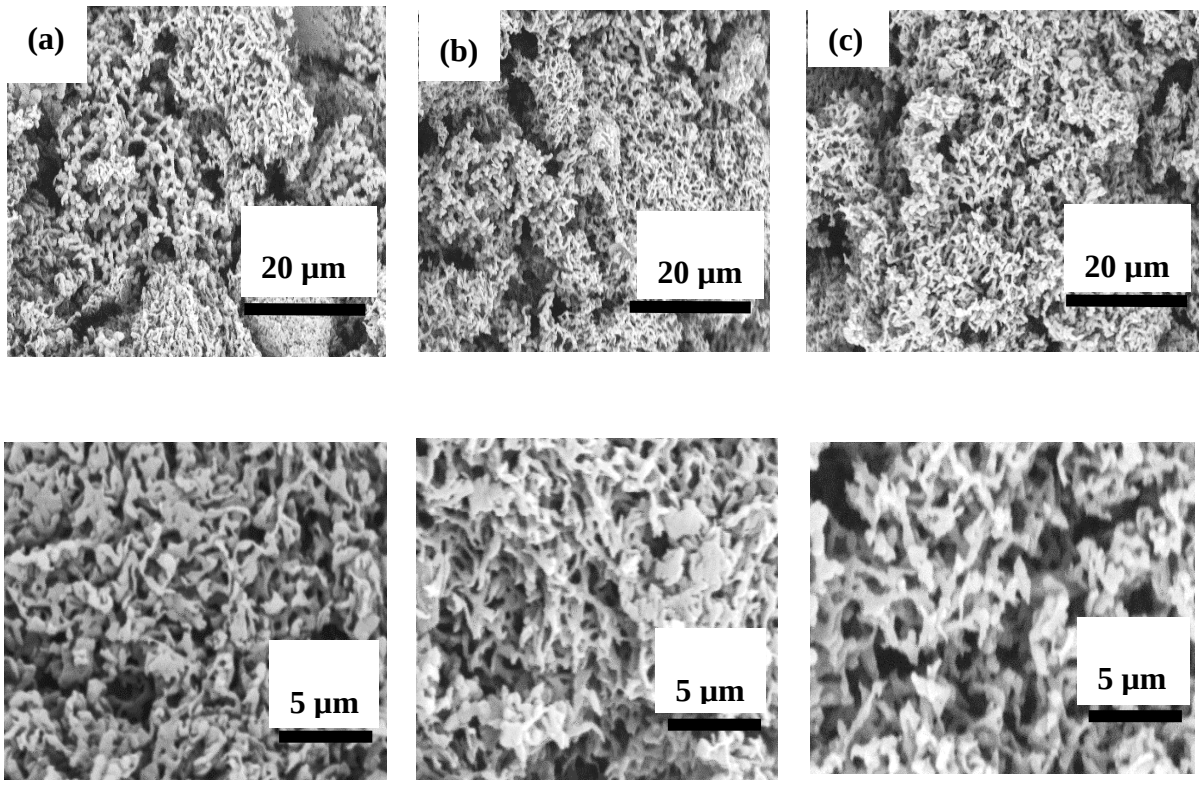

Figure 6.4. SEM images of PI-DMSO samples with (a) 0.0; (b) 5.0, and (c) 30% DMSO

6.2.3 Thermogravimetric analysis (TGA) for PI-DMSO

The weight changes and rates of weight change against temperature for PI-DMSO samples are plotted in Figure 6.5. It can be seen in Figure 6.5(a) that there is no weight loss until the temperature reaches 430 °C for both neat PI and PI with DMSO. The small degree of overlap of the peaks confirms this temperature to be 430 °C for all the samples depicted in Figure 6.5(b). From 430-540 °C, thermal degradation accelerates in respect of all samples. The greatest weight loss can be observed as occurring for all samples between 540 and 590 °C. From the rate of weight change, it can be observed that the neat PI is slightly more thermally stable, having the lowest weight loss rate compared to PI-DMSO samples. In all PI-DMSO samples, degradation was completed by 670 °C. Adding different concentrations of DMSO did not significantly impact the thermal decomposition. As previously discussed, the reason for treating already synthesized PI particles with DMSO solvent relates to the goal of plasticizing the PI particles under the expectation that this solvent would be removed through the subsequent drying process. The minimum onset point is 540 °C in the 10% DMSO sample. Given the absence of significant weight loss before the decomposition point, it can be concluded that all the DMSO was removed during the drying process. The 10% weight loss and the onset temperatures are also summarised along with other characterised properties in Table 6.1.

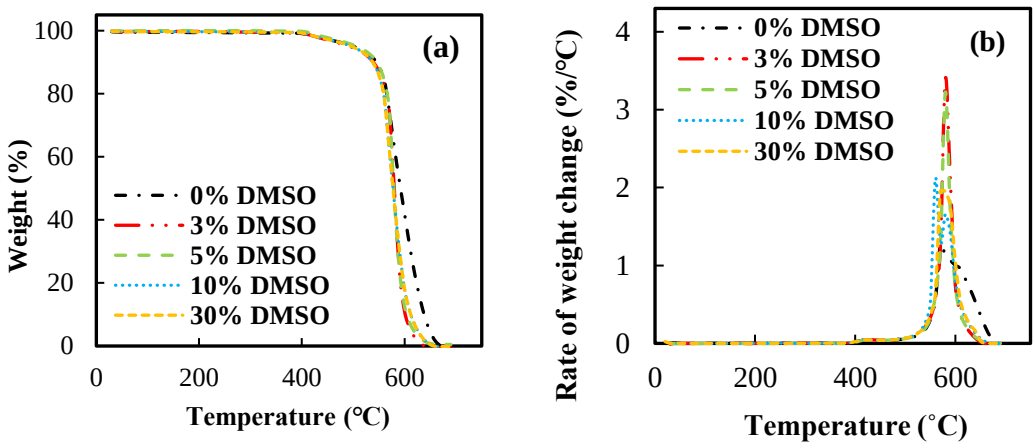

Figure 6.5. (a) Weight, (b) rates of weight change as a function of temperature for PI-DMSO samples

It can be observed that there is no massive change at the onset point as a result of changes in the concentration of DMSO. As might be expected, thermal stability depends on the chemistry of the materials [21]. Given that the material's chemistry is consistent across all the samples, it is unsurprising that not much difference can be observed in their thermal stability. It can be seen that the rate of weight change reduces through the addition of more DMSO.

6.2.4 Mechanical properties of PI-DMSO

The compressive properties of the samples were investigated using an Instron 5969 series universal testing system equipped with a video extensometer, followed by the application of ASTM D1621 [329]. The equipment was fitted with a 50 kN load cell to evaluate the effect of the DMSO and epoxy on the particle-converted stock shape material (see Figure 6.6). This involved testing cubic samples (three for each condition) with dimensions of 25 × 25 × 25 mm at a constant rate of 0.65 mm/min at room temperature.

Figure 6.6 Instron 5969 series universal used for mechanical testing

Compression tests of the PI stock shapes were carried out to evaluate the effect of DMSO treatment on the mechanical performance of the particle-converted PI stock shapes. As noted, at least three samples were tested for each condition, and the average of these measurements is presented below. Compressive modulus was taken as the

slope of the elastic domain in the stress-strain curves, and the resultant data are presented in Table 6.1. For all the DMSO concentrations, the stock shape samples were found first to show behaviour associated with elastics and then behaviour associated with plastics. The addition of DMSO can also significantly affect the mechanical properties of the PI stock shape. Figure 6.7 shows stress-strain curves for different concentrations of DMSO. As expected, given the samples' weak and brittle structure, they all disintegrated before applying 10% strain; therefore, no data is presented for this value.

Figure 6.8 shows the correlation between compressive modulus and concentration of DMSO. It can be observed that the addition of DMSO, which causes more porosity and larger pores due to plasticising between the particles, reduces the compressive modulus. The PI-DMSO samples were also observed to be powdery and brittle; therefore, they were expected to have undesirable mechanical properties.

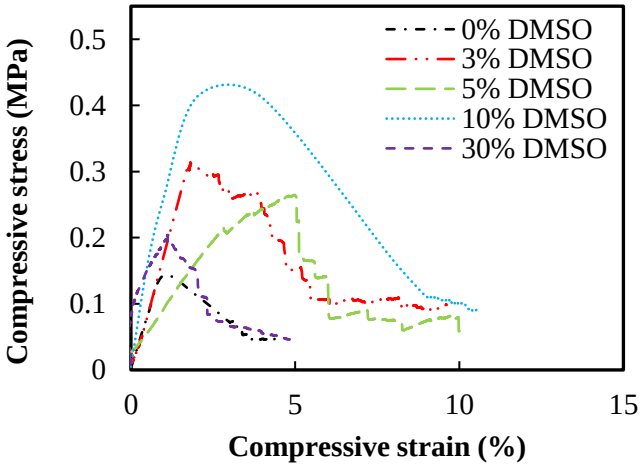

Figure 6.7. Stress-strain curve for PI-DMSO stock shape

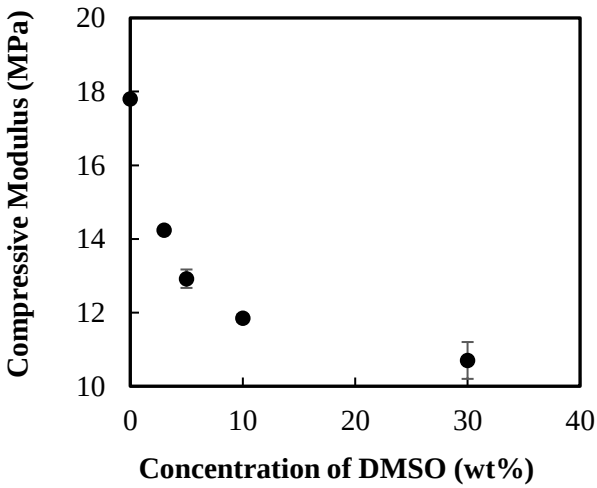

Figure 6.8. Compressive modulus of PI-DMSO stock-shape as a function of the concentration of DMSO

6.2.5 Thermal conductivity of PI-DMSO stock shape

The thermal conductivity of the PI stock shape samples was measured using a hot-wire instrument. The sensor was placed between two samples, and a 500 g weight was placed on top of the above sample to ensure complete contact between the surface of the sample and the sensor. Efforts were also made to sand the samples' surface to make it as soft as possible in reflection of the knowledge that the surface plays an essential role in taking such measurements. A non-soft or irregular surface can result in gaps filled with air between the sample and sensor, potentially causing measurement errors. Two samples for each condition were tested using this technique. All six sides of each sample were tested, and the average of the 11 measurements is presented in Table 6.1. By increasing the DMSO content, thermal conductivity was observed to decrease from 56 to 50 mW/m.K. A 30% increase in the thermal conductivity of the PI-DMSO samples can also be observed compared to the Blueshift PI stock shape (42 mW/m.K). The greater density of the DMSO samples means that their structure is more conducive for transforming heat.

Figure 6.9 presents the thermal conductivity of the PI stock shape samples as a function of the concentration of DMSO. Before the 30% sample, the thermal conductivity correlation seems almost linear at different concentrations of DMSO. Increasing the concentration of DMSO increases porosity such that thermal conductivity is reduced from 0.056 to 0.050 W/m.K.

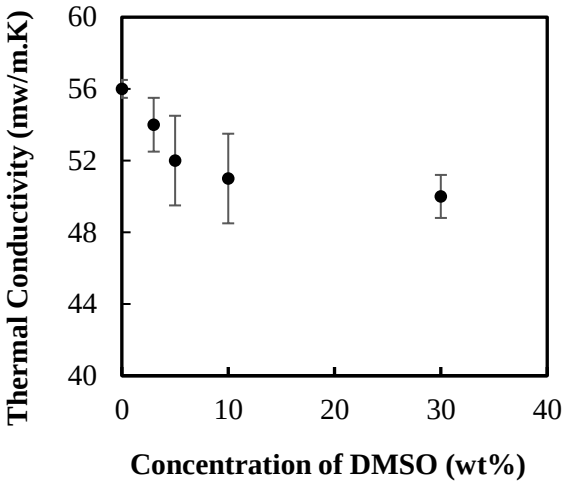

Figure 6.9. Correlation of thermal conductivity with (a) DMSO content, and (b) bulk density for PI-DMSO samples

Table 6.1. Key materials properties of PI stock-shapes produced with PI aerogel particles treated with DMSO

Sample (% DMSO)	**0.0**	**3.0**	**5.0**	**10**	**30**
Bulk density (g/cm^3)[a]	0.27 ± 0.04	0.28 ± 0.05	0.25 ± 0.01	0.24 ± 0.07	0.22 ± 0.01
Skeletal density (g/cm^3)[b]	1.49 ±0.02	1.50 ±0.01	1.50 ±0.01	1.47 ±0.01	1.49 ±0.01
TGA (10%) (°C)[c]	545	535	545	535	535
Onset temperature (°C)[c]	550.23	563.18	567.22	567.17	541.02
Specific surface area (m^2/g)[d]	7.70 ± 0.03	8.00 ± 0.05	8.51 ± 0.10	8.62 ± 0.05	8.40 ± 0.01
MIP Porosity (%)	78.80 ± 4.74	80.91±1.41	81.70 ± 0.18	82.60 ± 1.41	88.80 ± 1.5
MIP Median pore diameter (µm)	1.110 ± 0.022	1.360 ± 0.006	1.391± 0.071	1.570 ± 0.206	2.11 ± 0.102
Compressive modulus (MPa)[e]	17.80 ± 0.02	14.24 ± 0.04	12.92 ± 0.25	11.85 ± 0.11	10.70 ± 0.50
Thermal conductivity (W/m.K)[f]	0.056 ±0.002	0.054±0.001	0.052± 0.003	0.051± 0.004	0.050 ± 0.003

a) measured using mass and volume of the samples ($\rho=m/v$)., b) measured with Micromeritics Accupyc II 340 helium pycnometer, c) single measurement, d) average of three samples, e) slope of elastic part in stress-strain curve; f) average of two measurements

6.3 Characterization of the stock shape with epoxy (PI-epoxy)

As previously explained, epoxy was used in different concentrations of 0.0, 3.0, 5.0, 9.0 and 20% to consolidate the PI aerogel particles. The 1×1×1 inch moulded samples were stored in a plastic bag for subsequent investigation using characterisation techniques such as N_2 sorption, MIP, TGA, mechanical testing and thermal conductivity.

6.3.1 N_2 sorption

As mentioned before, the stock shape's pore structure and surface area were measured using N_2 sorption. Figure 6.10 shows these samples' pore size distribution and N_2 sorption isotherm. The pores were found to be in the range of 2 to 60 nm, with an average of 25 nm. Increasing the concentration of epoxy up to 9% causes an increase in the volume of the pores and, therefore, in the quantity of adsorbed gas. The hysteresis loops are apparent in every BET isotherm curve (Figure 6.10-b), demonstrating that mesopores exist in all cases. This loop also suggests that gas condenses inside the pores at low-pressure ranges and forms mono- and multilayers at higher pressure. The nitrogen adsorption isotherms rise above $P/P_0 = 0.9$ but do not reach the saturation plateau, indicating their status as type II isotherms. Overall, the very low quantity of gas adsorbs at the early stage of the adsorption and the large pores seen in the MIP pore size distribution prove that macropores constitute a significant proportion of the porosity.

The 20% epoxy sample shows the lowest level of adsorbed gas among the PI-epoxy samples. This may be due to blockage of the pores by epoxy or due to the existence of large pores that cannot be detected using N_2 sorption. For this reason, MIP was also used to investigate the nature of the pores as a whole.

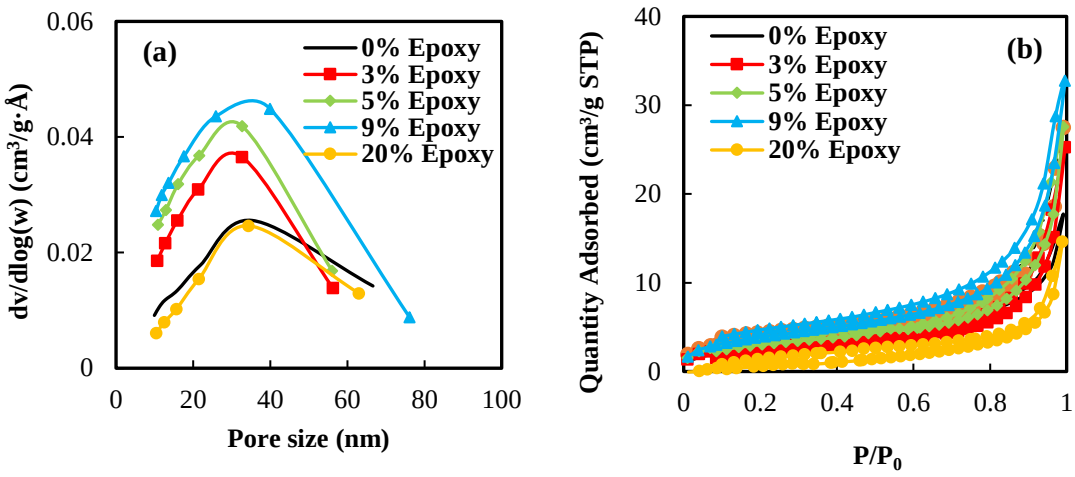

Figure 6.10. N_2 sorption PI-epoxy stock shape, (a) pore size distribution, (b) N_2 sorption isotherms (at -196 °C)

6.3.2 Mercury Intrusion Porosimetry (MIP) for PI-epoxy stock shape

The total degree of porosity and pore size distribution was measured using MIP for the PI-epoxy samples. Aside from the 0% concentration, for all the conditions, a bimodal distribution can be observed in the range of 600 nm to 10 µm (see Figure 6.11-a). Macropores were found to constitute largest proportion of the different types of pores in all the samples, and the 20% epoxy sample was found to have the largest pore size among all the samples. This result sheds light on why there was only a low degree of gas adsorption in terms of N_2 sorption characterization. Table 6.2 presents all the properties of the PI-epoxy samples. Figure 6.11-b shows that, for the PI-epoxy samples, porosity increased as epoxy concentration increased, except at 5%. This sample had a 0.4 g/cm^3 bulk density, the highest value among all samples. The bulk density for these samples was measured using the mass and volume and change in the range of 0.32-0.40 g/cm^3. As observed in the correlation of epoxy by porosity (Figure 6.12), the density increased up to 5% epoxy before starting to reduce. Different behaviour can be observed as having occurred before and after the 5% epoxy condition.

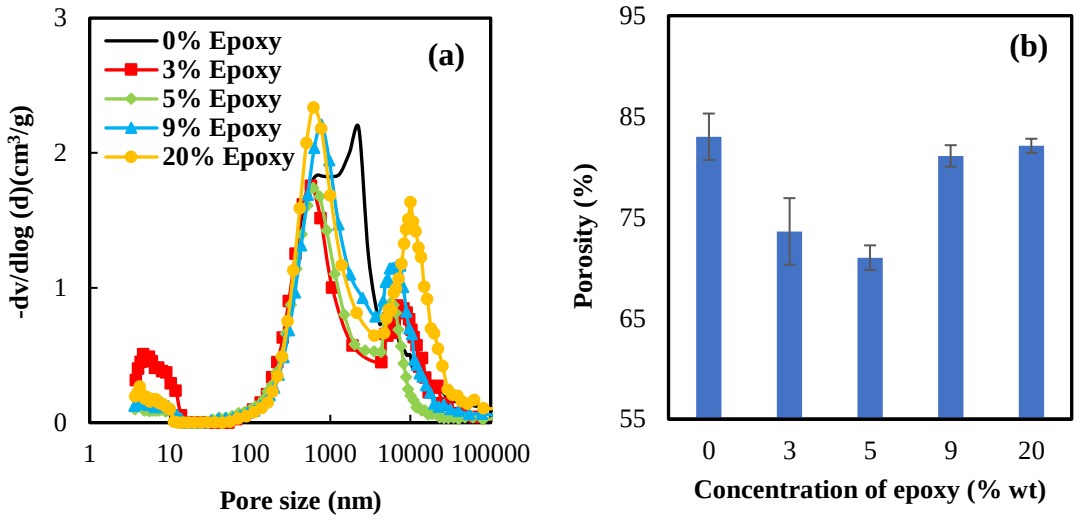

Figure 6.11. (a) MIP pore size distribution, (b) correlation of porosity with epoxy content for PI-epoxy samples

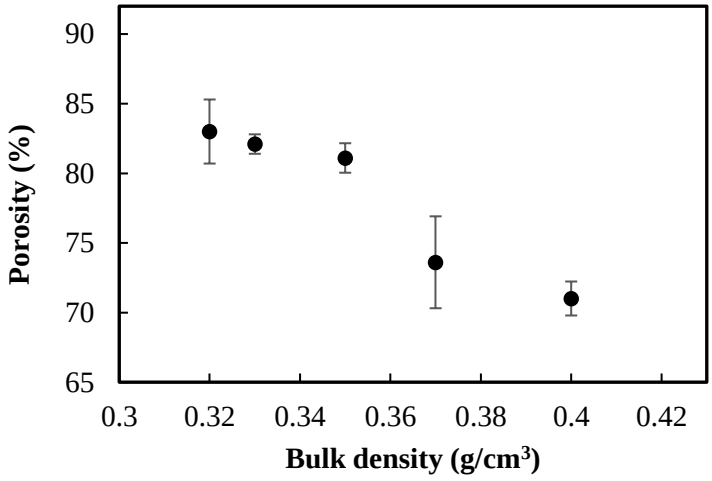

Figure 6.12. Correlation of porosity with density for PI-epoxy samples

The microstructure of the PI-epoxy sample at three different concentrations (0.0, 5.0 and 20%) is shown in Figure 6.13. The presence of epoxy is also visible in the samples in terms of the bond between the particles. It can be observed that adding 5% epoxy to the particle makes the structure denser as compared with the 0.0 % epoxy sample. This could be due to the presence of epoxy inside and between the particles. However, adding more epoxy, up to 20% may have resulted in the small pores inside the particles becoming filled with epoxy and the rest of the epoxy covering the surface of the particles in a way that resulted in these becoming bigger. Consolidation of the bigger

particles in this way would result in lower density. Support for this analysis was obtained by measuring median pore diameters using the MIP. The size of the pores was observed to increase with the addition of more epoxy, from 0.760 to 1.190 µm.

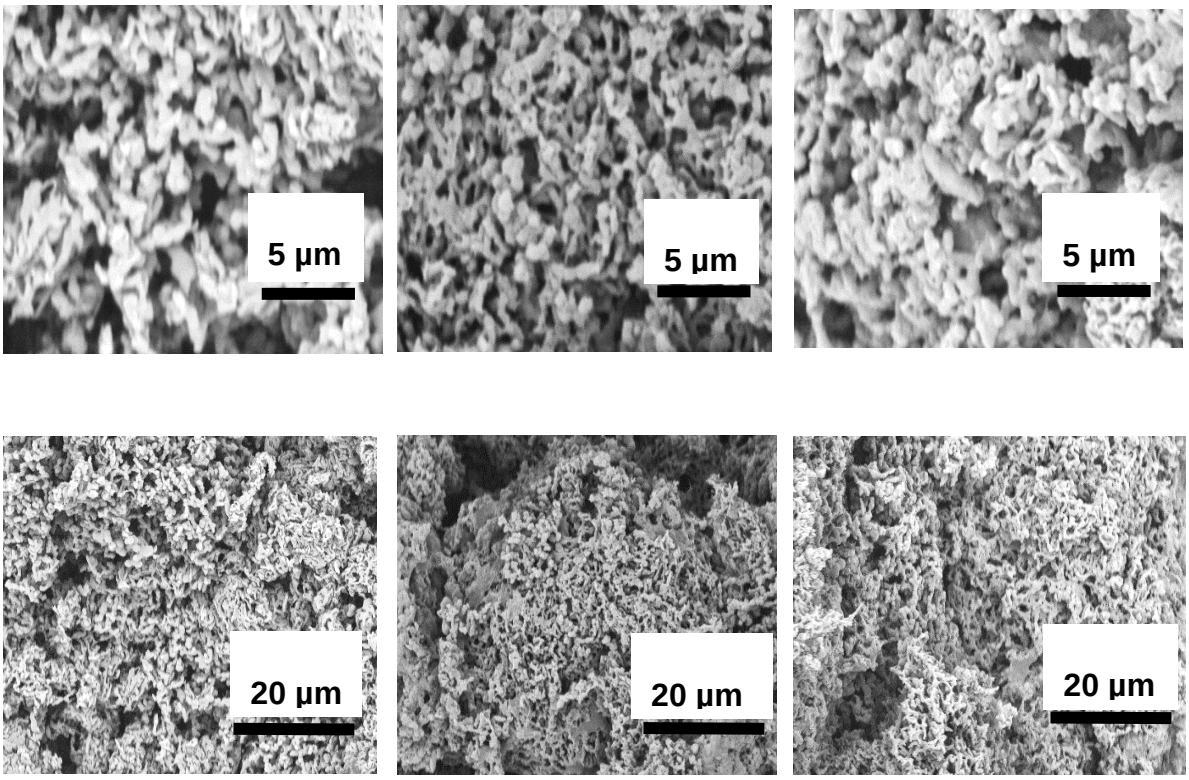

Figure 6.13. SEM microscopic images of PI-epoxy samples at (a) 0.0; (b) 5, and (c) 20% epoxy

6.3.3 Thermogravimetric analysis (TGA) of PI-epoxy

TGA at a rate of 10 °C/min was used in the temperature range of 20 to 700°C under air to investigate the thermal stability of the PI-epoxy samples. It can be noted that, for these samples, weight loss was seen to begin at around 200 °C (see Figure 6.14 -a). This process is marked by the presence of two primary peaks, one at 350 °C and another between 540 and 580 °C for samples with different concentrations of epoxy. Between these two peaks, weight loss occurs at a lower rate (see Figure 6.14 -b). The addition of more epoxy results in decreases in thermal stability in such a way that increasing the concentration of the epoxy from 0.0 to 100 wt% leads to a reduction in the temperature for 10% weight loss by 40%. This shows that samples with a higher

concentration of epoxy demonstrated higher degradation rates during the first decomposition step in a way that was reversed during the second.

The TGA results make it possible for the imidization process to be investigated, as the imidization process involves evaporating the solvent and cyclodehydration, followed by weight loss in the samples with incomplete imidization. Such imidization usually occurs between 100 and 200 °C [325], so neither of the methods used in this work resulted in the samples demonstrating a noticeable weight loss before 200 °C. This confirms that the solvent was removed and that imidization was completed during preparation and drying [33]. This finding generally aligns with those expressed in previous studies of the thermal properties of PI aerogels [22, 50].

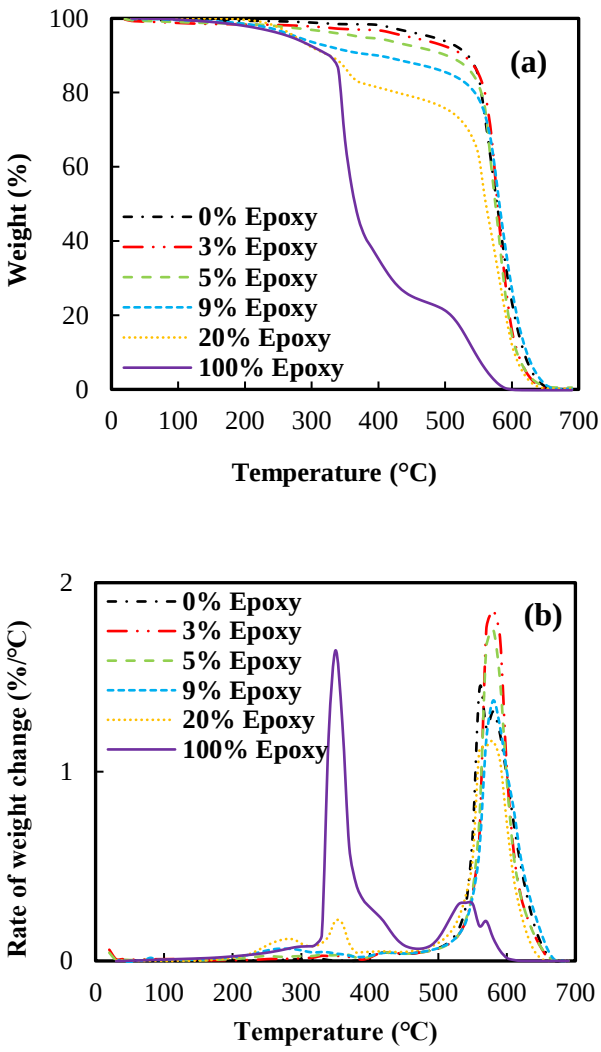

Figure 6.14. (a) Weight, (b) rates of weight change as a function of temperature for PI-epoxy samples

The relation between onset temperature and concentration of epoxy is plotted in Figure 6.15. This diagram indicates that the addition of more epoxy results in the samples becoming more sensitive to heating, leading to their decomposition at lower temperatures.

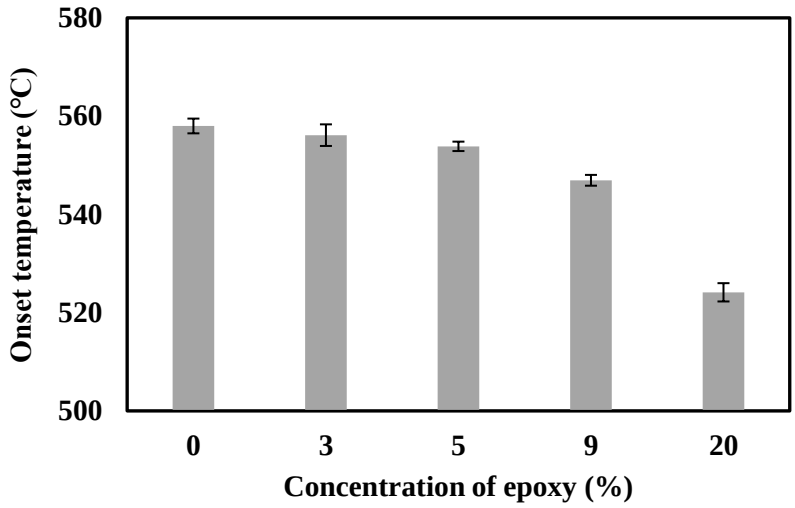

Figure 6.15. Relation between onset temperature and epoxy concentrations Mechanical properties of PI-epoxy

Epoxy samples were characterized with compression to test their mechanical properties. At least three samples were tested for each concentration of epoxy. The stress-strain curve is plotted in Figure 6.16, and ductile behaviour can be observed for each of the samples. Table 6.2 presents the compressive modulus measured from the linear part of the stress-strain curve and the samples' compressive strength, measured at 10% compressive strain.

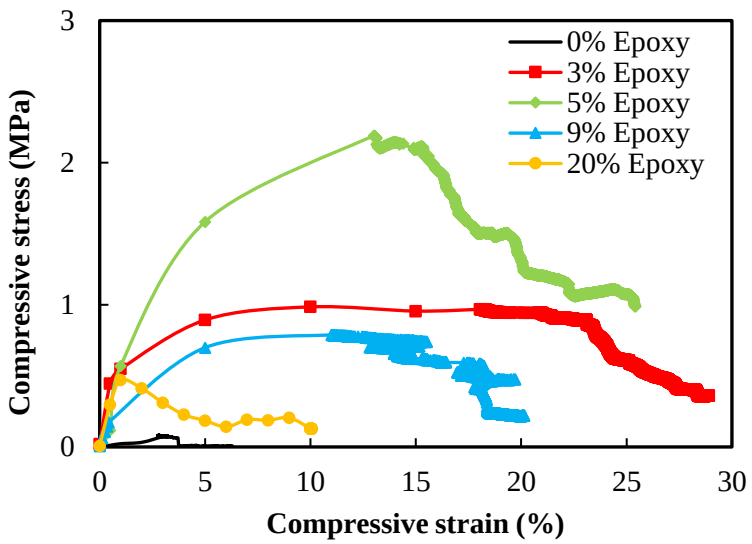

Figure 6.16. Correlation of stress with strain for PI-epoxy

Figure 6.17 (a) shows that increases in the concentration of epoxy up to 5% leads to increases in the compressive modulus to 43.2 MPa; then, for 9 and 20% epoxy, these values drop to 42.1 and 32.18 MPa, respectively. This behaviour may be explained in terms of the manufacturing process. In the case of samples with a higher quantity of epoxy, sticking in the mould meant that, although a release agent spray was used before the moulding process, more force had to be applied during the moulding and demoulding processes. The 5% epoxy sample had the highest compressive modulus of 43.2 MPa and the highest compressive strength of 2.19 at 10% strain (see Figure 6.17-b). This sample also had the highest value for density and the lowest for porosity. After 5% epoxy, the mechanical properties deteriorate as the concentration of epoxy increases. This may be due to the accumulation of epoxy between the particles, which results in a weaker structure. It should be borne in mind that a specific trend for changing the compressive strength and compressive modulus cannot be observed; however, they both change in the same direction with density in both series of samples. This is expected, as mechanical properties typically track with density. These results are in line with the porosity measurements reported.

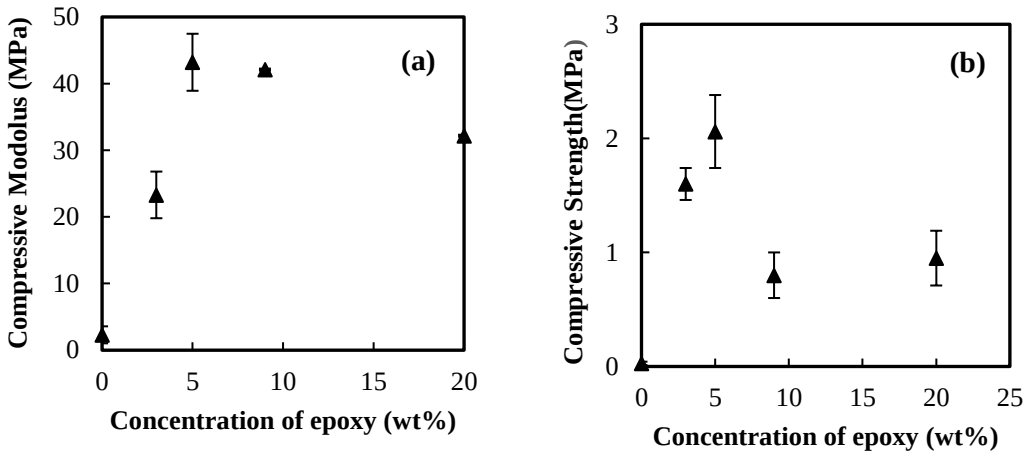

Figure 6.17. (a) Compressive strength and (b) compressive modulus of PI-epoxy stock shape as a function of the concentration of epoxy.

6.3.4 Thermal conductivity for PI-epoxy

Figure 6.18-a presents the thermal conductivity of the PI-epoxy samples as a function of the concentration of epoxy used to treat the PI aerogel particles. It can be seen that thermal conductivity is changed in the range of 52 to 78 mW/m.K. Up to 5% epoxy, the thermal conductivity increases to 78 mW/m.K as a result of the addition of more epoxy, which is in line with what was found in respect of density and porosity. After this, a decrease is noted to 69 mW/m.K. The addition of more epoxies induces the infiltration of the pores, increasing the heat transfer rate. The density correlation with thermal conductivity also shows a step change in respect of the 5% sample (see Figure 6.18-b). As previously discussed, this might be explained in terms of the manufacturing process.

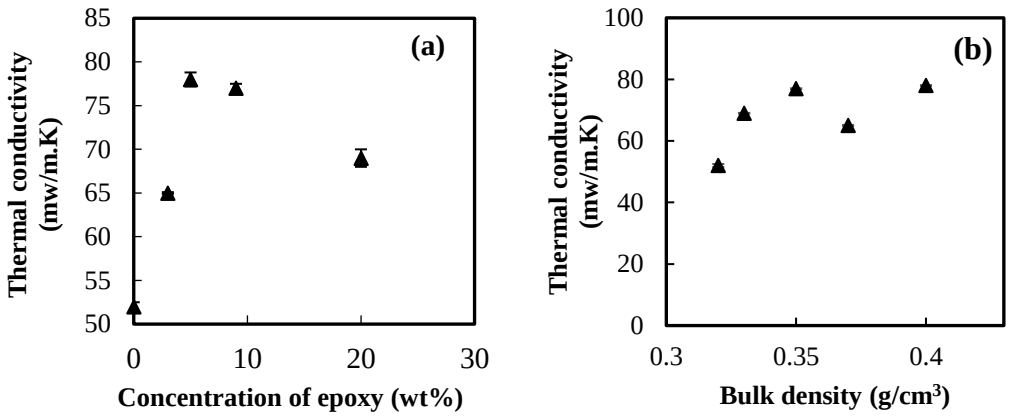

Figure 6.18. Correlation of thermal conductivity of PI-epoxy stock shape samples with (a) concentration of epoxy, and (b) density of stock shape

Table 6.2. Key materials properties of PI stock-shapes produced using PI aerogel particles treated with epoxy

Sample (% DMSO)	**0.0**	**3.0**	**5.0**	**9.0**	**20**
Bulk density (g/cm^3)[a]	00.32 ± 0.02	0.37 ± 0.01	0.40 ± 0.01	0.35 ± 0.01	0.33 ± 0.01
Skeletal density (g/cm^3)[b]	1.48 ± 0.01	1.48 ± 0.01	1.44 ± 0.01	1.46 ± 0.01	1.42 ± 0.01
TGA (10%) (°C)[c]	530	520	500	390	320
Onset temperature (°C)[c]	541.84	556.13	553.85	546.94	524.14
Specific surface area (m^2/g)[d]	8.8 ± 0.1	9.4 ± 0.1	13.1 ± 2.1	14.3 ± 1.21	7.8 ± 1.0
MIP Porosity (%)	66.50 ± 2.30	73.61 ± 3.30	71.01± 1.22	81.10 ± 1.06	84.80 ± 0.70
MIP Median pore diameter (µm)	1.201± 0.302	0.760±0.011	0.861±0.015	1.060±0.108	1.190±0.229
Compressive modulus (MPa)[e]	2.30 ± 1.30	23.30 ±3.50	43.20 ± 4.31	42.10 ± 0.10	32.20 ± 0.10
Compressive Strength, 10% strain (MPa)[f]	-	0.99	2.19	0.78	0.13
Thermal conductivity (W/m.K)[c]	0.052 ±0.005	0.065±0.002	0.078±0.001	0.077±0.005	0.069±0.001

a) measured using mass and volume of the samples ($\rho=m/v$), an average of three samples., b) average of three measurements with pycnometer, c) single measurement, d) average of three samples, e) slope of elastic part in stress-strain curve, f) average of two measurements

6.4 Comparison between different types of stock shape in this work

As previously discussed, this project was undertaken to find new methods to produce PI aerogel stock shape in a direct and more economically competitive way. Table 6.3 presents data relating to the properties of the PI stock shape received from this project's industrial partner (Blueshift stock shape). The comparison between the properties of all three types of stock shape shows that, in respect of the epoxy samples, the addition of epoxy and increases in the density of the samples results in greater thermal conductivity and a lower porosity as compared with the Blueshift stock shape and PI-DMSO samples. On the other hand, in the cost of most applications, PI aerogel will be selected due to its more desirable mechanical properties, which highlights the importance of focusing on how this property can be improved. The epoxy samples show a high compressive modulus (up to 43.20 ± 4.31 MPa).

Compared to the PI stock shapes fabricated using the methods previously introduced in this study, a porous uniform structure can be observed for the PI stock shape produced directly by Blueshift (Figure 6.19). This sample had 84.70% porosity and 0.23 g/cm3 density, as shown in Table 6.3. It is noted that PI-DMSO-30% had properties that were very close to this sample (with a porosity of 88.80% and a density of 0.22 g/cm^3), though the porous structures are quite different. The sample produced by Blueshift was found to feature a network of small particles interconnected throughout the porous structure in such a way that they resembled a fibrous structure.

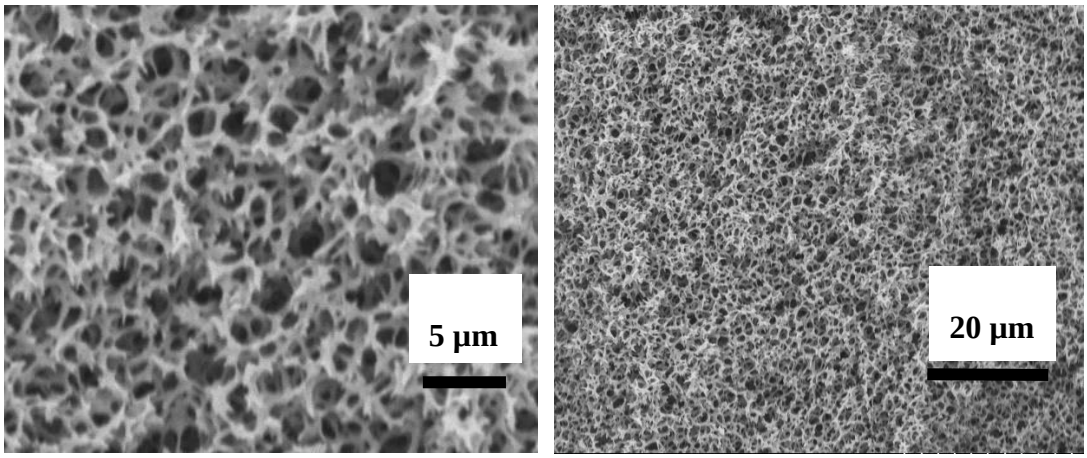

Figure 6.19. SEM microscopic images of Blueshift stock shape

The PI-epoxy samples had lower porosity, greater density and mechanical properties than the PI-DMSO samples and the PI stock shape directly produced by Blueshift.

This work results in a new procedure for producing PI stock shapes using aerogel particles, involving the treatment of PI aerogel particles and the subsequent consolidation of these particles into stock shape samples. This process involved investigating the stock shapes' porous texture and thermal and mechanical properties. This showed that the incorporation of epoxy in the PI aerogel particles (up to 5 wt%) can significantly improve the stock shape's mechanical properties. The PI-DMSO samples were found to be thermally stable up to 500 °C. It was also shown that the thermal conductivity of the particle-converted stock shape increased as a result of the addition of more epoxy and this was due to the infiltration of the pores. Both methods created samples with pores larger than 50 nm, indicating the presence of macroporosity in their pore structure. However, the densities of stock shape samples with epoxy were higher due to the presence of the epoxy molecules between the aerogel particles. Although the mixture was left at room temperature before and after moulding, infiltration might have occurred, potentially reducing the porosity and thus increasing density. Nevertheless, the results of this study demonstrate that it is feasible to produce PI stock shapes using PI aerogel particles. Overall, the presented techniques can be used to prepare PI stock shape with reasonable thermal and mechanical properties in a short time compared to the stock shape fabricated directly by Blueshift.

Generally, fabricating stock shape with epoxy method yields a more attractive outcome in terms of appearance and mechanical properties. On this basis, this method was selected for consolidating the aerogel particles synthesized in this project.

Table 6.3. Key material-related properties of directly produced PI stock shapes with Blueshift

Sample	Bulk density (g/cm^3)	TGA (10%) (°C)	MIP porosity (%)	Compressive modulus (MPa)	Compressive strength, 10% strain (MPa)	Thermal conductivity (W/m.K)
Blueshift PI stock shape	0.23	550	84.70	21.00	1.80	0.42±0.005

6.5 Characterization results of wet gel ground powder stock shape (PI-WGG-epoxy)

After the synthesis of the PI aerogel microparticles using the WGG in different dilution ratios, they needed to be treated and consolidated in a specific size and shape and characterized. Considering the results found and conclusion reached regarding Aero-Zero, adding epoxy was selected as the sole method for consolidating the WGG. The characterization results for PI-epoxy samples show that the 5% epoxy had better mechanical properties. Therefore, the PI-WGG particles were consolidated with 0 and 5% epoxy in a 1×1×1 inch mould and cured for 24 h at room temperature, followed by a further 6 h at 80 °C. Unfortunately, the sample produced without the use of epoxy was unsuccessful, as the PI-WGG-0% epoxy could not be shaped or retained in powder form after the demoulding process, as shown in Figure 6.20. For this reason, PI-WGG stock shape samples were produced using 5% epoxy.

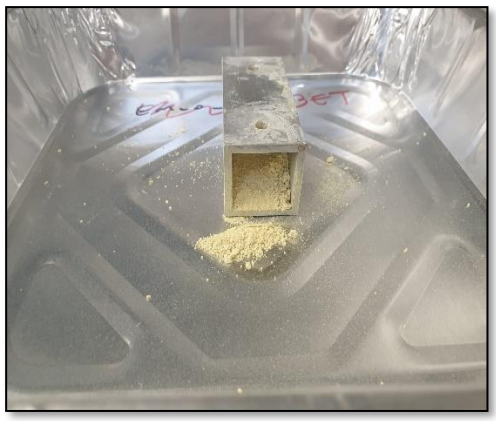

Figure 6.20. PI-WGG-0% epoxy sample after demoulding

6.5.1 N_2 Sorption for PI-WGG-epoxy stock shape

The pore structure and surface area of the PI-WGG-5% epoxy stock shape were characterised using N_2 sorption, and the results are shown in Figure 6.21 and Table 6.4. Figure 6.21-a shows the bimodal distribution in the range of 3 to 16 nm, indicating the mesoporous status of all the pores. Increasing the dilution ratio in the PI-WGG powders can lead to decreases in the volume of the adsorbed gas in the stock shape. This observation indicates the presence of microporosity for the samples with a higher dilution ratio. The nitrogen adsorption isotherms rise above $P/P_0 = 0.9$ but do not reach the saturation plateau, indicating that they are type II isotherms Figure 6.21. The sharp increment observed for the higher pressures also confirms the presence of microporosity in these samples. The surface area is changed in the range of 0.30 to 6.93 m^2/g due to the ambient pressure drying method used in fabricating these samples.

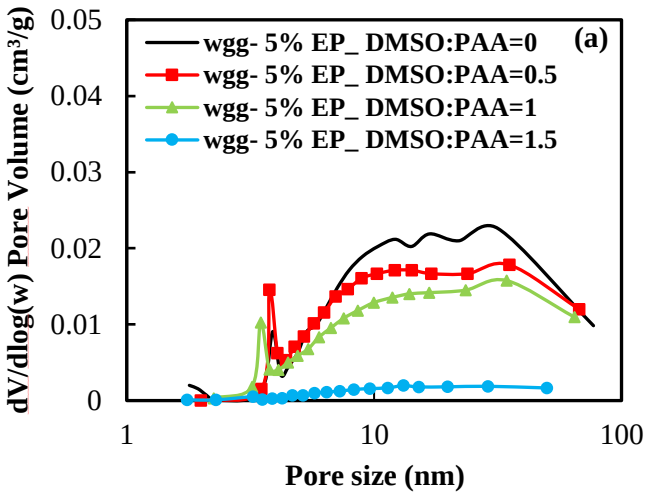

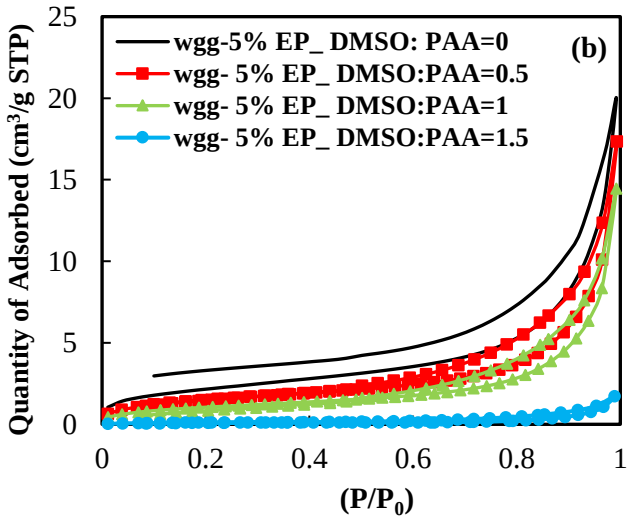

Figure 6.21. N_2 sorption of PI-WGG-epoxy stock shape, (a) pore size distribution, (b) N_2 sorption isotherms (at -196 °C)

6.5.2 MIP for PI-WGG-epoxy stock shape

The MIP was used in order to investigate the total porosity, pore size distribution and bulk density of the produced stock shape samples. The porosity for these samples was calculated using bulk and skeletal density and the MIP pore size distribution is plotted in Figure 6.22. Aside from the stock shape sample produced from powder with DMSO: PAA=1.5, a bimodal distribution can be seen to have been yielded for all the samples. As mentioned in respect of N_2 sorption, the porous structure for this sample was found to be primarily macroporous in its nature. As previously discussed in respect of the PI-

WGG particles, increasing the ratio of dilution results in the size of the particles reducing, with smaller particles existing closer to each other during the consolidation process such that density increases. This result is confirmed in the SEM images (see Figure 6.23), which clearly show the presence of epoxy inside the samples. An increase in the dilution ratio results in lower porosity in the powder source for producing the stock shape. As a result, adding the quantity of epoxy during the consolidation process results in the particles sitting closer to each other in a way that increases density; however, the MIP median pore diameter also increases. As the SEM image confirms, this is mostly evident in respect of the intra-pores. The epoxy infiltrates the small pores inside the particles, giving rise to larger chunks and, thus also larger pores between these chunks. It seems that, through the addition of epoxy and increasing the ratio of dilution, small pores become filled due to infiltration; as a result, the pore size is increased while the total overall porosity is reduced. Bulk density was measured using both MIP and the samples' mass and volume.

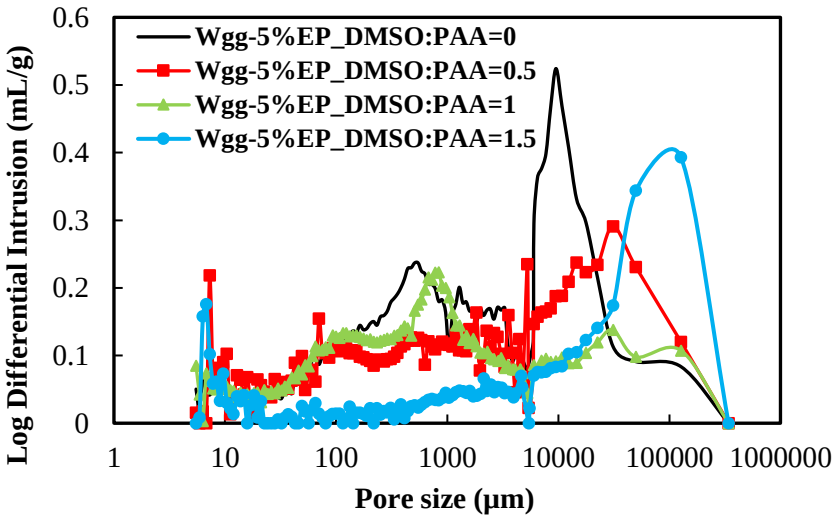

Figure 6.22. MIP pore size distribution for PI-WGG-epoxy

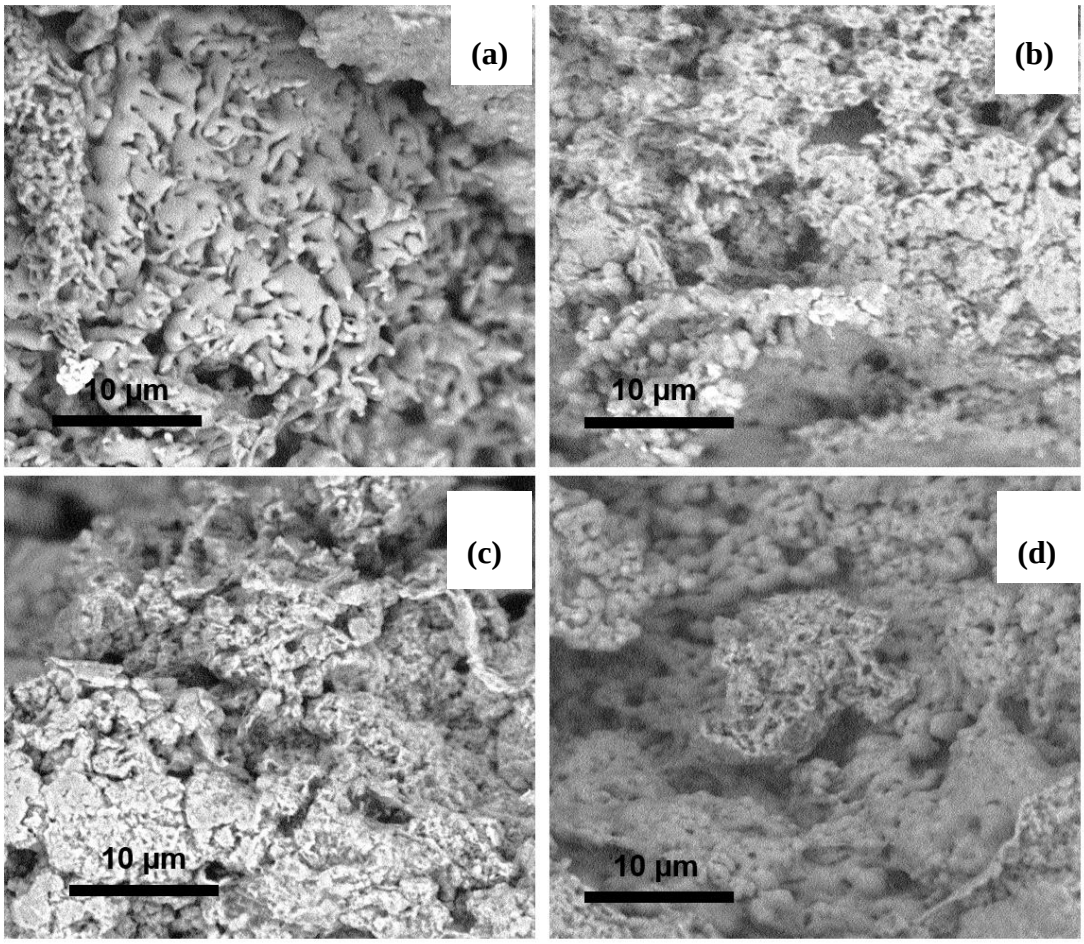

Figure 6.23. SEM for PI-WGG stock shape with 5% epoxy with different dilution ratios in powders; (a) 0.0; (b)0.5; (c) 1.0; (d) 1.5

6.5.3 TGA for PI-WGG-epoxy stock shape

The correlation of weight change with temperature is reported in Figure 6.24. This shows that thermal stability reduces as a result of an increase in dilution in the particle synthesis process. In the first step (0-200 ℃), weight change can be observed at a low rate, potentially due to residual DMSO or water added during manufacturing. In the next step, from 200 to 500 ℃, the weight change corresponds to the decomposition of the added epoxy. Finally, all the samples can be seen to have decomposed at different rates during the last stage, although the rate of decomposition reduces as the ratio dilution increases across the board. The presence of larger pores can be analysed as having trapped more solvent inside than on the sample's surface; therefore, more time is required for complete decomposition. Furthermore, aside from in the case of ratio 0, increasing the temperature to 700 ℃ does not result in the samples' complete

decomposition, suggesting that this would necessitate allowing more time for this process and/or the presence of higher temperatures.

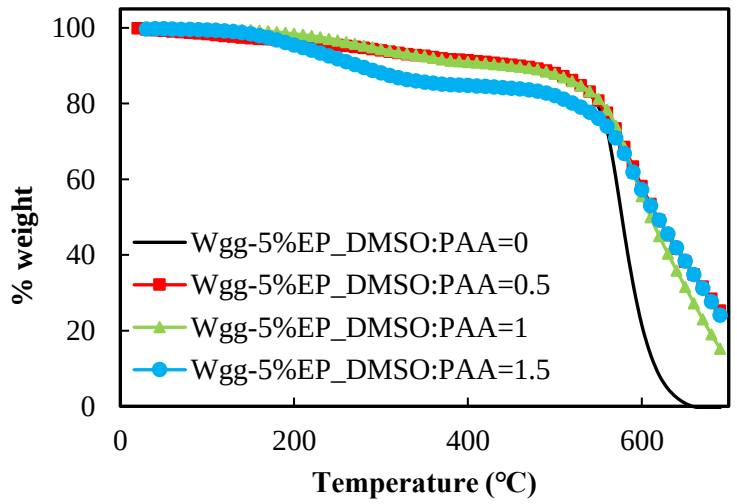

Figure 6.24 Correlation of weight change with temperature for PI-WGG-epoxy

Only one of the samples was tested with TGA for a longer time in order to establish whether complete decomposition would be achieved. The PI-WGG-5%EP sample with a ratio of 1.5 was tested under air with a heating rate of 10 °C/min from 20 to 700°C and then isotherm for 2 h at 700 °C. The correlation of the weight change with time indicates that allowing more time to the sample in the same condition would cause complete decomposition (see Figure 6.25).

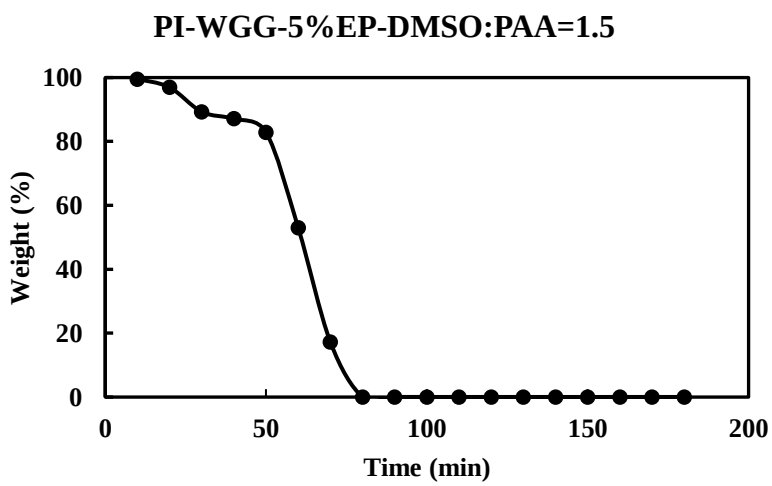

Figure 6.25. Correlation of weight change with time for PI-WGG-5%EP sample under the isotherm condition

6.5.4 Mechanical properties of PI-WGG-epoxy

Investigating the mechanical properties of the PI-WGG stock shape samples was undertaken using a compression test. As mentioned, all the samples were produced using 5% epoxy. Two samples were tested, and the measurement average is plotted in the following. Figure 6.26 shows the stress-strain plot for the PI-WGG-5% epoxy samples. This graph shows that ductile behaviour can be observed for all the samples, which demonstrated elastic behaviour up to the failure point. Compressive modulus was measured from the first linear part of the stress-strain curve. The correlation between compressive modulus and compressive strength is plotted in Figure 6.27. These results show that, for the samples with a ratio of 0.5 to 1.5, increases in the dilution ratio as a result of increases in the size of the pores resulted in decreases in compressive strength and modulus. The correlation of compressive modulus with density (see Figure 6.28) indicates that increasing the density results in a greater modulus, increasing from 7.2 to 36.6 MPa for these samples. These samples all demonstrate reduced mechanical properties as compared with PI- 5% epoxy produced using Aero-Zero particles (with a compressive modulus of 43.2 MPa).

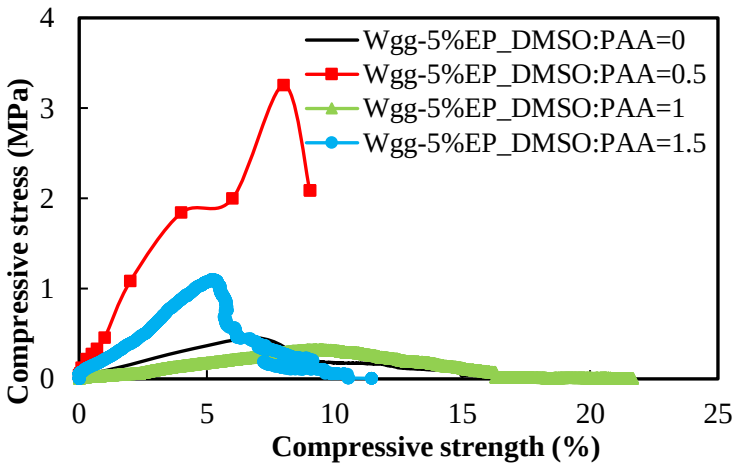

Figure 6.26. Stress-strain curve for PI-WGG-epoxy stock shape

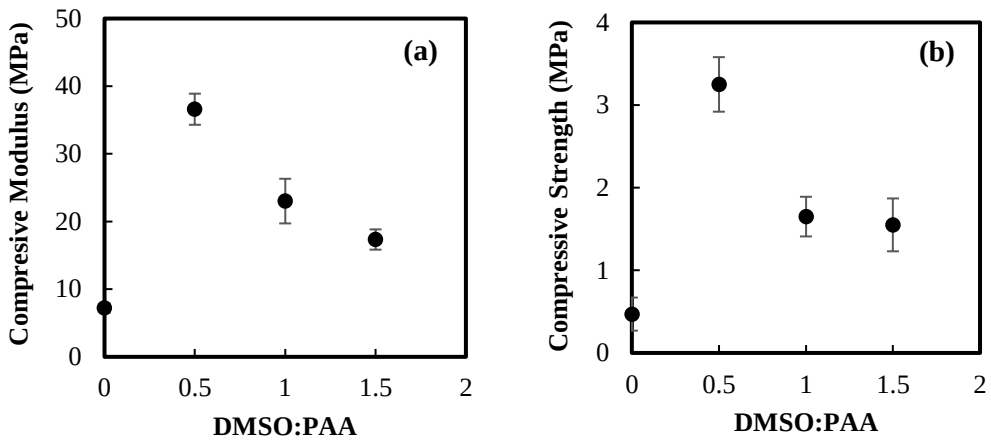

Figure 6.27. Correlation of (a) compressive modulus and (b) compressive strength with types of powder for PI-WGG-5% epoxy stock shape

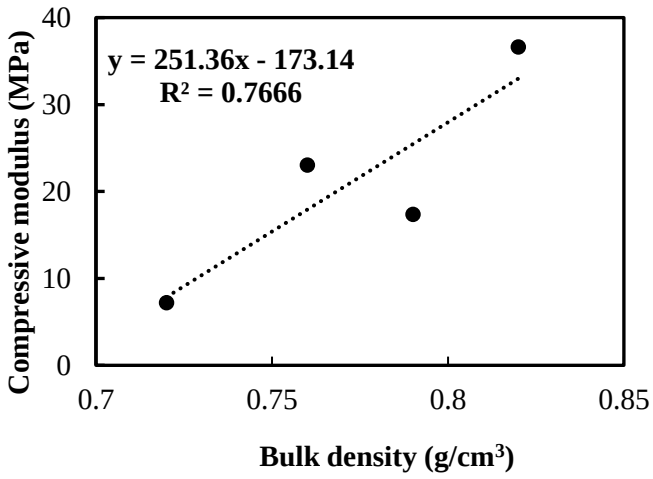

Figure 6.28. Compressive modulus-density for PI-WGG-5% epoxy samples

6.5.5 Thermal conductivity of PI-WGG-epoxy stock shape

Two stock shape samples were tested using the hot-wire technique to ascertain the degree of thermal conductivity of these samples. All six sides of each sample were tested for this purpose. For each condition, the average of 11 measurements is presented in Table 6.4, and thermal conductivity can be seen to increase from 70 to 140 (mW/m.K). This indicates that, in respect of the WGG powder, the size of the particles reduces as the dilution ratio increases, with smaller particles packing closer to each other such that density and thermal conductivity increase. A greater thermal conductivity can also be observed due to the increased density and lower degree of

porosity in these samples as compared with the Aero-Zero stock shape produced with 5% epoxy.

Table 6.4. Key properties of PI-WGG-5%EP at a different dilution ratio of powder

Sample (% DMSO)	PI-WGG-5%EP DMSO:PAA=0	PI-WGG-5%EP DMSO:PAA=0.5	PI-WGG- 5%EP DMSO:PAA=1	PI-WGG- 5%EP DMSO:PAA=1.5
Specific surface area (m^2/g)[a]	6.9 ± 1.3	4.8 ± 1.0	4.1 ± 0.3	0.3 ± 0.2
Skeletal density (g/cm^3)[b]	1.390± 0.004	1.370 ± 0.003	1.390 ± 0.003	1.420 ± 0.006
MIP median pore diameter (nm)[c]	5.50	5.63	11.23	74.52
MIP bulk density (g/cm^3)[c]	0.72	0.82	0.76	0.79
Bulk density (g/cm^3)[d]	0.57±0.15	0.65±0.05	0.61±0.02	0.63±0.03
MIP Porosity (%)[c]	53.50	33.90	40.10	40.08
Porosity (%)[e]	45.30	40.10	48.01	44.40
Thermal conductivity (W/m.K)[a]	0.07±0.01	0.13±0.04	0.12±0.03	0.14±0.01
TGA (10%) (°C)[f]	455	452	450	273
Compressive modulus (MPa)[g]	7.20± 0.30	36.60 ±2.30	23.02 ± 3.30	17.34 ± 0.50

a) average of three samples; b) average of three measurements using pynometry; c) MIP, single measurement, d) Via $\rho=m/v$ an average of three measurements; e) Via $\Pi= 100 \times (\rho s-\rho b)/\rho s$; f) under air; g) slope of linear segment at the stress-strain curve

6.5.6 Summary

This section detailed how the PI-WGG stock shape samples that were produced with 5% epoxy were characterized and analyzed using several different techniques. The production process showed that it was essential to use epoxy despite the consolidation method used with the Aero-Zero powder. The PI-WGG-epoxy stock shape samples were found to have higher density, lower porosity and higher thermal conductivity compared to PI-epoxy samples and the stock shape produced directly by Blueshift. Among the stock shapes made with powders with different dilution ratios, the sample made with DMSO: PAA= 0.5 emerged as having the most optimal properties. Figure 6.29 presents the comparative results between this sample, PI-5% epoxy (made with Aero-Zero) and the PI stock shape produced directly by Blueshift. This indicates that the PI stock shape that is produced directly is associated with better results in terms of thermal stability, porosity and density. The stock shape samples produced by consolidating the particles using epoxy were found to demonstrate more desirable mechanical properties. The compressive modulus for PI-5% epoxy and PI-WGG (ratio=0.5) showed 51 and 42% increases, respectively, compared with the stock shape produced directly.

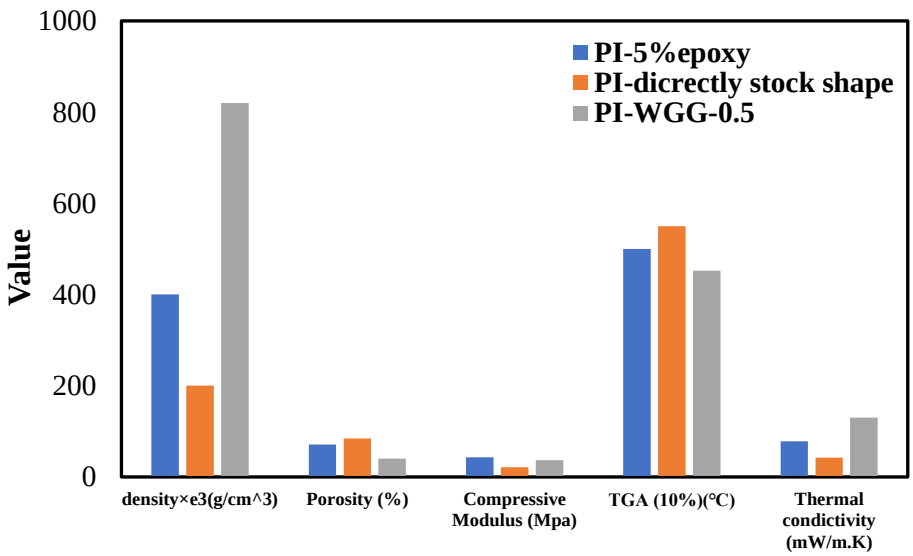

Figure 6.29. Comparison between properties of the most optimal PI-WGG stock shape and the Aero-Zero stock shape with 5% epoxy and the stock shape produced directly by Blueshift

6.6 Characterization results for emulsion powder stock shape (PI-EM-stock shape)

The stock shape was produced using particles synthesized by means of the emulsion process at different dilution ratios and consolidated using epoxy 0.0 and 5% epoxy. Similar to the PI-WGG stock shape, the production of stock shape using emulsion particles also relies on the addition of epoxy. Therefore, only PI-EM-5% epoxy samples at different dilution ratios for the powder's source were produced and characterised. The moulded particles were cured and dried for 24 h at room temperature and then another 6 h at 80 °C. All the samples were fully characterized, and their properties were compared with the previous stock shape samples.

6.6.1 N_2 sorption for PI-EM-epoxy

The PI-EM-5% epoxy stock shape was characterised using N_2 sorption to investigate pore structure and surface area.

Figure 6.30-a shows the samples' bimodal pore size distribution between 3 and 36 nm. This result indicates that the types of pores in the samples are primarily mesoporous. PI-EM stock shape with DMSO: PAA=0.5 was found to have adsorbed the greatest volume of N_2, indicating that this sample had a greater pore volume as compared with the others (see Figure 6.30-b). As can be observed in Table 6.5, the surface area for these samples is in the range of 2 to 9 m^2/g. Having a low surface area is associated with a high degree of shrinkage, mainly during the ambient pressure drying process. As discussed in Chapter 4, the emulsion particles with a ratio of 1.5 are the largest, with this being due to a high degree of agglomeration. Large particles are prevented from sitting close to each other, giving rise to large pores that cannot be detected using N_2 sorption. For this reason, investigating the porous structure of the PI-EM-epoxy samples necessitated using MIP. The results of this process are presented in the next session.

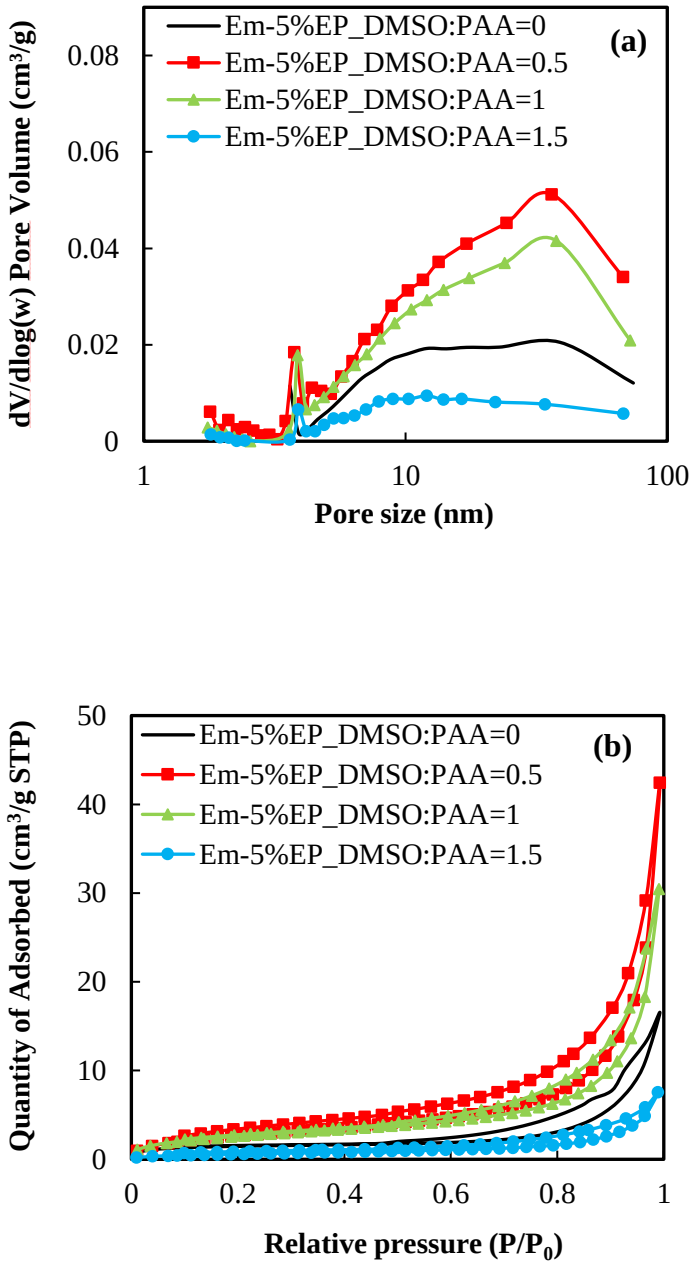

Figure 6.30. a)Pore size distribution, (b) N_2 sorption isotherms (at -196 °C) for PI-EM-5% EP at different dilution ratios

6.6.2 MIP for PI-EM-epoxy

MIP was used to measure the PI-EM-epoxy samples' pore size distribution, bulk density, and porosity. Low and high pressure was applied in the range of 0-30 psi, followed by a sweep of 30-33000 psi. The bulk density of the stock shape was

measured using MIP in terms of mass and volume. The figures reflecting MIP-calculated porosity and the porosity calculated using bulk and skeletal density are presented in Table 6.5.

The bimodal pore size distribution between 200 nm to 20 µm for the PI-EM-epoxy with ratios 0.5 and 1 is very similar. Figure 6.31, which presents the emulsion powder's pore size distribution, also demonstrates similar behaviour for these two powders. The sizes of the particles for ratios 0.5 and 1 are 7.9 and 8.1 µm, respectively, confirming that increasing the dilution from 0.5 to 1 affects the pore size of neither the powder nor the stock shape form. Comparing the pore size distribution for the stock shape with ratio = 0 shows that smaller pores in the powder shape (around 300nm) are removed in the stock shape. This could be due to infiltration of the pores by epoxy. Furthermore, some of the pores likely collapsed during the moulding process and as a result of the compression force. The PI-EM-epoxy stock shape sample with ratio=1.5 shows a considerable peak at 100 µm. Smaller pores around 1 µm in the powder form were removed in the stock shape sample. As previously explained, the reason for the presence of such huge pores in this sample relates to the presence of such large, agglomerated particles.

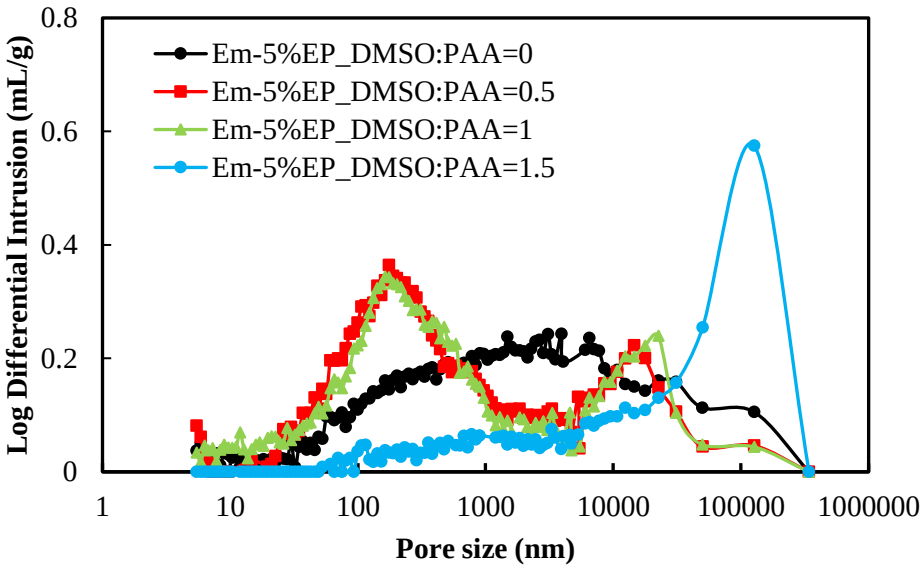

Figure 6.31. MIP pore size distribution for PI-EM-5% EP

Both measured bulk density (MIP and density calculated with the mass and volume of the sample) increases in the PI-EM-epoxy samples as a result of increases in the dilution ratio. Compared to the powder shape, the addition of the epoxy and the density

associated with the moulding process of the stock shape is increased by up to 60%. The MIP bulk density ranges from 0.7 to 0.76 g/cm^3. Figure 6.33Figure 6.32 shows the correlation of porosity and density with the powder type in the stock shape samples. For the emulsion particles, it emerged that increasing dilution results in larger particles. Moulding such larger particles using the same quantity of epoxy necessitates that greater pressure be used compared to the same process performed with smaller particles. It is likely that this process resulted in the destruction of some pores, resulting in lower porosity and greater density.

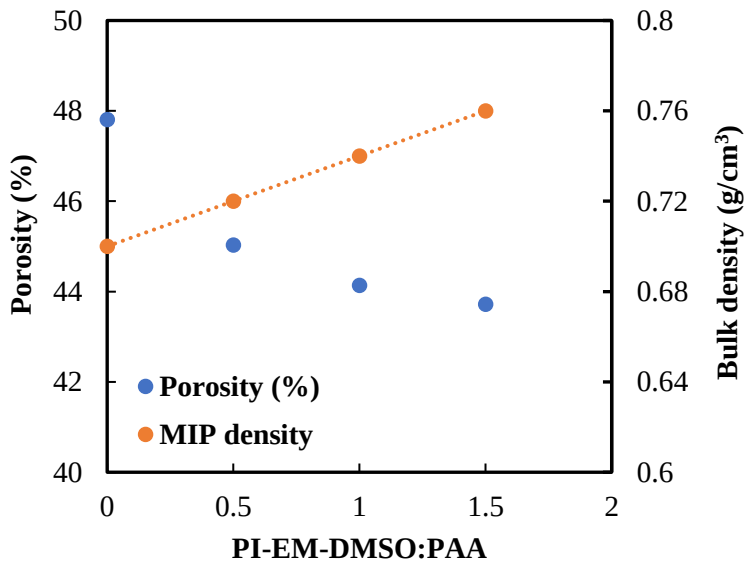

Figure 6.32. Correlation of porosity and density with the type of powder in the stock shape samples

The SEM images for the PI-EM-EP at different ratios of dilution exhibit a porous structure on the surface and inside the stock shape samples (see Figure 6.32). In addition, they show that the samples increase in density as dilution increases. The porous structure can be observed on the surface of the samples, as can the role of the bond between the particles featuring the presence of epoxy. Using the MIP characterization, it emerged that the average pore size for the sample with ratio=0 was higher compared to the ratios of 0.5 and 1. SEM was also used to confirm this measurement in terms of the particles' size and morphology.

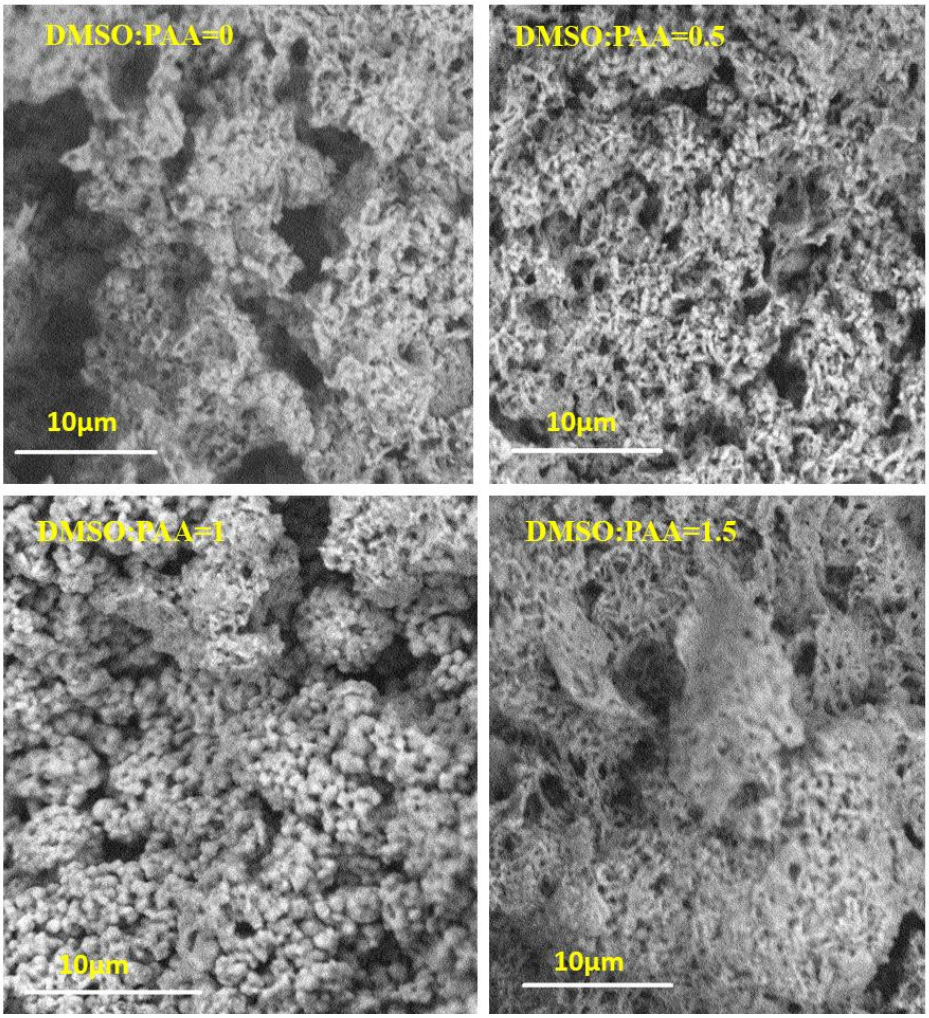

Figure 6.33. SEM micrograph of the PI-EM-5%EP stock shape sample with powder of different dilution ratios

6.6.3 TGA for PI-EM-epoxy stock shape

To investigate the thermal stability of the stock shape samples, TGA was run between 20 to 700 ℃ at the rate of 10 ℃/min. The correlation of weight change with temperature is shown in Figure 6.34. A weight loss can be observed for all samples at around 100 ℃. This may be due to the evaporation of the residual water inside the samples used during the manufacturing process or humidity adsorption that occurred during the ageing process. The following weight loss peak is at around 350 ℃, due to the curing of the epoxy present inside the samples. At the next step, all the samples start to degrade at different rates in such a way that suggests that 700 ℃ would be insufficient to result in completed degradation. To investigate whether this was the case, for PI-EM-5%EP with DMSO: PAA=1.5, 2 h of isotherm was added to the TGA cycle at 700 ℃.

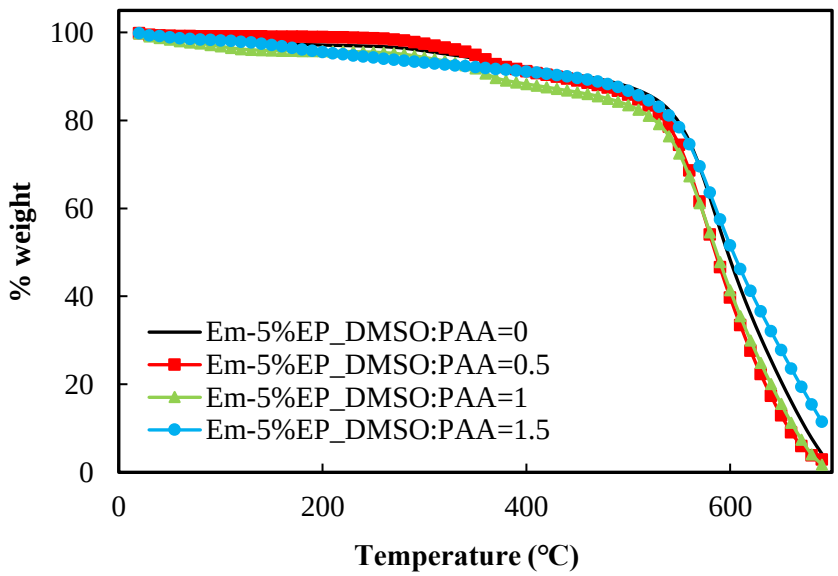

Figure 6.34. Correlation of weight change with temperature for PI-EM-5%EP

Figure 6.35 presents the weight change as a function of time for PI-EM-5%EP with a ratio of 1.5. The results show that after 70 min, all the samples decomposed.

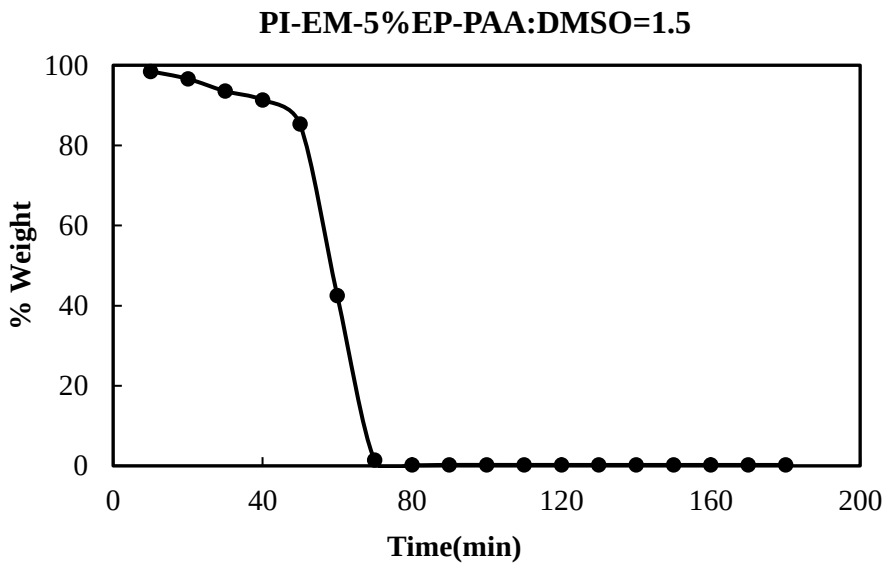

Figure 6.35. Correlation of weight change with time for PI-EM-5%EP sample under the isotherm condition

6.6.4 Mechanical properties of PI-EM-epoxy stock shape

Investigating the mechanical properties of the stock shape samples was performed using a compression test. For each condition, two samples were tested, and the stress-

strain curve shows ductile behaviour in respect of all the samples (see Figure 6.36). The failure point for all the samples is before 10% strain. As a result, the compressive strength at 10 % strain could not be defined for these samples. The correlation of compressive modulus with density is plotted in Figure 6.37. The compressive modulus is in the range of 15 to 24 MPa. As was expected from the SEM image, a denser structure was detected for the stock shape with ratios 1.0 and 1.5.

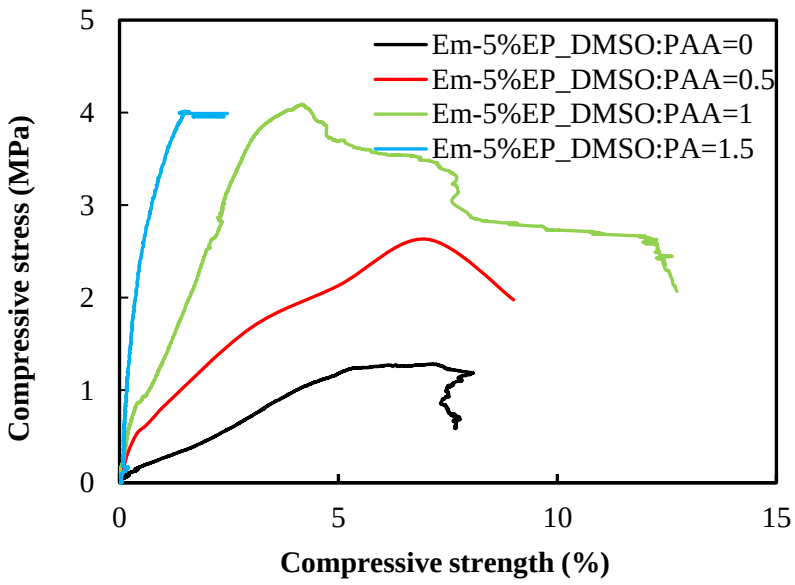

Figure 6.36. Stress-strain curve for PI-EM-5%EP samples with powders with different dilution ratios

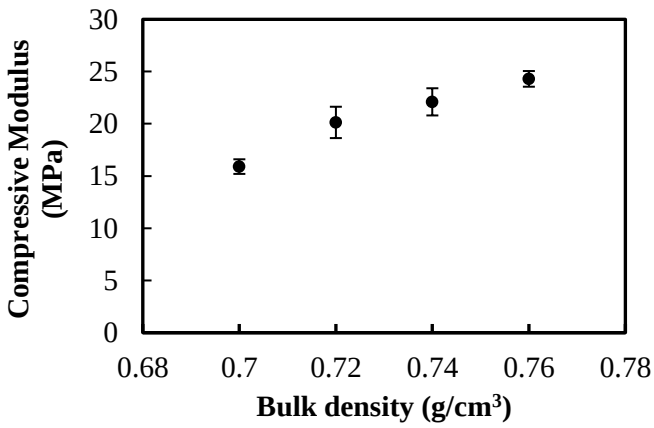

Figure 6.37 Compressive Modulus-density correlation for PI-EM-EP samples

6.6.5 Thermal conductivity of PI-EM-epoxy stock shape

This section details how the thermal conductivity of the PI-EM-epoxy stock shape samples was investigated (see Figure 6.38). As expected, increases in density were associated with increases in thermal conductivity, indicating that, for the emulsion powders, increasing the dilution ratio (and thereby reducing the solid content) resulted in the creation of larger pores inside the particles. Likely, infiltrating of epoxy during the consolidation process inside the larger pores resulted in an increase in density and a reduction in the porosity of the resultant stock shape, with the filled large porous area giving rise to a solid path by which heat could be more easily transferred. On this basis, increasing the dilution ratio from 0 to 1.5 is assumed to increase the stock shape's thermal conductivity (44%).

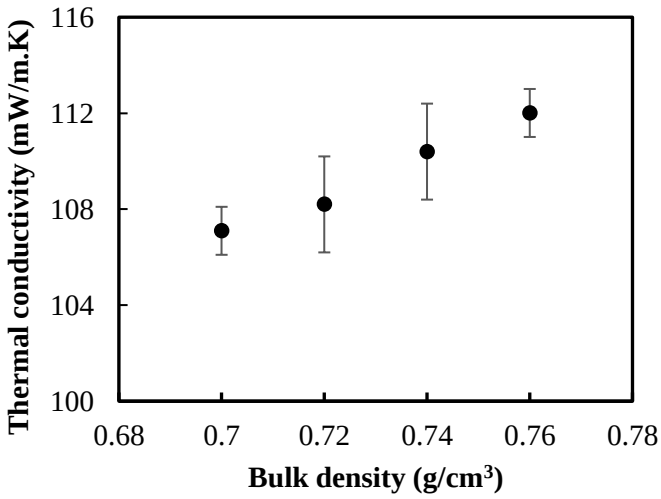

Figure 6.38. Change in thermal conductivity as a function of density for PI-EM-EP stock shape

Table 6.5 Key properties of PI-EM-5%EP with different dilution ratios

Sample (% DMSO)	PI-EM-5%EP DMSO:PAA=0	PI-EM-5%EP DMSO:PAA=0.5	PI-EM-5%EP DMSO:PAA=1	PI-EM -5%EP DMSO:PAA=1.5
Specific surface area (m^2/g)[a]	5.7 ± 1.0	9.2 ± 0.4	9.9 ± 0.3	2.3 ± 0.2
Skeletal density(ρ_s) (g/cm^3)[b]	1.35± 0.002	1.38 ± 0.004	1.40 ± 0.004	1.40 ± 0.003
MIP median pore diameter (nm)[c]	2.64	0.48	0.52	74.52
MIP bulk density(ρ_b) (g/cm^3)[c]	0.70	0.72	0.74	0.76
Bulk density (g/cm^3)[d]	0.60 ±0.02	0.62 ±0.01	0.63±0.02	0.73±0.1
MIP Porosity (%)[c]	42.85	50.20	44.70	40.70
Porosity (%)[e]	47.81	45.03	44.14	43.72
Thermal conductivity (W/m.K)[a]	0.07±0.001	0.108±0.002	0.110±0.002	0.112±0.001
TGA (10%) (°C)[f]	450	425	362	430
Compressive modulus (MPa)[g]	15.9± 0.70	20.13 ±1.50	22.10 ± 1.30	24.30 ± 0.7

(a) average of three samples; b) average of three measurements using pycnometry; c) MIP, single measurement, d) Via ρ=m/v an average of three measurements; e) Via $\Pi = 100 \times (\rho_s - \rho_b)/\rho_s$; f) under air; g) slope of linear segment at the point of stress-strain

6.6.6 Summary

As with PI-WGG, the production of the stock shape using the emulsion powders necessitated the use of epoxy in that, without epoxy, the samples would not form. The characterization procedures showed that reducing the solid content in the original powder resulted in a stock shape with higher density, lower porosity and thermal stability, higher thermal conductivity and a compressive modulus. Overall, compared to the PI stock shape produced directly by Blueshift, the P-EM-EP samples were found to have a higher compressive modulus. Among the PI-EM-5% samples, the sample with DMSO: PAA=1 emerged as being the most optimal in terms of mechanical properties. Figure 6.39 compares the different properties of this sample with PI-epoxy (Aero-Zero stock shape) and Blueshift stock shape. The results show that PI-EM demonstrates an improvement of 5% over the mechanical properties of the PI stock shape compared to the PI stock shape produced directly by Blueshift.

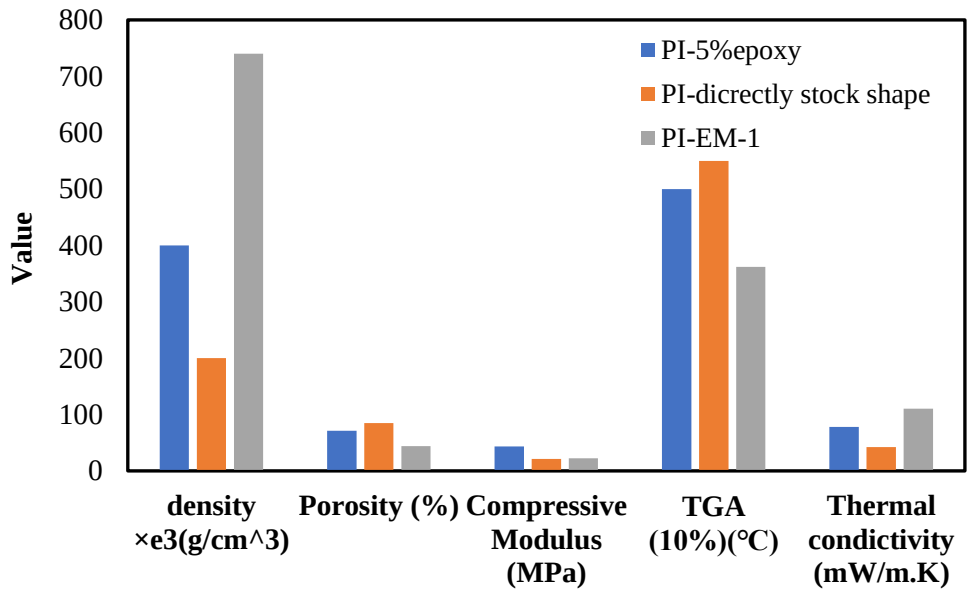

Figure 6.39. Comparison between properties of PI-EM-1 stock shape, the Aero-Zero stock shape with 5% epoxy and the stock shape produced directly

The powder produced using the dry milling process, wet gel grinding method and emulsion process were consolidated using epoxy. The various stock shape properties are plotted in Figure 6.40. Due to the addition of epoxy, these stock shapes' density is

higher than those of the directly-produced stock shapes. In addition, as a result of the degradation point of epoxy being around 300 °C, these samples were found to be less thermally stable. Comparing the results of PI-WGG-0.5 and PI-EM-1 shows that the thermal stability of the WGG is 20% higher in terms of the temperature for 10% decomposition. The density of this sample is 0.82 g/cm^3, which is 9.5% higher than is the case for PI-EM-1, giving rise to greater heat transfer through this sample. The surface area of PI-EM-1 is also 51% higher than PI-WGG, giving rise to more surface area with the air and thus increasing the combustion rate.

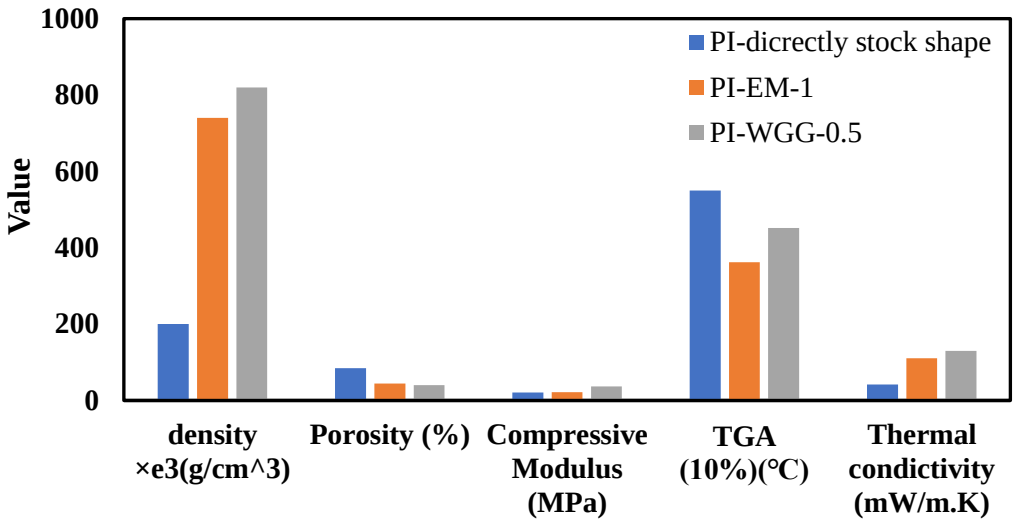

Figure 6.40. Comparison between properties of the most optimal PI-EM-1 stock shape, the directly-produced Blueshift stock shape and PI-WGG-0.5

In the next chapter the conclusion for the whole work is summarised, followed by the possible future work.

Chapter 7 Conclusion and future work

This chapter concludes the project before pointing the direction for the potential future work focusing on further improvement in the manufacturing of PI stock shape.

7.1 Conclusion of thesis

Aerogels have attracted the attention of scientists due to the wide variety of applications for which they are suitable as a result of their unique properties. Compared to silica aerogel, PI aerogel has both greater thermal properties and more desirable mechanical properties. For the current project, the main goal was to introduce and develop a new method for fabricating the PI aerogel stock shape to reduce the manufacturing cost for this project's industrial partner, Blueshift. The findings of this project suggest that there is promise in the prospect of producing stock shape by consolidating PI aerogel particles as a means of changing the place of solvent exchange. By synthesizing the powder and converting the powder into the stock shape, the solvent exchange is conducted with a powder form, necessitating less time, chemicals and energy to be used to form the PI aerogel stock shape as compared with the fabrication of such PI aerogel in a more direct fashion.

There are also benefits to the process proposed here in terms of the drying method. Using ambient pressure drying results in less energy consumption as compared with supercritical drying despite the fact that such a drying process takes more time. This makes it possible to get around certain problems with supercritical drying, such as the high temperature and pressure that using this method necessitates. There are also problems with supercritical drying in terms of the sample size. Supercritical drying cannot be used on an industrial scale as the instruments used to perform this style of drying are small and would therefore have to be used several times with a 1 litre chamber dryer to obtain 1 kg of powder, necessitating that the overall process takes between 10 and 14 days. Safety-related problems are also associated with conducting such a drying process at high pressure.

The fabricated particles were characterised and analysed using different thermal and mechanical techniques to synthesise the primary PI aerogel particles in this project. Depending on the required application, any synthesized powder can be used. An emulsion-based method can be used in the case of applications to which the size of the

powder is relevant as using this technique makes it possible for smaller particles to be formed. In addition, the particle size can be changed and controlled by changing different effective parameters in the emulsion polymerization. If it is desirable to obtain low density, high porosity and low thermal conductivity, then particles produced using wet gel or dry milled procedures could be an option. Dilution can also significantly change the different properties of the particles produced in this way. The solvent exchange and drying process, which tend to be the most costly aspects of the aerogel manufacturing process, were also optimized in this project. The solvent exchange was completed in less than 3 h using these techniques for synthesizing the PI particles. Furthermore, despite claims made in much of the relevant literature regarding the necessity of using supercritical drying with aerogel, ambient pressure drying was found to provide a workable approach for producing the required aerogel in this study.

The fabricated particles were converted into a specific size and stock shape, with epoxy as a binder and DMSO as a solvent. The thermal and mechanical properties of the produced stock shape were compared with those of the stock shape manufactured by Blueshift. Due to the addition of epoxy, the density for these stock shapes is higher compared with the directly-produced stock shapes. In addition, as epoxy degrades at around 300 °C, these samples have less thermal stability. Among all the stock shapes made using WGG and EM methods, PI-WGG-0.5 and PI-EM-1 were found to demonstrate the most optimal properties. In terms of the thermal stability of the epoxy samples, it was observed that the presence of epoxy led to them exhibiting lower thermal stability. Comparing PI-WGG-0.5 and PI-EM-1 showed that the thermal stability of the WGG was 20% higher in terms of the temperature required to induce 10% decomposition. In addition, the surface area of PI-EM-1 was found to 51% higher than that of PI-WGG. A greater surface area results in greater overall contact with the surrounding air, leading to an increased combustion rate. The directly-produced stock shapes were also found to have generally preferable thermal properties (higher thermal stability and lower thermal conductivity), a more porous structure and lower density. In terms of mechanical properties, the dry-milled converted particles were found to have a higher compressive modulus compared to the other types of stock shapes. Overall, these results suggest that the proposed method for producing the stock shape is promising and that it is a competitive option in terms of potential properties compared to those of the stock shape that Blueshift produces directly.

7.2 Future work

This study focused on tackling the issues associated with PI aerogel stock shape fabrication costs. The following section highlights future work that might be undertaken to increase the quality of PI aerogel particles and their converted stock shapes.

Because this is the first time PI aerogel has been formulated using the methods introduced here, a wide range of improvements could be made in the context of future work.

1- First, synthesizing the particles necessitated that PAA be synthesized, imidized and then converted to PI. This project was done using the quantity and type of amide and anhydrides used by Blueshift as specified in their patent. The viscosity and molecular weight of PAA significantly affect the density of the resultant particles, which depend on the type and quantity of amines and anhydride used. Further work could be undertaken to investigate alternative kinds of diamine and dianhydride to be used in this work or select other types of solvent to synthesise PI in order to investigate the effect on the viscosity of the PAA.

2- In addition, in sol-gel processing, gelation time is an essential factor affecting the properties of the final product. In this work, gelation was taken to occur during 24 h of ageing. This part of the process could also be optimized to reduce the total processing time. It might also be beneficial to investigate the gelation time's effect on the product's final properties, especially in terms of the degree of shrinkage.

3- For the present work, chemical imidization was performed through the addition of 2-MI and BA. Adding heat to this part of the process would mean that both thermal and chemical imidization could be investigated in terms of the degree of imidization and the final thermal properties of the resultant particles.

4- Dilution was achieved in this study through the addition of DMSO in different ratios to the PAA before the catalyst was added. It may be fruitful to add this quantity of excess DMSO at the beginning of synthesizing PAA and investigate

the difference between these two protocols in terms of the properties of the final product.

5- This study also introduced different methods for synthesizing the PI aerogel particles. At present, Blueshift uses the dry-milling method. For synthesizing the particles using the WGG method, an ordinary kitchen blender was used at one speed for 3 min. In order to investigate the effect of the blending process on the properties of the final particles, different blending speeds could be tried for different durations of mixing. The WGG particles were dried in the RT for 24 h and then 30 min at 250 °C. It was detected that, after almost 19 h, any subsequent weight change was negligible. It could be beneficial to investigate how a vacuum oven could be used in terms of whether the drying duration could be reduced to save time and energy.

6- Acetone was the only solvent used for the solvent exchange process in this study. It might therefore be beneficial to use different solvents in various concentrations to investigate the effect of these on the properties of the final particles.

7- In terms of the fabrication of the PI particle using the emulsion-based method, Span 80 and Hypermer were the only emulsifiers used, and only in the given concentrations. Further study could feature different ratios of the current emulsifiers or include other types of emulsifiers to investigate this effect on the product's final properties.

8- The stirring speed was found to significantly affect the size of the particles and the degree of agglomeration in the emulsion process. A speed of 500 rpm was selected for the mixture at a larger volume. Future studies in this area could look to optimize this speed to synthesize the particles with less agglomeration and at a superior quality.

9- The synthesized particles were characterized without any further work being carried out in this study. Crushing the produced particles may be an option to ensure a fine and uniform consistency. It is predicted that the consolidation of these particles would be relatively straightforward and yield superior results. The properties of the crushed particles would have to be compared to

investigate whether crushing affects the thermal and mechanical properties of the particles.

10- The size of the particles was measured using image processing. It may be useful to use other techniques, such as light scattering, to measure the size of these particles and to compare them using this method.

This project was undertaken to determine how to modify the conditions for fabricating the PI aerogel stock shape to reduce production costs. The introduced methods in this work could be optimized. This could be done in the following ways:

1- One of the processes for consolidation of the PI microparticles involved adding one solvent to make the particles soft and easier to mould. DMSO, the main solvent used in this process, was selected on the basis of its properties relating to non-toxicity, its medium boiling point and its simple structure. In order to gain further insight into the role of softening agents, other types of solvents, such as dimethyl acetamide (DMAC), dimethyl formamide (DMF), and N-methyl pyrrolidone (NMP), could be considered. Depending on the selected solvent, a specific drying process would have to be chosen and optimized.

2- The PI stock shape was made using epoxy as a binder operating between the particles in the introduced second method. Depending on the resin and curing agent used, different curing times, temperatures, and final properties could be obtained. IN2 was the only epoxy used in this project. However, by altering the types of epoxies (resin and hardener), it would be possible to gain further insight into the effect of epoxy on the binding process.

3- In addition to fabricating the PI-EP stock shape, water was used to ensure more optimal dispersion between the different parts of the mixture. This was done on the basis that adding another solvent, such as ethanol, would assist with preserving the pores against infiltration by epoxy. By keeping other parameters constant, comparing the PI-ethanol-EP and PI-EP would help to determine whether ethanol can protect the pores in this way.

References

[1] Azum. N; Malik .A. R ;Khan, A; Khan. A; Asiri. A. M. Chapter 19 - Aerogel applications and future aspects. Advances in Aerogel Composites for Environmental Remediation: Elsevier; 2021; p. 357-367.

[2] Maleki. H. Recent advances in aerogels for environmental remediation applications: a review. Chemical Engineering Journal. 2016; 300, p. 98-118.

[3] Kistler. S.S, Coherent Expanded Aerogels. Journal of Phys Chem. 1932; 36(1). p. 52-64.

[4] Shinko. A., Jana. S.C., Meador. M.A. Crosslinked polyurea aerogels with controlled porosity. Journal of RSC Advances. 2015; 5(127), p.105329-105338.

[5] Yi. L., Yun. L., Wei. Y., Xue-Tong. Zh. Polyimide Aerogels Crosslinked with Chemically Modified Graphene Oxide. Acta Phys -Chim Sin. 2015;31(6), p.1179-1185.

[6] Chunhao. Zh. Polyimide Aerogel And Their Applications In Removal Of Airborn Nanoparticles [Master of Science]: University of Akron; 2016.

[7] Pierre. A. C., Pajonk.G. M. Chemistry of Aerogels and Their Applications. Chem Rev. 2002;102(11), p. 4243-4266.

[8] Soleimani. A., Abbasi, M.H. Silica aerogel; synthesis, properties and characterization. Journal of Materials Processing Technology. 2008;199(1-3), p.10-26.

[9] Meador. M.A. B., Aleman. Ch. R., Hanson. K., Ramirez. N., Wilmoth. V. N., McCorkle. L. Polyimide aerogels with amide cross-links: a low cost alternative for mechanically strong polymer aerogels. ACS Appl Mater Interfaces. 2015;7(2),1240-1249.

[10] Duan. Y., Jana. S.C., Lama. B., Espe M. P. Reinforcement of silica aerogels using silane-end-capped polyurethanes. Langmuir. 2013; 29(20), p. 6156-65.

[11] Baetens. R., Jelle. P.J., Gustavsen. A. Aerogel insulation for building applications: A state-of-the-art review. Energy and Buildings. 2011;43(4), p.761-769.

[12] Armor. J.N., Carlson. E. J., Zambri, P. M. Aerogels As Hydrognation Catalysts. Applied Catalyssis. 1985;19(9), p. 339-348.

[13] Ahmed. M. S., Attia, Y. A. Multi-metal oxide aerogel for capture of pollution gases from air. Applied Thermal Engineering. 1998; p.1-13.

[14] Meador. M. A. B., Weber. A. S., Hindi. A., Naumenko. M., McCorkle. L., Quade. D., Vivod. S. L., Gould. G. L., White. Sh. Structure-property relationships in porous 3D nanostructures: epoxy-cross-linked silica aerogels produced using ethanol as the solvent. ACS Appl Mater Interfaces. 2009;1(4), p.894-906.

[15] Pekala. R. W. Organic aerogels from the polycondensation of resorcinol with formaldehyde. Journal of Materials Science. 1989;24, p.3122-3127.

[16] Gu. S., Li. Zh., Miyoshi. T., Jana. S. C. Polybenzoxazine aerogels with controllable pore structures. RSC Advances. 2015; 5(34), p. 26801-26805.

[17] Biesmans. G., Martens. A., Duffours. L., Woignier. T., Phalippou. J. Journal of Non-Crystalline Solids. 1998; 225(4), p.64-68.

[18] Aegerter. M. A. LN, Koebel. M. M. Aerogel Handbook: Springer; 2011.

[19] A FP. Foamed polymers, cured aerogels or air gaps as isulation medium. U.S2004.

[20] Kawagishi. K. Sh., Furukawa. H., Horie. K. Superior Nanoporous Polyimides via Supercritical CO_2 Drying of Jungle-Gym-Type Polyimide Gels. Macromolecular Rapid Communication. 2007; 28. p.96-100.

[21] Meador. M. A. A., Hanson. K., Ramirez. N,. Vivod. S. L., Wilmoth. N., McCorkle. L. Polyimide aerogels with amide cross-links: a low cost alternative for mechanically strong polymer aerogels. ACS Appl Mater Interfaces. 2015;7. p.1240-1249.

[22] Nguyen. B.N., Meador. M. A. B., Scheiman. D., McCorkle. L. Polyimide Aerogels Using Triisocyanate as Cross-linker. ACS Appl Mater Interfaces. 2017; 9(32). p.27313-27321.

[23] Meador. M. A. B., McMillon. E., Sandberg. A., Barrios. E., Wilmoth. N. G., Mueller. Ch. Dielectric and Other Properties of Polyimide Aerogels Containing Fluorinated Blocks. ACS Applied Materials & Interfaces. 2014; 6. p. 6062-6068.

[24] Meador. M. A. B., Malow. E. J., Silva. R., Wright. S., Quade. D., Vivod. S. L. Mechanically Strong, Flexible Polyimide Aerogels Cross-Linked with Aromatic Triamine. ACS Applied Materials & Interfaces. 2012; 4. p. 536-544.

[25] Guo. H. DOS, McCorkle. L. S., Meador. M. A. B., Pasquali. M. Polyimide Aerogels as Lightweight Dielectric Insulators for Carbon Nanotube Cables. ACS Appl Polym Mater. 2019;1. p.1680-1688.

[26] Guo. H., Meador. M. A., McCorkle. L., Quade. D. J., Guo. J., Hamilton. B., Cakmak. M. Tailoring properties of cross-linked polyimide aerogels for better moisture resistance, flexibility, and strength. ACS Appl Mater Interfaces. 2012;4(10) p. 5422-5429.

[27] Duong. H. M. LP, Jewell. D. Advanced fabrication and multi-properties of polyimide aerogels and their composites. In: Murphy C, editor. Polyimides synthesis, applications and research: Nova 2017.

[28] Lee. S. B. Mitchell. D. T., Trofin. L., Nevanen. T. K., Soderlund. H., Martin. C. R. Antibody-based bio-nanotube membranes for enantiomeric drug separations. Science. 2002; 296 (5576), p.2198-2200.

[29] Simon. P., Gogotsi. Y. Materials for electrochemical capacitors. Nature Materials. 2008;7. p.845-854.

[30] Folter. J. W. J., Ruijven. M. W. M., Velikov. K. P. Oil in water Pickering emulsions stabilized by colloidal particles from the water-insoluble protein zein. Soft Matter. 2012; 8(25).p.6807-6815.

[31] Yang. S.Y. Advanced polyimide materials : synthesis, characterization, and applications: Amsterdam, Netherlands : Elsevier; 2018.

[32] Shen. D., Liu. J, Yang. H., Yang. S. Highly Thermally Resistant and Flexible Polyimide Aerogels Containing Rigid-rod Biphenyl, Benzimidazole, and Triphenylpyridine Moieties: Synthesis and Characterization. Chemistry Letters. 2013; 42(12). p.1545-1547.

[33] Chidambareswarapattar. C. L. Z., Sotiriou. C., Mang. J. T., Leventis. N. One-step room-temperature synthesis of fibrous polyimide aerogels from anhydrides and isocyanates and conversion to isomorphic carbons. Journal of MaterChem. 2010; 20. p. 9666-9678.

[34] Hu. J. A simple method to synthesizing the polyimide nano-spheres: Jilin University; 2012.

[35] Qian.Y. Study on preparation of polyimide molding powder based on isocyanate: Hefei University of Technology; 2018.

[36] Ke. H. Z. L., Zhang. X., Qiao. Y., Wang. G., Wang. X. Performance of high-temperature thermosetting polyimide composites modified with thermoplastic polyimide. Polymer testing. 2020; 90. 106746.

[37] Rhine. W., Begag. R. Production of polyimide aerogel for carbon aerogel, involves contacting diamine and aromatic dianhydride monomers in silvent, contacting resulting poly(amic acid) with dehydrating agent, and drying resulting polyimide gel. US2004.

[38] Lin.Y. C.C., Hu. Sh., Zhang. D., Wu. G. Facile Fabrication of Mechanically Strong andThermal Resistant Polyimide Aerogels with anExcess of Cross-Linker. Journal of Materials Research and Technology. 2020; 9(5). 10719-10731.

[39] Shi. B., Bin. M., Wang. Ch., He. H., Qu. L., Xu. B., Chen. Y. Fabrication and applications of polyimide nano-aerogels. Composites Part A. 2021;143. p. 106283-106289.

[40] Mosanenzadeh. Sh., Tafreshi. O. A., Karamikamkar. S., Saadatnia. Z., Rad. E., Meysami. M., Naquib. H. E. Recent advances in tailoring and improving the properties of polyimide aerogels and their application. Advanced in Colloid and Interface Science. 2022;304. p. 102646-102630.

[41] Zhang. R., Gu. H., Hou. X., Zhou .P. High-temperature resistant Y2SiO5–TiO2 aerogel composite for efficient thermal insulation. Journal of Porous Material. 2021; 28. p. 57-64.

[42] Chen. Y., Shao. G., Kong. Y., Shen. X., Cui. Sh. Facile preparation of cross-linked polyimide aerogels with carboxylic functionalization for CO_2 capture. Chemical Engineering Journal. 2017; 322, p.1-9.

[43] Yang. S. Y. Advanced Polyimide Materials: Amsterdam, Netherlands : Elsevier; 2018.

[44] Hou. X., Li. Y., Luo. X., Zhang. R. SiC whiskers-reinforced polyimide aerogel composites with robust compressive properties and efficient thermal insulation performance. Applied Polymers. 2020.

[45] Zhong. Y. K. Y., Zhang. J., Chen. Y., Li. B., Wu. X., Liu. S., Shen. X., Cui. S. Preparation and Characterization of Polyimide Aerogels with a Uniform Nanoporous Framework. Langmuir. 2018; 34. p.10529-10536

[46] Leventis. N., Chidambareswarapattar. C., Mohite. D.P., Larimore. Z.J., Lu. H., Sotiriou-Leventis. C. Multifunctional porous aramids (aerogels) by efficient reaction of carboxylic acids and isocyanates. Journal of Materials Chemistry. 2011; 32 (21). p. 11981-11986.

[47] Leventis N., Sotiriou-Leventis. C., Mohite. D. P., Larimore. Z. J., Mang. J. T., Churu. G . Polyimide Aerogels by Ring-Opening Metathesis Polymerization (ROMP). Chemistry of Materials. 2011; 23(8), p. 2250-2261.

[48] Zhong. Y. K., Y. Zhang. J., Chen. Y., Li. B., Wu. X., Liu. S., Shen. X., Cui. S. Preparation and Characterization of Polyimide Aerogels with a Uniform Nanoporous Framework. Langmuir. 2018; 34(36). p.10529-10536.

[49] Meador. M. A., Malow. E.J., Sliva. R., Wright. S., Quade. D., Vivod. S., Guo. H., Guo. J., Cakmak. M. Mechanically strong, flexible polyimide aerogelscross-linked with aromatic triamine. ACS Appl Mater Interfaces. 2012; 4(2), p.536-544.

[50] Feng. J. W. X., Jiang. Y., Du. D., Feng. J. Study on Thermal Conductivities of Aromatic Polyimide Aerogels. ACS Appl Mater Interfaces. 2016; 8(20). p. 12992-12996.

[51] Nguyen. B. N., Cudjoe. E., Douglas. A., Scheiman. D., McCorkle. L., Meador. M., Rowan. S. Polyimide Cellulose Nanocrystal Composite Aerogels. Macromolecules. 2016; 49(5), p. 1692-1703.

[52] Zhai. CH JSC. Tuning porous networks in polyimideaerogels for airborne nanoparticle filtration. ACS Appl Mater Interfaces. 2017; 9(35) p.30074-30082.

[53] Li. X., Wang. J., Zhao. Y., Zhang. X. Template-Free Self-Assembly of Fluorine-Free Hydrophobic Polyimide Aerogels with Lotus or Petal Effect. ACS Applied Materials & Interfaces. 2018; 10(19). p. 16901-16910.

[54] Guo. H., Meador. M. A. B., McCorkle. L., Quade. D. J., Guo. J., Hamilton. B., Cakmak. M., Sprow. G. Polyimide Aerogels Cross-Linked through Amine Functionalized Polyoligomeric Silsesquioxane. ACS Appl Mater Interfaces. 2011; 3(2). p. 546-552.

[55] Teo. N., Jana. S. C. Solvent Effects on Tuning Pore Structures in Polyimide Aerogels. Langmuir. 2018; 34 (29). p.8581-8590.

[56] Teo. N., Jana. S. C. Surfactant-Free Process for the Fabrication of Polyimide Aerogel Microparticles. Langmuir. 2019; 35(6). p.2303-2312.

[57] Teo. N., Jana. S. C. Polyimide-based aerogel foams, via emulsion-templating. Polymer. 2018; 157. p.95-102.

[58] Fan. H., Yang. R. Flame-Retardant Polyimide Cross-Linked with Polyhedral Oligomeric Octa(aminophenyl)silsesquioxane. Ind Eng Chem Res. 2013; 52(7), p.2493-2500.

[59] Viggiano. R. P., Williams. J. C., Schiraldi. D. A., Meador. M. A. B. Effect of Bulky Substituents in the Polymer Backbone on the Properties of Polyimide Aerogels. ACS Appl, Mater Interfaces. 2017; 9(9). p.8287-8296.

[60] Ghaffari. Sh., Saadatnia. Z., Shi. F., Park. Ch. B., Naguib. H. E. Structure to properties relations of BPDA and PMDA backbone hybrid diamine polyimide aerogels. Polymer. 2019; 176. p.213-226.

[61] Jiang. Y., Zhang. T., Wang. K., Yang. J. Synthesis and characterization of rigid and thermostable polyimide aerogel crosslinked with tri(3-aminophenyl)phosphine oxide. Journal of Porous Materials. 2017; 24. p.1353-1362.

[62] Ma. P., Dai. Ch., Wang. H, Li. Zh, Liu. H, Li. W., Yang. Ch. A review on high temperature resistant polyimide films: Heterocyclic structures and nanocomposites. Composites Communications. 2019; 16. p. 84-93.

[63] Zhang. X., He. M., Gao. Y., Li. Ch., Mo. X, Sun. G., You. B. A synergistic strategy for fabricating an ultralight and thermal insulating aramid nanofiber/polyimide aerogel. Materials Chemistry Frontiers. 2021; 5. p.804-816.

[64] Feng. Ch., Yu. Sh. Sh. 3D Printing of Thermal Insulating Polyimide/Cellulose Nanocrystal Composite Aerogels with Low Dimensional Shrinkage. Polymer. 2021;13(21). p. 3614-3620.

[65] Meador. M.A. B., Million. E. M., Sandberg. A., Barrios. E., Wilmoth. N. G., Mueller. C. H., Miranda. F. A. Dielectric and other properties of polyimide aerogels containing fluorinated blocks. ACS Appl Mater Interfaces, 2014. 6(9): p. 6062-6068.

[66] Kwon. J., Kim. J., Yoo. T., Park. D., Han. H. Preparation and Characterization of Spherical Polyimide Aerogel Microparticles. Macromolecular Materials and Engineering. 2014; 299(9). p.1081-1088.

[67] Chao. M. Synthesis and Characterization of Semicrystalline Polyimides Containing Bridged Linkages. International Journal of Polymer Science. 2018; 2018; p.1-7.

[68] Tao. Li., Enshuang. Zh., Jinyang. Zh., Fan. Zh., Yuanyuan. L., Yingmin. Zh. Preparation and Properties of Flexible Cross-linked Polyimide Aerogels. Chemical Journal of Chinese Universites. 2019; 40. p.403-409.

[69] Zhou.C. Reasearch progress in preparation of polyimide via isocyanate method. Synthesis Technol Appl. 2015; 20. P. 26-30.

[70] Paraskevopoulou. P. Chriti. D., Raptopoulos. G., Anyfantis. G. C. Synthetic Polymer Aerogels in Particulate Form. Materials Chemistry Frontiers. 2019; 12(9), 1543-1550.

[71] Chidambareswarapattar. Ch., Leventis. Ch., Leventis.N. Robust monolithic multiscale nanoporous polyimides and conversion to isomorphic carbons. Royal Society of Chemistry. 2013; 3. p. 26459-26469.

[72] Schwan. M., Nefzger. S., Zoghi. B., Oligschleger. Ch., Milow. B. Improvement of Solvent Exchange for Supercritical Dried Aerogels. Frontiers in Materials. 2021;8.

[73] Chen. D., Dong. K., Gao. H., Zhuang. T., Huang. X., Wang. G. Vacuum-dried flexible hydrophobic aerogels using bridged methylsiloxane as reinforcement: performance regulation with alkylorthosilicate or alkyltrimethoxysilane co-precursors. new journal chemistry. 2019; 43(5). p. 2204-2212.

[74] He. S., Chen. X. Flexible silica aerogel based on methyltrimethoxysilane with improved mechanical property. Journal of non crystalline solids. 2017; 463. p. 6-11.

[75] Yang. G., Zhao. W., Denga. W., Liu. X. Robust ambient pressure dried polyimide aerogels and their graphene oxide directed growth of 1D–2D nanohybrid aerogels using water as the only solvent; RSC Adv. 2017; 7. p. 16210-1626.

[76] Leventis. N., McCorkle. L., Zhang. G., Sotiriou-Leventis. C. Nanoengineered silica-polymer composite aerogels with no need for supercritical fluid drying. journal sol gel science and technology. 2005; 35. p. 99-105.

[77] Lee. D. H., Han. S. W., Yu. S., Park. H. Polyimide aerogel with controlled porosity: Solvent-induced synergistic pore development during solvent exchange process. Polymer. 2020; 205. p.122879.

[78] Wu. Q., Wang. H., Deng. W., Yang. G., Liu. X. A green and scalable method for producing high-performance polyimide aerogels using low-boiling-point solvents and sublimation drying. Polymer. 2015; 48. p.169-175.

[79] Pierre. A. C. Introduction to Sol-Gel Processing: Springar; 2020.

[80] Wan. W., Zhang. R., Ma. M., Zhou. Y., *Monolithic aerogel photocatalysts: a review*. Journal of Materials Chemistry A, 2018. **6**(3): p. 754-775.

[81] Maleki H., Duraes, L., Garcia-Gonzalez, C.A., Gaudio, P., Mahmoudi, M. Synthesis and biomedical applications of aerogels: Possibilities and challenges. Advances in Colloid and Interface Science. 2016; 236. p.1-27.

[82] Pierre. A. C. Introduction to Sol-Gel Processing: Springar; 2020.

[83] Brinker. C. J. Hydrolysis And Condensation Of Silicates- Effects On Structure. Journal of Non-Crystalline Solids. 1988; 100)1-3), p. 31-50.

[84] Gurav. J., Keun. J., Park. H., Kang. E. Silica aerogel: synthesis and applications. Journal of Nanomaterials. 2010; 24. p. 1-11.

[85] Iswar. S., Malfait. W.J., Balog. S., Winnefeld. F., Lattuada. M. Koebel. M.M. Effect of aging on silica aerogel properties. Microporous and Mesoporous Materials. 2017; 241. p. 293-302.

[86] Haereid. S., Anderson. J., Einarsrud. M. A., Hua. D.W., Smith. D.M. Thermal and temporal aging of TMOS-based aerogel precursors in water. Journal of Non-Crystalline Solids. 1995; 185(3).p. 221-226.

[87] He. F., Zhao. H. L., Qu. X. H., Zhang. C.J., Qiu. W. H. Modified aging process for silica aerogel. Journal of Materials Processing Technology. 2009; 209(3). p.1621-1626.

[88] Einarsrud. M. A., Nilsen. E., Rigacci. A., Pajonk. G.M., Buathier. S., Valette. D., Durant. M., Chevalier. B., Nitz. P., Ehrburger-Dolle. F. Strengthening of silica gels and aerogels by washing and aging processes. Journal of Non-Crystalline Solids. 2001; 285. p.1-7.

[89] Maleki. H. D, L., Garcia-Gonzalez, C.A., Gaudio, P., Mahmoudi, M. Synthesis and biomedical applications of aerogels: Possibilities and challenges. Advances in Colloid and Interface Science. 2016; 236. p.1-27.

[90] Pei. X., Zheng. W. Preparation and Characterization of Highly Cross-Linked Polyimide Aerogels Based on Polyimide Containing Trimethoxysilane Side Groups. Langmuir. 2014; 30. p. 13375-13383.

[91] Hu. L. He. R., Lei. H., Fang. D. Carbon Aerogel for Insulation Applications: A Review. International Journal of Thermophysics. 2019; 40.

[92 Ibraham. S., Ozbakr. Y., Inonu. Z., Uiker. Z., Erkey. C. Kinetics of Supercritical Drying of Gels. Gels. 2018; 4(1). p. 3-10.

[92] Meador. M. A., Wright. S., Sandberg. A., Nguyen. B. N., Van. W., Mueller. Ch. Low dielectric polyimide aerogels as substrates for lightweight patch antennas. ACS Appl Mater Interfaces. 2012; 4. p. 6346-6353.

[93] Meador. M. A., McMillon. E., Sandberg. A., Barrios. E., Wilmoth. N. G., Mueller. Ch. Dielectric and other properties of polyimide aerogels containing fluorinated blocks. ACS Appl Mater Interfaces. 2014; 6. p. 6062-6068.

[94] Zhang. X. M., Liu. J. G., Yang. S.Y. Synthesis and characterization of flexible and high-temperature resistant polyimide aerogel with ultra-low dielectric constant. Express Polymer Letters. 2016; 10. p.789-798.

[95] Simón-Herrero. C., Chen. X.Y., Ortiz. M. L., Romero. A., Valverde. J. L, Sánchez-Silva. L. Linear and crosslinked polyimide aerogels: synthesis and characterization. Journal of Materials Research and Technology. 2019; 8. p. 2638-2648.

[96] Zhang. X., Song. P., You. B., Sun. G. Double-cross-linking strategy for preparing flexible, robust, and multifunctional polyimide aerogel. Chemical Engineering Journal. 2020; 381. p. 122784.

[97] Zhang. X., Hu. Z., Yu. J., Wang. Y., Zhu. J. Direct fabrication of poly(phenylene terephthalamide) aerogel and its composites with great thermal insulation and infrared stealth. Chemical Engineering Journal. 2020; 388. p. 124310.

[98] Malakooti. S., Mandal. C., Soni. R., Taghvaee. Y., Ren. Y., Chen. H., Tsao. N., Shiao. J., Kulkarni. S. S., Sotiriou-Leventis. C., Leventis. N., Lu. H. Low-cost, ambientdried, superhydrophobic, high strength, thermally insulating, and thermally resilient polybenzoxazine aerogels. ACS Applied Polymer Materials. 2019; 1. p.2322-2333.

[99] Zu. G., Maeno. A., Kaji. H., Nakanishi. K., Shen. J. Ambient-dried highly flexible copolymer aerogels and their nanocomposites with polypyrrole for thermal insulation, separation, and pressure sensing. Polymer Chemistry. 2019;10(4). p. 4980–4890.

[100] Li. Y., Liu. L., Wang. C., Tam. K. C., Liu. S., Mao. Z., Sui. X. Construction of functional cellulose aerogels via atmospheric drying chemically cross-linked and solvent exchanged cellulose nanofibrils. Chemical Engineering Journal. 2019; 366. p.531-538.

[101] Wang. Z., Wu. J., Zhao. N., Xu. J. Vacuum-dried robust bridged silsesquioxane aerogels. Advanced Material. 2013; 25: p. 4494–4497.

[102] Blueshift Materials Inc Pap. 2021 (Accessed 25 May 2021).

[103] L.L.C. Aerogel Technologies Ap. 2021 (Accessed 25 May 2021).

[104] Stojanovic. A., Comesana. S.L., Rentsch. D., Koebel. M.M., Malfait. W. J. Ambient pressure drying of silica aerogels after hydrophobization with mono-, di- and tri-functional silanes and mixtures thereof. Microporous and Mesoporous Materials. 2019; 284, P. 289-295.

[105] Francon. H., Wang. Zh., Marais. A., Mystek. K., Piper. A., Gramnerg. H., Wagberg. L. Ambient-Dried, 3D-Printable and Electrically Conducting Cellulose Nanofiber Aerogels by Inclusion of Functional Polymers. Advanced Functional Materials. 2020; 30(12). 1909383.

[106] Han.X., Williamson. F., Bhaduri. G., Harvey. A., Siller.L. Synthesis and characterisation of ambient pressure dried composites of silica aerogel matrix and embedded nickel nanoparticles. The Journal of Supercritical Fluids. 2015; 106. p.140-144.

[107] Pisani. L. Simple Expression for the Tortuosity of Porous Media. Transp Porous Media. 2011; 88. p.193-203.

[108] Bisson. A. R., Lecomte. D., Rodier. E., Achard. P. Drying of Silica Gels to Obtain Aerogels: Phenomenology and Basic Techniques. Dry Technol. 2003; 21. p. 593-628.

[109] Hench. L.L; West JK. The sol-gel process. Chem Rev. 1990; 90. p. 33–72.

[110]Vareda. J. P., Matias. T., Duraes. L. Facile preparation of ambient pressure dried aerogel-like monoliths with reduced shrinkage based on vinyl-modified silica networks. Ceramics International. 2018; 44(14). P. 17453-17458.

[111] Fidalgo. A., Farinho. J. P. S., Martino. J. M. G., Rosa. M. E. Hybrid Silica/Polymer Aerogels Dried at Ambient Pressure. Chem Mater. 2007;19(10) . P. 2603–2609.

[112] Kim. J., Kwon. J., Kim. M., Lee. D., Lee. S., Kim. G., Lee. J., Han. H. One-step synthesis of nano-porous monolithic polyimide aerogel. Microporous and Mesoporous Materials. 2016; 234. p. 35-42.

[113] Pajonk. G. M., Lacroix. M. R., Abouarnadasse. S., Chaouki. J., Klavana. D . From sol-gel to aerogels and cryogels. J Non Cryst Solids. 1990;121(1-3). p.66-67.

[114] Gurav. J. L., Nadargi. D. Y., Park, Hyung-Ho. Ambient pressure dried TEOS-based silica aerogels: good absorbents of organic liquids. Journal of Materials Science. 2010; 45(2). p. 503-510.

[115] Hering. N., Schreiber. K., Riedel. R., Lichtenberger. O., Woltersdorf. Jr. Synthesis of polymeric precursors for the formation of nanocrystalline Ti-C-N/amorphous Si-C-N composites. Applied Organometallic Chemistry. 2001;15. p.879-886.

[116] Matson. D., Smith. R.D. Supercritical fluid technologies for ceramic-processing applications. J Am Ceram Soc. 1989;72 (6). p.871–881.

[117] Tamon. H., Ishizaka. H., Yamamoto. T., Suzuki. T. Freeze drying for preparation of aerogel-like carbon. Drying Technology, 2001; 19(2): p. 313-324.

[118] Wu. H. K., Li. X. M., Zhao. W., Meng. Zh., Zhang. W. J., Qian. L. Freeze-Drying Graphene Aerogels and their Adsorption Ability towards Organic Reagents. Materials Science Forum, 2017; 898. p. 1923-1928.

[119] Huab. L., Zhang. L., Zhang. K., Baia. X. *S*tep-freeze-drying method for carbon aerogels: a study of the effects on microstructure and mechanical property. Royal Society of Chemistry, 2019; 9. p. 9931-9936.

[120] Hu. L., He. R., Lu. Z., Zhang. K., Bai. X. Step-freeze-drying method for carbon aerogels: a study of the effects on microstructure and mechanical property RSC Advances. 2019; 9(18). p. 9931-9936.

[121] Herrero. C. S., Caminero. S., Romero. A.,Valvarde. J. L., Sanchez. L Effects of freeze-drying conditions on aerogel properties. Journal of Materials Science 2016; 51. p. 8977– 8985.

[122] Liu. M., Ji. J., Chang. X., Xu. Q., Liu. X., Qin. J. A facile method to fabricate the polyimide aerogels with controllable microstructure by freeze-drying. Matterials Letters. 2020; 267. 127558.

[123] Xu. G., Wu. T., Teng. C. Highly compressible and anisotropic polyimide aerogels containing aramid nanofibers. Reactive and Functional Poymers. 2020;154. 104672.

[124] Bozbag. S. E., Sanli. D., Erkey. C. Synthesis of nanostructured materials using supercritical CO_2 : Part I. Physical transformations. J Mater Sci. 2012; 47. p.3469-3492.

[125] Jin. H., Nishiyama. Y., Wada. M., Kuga. Sh. Nanofibrillar cellulose aerogels. Colloids Surf. A PhysicochemEng Asp. 2004; 240 (1-3). p. 63-67.

[126] Ciftic. D., Ubeyitogullari. A., Huerta. R.R., Saldana. M. D. A. Lupin hull cellulose nanofiber aerogel preparation by supercritical CO2 and freeze drying. J SupercritFluids. 2017;127. p.137–45.

[127] Gonzalez. C. A. G., Jin. M., Gerth. J., Lorenozo. C. A., Smirnova. I. Polysaccharide-based aerogels—Promising biodegradable carriers for drug delivery systems. Carbohydr Polym. 2011; 86. p. 1425–1438.

[128] Tewari. P. H., Hunt. A. J., Lofftus. K. D. Ambient-temperature supercritical drying of transparent silica aerogels. Mater Lett. 1985; 3 (9-10):363–7.

[129] Kang. P. L., Sudbury. M. A., Redouane. B., Marlboro. M., Zlatko. A., Shrewsbury. M. Rapid aerogel production process. 2001;WO 01/28675 A1.

[130] Blaszczynski. T., Slosarczyk. A., Maciej. M. Synthesis of Silica Aerogel by Supercritical Drying Method. Procedia Engineering. 2013; 57. p.200-206.

[131] Gonzalez. C. A., Camino-Rey. M. C., Alnaief. M., Zetzl. C., Smirnova. I. Supercritical drying of aerogels using CO2: Effect of extraction time on the end material textural properties. The Journal of Supercritical Fluids. 2012; 66. p. 297-306.

[132] Zhang. T., Zhao. Y., Wang. K. Polyimide Aerogels Cross-Linked with Aminated Ag Nanowires: Mechanically Strong and Tough. Polymers. 2017; 9(10). p. 530.

[133] Pantoja. M., Cavicchi. K. A., Dosa. B., Cashman. J. L., Meador. M. A. B. Increased Flexibility in Polyimide Aerogels Using Aliphatic Spacers in the Polymer Backbone. ACS Appl Mater Interfaces. 2019; 11. p. 9425-9437.

[134] Cashman. J. L., Dosa. B., Meador. M. A. B. Flexible Polyimide Aerogels Derived from the Use of a Neopentyl Spacer in the Backbone. ACS Applied Polymer Materials. 2020; 2. p. 2179-2189.

[135] Guo. H., Cashman. J. L., Tresp. D., Dosa. B., Scheiman. D. A., McCorkle. L. S. Flexible Polyimide Aerogels with Dodecane Links in the Backbone Structure. ACS Appl Mater Interfaces. 2020; 12(29). p. 33288-33296.

[136] Li. B., Yu. Sh., Chen. Y., Tang. X., Wu. X., Zhong. Y., Shen. X., Cui. Sh. Co-polyimide aerogel using aromatic monomers and aliphatic monomers as mixing diamines. Journal of Sol-Gel Science and Technology. 2018; 88. p.386-394.

[137] Qiao. Sh., Hu. Z., Yu. j., Wang. Y., Zhu . J. Moisture-resistance, mechanical and thermal properties of polyimide aerogels. Journal of Porous Material. 2020; 27. p.237-247.

[138] Wu. T., Gan. F., Fang. Y., Zhao. X., Zhang. Q. Low dielectric constant and moisture-resistant polyimide aerogels containing trifluoromethyl pendent groups. Applied Surface Science. 2018; 440. p. 595-605.

[139] Zhu. Zh., Dong. J., Qian. Zh., Dong. w., Long.W, High-mechanical-strength polyimide aerogels crosslinked with 4, 4′-oxydianiline-functionalized carbon nanotubes. Carbon, 2019; 144: p. 24-31.

[140] Kim. J., Kwon. J., Kim. .S, Kim. M., Lee. D., Lee. S. One-step synthesis of nano-porous monolithic polyimide aerogel. Microporous Mesoporous Mater. 2016; 234. p. 35-42.

[141] Vivod. S. L., Pugh. C., Wilkosz. M., Calomino. K., McCorkle. L. Toward Improved Optical Transparency of Polyimide Aerogels. ACS Applied Material Interfaces. 2020;12. p.8622-8633.

[142] Ting. L., Xiao-dong. W., Jun. Sh., Zc. Zh., Sh. X., Qun. L. Preparation and application of polyimide aerogel materials. Chinese Journal of Engineering. 2020; 42. p. 39-47.

[143] Hou. X., Fang. D. Flexible, fatigue resistant, and heat-insulated nanofiber-assembled polyimide aerogels with multifunctionality. Polymer testing. 2020; 81. 106246.

[144] Ren. R. P., Ren. J., Lv. Y. K. Highly compressible polyimide/graphene aerogel for efficient oil/water separation. Journal of Materials Science. 2018; 54. p. 5918-5926.

[145] Zihao. S., Boyu. D., Qiuyang. D., Jinghong. L., Yinghui. J., Sheng. C. Progress in preparation and performance application of polyimide aerogel. Chemical Industry and Engineering Process. 2022; 41. p. 816-826.

[146] Sanli. D., Bozbag. E. E., Erkey. C. Synthesis of nanostructured materials using supercritical CO_2 : Part I. Physical transformations. Journal of Materials Science, 2011; 47. p. 2995-3025.

[147] Maleki. H. Recent advances in aerogels for environmental remediation applications: A review. Chemical Engineering Journal. 2016; 300. p. 98-118.

[148] Hrubesh. L. W. Aerogel applications. Journal of Non-Crystalline Solids. 1998; 225. p.335-342.

[149] Gao. Y., Zhang. F., Ma. H., Li. Y. Constructing Polyimide Aerogels with Carboxyl for CO_2 Adsorption. Polymer. 2022;14(3). p. 359.

[146] Richard. P., Hill. P., Hrubesh. L. W. Compression molding of aerogel microspheres. Regents of the University of California 1996.

[147] Joshi. S. Ch., Jothi. Y. Enhancement Studies on Manufacturing and Properties of Novel Silica Aerogel Composites. gels. 2018;4(1). p.5.

[148] Chidambareswarapattar. Ch., Leventis. Ch., Leventis. N. Robust monolithic multiscale nanoporous polyimides and conversion to isomorphic carbons. RSC Advances. 2013; 3(48). p. 26459-26469.

[149] Jin. Ch., Teo. N., Jana. S. C. Fabrication of Pill-Shaped Polyimide Aerogel Particles Using Microfluidic Flows. Industrial and Engineering Chemistry Research. 2020; 60(1). p. 361-370.

[150] Poe. G., Lambdin. N, Koldan. K, Highly Branched Non-crosslinked Aerogel, Methods of Making, and Uses Thereof. 2017.

[151] Ayoola, W.A., Adeosun. S. O., Sanni. O. S., Oyetunji. A. Effect of casting mould on mechanical properties of 6063 aluminum alloy. Journal of engineering science and technology, 2012. 7(1): p. 89-96.

[152] Kryachek. V.M. Injection moulding. Powder Metallurgy and Metal Ceramics, 2004; 43: p. 336-348.

[153] Lee. N.C., Practical guide to blow moulding. 2006: iSmithers Rapra Publishing.

[154] Greene. J.P. Compression Molding, in Automotive Plastics and Composites. 2021, William Andrew Publishing. p. 265-278.

[155] Pekela. R. W., Hrubesh. L. W. Compression molding of aerogel microspheres. 1996, Regents of the University of California.

[156] Joshi. S. Ch., M.P., Jothi. Y, Enhancement Studies on Manufacturing and Properties of Novel Silica Aerogel Composites. gels, 2018. 4(1). p. 5.

[157] Chidambareswarapattar. Ch., X.L., Leventis. Ch., Leventis. N, Robust monolithic multiscale nanoporous polyimides and conversion to isomorphic carbons. RSC Advances, 2013. **3**(48).p. 26459-26469.

[158] Jin. Ch., K.A., Teo. N., Jana. S. C, Fabrication of Pill-Shaped Polyimide Aerogel Particles Using Microfluidic Flows. Industrial and Engineering Chemistry Research, 2021. 60: p. 361-370.

[159 Bardy. E. R., Pendergast. D. R. Thermal Conductivity and Compressive Strain of Aerogel Insulation Blankets Under Applied Hydrostatic Pressure. Journal of Heat Transfer. 2007; 129. p.232-235.

[160] Chakraborty. S., Kothari. V. K., Rao. A. V. Synthesis and Characterization of Fibre Reinforced Silica Aerogel Blankets for Thermal Protection. Advanced in Materials Science and Engineering. 2016.

[161] Mi. H. Y., Meador. M. A. B., Guo. H., Turng. L-Sh., Gong. Sh. Triboelectric Nanogenerators Made of Porous Polyamide Nanofiber Mats and Polyimide Aerogel Film: Output Optimization and Performance in Circuits. ACS Appl Mater Interfaces. 2018; 10. p. 30596-30606.

[162] Qian. Zh., Chen. Y.,Tong. Sh., Ge. M., Zhao. N., Xu. J. Superelastic and ultralight polyimide aerogels as thermal insulators and particulate air filters. Journal of Materials Chemistry A. 2018; 6(3). p. 828-832.

[163] Stojanovic. A., Angelica. E., Malfait. W. J., Koebel. M. Three routes to superinsulating silica aerogel powder. Journal of Sol-Gel Science and Technology. 2019; 90. p.57-66.

[164] Gu. S., Jana. S. C. Aerogel microparticles from oil-in-oil emulsion systems. Langmuir. 2016; 32. p.5637-5645.

[165] García-Gonzalez. C. A., Alnaief. M. SI. Poly- saccharide-Based Aerogels Promising Biodegradable Carriers for Drug Delivery Systems. Carbohydrate Polymers. 2011; 86. p.1425-1438.

[166] Ren. X., Cao. J., Tian. Sh., Zhang. K., Guo. J., Wen. L., Liang. G. Enhanced Rate Performance of the Mortar-Like LiFePO4/C Composites Combined with the Evenly Coated of Carbon Aerogel. Journal of Alloys and Compounds. 2021;867.158776.

[167] Pan. Y., Zhou. T., Gong. L., Zhang. H. Spray Freeze-Dried Monolithic Silica Aerogel Based on Water-Glass with Thermal Superinsulating Properties. Material Letters. 2018; 15. p.265-268.

[168] Bheekhun. N., Mustapha. S., Ibrahim. R., Hassan. M. R. Towards an aerogel-based coating for aerospace applications: reconstituting aerogel particles via spray drying. IOP Conference Series: Materials Science and Engineering. Kuala Lumpour, Malaysia. 2016.

[169] Teo. N., Jana. S. C. Polyimide-based aerogel foams, via emulsion-templating. Polymer. 2018;157. p.95-102.

[170] Liu. M., Pang. Y., Xu. Z., Hao. Z., Chen. L. Synthesis of Titania–Silica Aerogel-Like Microspheres by a Water-in-Oil Emulsion Method via Ambient Pressure Drying and Their Photocatalytic Properties. Colloids and Surfaces A. 2008; 317. p. 490-495.

[171] Baudron. V., Smirnova. I. A continuous approach to the emulsion gelation method for the production of aerogel micro-particle. Colloids and Surfaces A. 2019; 566. p.58-69.

[172] Teo. N., Sadhan. C. J. Surfactant-Free Process for the Fabrication of Polyimide Aerogel Microparticles. Langmuir. 2019; 35(6). p. 2303-2312.

[173] Ji. J., Liu. X., Qin. J. Fabrication of porous polyimide hollow microspheres through O/W/O multiple emulsion. Colloids and Surfaces A. 2020; 591.124537.

[174] Preibisch. I., Yusufoglu. Y., Gurikov. P., Milow. B., Smirnova. I. Polysaccharide-Based Aerogel Bead Production via Jet Cutting Method. Materials 2018; 11(8). 1287.

[175] Schroeter. B., Niemeyer. N. A. M., Jung. I., Preibisch. I., Gurikov. P., Smirnova. I. Cellulose Aerogel Particles: Control of Particle and Textural Properties in Jet Cutting Process. Cellulose. 2020; 28. p. 223-239.

[176] Lopez-Iglesias. C., Ardao. I., Grikov. P.,Garcia-Gonzaiez. C. A., . Jet Cutting Technique for the Production of Chitosan Aerogel Microparticles Loaded with Vancomycin. Polymers (Basel).12.

[177] Wu. S., Du. A., Xiang. Y., Liu. M., Li. T., Shen. J. Silica-aerogel-powders “jammed” polyimide aerogels with excellent hydrophobicity and conversion to ultra-light polyimide aerogel. RSC Advances. 2016; 6. p. 58268-58278.

[178] Zhang. Y., Huang. Y., Zhang. Ch., Liu. T. Graphene/Carbon Aerogels Derived from Graphene Crosslinked Polyimide as Electrode Materials for Supercapacitors. Royal Society of Chemistry. 2015; 5. p.1301-1308.

[179] Lee. D., Kim. S., Kim. G., Roh. J., Lee. S., Han. H. Tunable pore size and porosity of spherical polyimide aerogel by introducing swelling method based on spherulitic formation mechanism. Microporous and Mesoporous Materials. 2019; 288. 109546.

[180] Yamaguchi. H. Process for production of polyimide powder, polyimide powder moulded bodies and process for their production. 2003.

[181] Cano. C. I., Kyu. T., Pipes. R. B. Polyimide foams from powder: Experimental analysis of competitive diffusion phenomena. Polymer. 2005; 46(22).p. 9296-9303.

[182] Yan-Liang. W., Li-Na. W., He. J., Guo-Dong. D. Synthesis and Characterization of Polypyromelliticimide Polyimide Molding Powders. Chemical Journal of Chinese Universites. 2013; 33. p.2356-2360.

[183] Vaganov. G., Kova. E. I., Popova. E., Kuznetsova. T., Kobykhno. I., Yudin. V. Investigation and Characterization of New Polyimide Powder for Selective Laser Sintering. Key Engineering Materials. 2019; 822. p. 208-214.

[184] Meador. M. A. Hindi, A. Naumenko. M., McCorkle. L., Quade. D.,Vivod. S. L., Gould. G. L., Deshpande. K. Structure-property relationships in porous 3D nanostructures: epoxy-cross-linked silica aerogels produced using ethanol as the solvent. ACS Appl Mater Interfaces. 2009; 1. p.894-906.

[185] Gardiner. R. W., Goodwin. P. S., Dodd. S. B. Powder consolidation. Non-equilibrium Processing of Materials. Pergamon Mterial Series; 1999. p. 347-72.

[186] Woignier. T. Densification and strengthening of aerogels by sintering heat treatments or plastic compression. gels. 2018;4(1). 12.

[187] Gibson. L. J. Cellular Solids Structure and Properties: Pergamon Press, Oxford, UK; 1988.

[188] Ellis. B. Chemistry and Technology of Epoxy Resins: Springer Netherlands; 2012.

[189] C M. Epoxy Resins,Chemistry and Technology. 2nd Edn ed: NY; 1988.

[190] Acocella. M. R., Giuri. A., Maggio. M, Maffezzolib. A., Guerraa. M, Graphene oxide as a catalyst for ring opening reactions in amine crosslinking of epoxy resins. RSC Adv, 2016. 6(28): p. 23858-23865.

[191] A BJ. Plastic Materials. Oxford: Butterworth-Hetnemann Ltd; 1995.

[192] Lee. H. NK. Handbook of epoxy resin. NY: McGraw-Hill; 1967.

[193] Lee. S. B., Hong. I. K. Diluent filler particle size effect for thermal stability of epoxy type resin. Journal of Industrial and Engineering Chemistry. 2012;18. p.635-641.

[194] Das. G., Deka. H., Buragohain. A. K., . Biodegradation, cytocompatability and performance studies of vegetable oil based hyperbranched polyurethane modified biocompatible sulfonated epoxy resin/clay nanocomposites. Progress in Organic Coatings. 2013; 76. p.1103-1111.

[195] Mohammed. I. A., Daud. W. R. W. New class of liquid crystalline epoxy resins: Synthesis and properties. Journal of Industrial and Engineering Chemistry. 2012; 18. p.364-372.

[196] Jin. F. L., Park. S. J. Polymer matrices for carbon fiber-reinforced polymer composites. Carbon Lett. 2013;14(2). p.76-88.

[197] Kawahara. T., Hashimoto. K., Fujiki. K., Yamauchi. T., Tsubokawa. N. Immobilization of flame-retardant onto silica nanoparticle surface and properties of epoxy resin filled with the flame-retardant-immobilized silica. Reactive and Functional Polymers. 2013;73. p.613-618.

[198] Totu. E., Ruse. E., Josceanu. M. Influence of Plasticizers on Ion-Selective Polyimide Membranes. Annali di Chimica. 2006; 96. p.237-246.

[199] Turaif. Al., Hamad. A. Relationship between tensile properties and film formation kinetics of epoxy resin reinforced with nanofibrillated cellulose. Progress in Organic Coatings. 2013; 76(2). p.477-481.

[200] Dannenberg. H., Harp. W. R. Determination of Cure and Analysis of Cured Epoxy Resins. Analytical Chemistry. 1956; 28(1). p. 86-90.

[201] Gibson, G., Epoxy resins, in Brydson's Plastics Materials. 2017, Elsevier. p. 773-797.

[202] Pham. V. H., Kim. S. H., Jeong. H. T., Jung. M. Y., Ko. B. S., Hwang. Y. J., Chung. J. S. Synthesis of epoxy encapsulated organoclay nanocomposite latex via phase inversion emulsification and its gas barrier property. Journal of Industrial and Engineering Chemistry. 2014; 20.p. 108-112.

[203] Li. Y., Kessler. M. R. Liquid crystalline epoxy resin based on biphenyl mesogen: Thermal characterization. Polymer. 2013; 54. p.3017-3025.

[204] Mousavifard. S. M., Attar. M. M., Ramezanzadeh. B. The effects of zinc aluminum phosphate (ZPA) and zinc aluminum polyphosphate (ZAPP) mixtures on corrosion inhibition performance of epoxy/polyamide coating. Journal of Industrial and Engineering Chemistry. 2013;19. p.1031-1039.

[205] Na. T., Zhu. J., Sun. H., Xu. D., Zhang. Zh., Lew. Ch. M., Zhang. G. Composite membranes based on fully sulfonated poly(aryl ether ketone)/epoxy resin/different curing agents for direct methanol fuel cells. Journal of Power Sources. 2013; 230. p.290-297.

[206] Jin. F. L., Park. S. J. Synthesis and application of epoxy resins: A review. Journal of Industrial and Engineering Chemistry. 2015; 29. p.1-11.

[207] Nguyen. H. V., Kristiansen. H., Johannessen. R., Hoivik. N., Aasmundtveit. K. E. Rheological characterization of a novel isotropic conductive adhesive – Epoxy filled with metal-coated polymer spheres. Materials & Design. 2013; 46. p. 484-793.

[208] Park. Ch. H., Park. J. W., Kim. H. J. Preparation and characterization of dual curable adhesives containing epoxy and acrylate functionalities. Reactive and Functional Polymers. 2013;73. p. 641-646.

[209] Azeez. A. A., Park. S. J., Hui. D. Epoxy clay nanocomposites – processing, properties and applications: A review. Composites Part B: Engineering. 2013; 45. p. 308-320.

[210] Kandare. E., Myler. P. Evaluating the influence of varied fire-retardant surface coatings on post-heat flexural properties of glass/epoxy composites. Fire Saftey Journal. 2013; 58. p.112-120.

[211] Xu. H., Park. S. J. Synthesis of a novel phosphorus-containing flame retardant for epoxy resins. Bulletin of Korean Chemical Society. 2009; 30. p.2643-2646.

[212] Jin. F. L. Interfacial toughness properties of trifunctional epoxy resins/calcium carbonate nanocomposites. Material Science and Engineering: A. 2008; 475. p.190-193.

[213] Jin. F. L., Park. S. J. Thermal properties of epoxy resin/filler hybrid composites. Polymer Degradation and stability. 2012; 97. p.2148-2153.

[214] Choochottiros. Ch., Chin. I. J. Synthesis and characterization of polylactide–poly(methyl methacrylate) copolymer by combining of ROP and AGET ATRP. Journal of Industrial and Engineering Chemistry. 2012;18(3). p. 993-1000.

[215] Lee. Ch-T. Preparation of porous, nano-sized urea–formaldehyde polymer powder. Journal of Industrial and Engineering Chemistry. 2012; 18 (3). p. 919-925.

[216] Dittanet. P. Pearson. R. A. Effect of bimodal particle size distributions on the toughening mechanisms in silica nanoparticle filled epoxy resin. Polymer. 2013; 54(7). p.1832-1845.

[217] Rico. M., Montero. B., Bellas. R. Phase separation and morphology development in a thermoplastic-modified toughened epoxy. European Polymer Journal. 2012; 48(10). p.1660-1673.

[218] Rutledge. C. D. An Investigation and Research Regarding the Adhesive Qualities of Epoxy Resins in Architectural Construction: Kansas State University; 1961.

[219] Kut. S. EPOXY RESIN: surface coatings PART ONE. Anti-corrosion Methods and Materials. 1964; 11(8). p. 18-22.

[220] Hoontrakul. P., Pearson. R.A. Surface reactivity of polyimide and its effect on adhesion to epoxy. Journal of Adhesion Science and Technology. 2006; 20(16). p. 1905-1928.

[221] Akhter. T., Siddiqi. H. M., Akhter. Z., Butt. M. S. Synthesis and characterization of some polyimide-epoxy composites. e-Polymers. 2011;11(1).

[222] Kim. H. M., Kim. Y. S., Youn. J. R. Silica aerogel/epoxy composites with preserved aerogel pores and low thermal conductivity. e-Polymers. 2015;15.

[223] Ge. D., Yang. L., Li .Y., Zhao. J. Hydrophobic and thermal insulation properties of silica aerogel/epoxy composite. Journal of Non-Crystalline Solids. 2009; 355. p.2610-2615.

[224] Joo. P., Teo. N., Jana. S. Modular aerogel brick fabrication via 3D-printed molds. Additive Manufacturing. 2021; 46. 102059.

[225] Agrawal. D. Microwave sintering of ceramics, composites and metal powders. In: Fang ZZ, editor. Sintering of advanced materials; 2010. p. 222-248.

[226] Mondal. A., Shukla.A., Agrawal. D., Upadhyaya. A. Effect of Porosity and Particle Size on Microwave Heating of Copper. Science of sintering. 2010; 42(2).

[227] Kim. S. Y., Noh. Y.J., Lim. J. Silica aerogel/polyimide composites with preserved aerogel pores using multi-step curing. Macromolecular Research. 2013; 22. p.108-111.

[228] Cai. H., Liu. W., Mu. W., Liu.W., Zhang. X., Deng. Y. Aerogel Microspheres from Natural Cellulose Nanofibrils and Their Application as Cell Culture Scaffold. Biomacromolecules. 2014;15.p. 2540 –2547.

[229] Grace. H. P. Dispersion Phenomena in High Viscosity Immiscible Fluid Systems and Application of Static Mixers as Dispersion Devices in Such Systems. Chemical Engineering Communications Journal. 1982; 14. p.225-277.

[230] Sarawade. P. B., Hilonga. A., Jeon. S. J., Kim. H. T. Synthesis and characterization of micrometer-sized silica aerogel nanoporous beads. Material Letters. 2012; 81. p.37-40.

[231] Alnaief. M., Garcia- Gonzalez. C. A., Smirnova. I. Preparation of biodegradable nanoporous microspherical aerogel based on alginate. Carbohydrate Polymers. 2011; 84. p.1011-1018.

[232] Nalluri. V. R. Advancing Pharmaceutical Dry Milling by Process Analytics and Robustness Testing. Journal of Pharmaceutical Innovation. 2010; 5. p.100-108.

[233] Parrott. E.L. Milling of Pharmaceutical Solids. Journal of pharmaceutical sciences. 1974; 63(6). p. 813-829.

[234] Shekunov. B. Y., Tong. H. H., Chow. A. H. L. Particle size analysis in pharmaceutics: principles, methods and applications. Pharmaceutical Research. 2007; 24(2). p. 203-227.

[235] Lee. K. P. Georgel. G. Aerogel powder therapeutic agents. United states: Aspen Aerogels, Inc., Marlborough, MA (US) 2002.

[236] Randolph. R. B., Cardenas. T . Dry-Machining of Aerogel Foams, CH Foams, and Specially Engineered Foams Using Turn-Milling Techniques. Fusion Science and Technology. 2017.

[237] Bauer. U., Field. R., Floess. J. K., Frundt. J., Rouanet. S., Doshi. D. A. Aerogel particles and methods of making same. United States 2008.

[238] Aveyard. R., Bink. B. P., Clint. J.C. Emulsions stabilised solely by colloidal particles. Advances in colloid and interface science, 2003; 100-102. p. 503–546.

[239] Bajpai. P. Colloid and Surface Chemistry. Biermann's Handbook of Pulp and Paper. Elsevier 2018. p. 281-400.

[240] Yang. L., Du. K., Zhang. X-S. Influence factors on thermal conductivity of ammonia-water nanofluids. Journal of Central South University, 2012. 19(6): p. 1622-1628.

[241] Calderon. F. L., Bibette. J. Emulsion Science: Springer New York; 2007.

[242] Freddy. A., Walstra. P. Modern Aspects of Emulsion Science. 2007: Royal Society of Chemistry.

[243] U PS. Emulsions. Journal of Chemical Society. 1907; 91:2001-21

[244] Chen. L. AF, Ge. X., Shen. W. Food-grade pickering emulsions: preparation, stabilization and applications. Molecules. 2020; 25.

[245] Binks. B. P. Particles as surfactants—similarities and differences. Current Opinion in Colloid & Interface Science. 2002; 7(1-2). p. 21-41.

[246] Eow. J. S., Sharif. A. O, Williams. T. J. Electrostatic enhancement of coalescence of water droplets in oil: a review of the current understanding. Chemical Engineering Journal. 2001; 84. p.173-192.

[247] Ivanov. I. B. Stability of emulsions under equilibrium and dynamic conditions. Colloids and Surfaces A: Physicochemical and Engineering Aspects. 1997; 128. p.155-175.

[248] Yamashita. Y., Sakamoto. K. Emulsion and Emulsification Technology. In: Elsevier, editor. Cosmetic Science and Technology 2017.

[249] Krebs. T., Boom. R. Coalescence dynamics of surfactantstabilized emulsions studied with microfluidics. Soft Matter. 2012; 8(41). p. 10650-10657.

[250] Ferrari. P. Designing novel colloidal materials from polyphenol-polymer complexes: University of Oxford; 2016.

[251] Erbring. H. Introduction to colloid and surface chemistry: Elsevier Science; 1992.

[252] Griffin. W. C. Classification of Surface-Active Agents by “HLB”. Journal of cosmetic science. 1949; 1. p.311-1326.

[253] Rosen. M. Surfactants and Interfacial Phenomena: Wiley online library; 2012.

[254] Americas. I. The HLB system : a time-saving guide to emulsifier selection: Wilmington; 1984.

[255] Sakamoto. K., Majbach. H., Yamashita. Y. Cosmetic sciencand technology: Elsevier; 2002.

[256] Klapper. M., Haschick. R., Müller. K., Müllen. K. Oil-in-Oil Emulsions: A Unique Tool for the Formation of Polymer Nanoparticles. Accounts of Chemical Research Journal. 2008; 41. P.1190–1201.

[257] Zia. A., Thickett. S., Kempe. K. Advances and Opportunities of Oil-in-Oil Emulsions. CS Applied Materials & Interfaces 2020; 12(35).p. 38845-38861.

[258] Lu. X., Schmitt. A. K., Moore. J. S. A Robust Oil-in-Oil Emulsion for the Nonaqueous Encapsulation of Hydrophilic Payloads. Journal of the American Chemical Society 2018; 140. p.3619- 3625.

[259] Thompson. K. L., Derry. M. J., Armes. S. P. Non-aqueous Isorefractive Pickering Emulsions. Langmuir. 2015; 31. p. 4373-4376.

[260] Teo. N., Kulkarni. A., Jana. S. C. Continuous fabrication of core-shell aerogel microparticles using microfluidic flows. Journal of Colloid Interface Science. 2020; 561.p.772-781.

[261] Alnaief. M. SI. In Situ Production of Spherical Aerogel Microparticles. The Journal of Supercritical Fluids. 2011; 55. p.1118– 1123.

[262] Quell. A., Drenckhan. W., Stubenrauch. C. Monodisperse polystyrene foams via microfluidics – A novel templating route. Advanced Engineering Materials. 2015; 17. p.604– 609.

[263] Lee. K. J., Lee. J. K., Hwang. H. J. Fast synthesis of spherical silica aerogel powders by emulsion polymerization from water glass. ChemistrySelect. 2018; 3. p.1257-1261.

[264] Liu. M., Ga.n L., Pang. Y., Xu. Z., Hao. Z., Chen. L. Synthesis of titania–silica aerogel-like microspheres by a water-in-oil emulsion method via ambient pressure drying and their photocatalytic properties. Colloids and Surfaces A: Physicochemical and Engineering Aspects. 2008; 317. p. 490-495.

[265] Eaton. P., Quaresma. P., Soares. C., Neves. C., Almeida. M.P., Pereira. E. A direct comparison of experimental methods to measure dimensions of synthetic nanoparticles. Ultramicroscopy. 2017; 182. p.179-190.

[266] Inkson. B.J., Scanning electron microscopy (SEM) and transmission electron microscopy (TEM) for materials characterization, in Materials characterization using nondestructive evaluation (NDE) methods. 2016, Elsevier. p. 17-43.

[267] Kim. J., Kwon. J., Kim. M., Do. J., Lee. D., Han. H. Low-dielectric-constant polyimide aerogel composite films with low water uptake. Polymer. 2016; 48. p. 829-834.

[268] He. Sh., Shi. X., Bi. Y., Luo. X., Zhang. L. Rapid and facile synthesis of a low-cost monolithic polyamide aerogel via sol–gel technology. Materials Letters. 2015; 144. p. 82-84.

[269] Wang. Y., Cheng. Zh., Liu. M., Ji. J., Chang. X., Xu. Q., Liu. Y., Liu. X., Qin. J. Mechanically strong and tough polyimide aerogels cross-linked with amine functionalized carbon nanotubes synthesized by fluorine displacement reaction. Composites Science and Technology. 2020; 195. 108204.

[270] Allen. T. Particle size measurment. Journal of Dispersion Dcience and Technology, 1990. 13(5): p. 258.

[271] Allen. T. Powder sampling and particle size determination. 2003: Elsevier.

[272] Saadatnia. Z., Esmailzadeh. E., Naguib. H. E. A High Performance Triboelectric Nanogenerator Using Porous Polyimide Aerogel Film. Scientific reports. 2019; 9.

[273] Nguyen. B. N., Meador. M. A. B., Hamilton. J. G. B., McCorkle. L. S. Effect of Urea Links in the Backbone of Polyimide Aerogels. ACS Applied Polymer Materials. 2021; 3. p. 2027-2037.

[274] Mosanenzadeh. Sh., Saadatnia. Z., Park. Ch. B., Naguib. H. E. Double Dianhydride Backbone Polyimide Aerogels with Enhanced Thermal Insulation for High-Temperature Applications. Macromolecular Materials and Engineering. 2020; 305(4).1900777.

[275] Myers. D. Surfaces, interfaces, and colloids: priciples and applications. John Wiley & Sons, Inc. 2002.

[276] Naderi. M. Surface Area: Brunauer–Emmett–Teller (BET), in Progress in Filtration and Sepration. 2015. p. 585-608.

[277] Nasrollahzadeh, M. *Chapter 6* - Plant-Mediated Green Synthesis of Nanostructures: Mechanisms, Characterization, and Applications, in Interface Science and Technology. 2019, Elsevier. p. 199-322.

[278] Thommes. M., Kaneko. K., Neimark. A.V., Olivier. J.P., Rodriguez-Reinoso. F., Rouquerol. J. Physisorption of gases, with special reference to the evaluation of surface area and pore size distribution (IUPAC Technical Report). Pure and applied chemistry. 2015; 87. p.1051-1069.

[279] Villarroel-Rocha. J., Barrera. D., Sapag. D. Introducing a self-consistent test and the corresponding modification in the Barrett, Joyner and Halenda method for pore-size determination. Microporous and Mesoporous Materials, 2014. 200. p. 68-78.

[280] Lowell. S., Shields. J. E., Powder surface area and porosity. Chapman and Hall Ltd, 1984. vol. 2.

[281] Gregg. S. J. Adsorption, Surface Area and Porosity. Series.1982: Academic Press.

[282] Rouquerol. F., Maurin. G, Adsorption by Powders and Porous Solids. 2012.

[283] Sing. K. S. W. Reporting physisorption data for gas/solid systems with spacial reference to determination of surface area and porosity. Pure and Applied Chemistry. 1982; 54(11). p. 2201-2218.

[284] Mosanenzadeh. Sh. Gh., Park. Ch. B., Naguib. H. E. Polyimide aerogels with novel bimodal micro and nano porous structure assembly for airborne nano filtering applications. Royal Society of Chemistry. 2020; 10. p. 22909-22920.

[285] ASTM. Standard Test Method for Compressive Properties of Rigid Cellular Plastics. Volume 08.01. p. 5.

[286] Fan.Yang. Simulation and Analysis of Mechanical Properties of Silica Aerogels: From Rationalization to Prediction. Materials 11(2):214. 2018;11.

[287] Woignier. T., Duffours. L. Densification and Strengthening of Aerogels by Sintering Heat Treatments or Plastic Compression. Gels. 2018;4(1).p.12.

[288] Zhang. X., He. M., Gao.Y., Li. Ch., Mo. X., Sun. G., You. B. A synergistic strategy for fabricating an ultralight and thermal insulating aramid nanofiber/polyimide aerogel. Royal Society of Chemistry. 2021; 5. p.804-816.

[289] Ren. B., Rong. Y., Wang. L., Lu. Y., Xi. X., Yang. J. Nanofibrous aerogel bulk assembled by cross-linked SiC/SiOx core–shell nanofibers with multifunctionality and temperatureinvariant hyperelasticity. ACS Nano. 2019; 13. p.11603-11612.

[290] Qiuxia. F., Duan. Ch., Yan. Z., Liu. L., Yu. J., Ding. B. Highly Carboxylated, Cellular Structured, and Underwater Superelastic Nanofibrous Aerogels for Efficient Protein Separation. Advanced Functional Materials. 2019; 29(13).1808234.

[291] Hong. J. Y. SEH, Park. S., Park. H. S. Highly-efficient and recyclable oil absorbing performance of functionalized graphene aerogel. Chemical Engineering Journal. 2015; 269. p. 229-235.

[292] Yuan. R., Lu. X., Dong. Zh., Lu. Q. Rigid and flexible polyimide aerogels with less fatigue for use in harsh conditions. Chemical Engineering Journal. 2022; 428.p.131193.

[293] Kistler. S.S. The Relation between Heat Conductivity and Structure in Silica Aerogel. J Phys Chem. 2002; 39(1). p.79–86.

[294] Listler. S. S. The calculation of the surface area of microporous solids from measurements of heat conductivity. Journal of Physical Chemistry. 1942; 46(1). p.19–31.

[295] White. J. F. Silica Aerogel: Effect of Variables on Its Thermal Conductivity. Industrial and Engineering Chemistry. 1939; 31(7). p. 827–831.

[296] Philip. D. Vortrage uber die Kinetische Theorie der Materie und der Elektrizitat. Berlin: B G Teubner. 1914.

[297] Xu. L. Transport Properties of Porous Media: University of Wurzburg, Germany; 1991.

[298] Scheuerpflug. P., Morper. H., Neubert. G. Low-Temperature Thermal Transport in Silica Aerogels. Journal of Physics D-Applied Physics. 1991; 24(8). p.1395–1403.

[299] Reif. F. Fundamentals of Statistical and Thermal Physics. McGraw-Hill, Inc. 1965.

[300] Zhao. D., Gu. X., Jajja. S. A., Yang. R. Measurement Techniques for Thermal Conductivity and Interfacial Thermal Conductance of Bulk and Thin Film Materials. Journal of Electronic Packaging. 2016; 138(4). 040802.

[301] Ghaffari. Sh., Park. Ch. B., Naguib. H. E. Double Dianhydride Backbone Polyimide Aerogels with Enhanced Thermal Insulation for High-Temperature Applications. Macromolecular Materials and Engineering. 2020 ;305(4).1900777.

[302] Hou. X. M. Y.,Zhang. R., Fang. D. Super-flexible polyimide nanofiber cross-linked polyimide aerogel membranes for high efficient flexible thermal protection. Chemical Engineering Journal. 2021; 417. 129341.

[303] Tang. G. H., Tao. W. Q. Thermal transport in nano-porous insulation of aerogel: Factors, models and outlook. Energy and Buildings. 2015; 90.p.701-721.

[304] Fang. B. L. A modified activated carbon aerogel for high-energy storage in electric double layer capacitors. Journal of Powder Sources. 2006; 163. p.616-622.

[305] Halasz. I. GH. Aerogel Columns in Gas Chromatography. Analytical Chemistry. 1966 ;38. p. 281-286.

[306] Goncalves. V. S. S., Poejo. J., Matias. A. A., Heinrich. S., Duarte. C. M. M., Smirnova. I. Alginate-based hybrid aerogel microparticles for mucosal drug delivery. European Journal of Pharmaceutics and Biopharmaceutics. 2016; 107.p.160-170.

[307] García-González. C.A., Alnaief . M., Smirnova. I. Polysaccharide-based aerogels—Promising biodegradable carriers for drug delivery systems. Carbohydrate Polymers. 2011; 86. p.1425-1438.

[308] Rose. M., Palkovits. R. Isosorbide as a renewable platform chemical for versatile applications. ChemSusChem, 2012; 5(1). p. 167-176.

[309] Kobayashi. H., Fukuoka. A. Synthesis and utilisation of sugar compounds derived from lignocellulosic biomass. Green Chemistry, 2013; 15(7). p. 1740-1763.

[310] Khoee. S., Yaghoobian. M. Niosomes: A novel approach in modern drug delivery systems, in Nanostructures for drug delivery. 2017, Elsevier. p. 207-237.

[311] Poe. G., Lambdin. A. A ., Koldan. N., Irvin. D, Highly Branched Non-Crosslinked Aerogel Having Macropores, Methods of Making, and Uses Thereof 2018: United state.

[312] Jin. Q., Horie. K.,Yokota. R., Mita. I. Polyimides with alicyclic diamines. I. Syntheses and thermal properties. Journal of Polymer Science. 1993; 31. p. 2345-2351.

[313] Hamciuc. E., Bruma. M., Belomoina. N. M. Synthesis and characterization of new poly phenylquinoxaline(ether)imides. Russian Chemical Bulletin. 2004; 53. p.2035-2040.

[314] Cheng. J., Zheng. G., Sun. Y. Synthesis and imidization of polyamic acid. Advanced Materials Research. 2011; 301. p.9-15.

[315] Dayarian. S., Majedi Far. H., Yang. L. Macroporous Polyimide Aerogels: A Comparison between Powder Microparticles Synthesized via Wet Gel Grinding and Emulsion Processes. Langmuir, 2023. 39(5): p. 1804-1814.

[316] Thommes. M., Neimark. A. V., Olivier. J. P., Rodriguez-Reinoso. F., Rouquerol. J ., Sing. K. W. Physisorption of gases, with special reference to the evaluation of surface area and pore size distribution (IUPAC Technical Report. Pure Applied Chmistry. 2015; 87. p.1051–1069.

[317] ASTM. Standard Test Method for Determining Pore Volume Distribution of Catalysts and Catalyst Carriers by Mercury Intrusion Porosimetry. 2012.

[318] Maghsoodi. M., Yari. Z. Effect of drying phase on the agglomerates prepared by spherical crystallization. Iran J Pharm Res. 2015; 14. p.51-57.

[319] Terence. A. Particle size measurement. New York: Chapman and Hall; 1990.

[320] Decuzzi. P. The adhesive strength of non-spherical particles mediated by specific interactions. Biomaterials. 2006; 27. p.5307-5314.

[321] Maghsoodi. M. Effect of drying phase on the agglomerates prepared by spherical crystallization. Iran Journal Pharm Res. 2015; 14. p.51-57.

[322] Muksin. S. Yulianto. S.N. Thermogravimetric study of the effect of particle size on the spontaneous combustion of indonesian low rank coal Applied Mechanics and Materials. 2013; 330. p. 101-105.

[323] Hussain. Z., Sahudin. Sh. Preparation, characterization and colloidal stabilityn of Chitosan-tripolyphosphate nanoparticles: optimisation of formulation and process parameters. International Journal of Polymer Science. 2016; 8(3). p. 297-308.

[324] Fan. W., Xu. Z., Ni. H. Formation mechanism of monodisperse, low molecular weight chitosan nanoparticles by ionic gelation technique. Colloids Surf B. 2012; 90. p.21-27.

[325] Xu. Y. Zhan. M., Wang. K. Structure and Properties of Polyimide Films during a FarInfrared-Induced Imidization Pro. Polymer Science. 2004; 42(13). p.2490-2501.

[326] Chen. W., Zhang. B., Yang. Sh., Liu. Ch-Y. Thermal imidization process of polyimide film: Interplay between solvent evaporation and imidization. Polymer. 2017; 109. p.205-215.

[327] Vermeir. L., Sabatino. P., Balcaen. M., Declerck. A., Dewettinck, K., Martins. J. C., Meeren. P. Effect of Molecular Exchange on Water Droplet Size Analysis in W/O Emulsions as Determined by Diffusion NMR. Journal of Colloid Interface Sci. 2016; 463. p.128-136.

[328] Balcean. M., Dewettinck. K., Vander Meeren. P. Effect of dilution on particle size analysis of w/o emulsions by dynamic light scattering. Journal of Dispersion Dcience and Technology. 2020; 42(6).p. 869-879.

[329] ASTM D-1621, A., Standard Test Method for Compressive Properties of Rigid Cellular Plastics.